2011

Numerical modeling of natural and anthropogenic impacts on the regional climate of Kilimanjaro (Tanzania)

Jonathan G. Fairman Jr.

NUMERICAL MODELING OF NATURAL AND ANTHROPOGENIC IMPACTS ON THE REGIONAL CLIMATE OF KILIMANJARO (TANZANIA)

by

JONATHAN G. FAIRMAN, JR.

A DISSERTATION

Submitted in partial fulfillment of the requirements
for the degree of Doctor of Philosophy
in
The Department of Atmospheric Science
to
The School of Graduate Studies
of
The University of Alabama in Huntsville

HUNTSVILLE, ALABAMA

2011

In presenting this dissertation in partial fulfillment of the requirements of a doctoral degree from The University of Alabama in Huntsville, I agree that the Library of this University shall make it freely available for inspection. I further agree that permission for extensive copying for scholarly purposes may be granted by my adviser, or in his absence, by the Chair of the Department or the Dean of the School of graduate Studies. It is also understood that due recognition shall be given to me and to the University of Alabama in Huntsville in any scholarly use which may be made of any material in this dissertation.

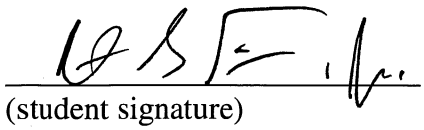

(student signature)

10/26/11

(date)

DISSERTATION APPROVAL FORM

Submitted by Jonathan G. Fairman, Jr. in partial fulfillment of the requirements for the degree of Doctor of Philosophy in Atmospheric Science and accepted on behalf of the Faculty of the School of Graduate Studies by the dissertation committee.

We, the undersigned members of the Graduate Faculty of the University in Alabama in Huntsville, certify that we have advised and/or supervised the candidate on the work described in this dissertation. We further certify that we have reviewed the dissertation manuscript and approve it in partial fulfillment of the requirements of the degree of Doctor of Philosophy in Atmospheric Science.

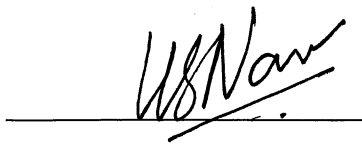
10/26/2011 Committee Chair
(date)

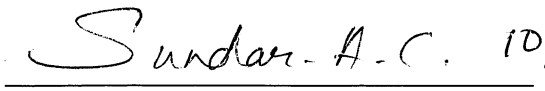

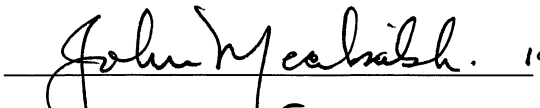

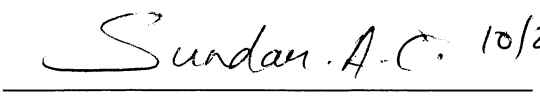
Department Chair


College Dean


Graduate Dean

ABSTRACT

The School of Graduate Studies
The University of Alabama in Huntsville

Degree Doctor of Philosophy College/Dept. Science/Atmospheric Science

Name of Candidate Jonathan G. Fairman, Jr.

Title Numerical Modeling of Natural and Anthropogenic Impacts on the Regional Climate of Kilimanjaro (Tanzania)

Glacier recession on Kilimanjaro has been linked to reduction in precipitation and cloudiness largely due to large scale changes in tropical climate. However, local terrain interaction with large scale flow field is an important modulator of precipitation and cloudiness at the top of Kilimanjaro and land use change has the potential to impact conditions at the peak. This study examines a typical annual cycle of orographic cloud and precipitation formation over Kilimanjaro utilizing Regional Atmospheric Modeling System (RAMS) at 1km grid spacing to simulate evolution of atmospheric conditions over this region for the period of July 2007 through June 2008. The RAMS simulation is analyzed to determine processes that modulate climate at the peak, and additional RAMS experiments are conducted to determine how these processes are impacted if current land cover is replaced by pristine and deforested landscapes.

Four flow regimes are found in RAMS experiment: southerly (JJA), east-southeasterly (SON), northeasterly (DJF) and southeasterly (MAM). Cloud and precipitation at the top of Kilimanjaro is most impacted during the northeasterly and southeasterly regimes. Flow oriented parallel to topographical gradient along the rim of a

concave terrain feature is the major contributor to high precipitation events at the peak. Terrain interactions with large scale flow contributes to ~60% and ~20% of the total precipitation at lower (2000-4000m) and higher elevations (>5000m), respectively, with the influence of terrain generated thermal circulations extending to the peaks of Kilimanjaro. Land cover change indeed impact cloud and precipitation formation at peak, with reforestation and total deforestation both increasing precipitation at the peak. The processes though which mountain top conditions are affected differs, with reforestation increasing the strength of the terrain generated circulation. Deforestation leads to an increase in surface wind speeds, low-level convergence which in turn enhances precipitation at higher elevations. However, deforestation reduces precipitation at lower elevations, while reforestation produces a general increase in precipitation at all elevations. This study finds that regional climate forcing due to land cover change impacts cloud formation and precipitation at Kilimanjaro and is a factor to be considered in the interpretation of observed changes, namely glacier recession.

Abstract Approval: Committee Chair _____

Department Chair Sundar. A. C. 10/26/2011

Graduate Dean Rhonda Kay Gaede 12/14/11

ACKNOWLEDGMENTS

Completion of this dissertation would not have occurred without the efforts of my adviser, Dr. Udaysankar S. Nair. Dr. Nair's work and support greatly helped me learn what I was capable of during my tenure in this department. I would also like to thank Dr. Sundar A. Christopher, who served as my co-adviser in 2006-07 and was instrumental in evaluating the quality of my work throughout my graduate career. Thanks are also due to Dr. John R. Christy, Dr. Robert O. Lawton, and Dr. John R. Mecikalsi for serving as members of my graduate committee. I wish to thank Drs. Christopher and Nair for supporting my research during 2006-07, with Dr. Nair supporting my research in 2007-08 and Fall 2011. From 2008-2011 this research was supported via the NASA Earth and Space Science Fellowship program. Resources supporting this work were provided by the NASA High-End Computing Program through the NASA Advanced Supercomputing Division at Ames Research Center, where the modeling runs were performed. I would also like to thank those current and former graduate students that have helped me greatly during my time here, including, in a very particular order: Dr. J. Cody Kirkpatrick, Dr. Will McCarty, Dr. Christopher Hain, Christopher Siewert, Christopher Schultz, Elise Schultz, Patrick Buckley, Paul Schmid, Aaron Naeger, Rob Junod, and Ryan Wade. I wish to also thank my parents, Jonathan Sr. and Rosemarie, for continually providing encouragement during my research. Finally, to the TNDC, CB, RJR, CC, and DGY, you know who you are.

TABLE OF CONTENTS

Page

LIST OF FIGURES

LIST OF TABLES

LIST OF ACRONYMS AND ABBREVIATIONS

AVHRR	Advanced Very High Resolution Radiometer
CTL	Control model simulation
DEF	Deforested model simulation
ESD	Error standard deviation
FAO	Food and Agricultural Organization
FOC	Frequency of cloud occurrence
GCM	Global circulation model
GFS	Global Forecasting System
ITCZ	Intertropical Convergence Zone
LWP	Cloud liquid water path
MODIS	Moderate Resolution Imaging Spectroradiometer
NOAA	National Oceanic and Atmospheric Administration
NDVI	Normalized difference vegetation index
NOTOPO	Model simulation without topographic variation
RAMS	The Regional Atmospheric Modeling System
REF	Reforested model simulation
RMSE	Root mean square error
SRTM	Shuttle Radar Topography Mission
TRMM	Tropical Rainfall Measuring Mission

USGS	United States Geological Survey
UTC	Coordinated Universal Time
WRF	The Weather Research and Forecast Model

CHAPTER 1

INTRODUCTION

Orographic effects on regional weather and climate are significant [*Barry,* 2008; *Pielke*, 2002; *Whiteman*, 2000] with the dominant effect being modification of the background flow via interactions with the terrain. Recent studies have indicated that mountain weather and climate can be disproportionately affected by both natural and anthropogenic forcing [*Pounds et al.,* 1999; *Still et al.,* 1999; *Nair et al.,* 2003, 2010; *Ray et al.,* 2006; *Fairman et al.,* 2011]. Since modification of mountain weather and climate has significant implications for regional water resources and ecological sustainability, there is a need to understand the impact of differing anthropogenic and natural climate forcings and their interactions. General circulation models (GCMs) are often used to investigate climate variability and potential global climate change, but do not often adequately resolve small scale terrain features. Thus orographic feedbacks related to climate change [*Salathe et al.,* 2008] are not captured, leading to incomplete views of climate change effects on a local to regional scale, where processes related to orographic feedbacks can dominate.

Quantification of natural and anthropogenic climate forcings is exceptionally important in locations like Mount Kilimanjaro (Tanzania), where glacial recession on the peak of Kibo has been linked to large scale climate variability and change [*Thompson et al.*, 2002; *Kaser and Osmaston,* 2002; *Kaser et al.*, 2004; *Cullen et al.*, 2006; *Mote and Kaser,* 2007.]. The climate signal related to the drying glaciers has been traced to coupled atmosphere-ocean dynamics in the Indian Ocean [*Molg and Kaser,* 2011] with studies documenting large scale drying in the region [*Molg et al.*, 2008], but the role of the naturally-occurring local feedbacks associated with these large scale changes are not known.

There is also much interest in the altitudinal variation of the proportion of precipitation generated by terrain forcing to that from large scale processes, which has been examined by *Molg et al.* [2009b] through the use of numerical modeling. *Molg et al.* [2009b] utilized model simulations assuming a bell shaped mountain of similar size and shape to Kilimanjaro, finding that terrain-generated convection is a substantial contributor of precipitation; however, it does not capture complex terrain features or seasonal variation. *Molg and Kaser* [2011] utilizes the Weather and Research Forecast Model (WRF) to simulate circulation patterns over East Africa and Kilimanjaro, utilizing complex topography. However, *Molg and Kaser* [2011] only considers two months: August 2005, and April 2006, and therefore does not account for the seasonal variation of atmospheric flow. The focus of *Molg and Kaser* [2011] is suitability of the WRF output for use as a glacier mass balance model, and not on the analysis of topographic influences on the regional climate. Work of *Pepin et al.* [2010] provides observational insights on the natural climate forcing, but is limited in space to one

transect on the southwest slope. Although observational analysis of *Pepin et al.* [2010] provides conceptual models of the naturally occurring circulations and topographic effects, it does not directly characterize spatial and temporal variations in precipitation an cloud cover.

Thus, there is a need for numerical modeling analysis that examine the changes in meteorology at relatively finer scales over long time periods (extending analysis to one year or more, contrasting the one month of *Fairman et al.* [2011] and two months of *Molg and Kaser*, [2011]), concentrating on extending conceptual models presented via observational analysis [*Pepin et al.*, 2010] as well as idealized modeling [*Molg et al.*, 2009] that consider the natural forcings of terrain generated circulations. Previous research exists on montane cloud formation [*Kirshbaum and Durran*, 2004; *Fuhrer and Schar*, 2005], as well as precipitation distribution via mountain-atmosphere interactions [*Jiang et al*, 2003; *Rottuno and Houze*, 2007], but these are limited in space and time with theoretical topographic forcing. Simulations using real topography [e.g., *Wastl and Zangl*, 2010] are generally limited in time to a few days.

It is important to understand the natural variations that force regional circulation systems such as montane-atmosphere interactions, but it is also necessary to consider the anthropogenic differences that modify the regional climate. On a global scale, the majority of anthropogenic influence associated with climate change is linked to greenhouse gas forcing [*IPCC*, 2007]. However, on a regional scale such as a tropical mountain, land cover change can have a substantial impact through secondary effects, even though the net climate forcing associated with the albedo changes from land use

(attributed as ~0.2 Wm^{-2}) is much lower than global greenhouse gas forcing (~2.64 Wm^{-2}).

Prior research [*Chase et al.*, 1999; *Lawton et al.*, 2001; *van der Molen*, 2002; *Nair et al.*, 2003, 2010; *Bruijnzeel*, 2004; *Ray et al.*, 2006; *van der Molen et al*., 2010] shows land use change can alter topographically generated circulation patterns as well as temperature and moisture of air masses that can ultimately impact orographic cloud formation. Atmospheric response of changes in upwind land cover is very dependent on geographic location. In Costa Rica, modeling analysis [*Lawton et al.*, 2001; *Nair et al.*, 2003, 2010; *Ray et al.*, 2006] and observational analysis *[Nair et al.*, 2008] show that deforestation increases cloud base height of boundary layer clouds via reducing available moisture. However, *van der Molen* [2002] found that coastal deforestation in an island setting in Puerto Rico resulted in enhanced slope circulations leading to invigoration of montane cloud formation.

Initial results from atmospheric numerical modeling of Mount Kilimanjaro *[Fairman et al.*, 2011] show that land cover change on the upwind side of Kilimanjaro has an impact on the altitude of maximum cloudiness and precipitation, but the primary differences are related to wind speed increases and flow pattern differences due to decreases in surface roughness with decreasing amounts of forest cover. However, *Fairman et al.* [2011] was limited to one month in the dry season, and therefore was unable to adequately resolve convection at high elevations. Extension of this analysis to annual time scales is needed to understand the role of terrain forcing on the mountain top climate of Kilimanjaro and the modulation of the same by land cover change.

From this previous work, two topics that require further investigation are the natural forcing caused by the terrain interactions with the atmosphere, and the modification of these natural forcings via anthropogenic change, specifically upwind land cover change. This research investigates these two topics in the region of Kilimanjaro (Tanzania) utilizing atmospheric numerical modeling. The Regional Atmospheric Modeling System (RAMS) is used to perform four numerical modeling experiments specifying: current-day vegetation and topography, current-day vegetation with smoothed topography (no mountain), a completely deforested land use scenario and a reforested land use scenario that replaces current farmland with tropical rainforest, and the analysis of these simulations is used to address the following specific questions:

- What is the nature of annual cycle of cloud and precipitation formation at the peak of Kilimanjaro and what are the dominant processes that govern this cycle?
- What is the role of large scale versus regional processes in determining the cloud and precipitation formation at the peak of Kilimanjaro?
- Are the regional scale processes sensitive to land use change, a dominant regional climate forcing factor?
- How is the mountain top climate impacted by land use change?
- What are the physical processes though which land use change affect conditions at the peaks of Kilimanjaro?

This dissertation is structured as follows. The area of interest for this study, namely Kilimanjaro in Tanzania, is discussed in Chapter 2. The discussions include an overview of regional climate patterns over East Africa, temporal evolution of spatial

distribution of glacial ice at the peak of Kilimanjaro, and history of the land use change in the region. Chapter 3 discusses the methodology employed, including a description of the Regional Atmospheric Modeling System [*Cotton et al.,* 2003] and also the design of numerical modeling experiments used in this study. Evaluation of performance of RAMS over the study region is discussed in Chapter 4. Also included is an analysis of annual cycle of orographic cloud and precipitation formation and also factors that influence conditions at the peak of Kilimanjaro. Contribution of terrain forcing to precipitation formation as function of altitude is also discussed in Chapter 4. Chapter 5 discusses the effects of land use change on regional climate for the dry season, when the impact of land use change is expected to be at a maximum due to higher reliance on local processes during the dry season. Chapter 6 extends the dry season analysis to other seasons and analyzes the processes through which land use change impacts climate at the peak of Kilimanjaro. Chapter 7 provides an overall summary of the study and a discussion on broader implications and future research directions.

CHAPTER 2

THE STUDY AREA OF MOUNT KILIMANJARO (EAST AFRICA)

Mount Kilimanjaro is located at 3.05° S and 37.33° E, near the border of Tanzania and Kenya. It represents an eroded ancient volcano occupying an area of approximately 75 km x 75 km, with three peaks (Shira, Mawenzi, and Kibo) rising from 800 m in the savannah plain to 5890 m at the peak of Kibo. Kilimanjaro is famous for the ice sheets that exist on the peak of Kibo, which served as the backdrop of Ernest Hemingway's short story "The Snows of Kilimanjaro," originally published in *Esquire* magazine in 1936, and the resulting 1952 film starring Gregory Peck.

In recent history, the glacier retreat on the peak of Kibo has been characterized as an apparent phenomenon of large-scale climate variability and change [*Thompson et al.*, 2002], although the mechanism of the change remains unclear. Glacial retreat has been attributed to both increasing temperatures [*Thompson et al.*, 2002; *Thompson et al.*, 2009] and regional differences due to changes in moisture [*Mölg et al.*, 2003; *Mölg et al.*, 2010] causing reduced clouds in higher elevations, resulting in less precipitation and more solar radiation at the peak of Kibo. However, prior studies [*Mote and Kaser*, 2007; *Molg and Kaser*, 2011; *Torbick et al.*, 2009; *Hemp et al*, 2005, 2009] suggest that regional climate forcing factors such as land cover change and biomass burning should also be considered in the analysis of changes occurring at Kilimanjaro. In this context, the present chapter will briefly review the regional climate setting of East Africa, history of the ice surfaces

throughout the Holocene on the peaks of Kilimanjaro and also the nature of land use change around Mount Kilimanjaro.

2.1 East African Climate

In order to discuss the natural and anthropogenic effects on the regional climate change on Kilimanjaro, it is first necessary to understand the nature of regional climate in the East African region. East African climate is dominated by a bimodal precipitation distribution that is dependent on the monsoon cycle within the Indian Ocean region [*Hastenrath*, 2000]. The transitions in the monsoon cycle lead to rainy seasons from March to May (the "long rains") and the "short rains" from October to December [*Molg et al.*, 2008]. These monsoon cycles are also characterized by the south-to-north transition of the ITCZ from March to May and the north-to-south transition of the ITCZ from October to December [*Camberlin and Philippon*, 2002]. Traditionally, studies have focused on seasonal mean area-average rainfall totals, mainly attempting to diagnose the mean flows [*Mutai and Ward*, 2000].

The general circulation patterns over East Africa are dominated by two main events: the passage of the ITCZ and the Indian Ocean monsoon cycle. Within these main synoptic events, there are several smaller features that can be mentioned, mainly the Eastward Equatorial Jet and East African Jet [*Paegle and Geisler*, 1986]. The Eastward Equatorial Jet brings in moisture from the Indian Ocean that then precipitates when the ITCZ is over East Africa. *Hastenrath* [1991] shows that the East African Low-Level Jet reaches the Horn of Africa from May to June, but is blocked by the ITCZ from February to April. The East African jet generally is an easterly motion of wind that turns towards the north when it encounters the topography of the East African rift. This turns the air so

that the flow is near southerly when it crosses the equator [*Paegle and Geisler*, 1986]. After the flow crosses the equator, the general mean flow turns westerly and turns into the monsoon situation for India. During ITCZ passage during the rainy seasons, the flow over East Africa is dominated by a northeasterly flow over the horn of Africa, bringing moisture from the Indian Ocean, whereas in the vicinity of Kilimanjaro the flow is of easterly orientation.

The highest precipitation amounts in East Africa occur during the two seasons when the ITCZ is in transition and an easterly flow regime dominates. These two seasons provide the majority of rainfall in East Africa: for example, the average annual rainfall at Moshi, Tanzania, near Kilimanjaro, is 103 cm, of which 69 cm generally falls during the "long rain" period from April to May. There have been much study on the potential teleconnections between the "short rains," "long rains" and other ocean phenomena, specifically Indian Ocean sea surface temperatures as well as the El Niño – Southern Oscillation. *Mutai and Ward* [2000] found a teleconnections between warm ENSO phase (El Niño), and September rainfall, with reduced rainfall during this phase. However, the October to December rainfall is enhanced during a warm ENSO phase while there is little on the MAM (March-April-May) rainfall. *Latif et al*. [1999] showed that during December-January of 1997/1998, Indian Ocean SST anomalies could account for up to 60% of the variance in observed East African rainfall that year. *Hastenrath* [2000] states that the MAM rains are far more abundant, but that the October-December (OND) rains are far more variable due to the variances between the Eastward Equatorial Jet and the other equatorial westerlies. When winds are from the south to southwest, there is little precipitation in the area around Mount Kilimanjaro. Winds from the east -northeast

along with passage of the ITCZ from March-May and October-November are the sources of most of the rainfall. During the rainy seasons, over 70% of the moisture originates from the Indian Ocean [*Molg et al.*, 2006].

There has been little research in temperature patterns over East Africa because of the lack of good temperature data in developing countries. However, recent analyses have been performed [*Christy et al.*, 2009] that show the maximum temperatures have not been changing over East Africa over the past century. Average temperatures in the Kilimanjaro region are around 23° C at Moshi, Tanzania, which is at the base of Mount Kilimanjaro. Temperatures at the peak are generally around -7° C [*Molg and Hardy*, 2004]. The temperatures are more dictated by solar radiation and the position in the tropics than anything else, and do not show significant warming over the previous few decades.

Paleoclimatic analysis [*Hastenrath*, 2000] shows significant change in the East African climate over the past two centuries. *Hastenrath* [2000] suggests that this climatic change, which is concentrated in the last two decades of the 19th century, coincides with the acceleration equatorial westerlies and oceanic jets. Prior to this, sedimentary records show substantially higher lake levels in East Africa as well as more extensive glaciation on Mount Kenya, Kilimanjaro, and Mount Ruwenzori. The slowing of the jets would allow more precipitation to take place in the boreal summer months (June-July-August) when the drier air is transported by these wind patterns. With stronger Southern Indian trade winds and weaker equatorial westerlies, precipitation is enhanced over East Africa.

Monthly mean temperature (Figure 2.1) and precipitation (Figure 2.2) variations over East Africa exhibits this seasonal variation. Temperature decreases in the austral winter (the months of June, July, and August) over the entire region, but the general temperature range is very small (at most 5° C), which is expected in tropical regions. The precipitation varies across central East Africa, with the more equatorial stations showing a bimodal distribution in rainfall during the "long" and "short" rains while the more poleward stations showing one rainy season timed with the larger excursions of the ITCZ. These monthly mean precipitation and temperature plots show station data from differing locations in the East African region over the course of an entire year. The lengths of records that are used to derive these databases vary considerably (between 10 to 60 years). However, these station plots show the bimodal distribution of rainfall in most of East Africa, with the Somali horn displaying a slightly different pattern of rainfall due to the prevailing winds in that location. It is also clearly visible that Kilimanjaro and other locations until around 10° S have a bimodal distribution in rainy seasons, as the ITCZ passes over the location twice. At further poleward locations, there is a singular rainy season that results in precipitation during one defined season (as seen in Malawi and Somalia).

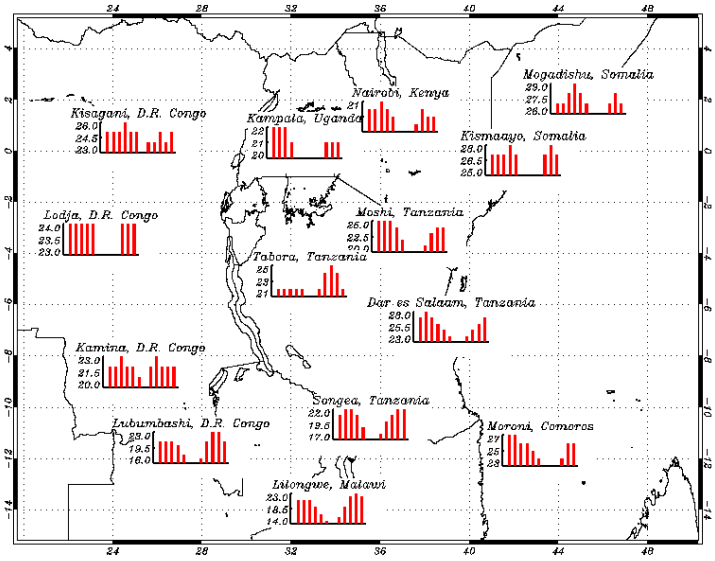

Figure 2.1 Monthly mean temperatures (degrees Celsius) at several locations in East Africa.

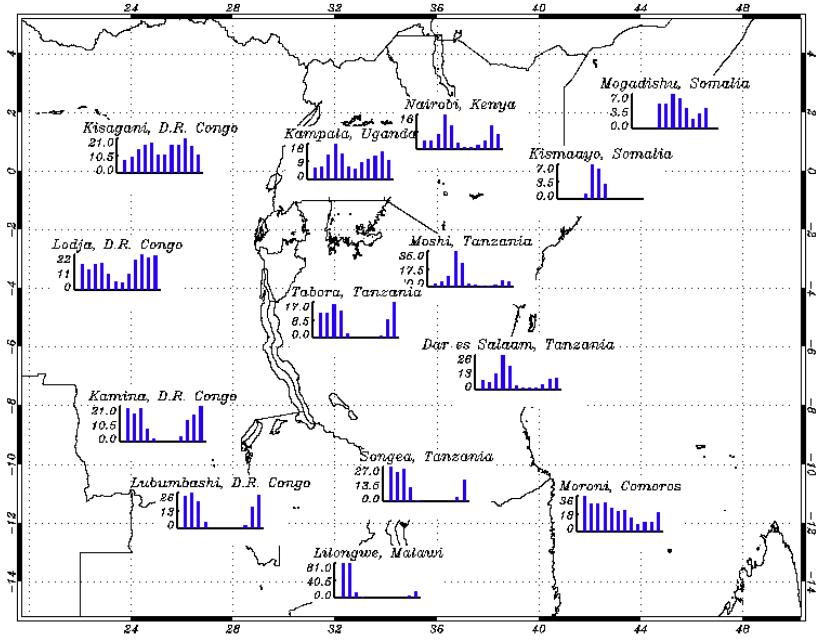

Figure 2.2 Monthly mean precipitation (cm) at several locations in East Africa.

2.2 History of Kilimanjaro Glaciers

The ice fields on Kilimanjaro exhibit significant variation during the Holocene. Before discussing the history of the ice on Kilimanjaro, it is necessary to discuss the nomenclature to avoid confusion. Currently, there exist several differing areas of permanent ice on the peak of Kibo, covering ~1.85 km^2 as of 2007 [*Thompson et al.,* 2009]. *Hastenrath and Greischar* [1997] describes nomenclature for ice fields on Mount Kilimanjaro, giving numbers for various ice features as well as letters for ice entities derived from a 1976 survey. Figure 2.3 shows the ice extent from *Thompson et al.* [2009] as well as nomenclature from *Hastenrath and Grieschar* [1997].

These 20 separate ice features can be grouped together to describe the summit ice field that existed in 1912. *Hastenrath and Greischar* [1997] group these glaciers into separate entities, named A-G. Figure 2.6 shows the main remaining glacial entities, with A denoting the current day Northern and Eastern Ice Fields, B denoting a very small feature near the Eastern Ice Fields, C denoting the small ice feature that existed between the Eastern Ice Fields and the southern slope fields, D denoting the southern slope fields, E being the ice feature that at one time contained Arrow, Little and Great Barranco and has currently devolved to only being Little Barranco (Little Breach), F being the Furtwangler Glacier, and G being a summit ice field at the center of the mountain that was last mapped in 1912.

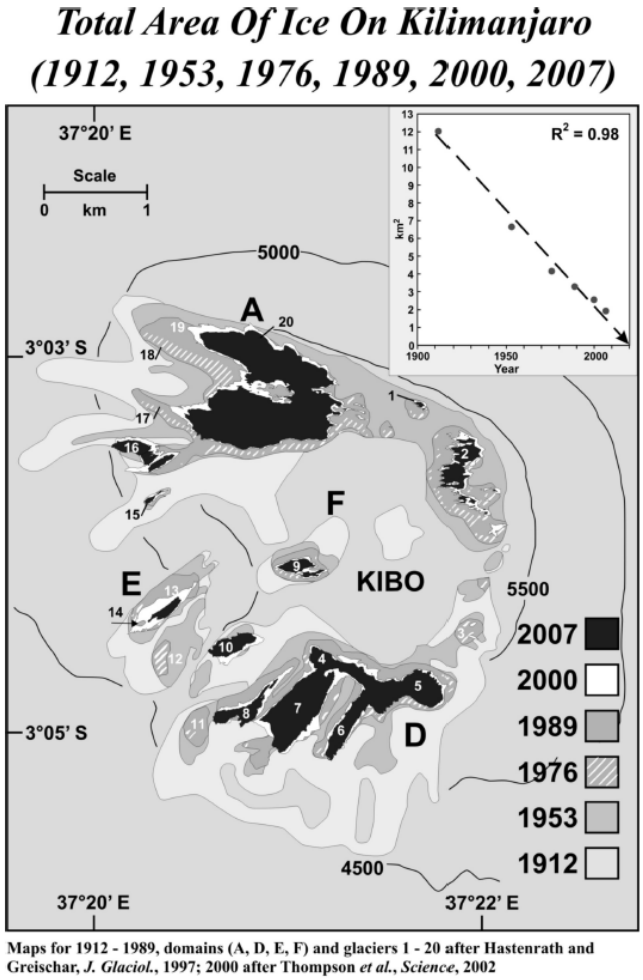

1	Eastern Ice Field
2	Eastern Ice Field
3	Ratzel Glacier
4	Southern Ice Field
5	Rebmann Glacier
6	Decken
7	Kersten
8	Heim
9	Furgwangler
10	Diamond
11	Baletto
12	Great Barranco (Breach)
13	Little Barranco (Breach)
14	Arrow
15	Uhlig
16	Little Penck
17	Great Penck
18	Drygalski
19	Credner
20	Northern Ice Field

Figure 2.3 Map of Kilimanjaro ice fields from *Thompson et al.* [2009]. Domains (letters) and numbers are added according to the classification of *Hastenrath and Greischar* [1997]. The table lists the glacier names.

After describing this nomenclature, it is possible to discuss the relative effects from the present day back through the early 20th century and into the Holocene. From these 20 ice features identified from 1976 mapping, four no longer exist: Ratzel Glacier, Baletto Glacier, Great Barranco, and Arrow Glacier. Ratzel Glacier was last mapped in 2000, when it had an area of 1,703 m^2, and had disappeared in analysis of *Cullen et al.* [2006], which used data from 2003. The smallest existing feature is Uhlig Glacier (#15). This feature is now only 3,904 m^2, a loss of 5,328 m^2 from the analysis performed in 2000.

The main features on the peak of Kilimanjaro are the Southern slope ice fields (Entity D), the Northern and Eastern ice fields (Entity A), Little Barranco (Entity E), and Furtwangler Glacier (Entity F). These total 1.85 km^2 as of 2007, but in 2001, comprised 2.51 km^2, meaning that there was a loss of approximately 3.43% of glacial area per year since then. Table 2.1 denotes the areal extent of the glaciers for each mapping denoted in Figure 2.3.

Table 2.1 Ice Area Historical Extent

Area (10^3 m^2)	**A**	**B**	**C**	**D**	**E**	**F**	**G**	**Total**
1912	5676	3	27	5011	811	372	158	12058
1953	3829	0	16	2156	493	181	0	6675
1976	2440	0	0	1409	209	113	0	4171
1989	1900	0	0	1168	147	90	0	3305
2000	1454	0	0	912	93	57	0	2516
2003	1304	0	0	1025	132	49	0	2510
2006	1162	0	0	692.5	34.6	40.2	0	1929
2007	1101	0	0	691.8	22.7	35.0	0	1851

There are discrepancies between the 2003 survey based on satellite imagery [*Cullen et al.,* 2006] due to differences in what was classified as transient snow and permanent ice, as well as the alteration by *Cullen et al.* [2006] to include Arrow Glacier into entity E. The glaciers have had approximately the same form since the 1976 inventory, with the split of the Northern and Eastern ice fields occurring between 1953 and 1976. In generally, there was massive reduction of glaciers in the early part of the century, with more glacial decline occurring from 1912 to 1953 then from 1953 to today. Since 1989, there has been a large hole in the Northern Ice Field that by 2007 caused it to split into two differing tongues. This will hasten the decline of the Northern Ice Field until its potential split into two completely different parts.

Each one of the glaciers that exists today on the mountain can be traced back to a large ice field that existed in the past. The Northern and Eastern ice fields once were one ice field that stretched along the entire side of the mountain crater and included slope glaciers on the western side of the mountain. These features were still visible in a 1964 analysis of the moraines surrounding the peaks of Kilimanjaro [*Osmaston,* 1965]. The southern slope fields stretched down to ~4500m from their current minimum altitude of ~5000 m.

Outside of the work done for the 20^{th}-21^{st} century decline of the glaciers of Kilimanjaro, there has been significant research performed on the past glaciations. *Mark and Osmaston* [2008] describes these glaciations based on dating moraines around the peaks of Kibo and Mawenzi. *Osmaston* [1965] mapped the main moraine flows on these two peaks for the last glacial maximum, shown in Figure 2.4.

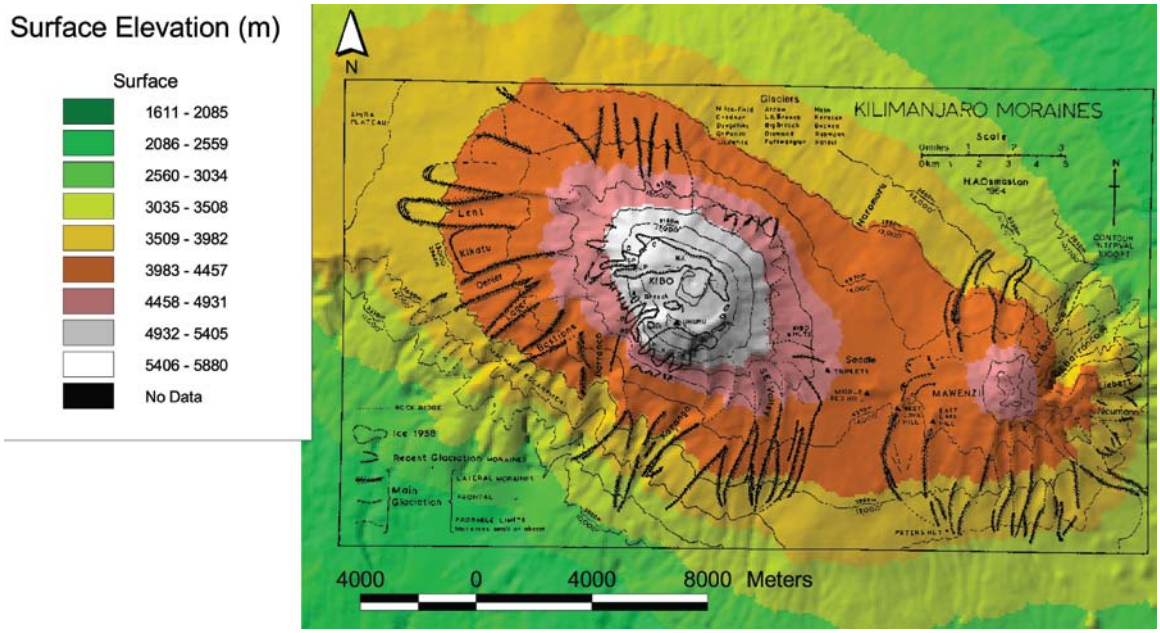

Figure 2.4 Moraines of Holocene glaciers overlaid on shaded digital elevation model of Kilimanjaro. From in *Mark and Osmaston* [2008].

Over the Holocene, there has been one main glaciation of Kilimanjaro. *Osmaston* [1965] created maps of what he considered to be the Last Glacial Maximum (LGM, ~20,000 years ago or 20 ka), and based on cosmogenic radionucliede ^{36}Cl dating [*Shanahan and Zreda*, 2000], they have dated moraines to 16.3±1.9 ka and 15.8±2.5 ka. Palaeoglaciers on Kilimanjaro had the form of several tongues from a central ice cap on the summits of Kibo and Mawenzi. It is possible that these two ice sheets joined in the middle of the "saddle" between the two peaks. Even though *Thompson et al.* [2002] gives details on several differing climate shifts over the past 11.7 ka, there is no moraine evidence for glacial advances over the remaining Holocene, indicating near-constant glacial decline since the LGM.

2.3 Regional Land Use and Land Cover Change

The southern slopes of Mount Kilimanjaro have experienced much land use and land cover change over recent history. The history of the land cover change described here is primarily based on the analysis of *Soini* [2005] that traces the arrival of humans and their resulting changes to the ecology of the region. Recent effects of the land use/land cover change as well as the effects caused by climate shifts have been studied by *Hemp* [2005, 2009] as well as others [*Lambrechts et al.*, 2002; *Torbick et al.*, 2009].

The original landscape on Kilimanjaro started to change with the arrival of the first immigrants to the area at least 500 or 600 years before present (ybp), who began to transform the original forested area into an agroforestry system. Bananas were introduced to the area during the 16th century as contact with outsiders (such as the early trading caravans) was established. Significant land use change began with the arrival of missionaries and early colonialists in the late 19th century, which increased with the arrival of the railroad to Moshi in 1912.

With the arrival of the railroad, former lands used for grazing were termed vacant and taken over by arriving Europeans. The Chagga people, natives of the area adopted growing of coffee in the 1930s, which led to major modifications of the farming system, changing the upland grazing area into coffee plantations. With this coffee income, farmers started to purchase improved cattle and moved to more of a stall-feeding approach versus range-feeding that is the norm for the natural Zebu cattle. Expanding coffee production and the introduction of home gardens took over the majority of the upland areas, leading to the food production shifting to the lowland areas. During this time, population density increased from 26 persons km^{-1} during the 1920s to

50 persons km^{-1} in 1948, with some areas over 200 persons km^{-1}. These high density areas were mainly in the large-scale plantations. Population doubled again from 1948 to 1967.

From 1961 to 2000, there was significant decline in the amount of bush land in the lower elevation areas, where they have been replaced by cultivated fields. Bush lands are now found only in the highland areas. Despite population densities of 650 persons km^{-1} on the higher slopes near Moshi, the home garden areas did not increase due to distance from the city. During this time period, the forested areas near the upper boundary of the study area of *Soini* [2005] stayed relatively similar due to being classified as a forest reserve. This "Half-mile zone" is open for fallen branch collecting as well as livestock fodder, however *Lambrechts et al.* [2002] noted illegal logging, burning, charcoal production, village establishment, grazing and cultivation and landslides and quarries in this area on the south slope of Kilimanjaro.

While *Soini* [2005] gives a historical background to the changing land on the southern slopes of Kilimanjaro, *Hemp* [2005, 2009] establishes the recent structural changes caused by fire as well as the impact of climate change on the natural system. By studying Landsat imagery from 1976 and 2000, *Hemp* [2009] showed that nearly 15% of Kilimanjaro's forest cover was destroyed by fire since 1976, being replaced with a bush land that extended its total area by 50 km^2 downslope. A total loss of 150 km^2 of upper montane and subalpine forests since 1976 was estimated as well, which corresponds to an estimated loss of 20 million m^3 of water lost per year due to the lack of fog deposition [*Hemp*, 2005]. This, combined with a loss of lower elevation forests of 450 km^2 since 1929, leads to a total loss of 600 km^2, or 1/3 of Kilimanjaro's former forest cover. This

does not include any deforestation that has occurred in the past 10 years, during which illegal logging has still been documented.

In contrast to the massive forest loss, evaluation of some satellite imagery over the course of the past 30 years has shown an increase in normalized differenced vegetation index (NDVI) over this same time span [*Torbick et al.*, 2009]. Detailed NDVI analysis from AVHRR analysis has shown that there has been an increase in NDVI in the upper elevation zones, which could be due to both enhanced bush vegetation taking over the former forested areas due to a potential upwards shift in precipitation maxima as well as an upward vegetation shift at the expense of ice accumulation.

CHAPTER 3

METHODOLOGY

This study uses numerical modeling experiments to examine the annual cycle of meteorology of Kilimanjaro. We also examine the hypothesis that land cover change at the lower slopes surrounding Mount Kilimanjaro impact topographically induced circulation patterns and convection, thereby altering the environmental conditions of the upper slopes and peak. The following sections provide a brief description of the RAMS, the model configuration used in this study, and the land cover scenarios.

3.1 The Regional Atmospheric Modeling System (RAMS)

The RAMS [*Cotton et al.*, 2003] is a nonhydrostatic numerical modeling system that uses finite difference formulation to solve conservation equations for atmospheric mass, momentum, heat and water (all three phases). The RAMS utilizes a polar-stereographic grid with Arakawa-C grid stagger in the horizontal and a sigma terrain-following coordinate in the vertical. Explicit microphysical parameterization [*Walko et al.*, 2000] and convective parameterization schemes [*Kain and Frisch*, 1990; *Tremback* 1990] are both available within RAMS. Parameterization of varying sophistication can be selected for accounting of sub-grid scale turbulence [*Smagorisnky*, 1963; *Lilly*, 1962;

Hill, 1974; *Mellor and Yamada*, 1982] and also atmospheric radiative transfer [*Mahrer and Pielke*, 1977; *Chen and Cotton*, 1983; *Harrington et al.*, 1997]. The temporally varying lateral boundary conditions in RAMS are usually specified using analysis and forecast fields from other global models. The Land Ecosystem Atmosphere Feedback 3 (LEAF-3) sub-model [*Walko et al.*, 2000] is used in RAMS for representing soil-vegetation-atmosphere transfer (SVAT).

Satellite observations of Normalized Difference Vegetation Index (NDVI) from the Advanced Very High Resolution Radiometer (AVHRR) are generally used to specify vegetation phenology, which, in combination with vegetation type, is used to parameterize vegetation characteristics such as Leaf Area Index (LAI), aerodynamic roughness, and other parameters within LEAF-3. However, in this study, mean monthly Moderate Resolution Imaging Spectroradiometer derived NDVI [*Justice et al.*, 1998] is used to specify current vegetation cover (see Section 3.2). This will allow the vegetation to be consistent with reality over the period of study. The global, 30-second resolution land use categorization data set of *Olson* [1994] is used to specify vegetation type. The United States Geological Survey 30 second global digital elevation dataset [http://edc.usgs.gov/products/elevation/gtopo30/gtopo30.html] is generally used by RAMS to specify terrain, but when appropriate the Shuttle Radar Topography Mission (SRTM) 90 m resolution topography dataset [*Jarvis, 2004*] is also utilized in this study (see Section 3.2). The global 1 degree United Nations Food and Agricultural Organization dataset [FAO 1971-1981, *Gerakis and Baer*, 1999] is used to specify the soil type in RAMS.

3.2 Numerical Model Experiments

We use four different numerical modeling experiments, assuming 4 differing land scenarios in which 1) the current vegetation coverage persists; 2) the area is completely deforested; 3) the area is completely reforested; and 4) the mountainous topography is deleted. The RAMS simulation assuming current vegetation coverage (referred as CTL from hereon) is used as the point of comparison for the other vegetation scenarios, as well as to evaluate the performance of RAMS over the study time by comparing it against surface observations and satellite observations of cloudiness. The model experiment is then repeated for deforested and reforested land use scenarios (referred from hereon as DEF and REF), as well as the simulation without any topography (referred to from hereon as NOTOPO).

All of the experiments utilized in this study use a hierarchy of four nested grids (Table 3.1), with the outermost grid of 64 km grid spacing covering a domain that includes substantial portion of east Africa and the Indian Ocean (Figure 3.1b). Three interior nested grids of progressively decreasing grid spacing are used to establish a central domain with grid spacing of 1 km that covers Kilimanjaro (Figure 3.1a). Details of numerical model configuration used in the experiments are given in Table 3.1.

In all the experiments utilized in this study, RAMS is integrated for 24 hours from July 2007 through June 2008, comprising 366 total days. Initial atmospheric conditions are specified using Global Forecast System (GFS-ANL) three-dimensional 1° by 1° grid analysis of wind, temperature and moisture fields at 0 UTC. The lateral boundaries and the model top are constrained by nudging it towards conditions consistent with the

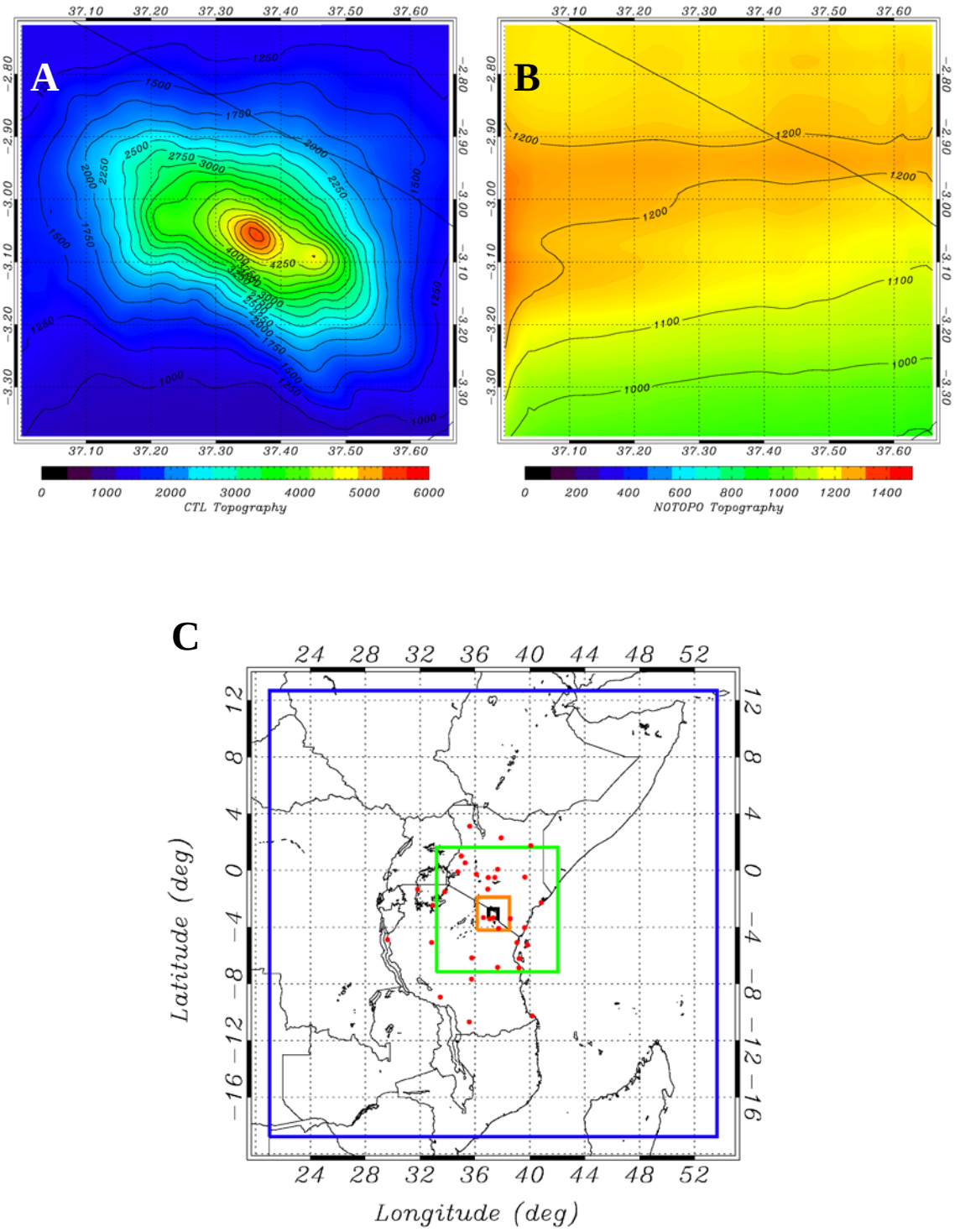

Figure 3.1 a) Model topography of Kilimanjaro for the CTL simulation. b) Model topography for the NOTOPO simulation. c) Model grid domains. Blue indicates Grid 1, green Grid 2, orange Grid 3, and black Grid 4. Also noted are sites used for analysis of temperature, dewpoint, and wind speed (red dots within the green grid).

Table 3.1: List of Model Configuration Parameters

Configuration	**Grid 1**	**Grid 2**	**Grid 3**	**Grid 4**
NX x NY	56 x 56	62 x 62	66 x 66	74 x 74
ΔX/ ΔY (km)	64	16	4	1
NZ	45	45	45	45
ΔZ (m) /Stretching Ratio	60 / 1.08	60 / 1.08	60 / 1.08	60 / 1.08
ΔT (sec)	90	22.5	5.625	1.41
Center Latitude/Longitude	3.05° S, 37.33°E	3.05° S, 37.33°E	3.05° S, 37.33°E	3.05° S, 37.33°E
Radiation Parameterization	Harrington	Harrington	Harrington	Harrington
Lateral Boundary Conditions	Klemp/ Wilhelmson	Klemp/ Wilhelmson	Klemp/ Wilhelmson	Klemp/ Wilhelmson
Convective Parameterization	Kain-Fritch	Kain-Fritch	Explicit	Explicit
Eddy Diffusion	Mellor-Yamada	Mellor-Yamada	Mellor-Yamada	Mellor-Yamada
Microphysics	Explicit	Explicit	Explicit	Explicit
LEAF-3	Yes	Yes	Yes	Yes
Soil Levels	4	4	4	4
Vegetation Patches	1	1	1	1

temporally varying GFS analysis fields available every 6 hours. This experimental design, which is consistent with the Type I dynamic downscaling classification of *Castro et al.* [2005], is chosen to retain realism of the large scale atmospheric conditions around the study area. However, the soil moisture and temperature conditions in the RAMS experiments are initialized from GFS analysis only once, at 0 UTC of 1 July 2007 and carried through the entire year. Thus, unlike the atmospheric conditions which are reinitialized every 24 hours, soil moisture and temperature is allowed to continuously evolve in all the experiments during the entirety of the study period. This follows a Type II dynamical downscaling approach in order to retain the evolution of the finer scale features of the land boundary conditions that have a longer memory compared to atmospheric conditions.

Land cover in the CTL experiment (Figure 3.2a, Table 3.2) is specified using the Olson Global Ecosystem (OGE) dataset, the default land over characterization dataset used by RAMS [*Loveland et al.,* 2000]. Note that RAMS LEAF-3 SVAT sub-model reduces the 96 land cover classes in the OGE dataset to 30 land cover classes. In the DEF experiment, all evergreen and deciduous forest as well as wooded grassland areas are converted to short grass (Figure 3.2b, Table 3.2) extending the extremes of deforestation found along the western and northern slopes shown in the land cover used in the CTL experiment. While the arbitrary conversion of 53.5 % of the total land cover from wooded grassland is not very realistic, it provides an upper bound for the effects of land use change. In the REF experiment, all the current areas that are farmland or urbanized are replaced by evergreen forests (Figure 3.2c) to match the land cover found at the middle elevations in the CTL experiment.

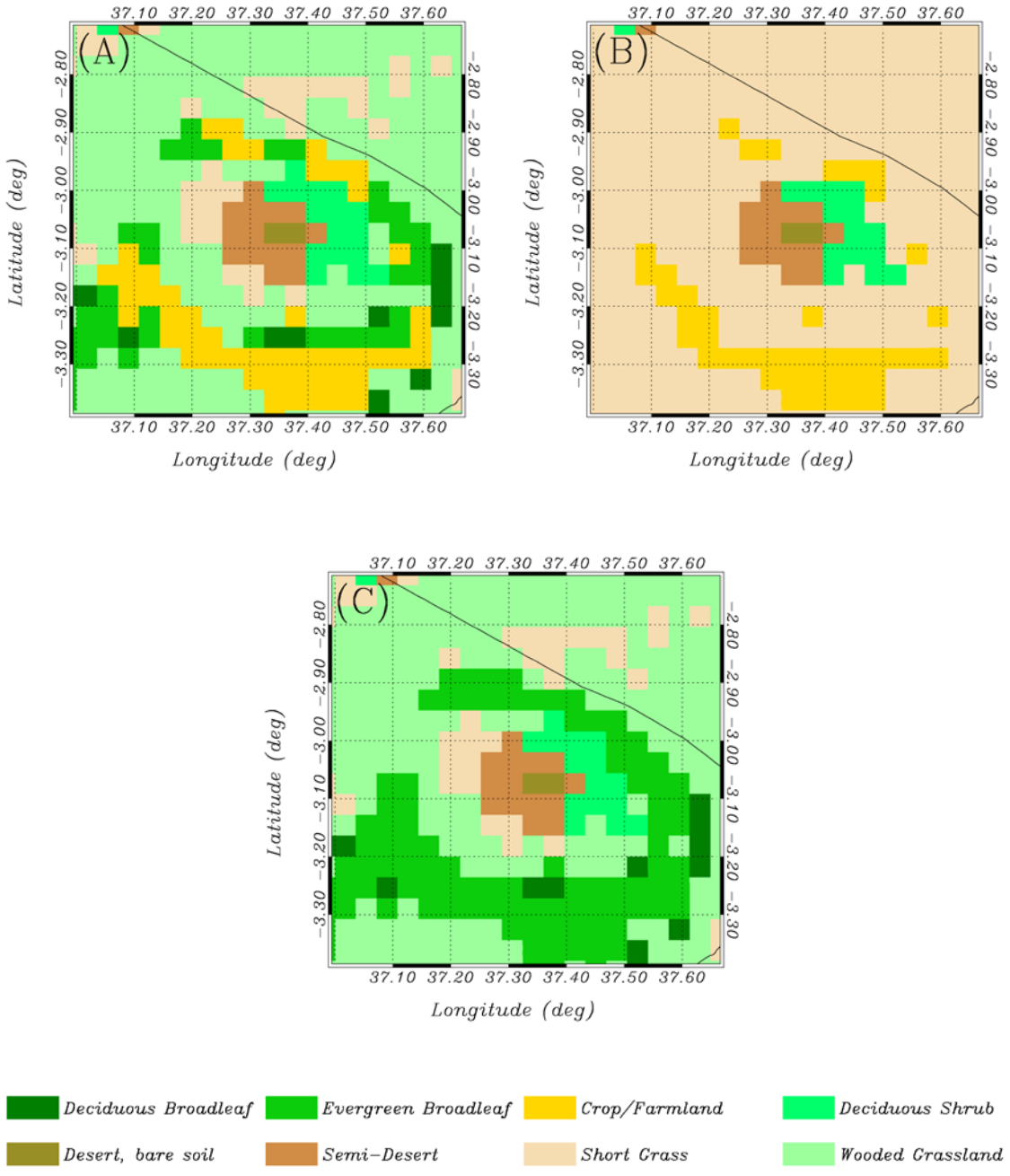

Figure 3.2 Land use change scenarios for the three model experiments for model Grid 4. Labels denote main land use classes. a) Control land use classification as given by LEAF-3. The high elevation areas are denoted by semi-desert (brown) and desert (dark brown) in the center of the domain. b) Deforested land use scenario. c) Reforested land use scenario. Kelly green denotes evergreen broadleaf classification, where dark green is the deciduous broadleaf classification.

Table 3.2 Area of Land Cover Classification for Model Experiments

LEAF-3 Classification	**CTL Area**	**CTL %**	**REF Area**	**REF %**	**DEF Area**	**DEF %**
Deciduous Broadleaf	184	3.4 %	184	3.4%	0	0%
Evergreen Broadleaf	544	9.9%	1436	26.2%	0	0%
Short Grass	508	9.2 %	508	9.2%	4316	78.8%
Cropland	788	14.4%	0	0%	672	12.3%
Wooded Grassland	2932	53.5 %	2844	51.9%	0	0%

As discussed briefly in Section 3.1, in the CTL scenario the spatial distribution of NDVI is specified using a more representative MODIS-Terra derived NDVI data set over the course of the year rather than the default AVHRR derived NDVI dataset used by RAMS. The domain averaged AVHRR and MODIS-Terra derived NDVI over Grid 4 are 0.522 to 0.553 respectively for July of 2007. Since the OGE land use characterization derived from AVHRR satellite observations in 1992, it does not account for additional land use change that has occurred in the recent years. Utilization of the MODIS derived NDVI field will partially account for these additional changes in land use since the fractional vegetation cover and leaf area indices and vegetation albedo are parameterized to be dependent on the annual cycle of NDVI. This also will take into account the changes found near Kilimanjaro from *Torbick et al.* [2008]. In the DEF and REF scenarios, average values of NDVI of the altered land use classifications were used. For example, an average NDVI for the evergreen forested class, determined from the MODIS NDVI data used in the CTL experiment, is used to specify the NDVI for evergreen forest that replaces urban or farmland regions in the REF experiment.

The NOTOPO scenario briefly discussed earlier is used to look at the effects that the topography has on the local circulations, and examines how those effects differ throughout the year as well as the percentage of precipitation that can be associated with local processes. The mountainous topography was removed and the surrounding topography was averaged to form the topography shown in Figure 3.1b.

The results from these four numerical modeling experiments, each comprising 8784 hours of model output, are discussed in detail in the following two chapters. Chapter 4 discusses the meteorology of Kilimanjaro, examining seasonal progression of meteorological fields as well as a thorough discussion of the verification methods utilized throughout this study. There is a consistent focus on local-scale events, and the meteorological dependency of the local circulations on synoptic fields. Chapter 5 discusses the meteorology and land use change effects using these model setups for one month (July) of the dry season, whereas Chapter 6 uses this model setup and methodology for one year of analysis over the same period of time for the analysis in Chapter 4.

CHAPTER 4

ANNUAL VARIATION OF CLOUD FORMATION, PRECIPITATION FORMATION AND TERRAIN-INDUCED CIRCULATIONS AT KILIMANJARO

This chapter utilizes the Regional Atmospheric Modeling System (RAMS) to simulate the annual cycle of atmospheric evolution over Kilimanjaro, with a grid spacing of 1 km. The high spatial resolution simulation along with other experiments are used to: 1) Develop conceptual models of cloud and precipitation patterns associated with differing flow regimes; 2) Determine flow regions/conditions under which precipitation accumulation occur at the peaks of Kilimanjaro and; 3) Determine the proportion of the total precipitation generated by terrain interactions as a function of altitude. The goal of the analysis presented is to develop a body of knowledge that will support further research on the role of large scale and regional climate forcing on glacier recession in Kilimanjaro.

4.1 Evaluation of the RAMS Simulations

The performance of RAMS over the study area is evaluated by comparing: 1) Surface meteorology in the CTL experiment to surface meteorological observations collected by the meteorological services in Kenya and Tanzania (Figure 3.1); 2) Special observations of surface meteorology [*Pepin et al.*, 2010] for nine sites located along a

transect on the southwestern slopes of Kilimanjaro extending from elevation of 1890 m to 5803 m; 3) Spatial distribution of accumulated rainfall in the CTL experiment to estimates derived from the Tropical Rainfall Mapping Mission satellite observations and also surface observations of rainfall, and 4) Comparing characteristics of orographic clouds in the CTL experiment to Moderate Resolution Imaging Spectroradiometer derived cloud products.

4.1.1 Large scale surface temperature, dew point and wind comparisons

The RAMS simulated 2 m temperature, dew point and winds are evaluated by comparing it against corresponding observations (Figures 4.1 a, b, and c) following the approach of *Zhong and Fast* [2003]. While it is ideal to conduct this analysis for the inner grids with finer grid spacing (grid 3 or 4), East Africa is a relatively observation-poor area [*Christy et al.,* 2009] and thus only few regular meteorological observations are available over grid 4. Thus hourly surface observations of 2 m temperature, dew point and winds [National Climate Data Center DS-3505 dataset] are compared to corresponding RAMS simulated values from grid G2 (16 km grid spacing, Figure 3.1b) in the CTL experiment to maximize the number of observations available for the analysis. Analysis is restricted to surface stations that provide observations for at least 50% of the study period. This criterion is satisfied by 30 stations within the NCDC DS-3505 dataset and hourly observations from these stations were compared to the CTL experiment to compute time series and average values (Table 4.1) of root mean square error (RMSE), bias, and error standard deviations.

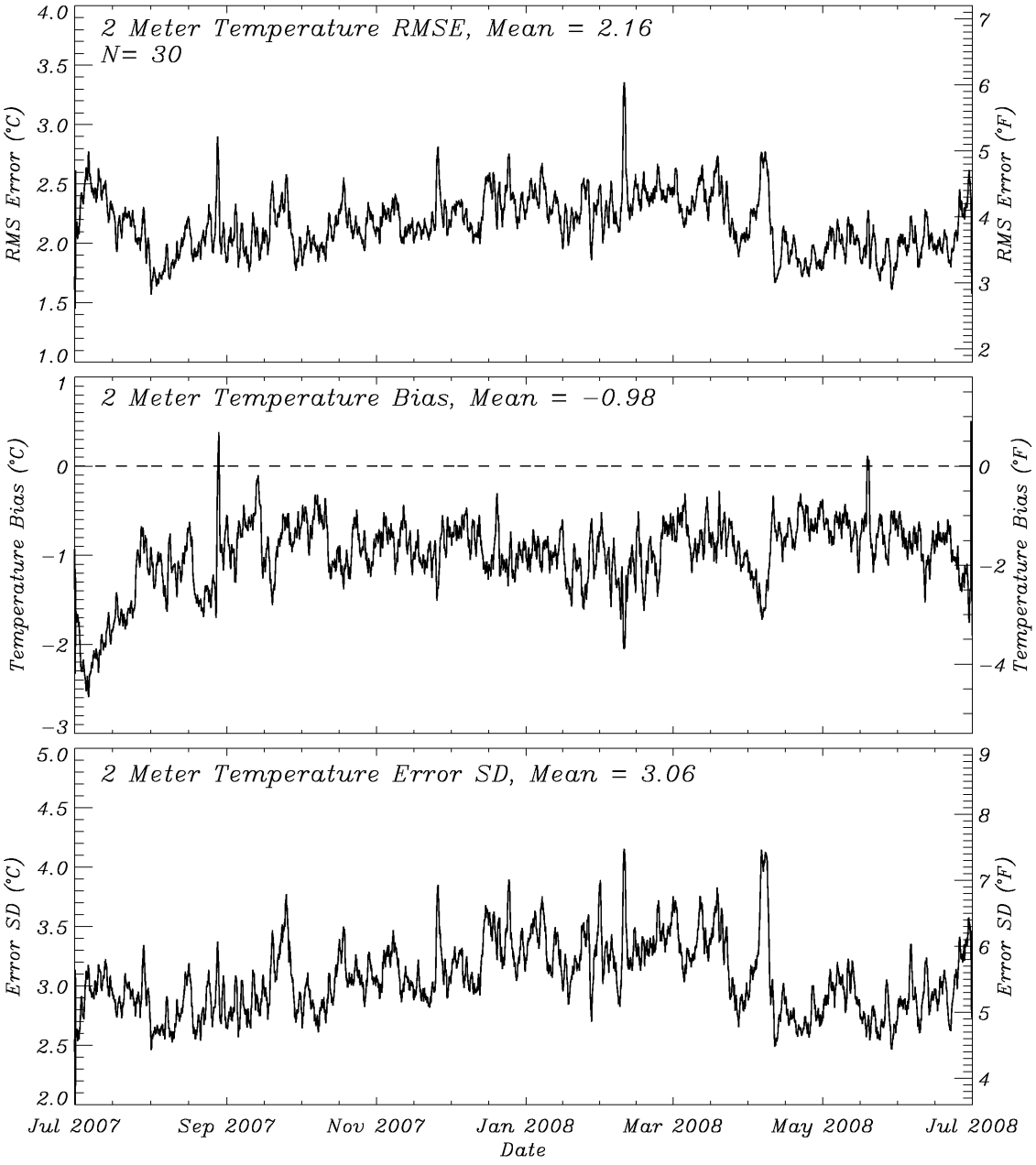

Figure 4.1 Root mean square error, bias, and error standard deviation of two meter temperature (a), dewpoint (b), and wind speed (c). Values are smoothed to daily means after being computed on an hourly basis. Mean values are for all hourly timesteps.

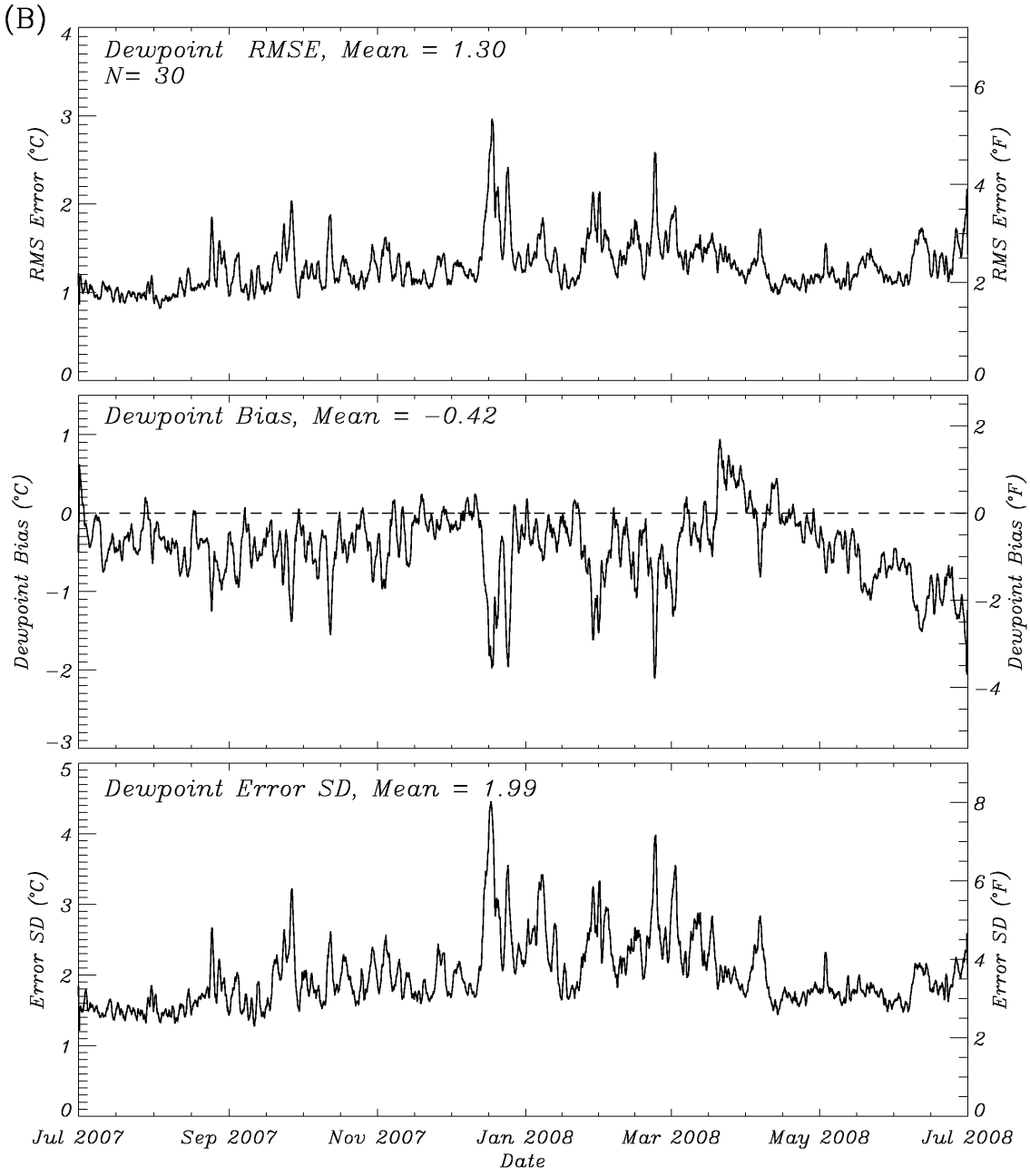

Figure 4.1 (continued).

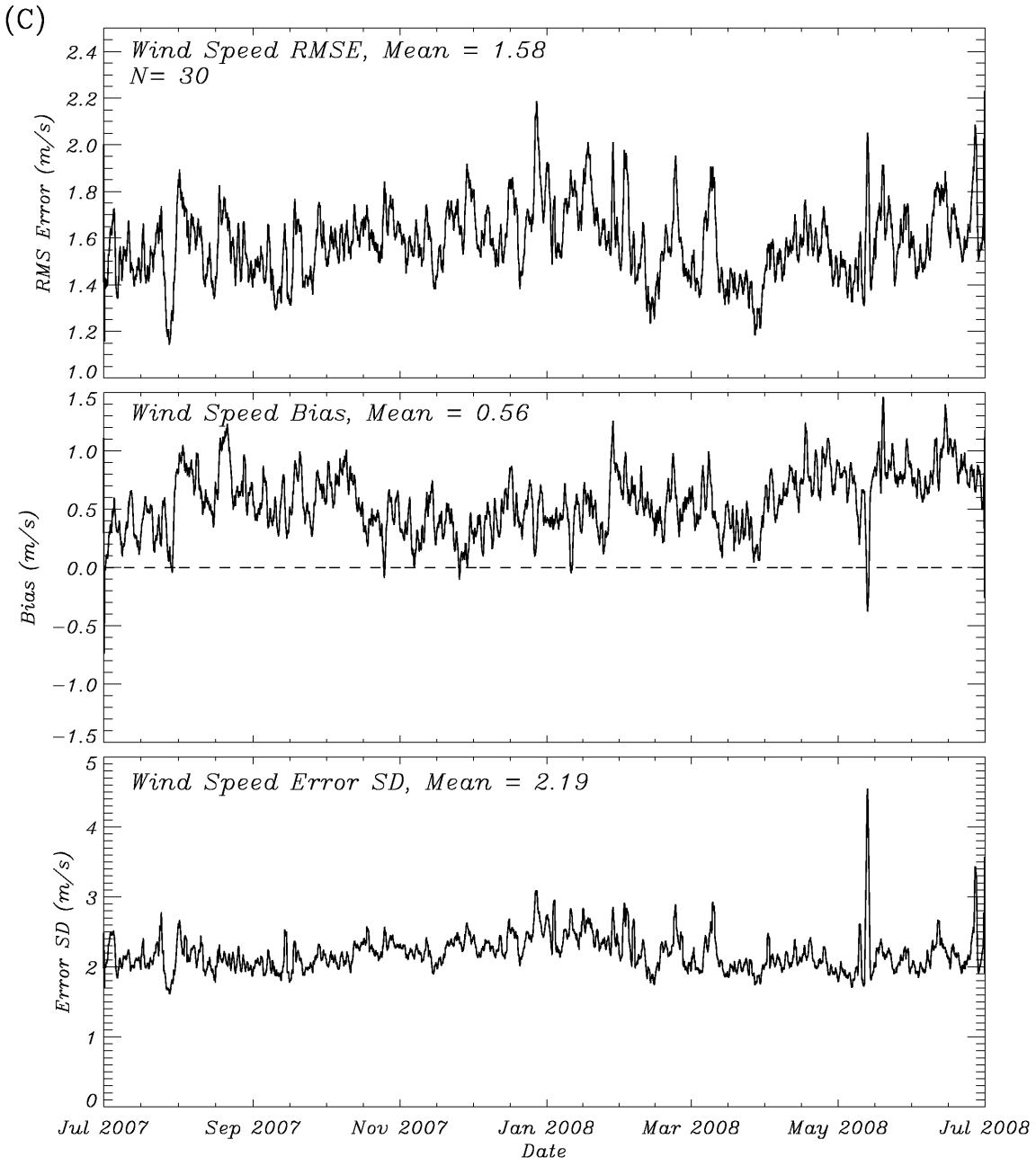

Figure 4.1 (continued).

Comparison against surface temperature observations (Figure 4.1a) shows an overall negative bias (mean value of ~ -0.98 °C). A linear, decreasing trend in the negative temperature bias, with the value varying from ~ -2°C that decreases to ~ -1° C is found during the first three weeks of the CTL experiment, while fluctuation in temperature bias from a mean value of ~ -1° C is found for rest of time period. The linear decline of temperature bias during the early stage of the experiment is also accompanied by a decreasing trend of RMSE, after which RMSE variation is also characterized by fluctuations centered on mean RMSE value of ~2°. Note that the spatial heterogeneity in soil temperature is not adequately captured by the coarse resolution FNL analysis used to initialize these fields in the numerical modeling experiments, and is potentially the cause for the linear trend in decrease of bias and RMSE found in the statistical analysis [*Fairman et al*., 2011, Chapter 5].

Table 4.1 Annual mean values of root mean square error, bias, and error standard deviation for temperature, dewpoint, and wind speed for the large scale (G2) domain.

	2m Temperature	**Dewpoint**	**Wind Speed**
RMSE	2.16 K	1.30 K	1.58 m/s
Bias	-0.98 K	-0.42 K	0.56 m/s
Error SD	3.06 K	1.99 K	2.19 m/s

Negative bias in simulated dewpoint temperature is found in CTL experiments (Figure 4.1b), with mean bias value being -0.42 °C for the period of study. Linear, increasing trends in negative dewpoint temperature biases are found in the CTL experiment, associated with the cessation of rainy periods. Such a linear trend in biases appears at the end of the "short rains" in December, and disappears towards the

beginning of 2008. Even more prominent is the increasing trend in negative dewpoint bias that occurs after the southward migration of the ITCZ at the end of March. This change in the average bias shows little impact on the RMSE and error standard deviation over this time period, indicating a homogenous change across all stations in the domain. This is reinforced by the drying trend in dewpoint seen in the direct station observations (not shown). This pattern of increasing trend in negative dewpoint bias following cessation of rainfall indicates suggests that soil moisture depletion in CTL simulation is faster than occurs in reality.

Comparison of wind speeds in CTL experiment to observations (Figure 4.1c) does not exhibit any patterns of systematic trends as found for surface temperature and dewpoint. Wind speeds in the CTL experiment exhibit a mean bias of 0.5 ms^{-1}, with variations of up to 1 ms^{-1}. The mean RMSE is 1.58 ms^{-1} and does not exhibit any systematic trends during the period of study. Comparison of wind speeds in CNTL experiment to observations (Figure 4.1c) does not exhibit any patterns of systematic trends as found for surface temperature and dewpoint. Wind speeds in the CTL experiment exhibit a mean bias of 0.5 ms^{-1}, with variations of up to 1 ms^{-1}. The mean RMSE is 1.58 ms^{-1} and does not exhibit any systematic trends during the period of study.

Coefficient of correlation between observed and model simulated values from CTL experiment for surface temperature and dewpoint ranged from 0.53-0.83 and 0.29-0.83 and average values were 0.7 and 0.6. Comparison of surface temperature, dewpoint and winds in the CTL experiment to observations show that the performance of RAMS in simulating these variable are comparable that reported in prior studies [*Zhong and Fast,* 2003; *Fairman et al.,* 2011].

4.1.2 Small scale surface temperature and vapor pressure comparison

Meteorological observations at higher altitude locations on Kilimanjaro are not routinely available, except for datasets collected during field studies [e.g., *Pepin et al*., 2010*; Molg et al.*, 2009a]. In this study, temperature and vapor pressure observations of *Pepin et al.* [2010], at 10 sites located along a transect on the southwestern slopes of Kilimanjaro, extending from elevations of 1890 m to 5803 m are is utilized for comparison to model simulations (Figure 4.2, Table 4.2). During our study period, we have full records at hourly resolution from 6 sites, with an additional 3 sites having partial coverage for the first few months (July-October) until coming fully online. Site 5 from *Pepin et al.* [2010] is missing throughout the study period of July 2007 – June 2008. Details of each site location are given in Table 4.2.

Table 4.2 Details of the stations from *Pepin et al.* [2010], utilizing the same nomenclature. Station 5 did not have any data for the entire year due to theft, and Stations 2 and 7 did not report any moisture data throughout the study period. Full coverage over our year would be 8784 hourly observations.

Station Number	Latitude	Longitude	Elevation (m)	Number of Temperature Observations	Number of Moisture Observations
1	-3.16989	37.2367	1890	8784	6636
2	-3.12992	37.2460	2340	7709	0
3	-3.10603	37.2585	2763	7700	6632
4	-3.09011	37.2689	3172	6614	6614
5	-3.07961	37.2796	3634	0	0
6	-3.06611	37.2880	4047	8784	8784
7	-3.06344	37.3224	4568	8784	0
8	-3.06939	37.3379	4971	8784	8784
9	-3.06700	37.3448	5470	8784	8784
10	-3.05694	37.3756	5803	8783	8783

Simulated values of surface temperature and vapor pressure in the CTL simulation at station locations along the observational transect of *Pepin et al*. [2010] are evaluated following the methods of *Zhong and Fast* [2003] (Figure 4.2). The model simulated values used in the comparison are for the model grid point on grid 4 that are closest to each observation location. Note that the elevations of surface stations and closest model grid point often differ. A correction in applied to model simulated surface temperature to account for altitudinal difference, computed as a product of average lapse rate of 6 K km^{-1} and the altitudinal difference. The annual average RMS error for temperature (Table 4.3) is similar to values found for comparison against regular meteorological observations available for the region (see Section 4.1.1). However, the annual average temperature bias is found to be positive and the error standard deviation is smaller compared to other regions (Table 4.3). Correlation between simulated surface temperatures in CTL experiment and observations range from 0.83 at the lower elevations to 0.49 at the peak. The decrease in correlation as elevation rises can be attributed to the decreasing of variance over the time period, as higher elevation temperatures vary little over a seasonal basis. Comparison against vapor pressure observations from the transect show a positive bias associated with the model simulated

Table 4.3 Annual mean values of root mean square error, bias, and error standard deviation for temperature, and vapor pressure on the small scale (G4) domain.

	2m Temperature	**Vapor Pressure**
RMSE	2.18 K	137.08 Pa
Bias	0.652 K	27.84 Pa
Error SD	2.24 K	142.29 Pa

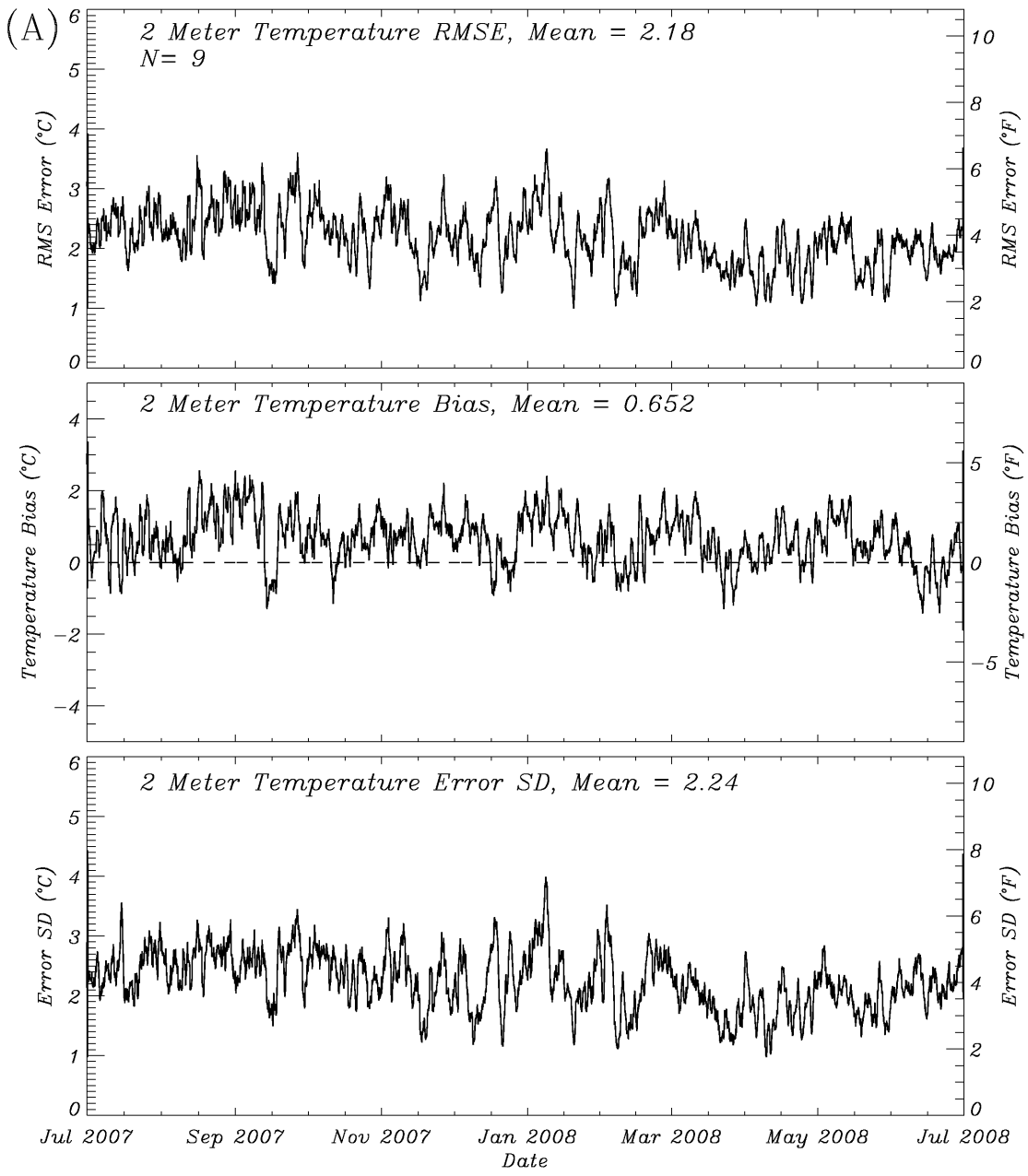

Figure 4.2 Root mean square error, bias, and error standard deviation of two meter temperature (a), and vapor pressure (b) comparing the model results to the data of *Pepin et al.* [2010]. Values are smoothed to daily means after being computed on an hourly basis. Mean values are for all hourly timesteps.

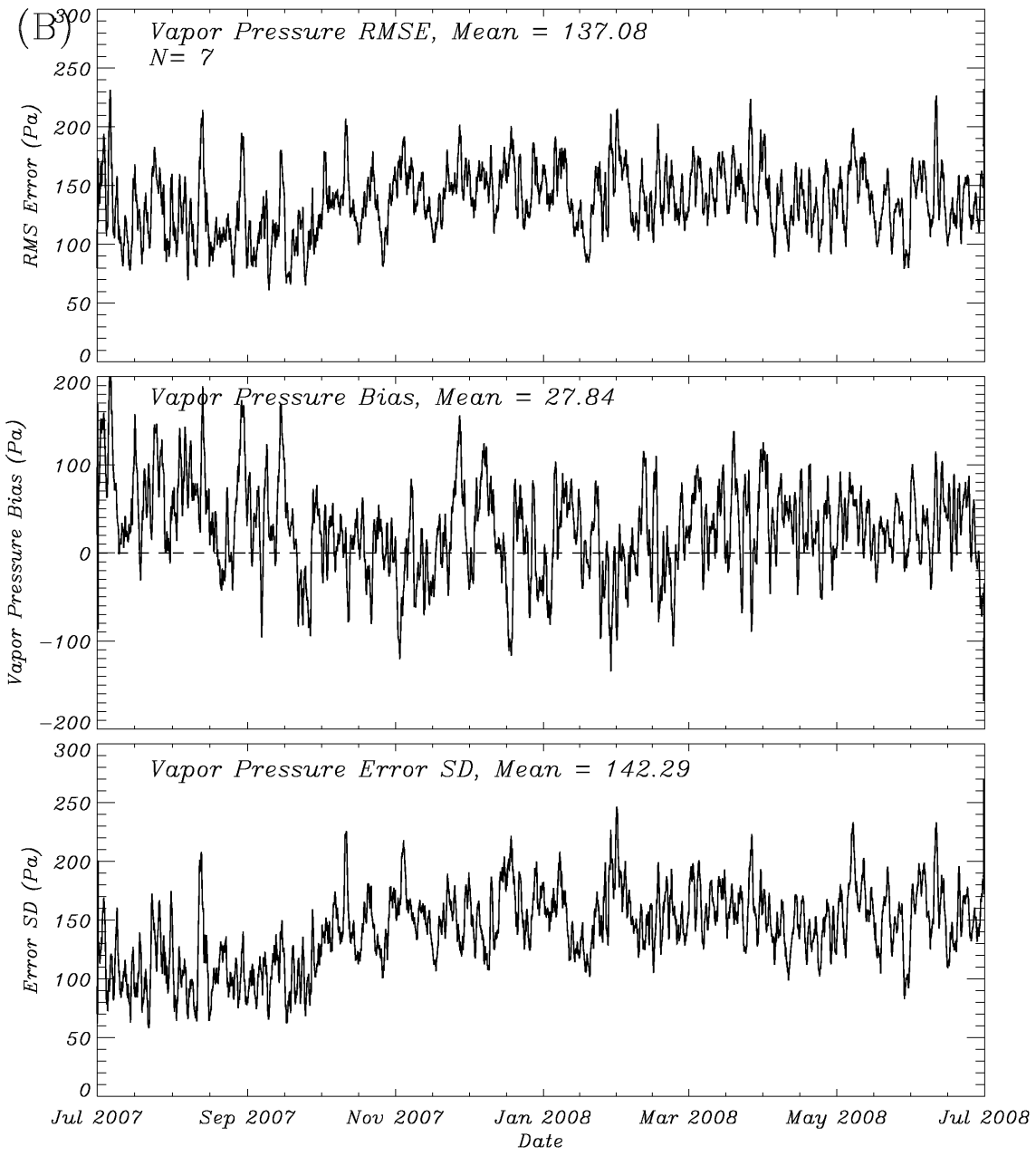

Figure 4.2 (continued).

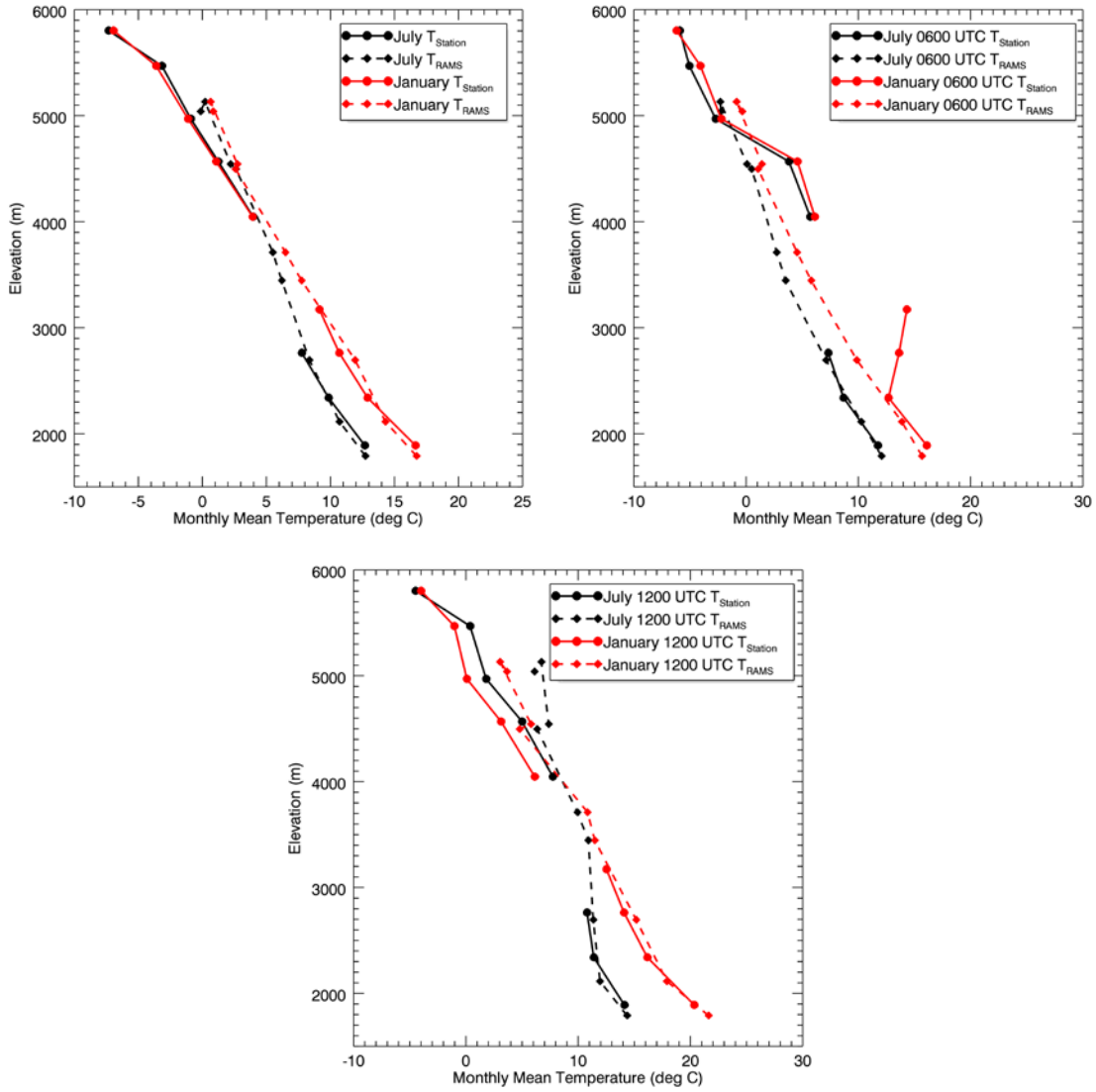

Figure 4.3 Model (dashed) and observed (solid) temperatures for the stations listed in Table 3, for monthly mean temperatures during January (red) and July (black) (a) and monthly mean temperatures at 0600 (b) and 1200 (c) UTC for January (red) and July (black).

vapor pressure. Correlations between observed and model simulated vapor pressure range from 0.41 to 0.62, with only one site having a correlation lower than 0.56. Computed error statistics are comparable to values reported in other studies indicating satisfactory performance of RAMS.

4.1.3 Surface rainfall comparison

The surface accumulated rainfall in the CTL experiment is compared against estimate derived from the Tropical Rainfall Measuring Mission (TRMM) [*Kummerow et al.,* 1998] and also surface rain gauge observations. The number of stations in the study area that report rainfall observations (Figure 4.4c) are substantially less (14) compared to those that report temperature, dew point and wind speed observations (30). Therefore, comparison to TRMM derived rainfall estimate is also employed to assess the nature of spatial heterogeneity of simulated rainfall. Spatial distribution of rainfall accumulation in the CTL experiment shows good agreement to surface rain gauge observations (Figure 4.4). The mean difference in simulated and observed rainfall is -388 mm, with RAMS underestimating accumulated rainfall. In comparison to TRMM, RAMS overestimates precipitation over the Indian Ocean region (R1), area southwest of Kilimanjaro (R2), Kenya-Somalia border (R3), Kenya-Uganda border region (R4). In contrast, RAMS underestimates precipitation over and the central region of Kenya and Mt. Kenya (R5), which is located to the north of Nairobi. Note that the grid spacing of 16km utilized for grid 2 is unable to adequately resolve Mt. Kenya, which is potentially the cause for the inability of CNTL experiment to capture this feature. Mean difference between RAMS simulated and TRMM derived estimate of precipitation is 51.2 mm, with RAMS overestimating the precipitation.

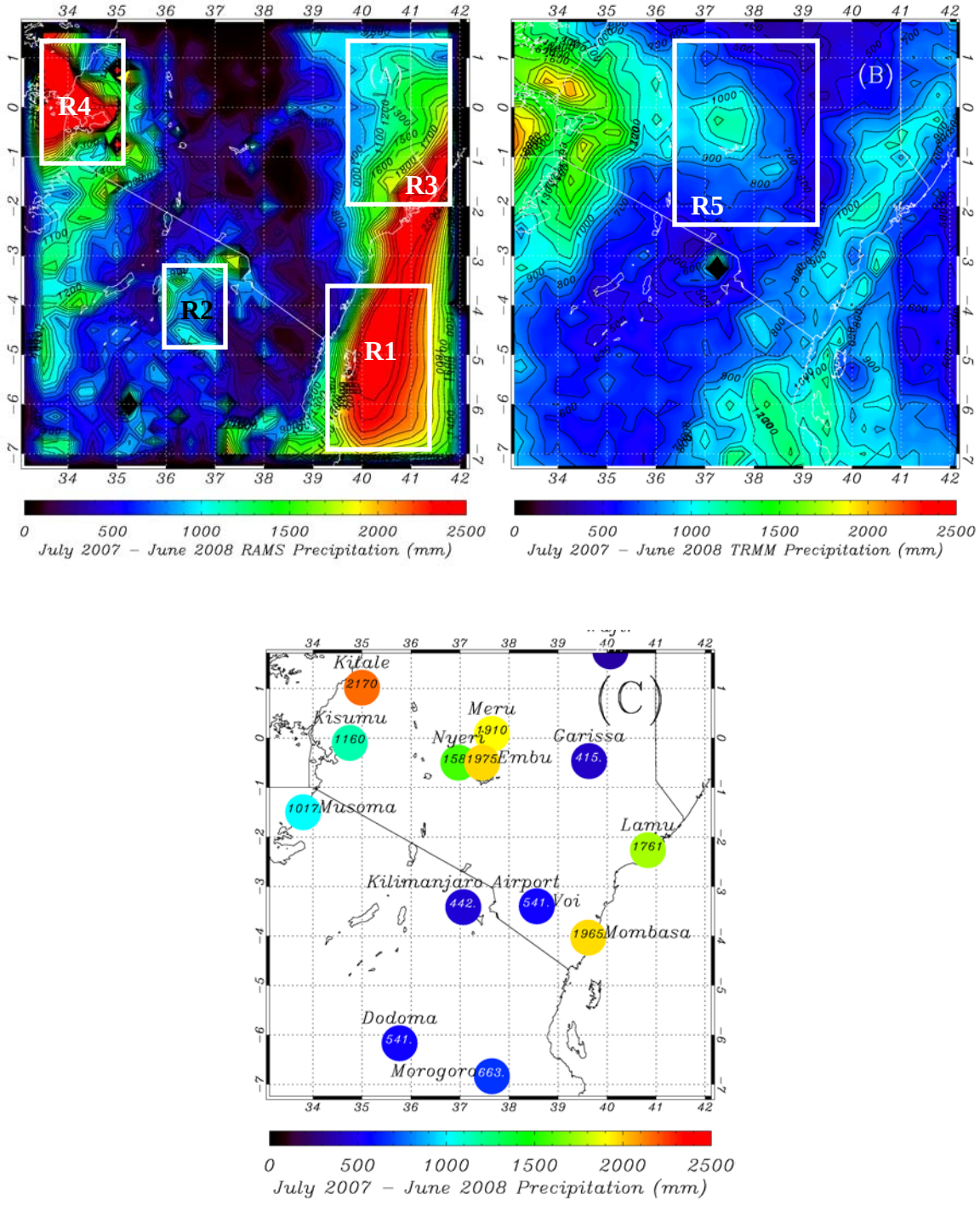

Figure 4.4 RAMS explicit and parameterized precipitation (a) in comparison to the TRMM precipitation (b) and station observations (c). There are significant spatial changes between the two, with the model output showing more heterogeneous precipitation and greatly overemphasizing the precipitation over water areas (Lake Victoria and the Indian Ocean). Of notice are the stations (Nyeri, Meru, and Embu) that get more precipitation due to the proximity with Mount Kenya and Abadare Range.

4.1.4 Cloud frequency comparison

Due to the low density of surface observations, this study also employs a spatially distributed strategy of comparing the simulated cloud fields in grid 4 against MODIS satellite observations of cloud cover. The 1 km spatial resolution cloud mask derived from daily MODIS observations [*Ackerman et al.*, 1998; *Frey et al.*, 2008], made approximately at 1100 local standard time (LST) (Terra platform) and 1400 LST (Aqua platform), and re-projected to the RAMS polar stereographic grid (G4) was used for this purpose. We used one year of MODIS data comprising of 458 granules from MODIS-Terra and 486 granules of MODIS-Aqua to compute indices of prediction accuracy (A), over prediction (O) and under prediction (U). To compare the satellite derived cloud mask to the numerical model simulated cloud field the following metrics were computed:

$$A = \frac{n_1}{n_1 + n_2 + n_3} \times 100\,; \quad O = \frac{n_2}{n_1 + n_2 + n_3} \times 100\,; \; U = \frac{n_3}{n_1 + n_2 + n_3} \times 100 \quad , \qquad (4.1)$$

where n_1, n_2 and n_3 respectively are the number of numerical model grid points for which cloud occurs 1) in both the simulation and satellite observation; 2) in the model simulation but not in the satellite observation; and 3) in the satellite observation but not in the model simulation. Thus the metrics *A*, *O* and *U* quantifies the percentage of comparisons where the model predicted cloudiness is in agreement (accuracy) with the observations, is false positive (over-prediction) and false negative (under-prediction). Note that the following considerations should be made when comparing model simulated cloud field to MODIS observations: 1) The comparisons are made not exactly at the time of satellite overpass, but at the hour closest to overpass time for which model output is available; 2) the MODIS cloud masking algorithm is less skillful at detecting optically

thin clouds [*Ackerman et al.*, 2008], whereas RAMS often produce thin clouds including surface fog. In order to minimize bias introduced due to the second consideration, only clouds with liquid water path (LWP) greater than 35 gm^{-2} is considered when comparing model simulated clouds to satellite observations. Note that more than 99% of all the clouds in MODIS imagery satisfy this condition. Analysis without this threshold produces similar accuracy numbers, but increases overprediction while decreasing underprediction nearly uniformly.

Table 4.4 Model accuracy, overprediction, and underprediction of cloud occurrence at MODIS-Terra and MODIS-Aqua overpasses for the one kilometer spacing domain

	Accuracy	**Overprediction**	**Underprediction**
MODIS-Terra	65.0%	7.7%	27.3%
MODIS-Aqua	60.9%	7.7%	31.4%

Spatial analysis of the cloud FOC (Figure 4.5a) show two main areas of convection: 1) Southwest slopes of the mountain with 70-80% FOC and 2) North slope with FOC values of 70%. Domain averaged FOC decreases with height, reaching values less than 30% at the peak. Mean accuracy of RAMS in predicting cloud occurrence is ~60%, but it increases to 70% in over prominent regions of the orographic cloud bank and up to 80% accuracy at the peak. Accuracy errors are primarily due to the tendency of RAMS to under predict cloud formation (average of ~30%, Figure 4.5c,d). Accuracy of RAMS in predicting orographic cloudiness is comparable to that reported in other studies.

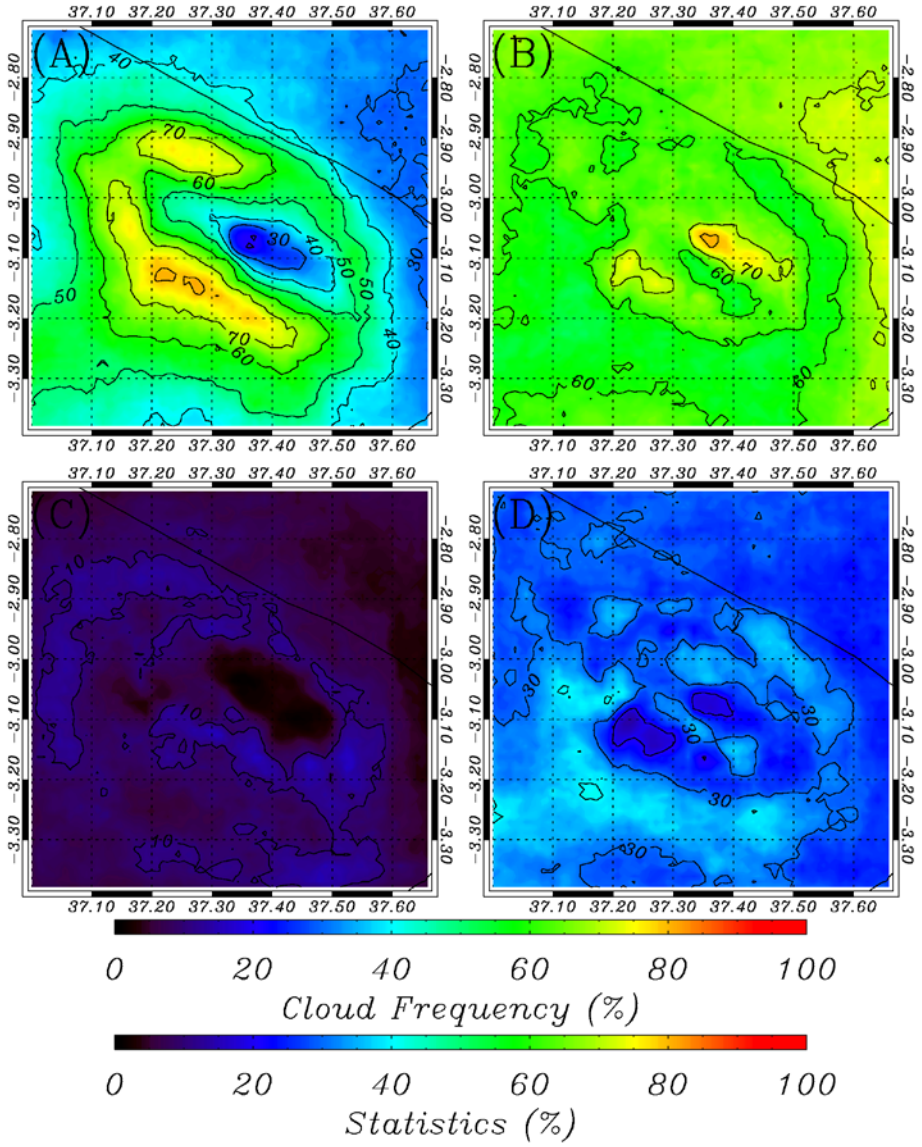

Figure 4.5 Combined cloud statistics based on analysis from MODIS-Terra and MODIS-Aqua cloud masks to the RAMS model output. Shown is MODIS cloud frequency for the year from June 2007 – July 2008 (a), the cloud prediction accuracy (b), overprediction (c), and underprediction (d).

4.2 Seasonal Progression of the Flow Regime around Kilimanjaro

Kilimanjaro is located in an area that experiences transitions of the ITCZ, and thus seasonal variation of winds are tied to north-south migration of the ITCZ. Seasonal mean wind over a 1000m layer above ground level in the CTL experiment show the existence of four distinct flow regimes: Southerly during JJA (Figure 4.6a), east-southeasterly during SON (Figure 4.6b), North easterly during DJF (Figure 4.6c) and southeasterly during MAM (Figure 4.6d). Maximum wind speeds in the 0-1000m above ground layer exceeds $10ms^{-1}$ during JJA and DJF, while it below this value during the other seasons. The variation in wind direction rather than wind speed is the determinant for strength of terrain generated updrafts (Figure 4.7). Maximum updrafts are often located on the faces of the mountain that are normal to the average wind direction, except during some times in DJF where flow diversion caused by the mountain leads to the formation of a lee vortex that channels flow against the rim of the concave terrain feature on the southern slopes of Kilimanjaro where a substantial topographical gradient exists (see discussion section). This phenomenon leads to the generation of strong updraft near the peak (see R1 in Figure 4.7c). Note that a strong updraft feature is also present during MAM (R2 in Figure 4.7), but caused by a different process. During MAM, southeasterly flow is channeled by the terrain leading to flow oriented more along the direction of the topographical gradient (See Figure 4.6). Note that the strength of this updraft feature is sensitive to the wind direction, as it is present during SON, but is weaker during the east-southeasterly wind regime (Figure 4.7b).

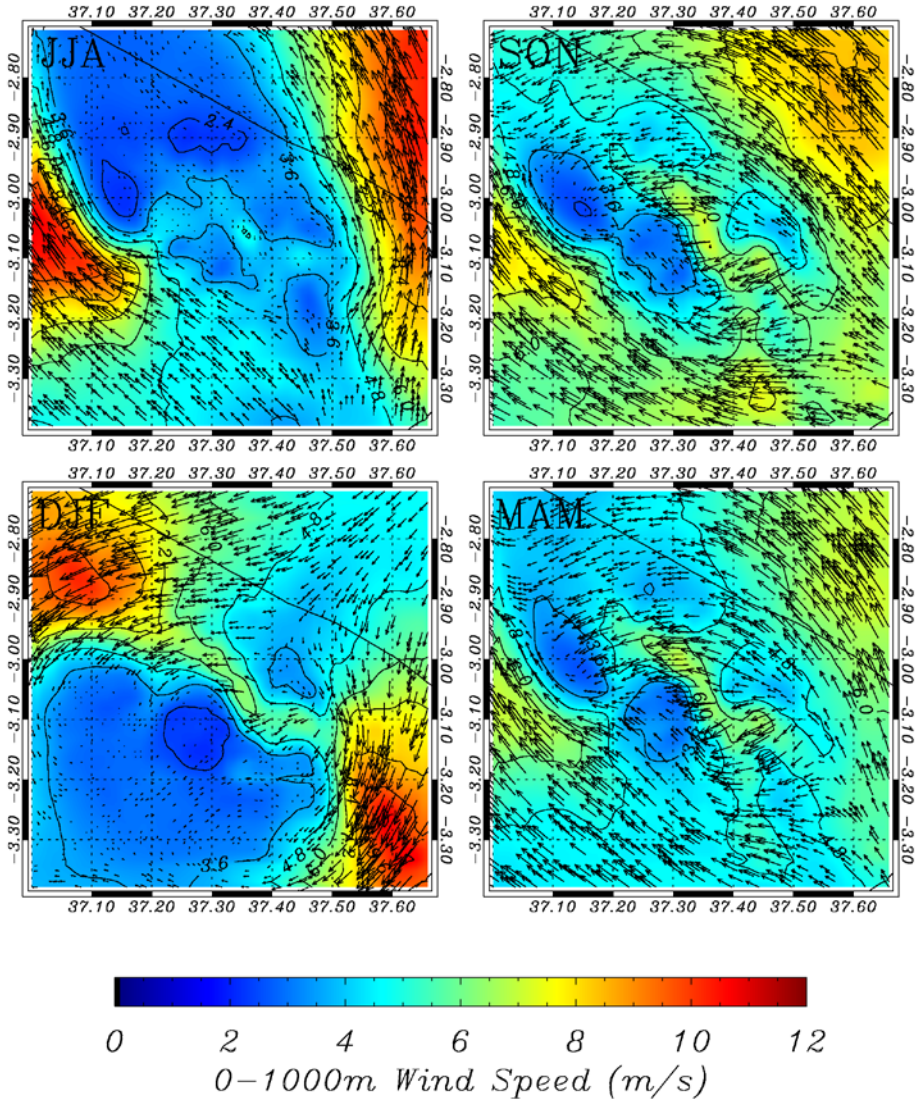

Figure 4.6 Seasonal progression of 0-1000m wind speed. There is significantly more blocking provided by the mountain in the dry seasons compared to the wet.

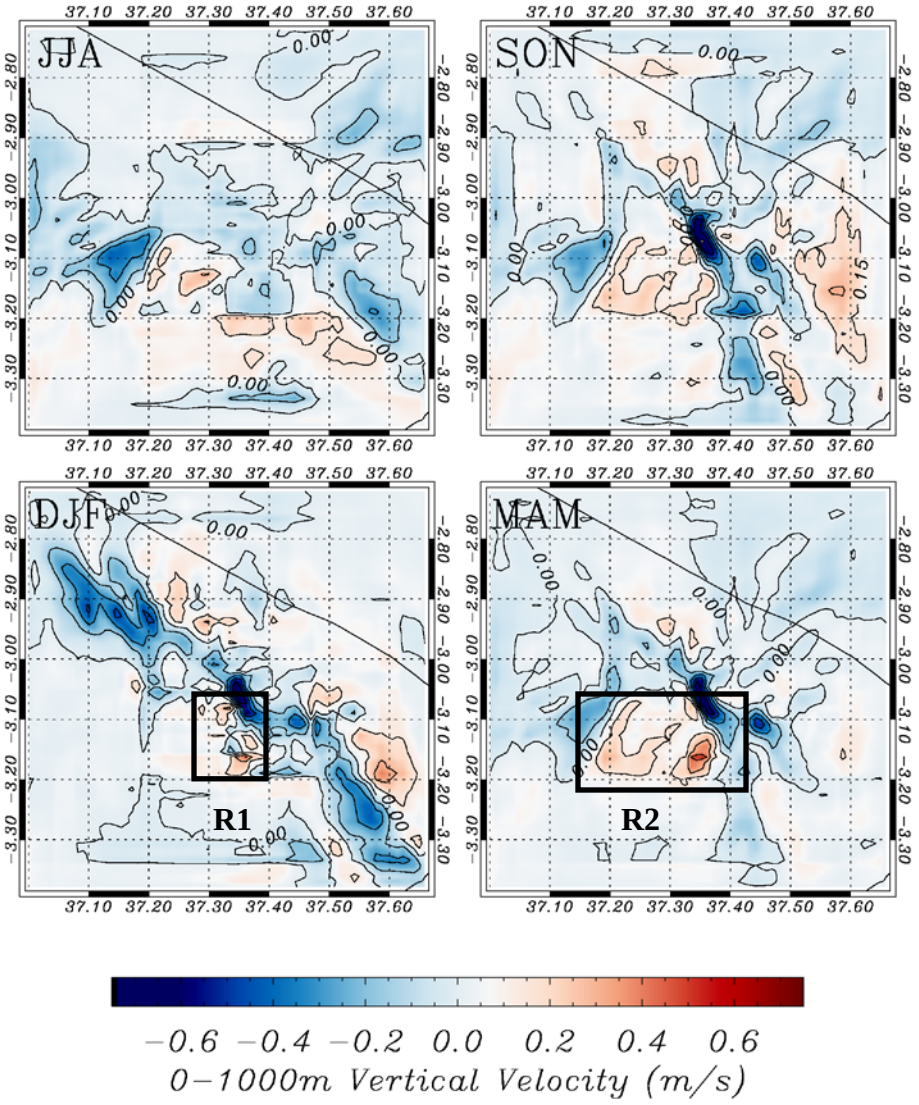

Figure 4.7 Seasonal progression of vertical wind speed. The main locations of the updraft vary according to season, but the majority of the convective activity on an annual basis is located within the southwest corner of the mountain.

4.3 Seasonal Variation of Orographic Cloud Formation

Seasonal variation in wind patterns are accompanied by changes in orographic cloud formation. The spatial distribution of FOC for all seasons (Figure 4.8) are well correlated to corresponding seasonal horizontal (Figure 4.6) and vertical wind fields (Figure 4.7). The FOC is computed for clouds with liquid water path greater than 35 gm^{-2}, which is the same criterion used when comparing against MODIS observations (see Section 4.1.4). During JJA, when Kilimanjaro is under the influence of southerly flow regime (Figure 4.6a), FOC is highest along the southern half of Kilimanjaro. Maximum values of FOC, in excess of 80%, are also found during JJA along the southern slopes. The FOC values at the peak of Kilimanjaro (region P in Figure 4.8) during JJA are less than ~10%.

During SON, as the winds transition to an east-southeasterly regime (Figure 4.6b), maximum extent of orographic cloudiness shifts over to the eastern slopes (Figure 4.8b), with a secondary maximum forming on the western slopes. East-southeasterly flow, diverted into two streams around Kilimanjaro converges on the western slopes (Figure 4.6b), leading to the formation of the orographic cloud bank along the western slopes (Figure 4.10b). The FOC values during SON season (maximum of 50%) is substantially lower compared to JJA season (maximum of ~80%). The FOC values at the peak of Kilimanjaro increases during SON, with the southwestern region of the peak experiencing up to 30% FOC.

Shift of wind regime to Northeasterly orientation in DJF (Figure 4.6c) is accompanied formation of orographic cloud banks along the northeastern and southwestern slopes of Kilimanjaro (Figure 4.8c). In general these cloud banks have

lower FOC values (maximum of ~40%) compared to those found during JJA and SON seasons, except for a region of localized maximum FOC (maximum of ~50%) on the southern slopes (M1 in Figure 4.8c). This feature is associated with the flow reversal phenomenon identified in Section 4.2, and will be further discussed in Section 4.5. Maximum values of FOC experienced by the peak of Kilimanjaro decreases slightly during DJF (20% < FOC at peak < 30%), but northeastern regions of the peak are exposed to higher FOC values (Figure 4.8c) compared to both JJA (Figure 4.8a) and SON (Figure 4.8b).

During MAM, under the influence of the southeasterly wind regime (Figure 4.6d), cloud banks form most frequently over the southwestern slopes (maximum FOC ~70%), with a secondary maximum (FOC ~50%) found on the lower southern slopes. Cloud bank also extends to southeastern and eastern slopes of Kilimanjaro, but associated with lower FOC values. Maximum FOC values are found at the peak of Kilimanjaro during MAM, with FOC values exceeding 50% in the northwest regions (Figure 4.8d).

In addition to frequency of clouds, thickness of orographic clouds is also important in determining the nature of orographic precipitation. Thus the seasonal variation of cloud liquid water path (LWP) is also examined. Spatial distribution of LWP (Figure 4.9) is well correlated to that of FOC (Figure 4.8). During JJA, highest LWP is found along the southern slopes (Figure 4.9a). Clouds with highest LWP are found on the eastern and western slopes, with the thicker clouds on the western slopes extending to the northwest regions of the mountain peak. During DJF, thicker clouds are found along

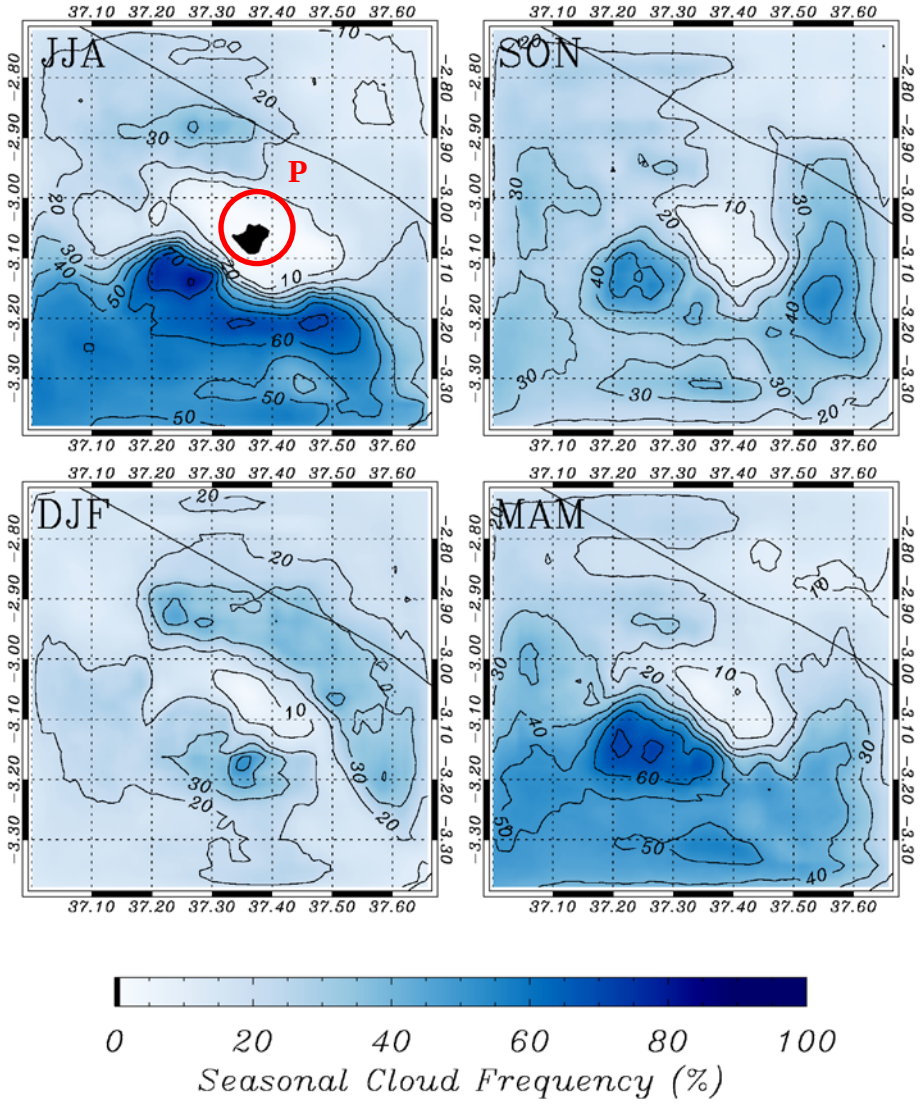

Figure 4.8 Spatial plots of cloud frequency of occurrence (FOC, %) on model grid G4 over the course of the year, separated by season. The red circle denotes region P.

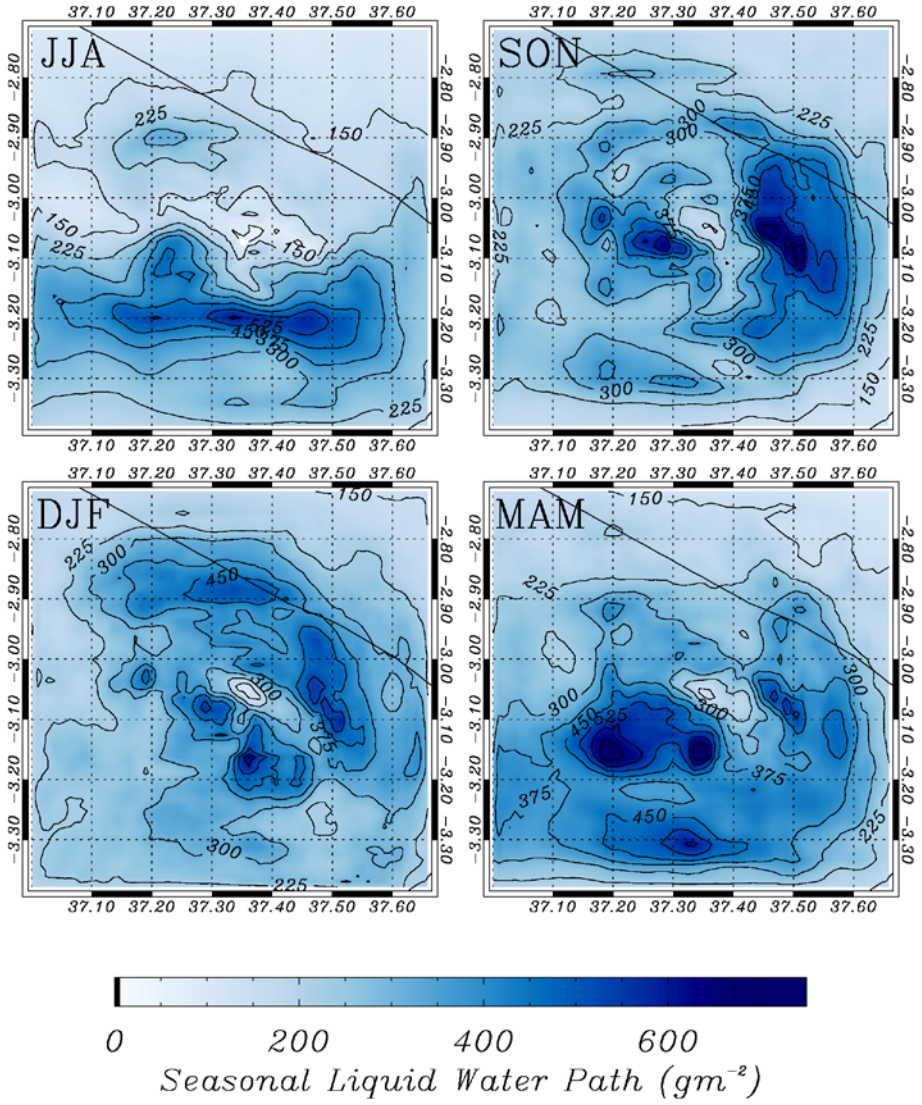

Figure 4.9 Average cloud liquid water path at times of cloud occurrence for model grid G4, separated by season. This shows the progression of the prevailing winds over the course of the year as well as the areas of highest convection.

the northeast and southwest slopes, with the thicker clouds being present over both northeastern and southwestern regions of the mountain peak. Thickest clouds (LWP in excess of 600 gm^{-2}), are found during the MAM season in the southwestern slopes (Figure 4.9d). The thickest clouds are also found over the mountain peaks during MAM.

4.4 Anomalies in Wind and Moisture Fields Associated with Cloud Formation at the Peak

In order to determine the primary factors that control cloud formation at the peak of Kilimanjaro, mean differences in wind and moisture fields is between times when cloudy and clear conditions occur at the peak of Kilimanjaro are determined (Figure 4.10). Differences in wind and moisture fields are examined because spatial distribution of FOC is primarily governed by winds, while ambient moisture is one of the important factor that govern the LWP of orographic clouds. Cloudy conditions at the mountain peak are with an associated positive anomaly in the moisture field (~0.8 gm^{-2}) along the lower elevation regions (<1000m elevation), potentially related to large scale transport of moisture into the region (Figure 4.10a). Anomalies in the wind field associated with cloudy conditions at the mountain peak are characterized by enhanced wind speeds along the northeastern and southwestern slopes of Kilimanjaro, oriented parallel to the direction of topographical gradient. Especially of interest are the anomalies along the rim of the concave terrain feature on the southern slopes. Wind field anomalies oriented approximately normal to the direction of topographical gradient are also present, for example along the northwest and southeast slopes. This pattern of wind

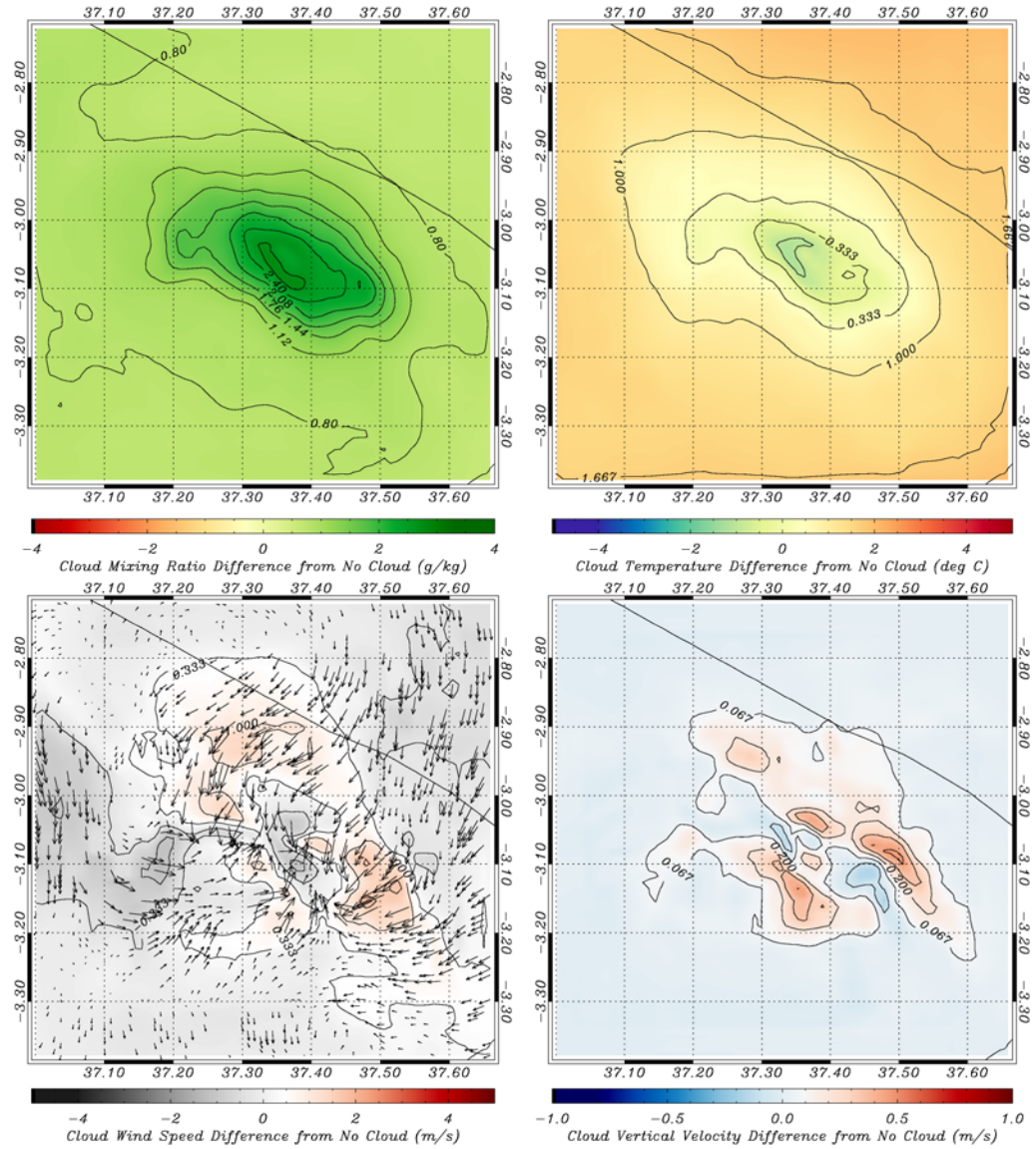

Figure 4.10 Differences in mixing ratio (a) temperature (b), wind speed (c) and vertical velocity (d) between simulation times where clouds with a liquid water path greater than 35 gm^{-2} do and do not exist at a point with a surface elevation exceeding 5000 m.

anomalies suggest that relatively small changes in wind speed (1-2ms^{-1}), in the direction parallel to topographical gradient have the potential to impact cloudiness at the peak of Kilimanjaro and are associated with positive anomalies of vertical wind speeds in excess of to 0.3 ms^{-1}. Wind speed changes in direction oriented normal to topographical gradient are potentially related to components of flow that are diverted around the mountain, which are often associated with convergence zones on the lee side of the mountain.

These meteorological anomalies associated with cloud formation have a seasonal and diurnal variance associated with them, so it is necessary to quantify the seasonal progression of cloud occurrence as well as the diurnal progression. Figure 4.11 shows the percentage of times that clouds occur at high elevations per month (Figure 4.11a) and on a diurnal basis (Figure 4.11b). From a monthly point of view, clouds do not often occur during JJA at high elevations, as was already shown in Figure 4.8a. However, the distribution of cloud occurrence at high elevations shows that the times where clouds are most likely to occur are the months of September and March, with March accounting for 18% of all times that clouds occur at the peak. On a diurnal basis (Figure 4.11b), the majority of clouds occur from 1000 UTC to 1400 UTC. This coincides with 1:00 – 5:00 PM local time, where the effects of the thermal circulation would be thought to be the greatest. The rest of the times have a ~3% rate of clouds occurring at high elevations, and there is fairly little variation. Over 50% of clouds that form at the peak form between 1000 and 1400 UTC.

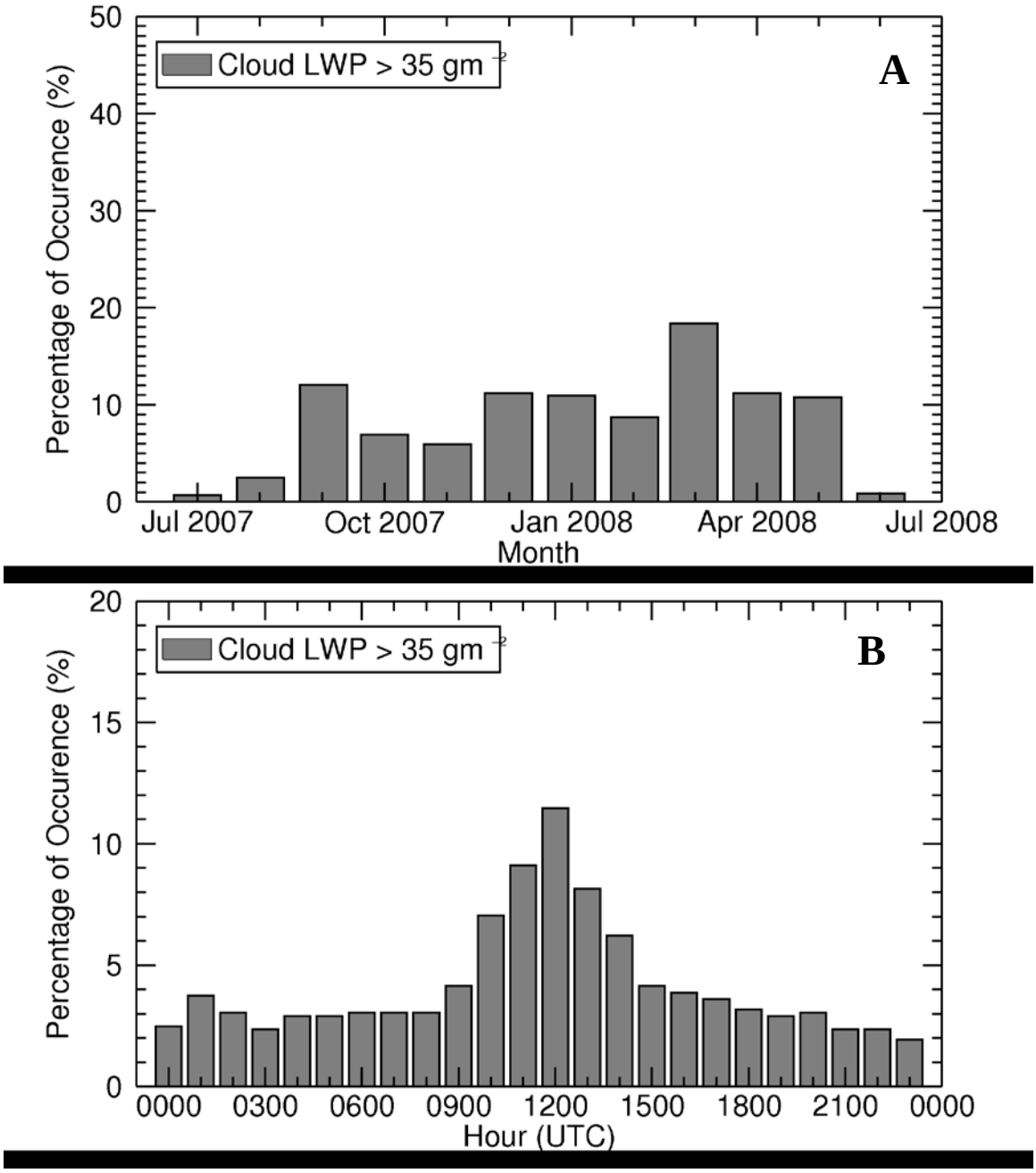

Figure 4.11 Plots of frequency of occurrence of clouds at points with elevations greater than 5000 m on (a) a monthly basis and (b) on a diurnal basis.

4.5 Seasonal Progression of Precipitation

The cloud and wind fields as presented in the previous sections lead to significant variations in the spatial patterns of precipitation on the one kilometer grid. The seasonal variations in precipitation rate are given in Figure 4.12. The most significant areas of precipitation are to the south of the mountain in JJA, DJF, and MAM, with the east side of the mountain receiving the most precipitation during SON. The northeast side receives the most precipitation during DJF, as the shifts in wind direction lead to that side being the "windward" direction whereas the southwestern corner could than be considered the "leeward" direction. During DJF, there is an interesting feature present on the south side of the mountain that is related to an induced circulation present due to the interactions with topography. The wettest season is obviously MAM, with the precipitation being centered on the south side of the mountain, with the main center being on the southwest side.

The variation of precipitation with elevation is found in Figure 4.13. This shows the average precipitation for the entire grid, with the most precipitation falling in an elevational band between 2700 and 3200 m in elevation, generally centered around 3000m in elevation. This makes sense when compared to the spatial plot (Figure 4.13b) of total precipitation. This elevation of maximum precipitation is higher than in *Fairman et al.* [2011], *Barry* [2008], and that found via the analysis *Rohr and Killingveit* [2003].

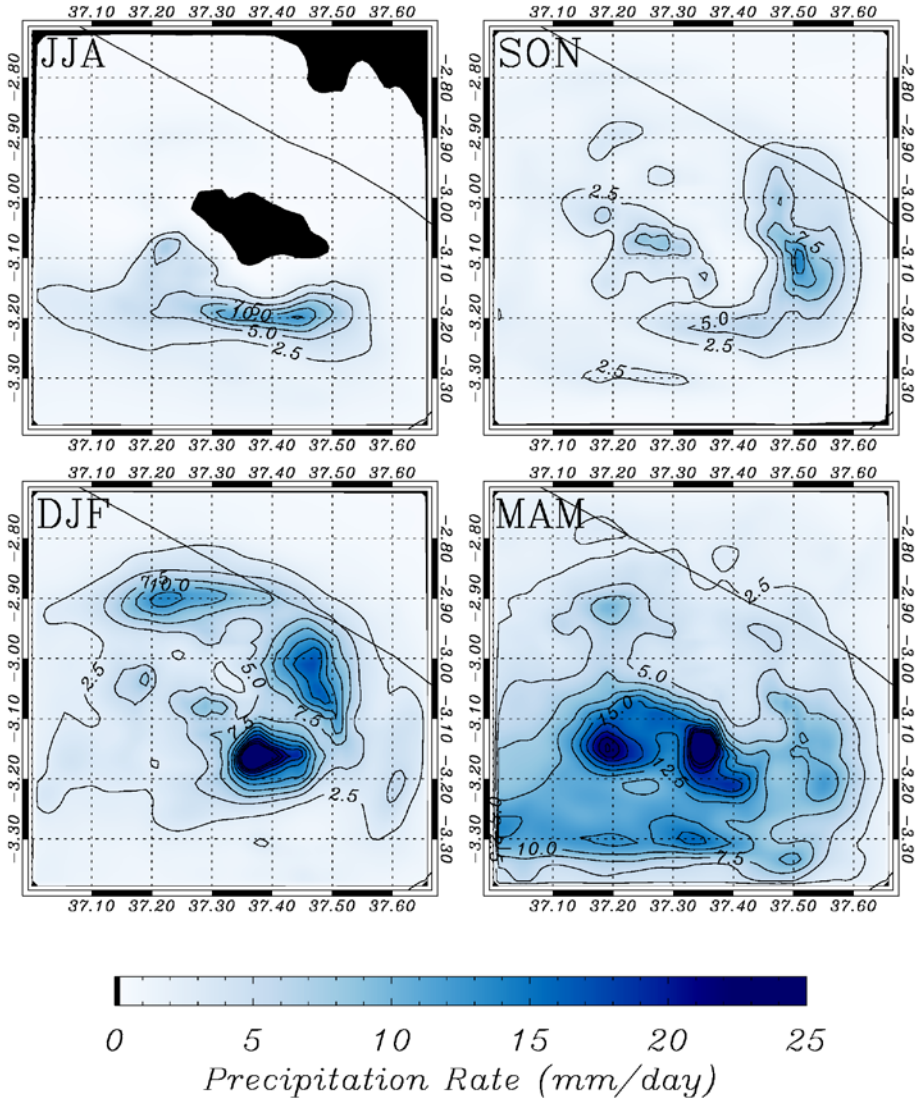

Figure 4.12 Seasonal values of precipitation rate (mm/day). The areas of maximum precipitation do not always occur in the area of the mountain normal to the wind direction, as is shown for the months of DJF.

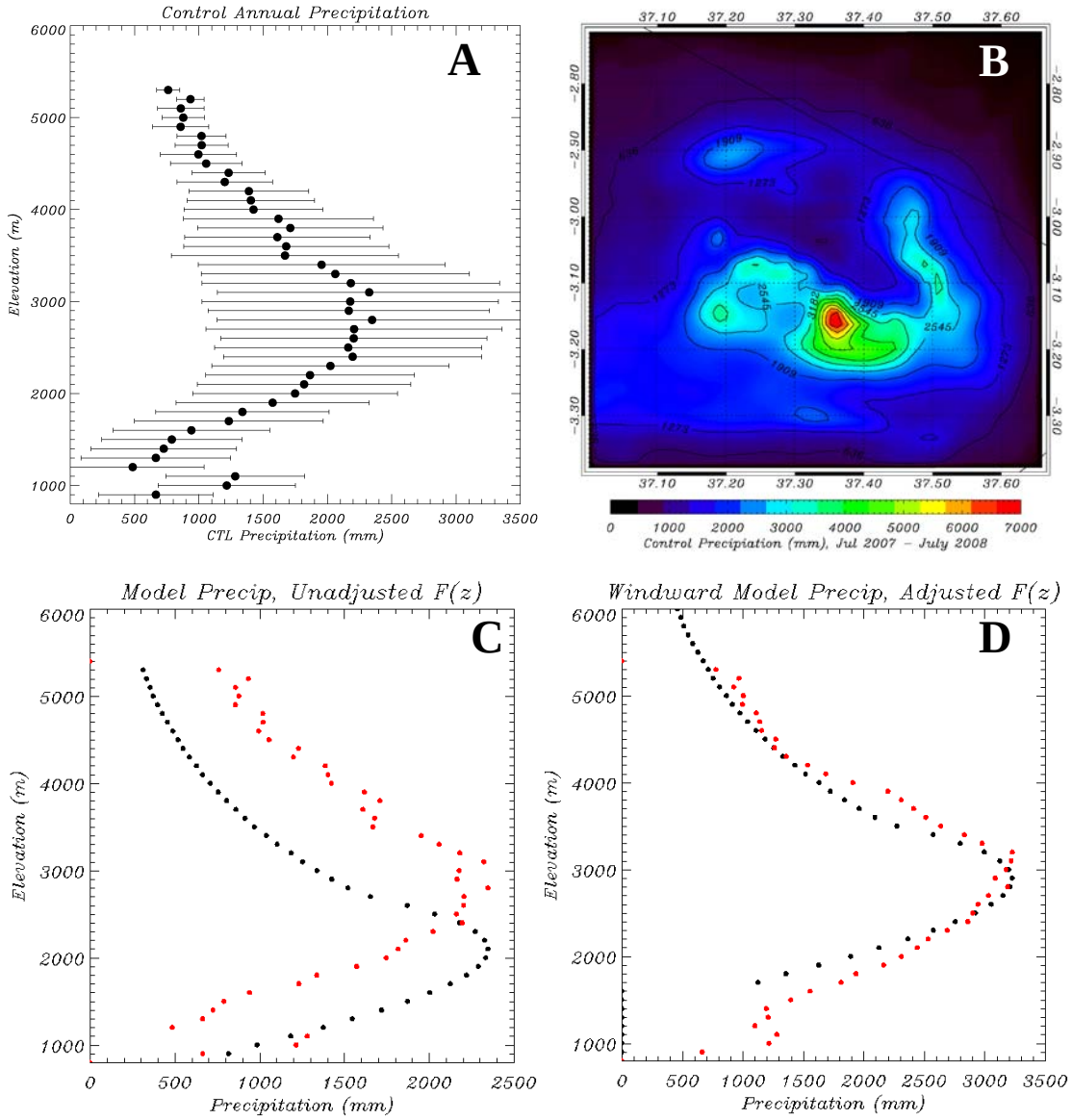

Figure 4.13 Variation of annual total precipitation with elevation (a), as well as spatial plots of total accumulated precipitation (b), along with comparison to the function derived by *Rohr and Killingtveit* [2003] (c). The function is adjusted to the maximum value found for our year (d). The maximum value of the function is ~800 m below the model predicted elevation of maximum precipitation.

The function of *Rohr and Killingveit* [2003] is shown in Figure 4.13c in its unadjusted form, normalized to the maximum value of ~2300 mm of precipitation found at the elevation bin of 2700 m and 3100 m of elevation. What is interesting to note is that via a simple additive adjustment of 800 m, the function of *Rohr and Killingveit* [2003] fits the model derived precipitation quite well, accounting for the majority of the variation for the south side of the mountain (Figure 4.13d). Part of the reason for the rise in the elevation of maximum precipitation can most likely be explained to averaging of terrain in these high relief areas, since on the southern slopes the gradient of topography is very high.

4.6 Anomalies in Wind and Moisture Fields Associated with Cloud Formation at the Peak

As we did in Section 4.4 for cloud formation, we look at the basic meteorological fields associated with the development of precipitation at high elevations (surface elevations exceeding 5000 m). We define precipitation events as hours where precipitation rates exceeded 2.5 mm hr^{-1}, of which there were 143 specific hours over the course of our year-long model run (total of 8784 hours of model simulation). The meteorological fields associated with the generation of precipitation are shown in Figure 4.14. Whereas the cloud fields were fairly uniform, there is a marked skew to the moisture fields associated with precipitation times versus times that had no precipitation (NOPRECIP).

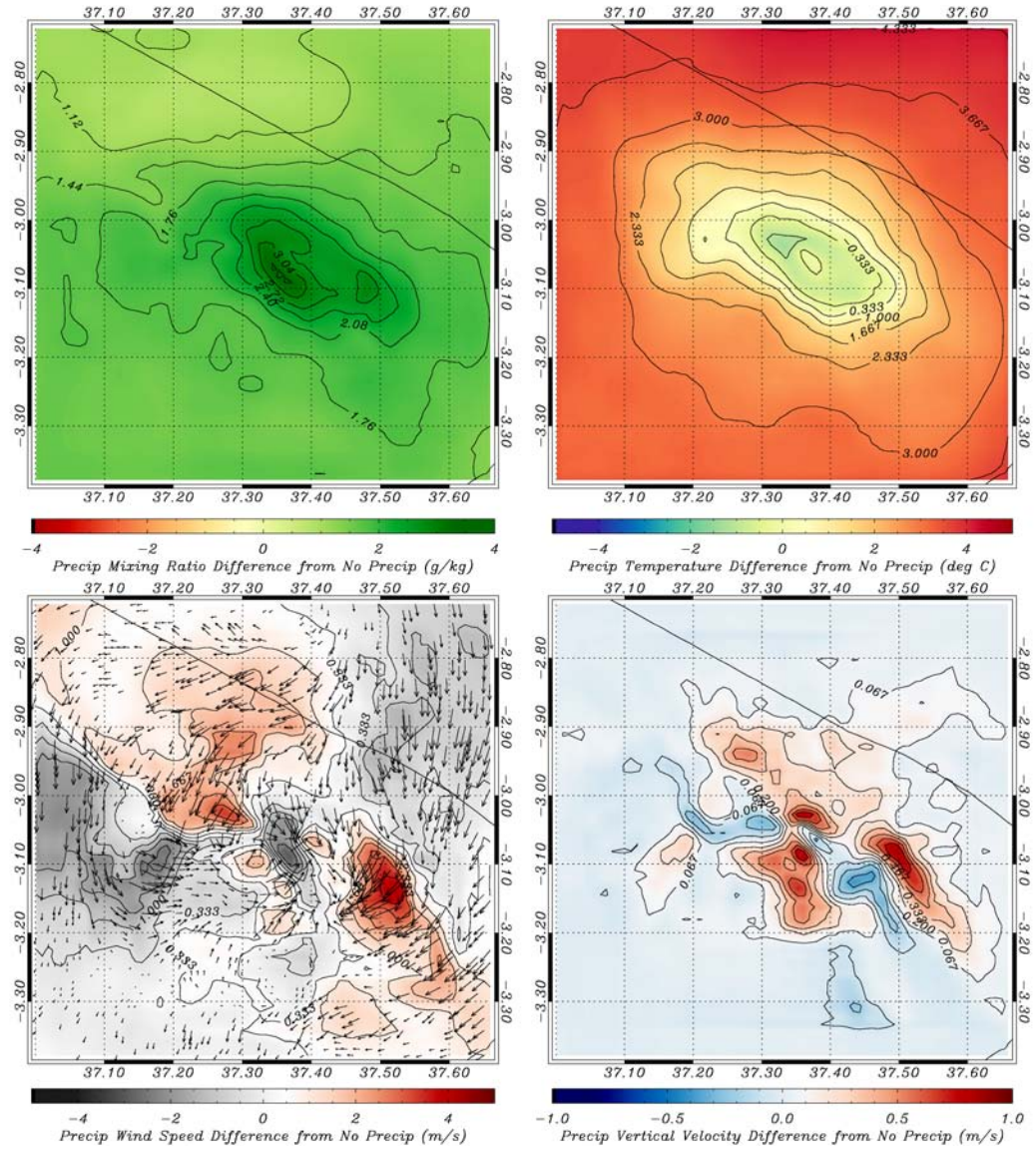

Figure 4.14 Differences in mixing ratio (a) temperature (b), wind speed (c) and vertical velocity (d) between simulation times where the precipitation rate is greater than 2.5 mm hr^{-1} versus no precipitation times at point with a surface elevation exceeding 5000m.

Surface level mixing ratios (Figure 4.14a) are ~1.75 gm^{-2} greater at low elevations on the southeast side of the mountain, with enhancements of moisture of around 1.5 gm^{-2} present on the south and west sides. The northern side of the mountain, however, has a much smaller moisture enhancement. The temperature field (Figure 4.14b) is nearly 4° warmer during high elevation precipitation times. The wind field (Figure 4.14c) shows seasonality effects, with a much stronger northerly component during times where there is precipitation, and wind speed enhancements on the southeast and northwest slopes. Vertical velocities on the normal surfaces (Figure 4.14d) is much higher, approaching enhancements of up to 1 ms^{-1} over certain areas to the south.

Whereas the frequency of cloud occurrence over high elevations was fairly well spread out among the different months of the year, excluding the dry season, the number of times where rainfall occurs at high elevations is not. Monthly distribution (Figure 4.15a) of hourly rainfall rates greater than 2.5 mm hr^{-1} shows a distinct peak in February and March, which combine for over 60% of the total annual rainfall occurrence. Outside of those two months, December and November are the next where rainfall at rates > 2.5 mm hr^{-1} appears most frequently. This is consistent with the precipitation totals across this domain, which shows that the wettest months were February-April and November-December. Hourly distributions of precipitation (Figure 4.15b) show that 60% of the precipitation falls between 1000 UTC and 1500 UTC, the local afternoon, corresponding to the hours of maximum cloud cover present in Figure 4.13b. This also indicates a strong dependence on the thermal circulation.

When differences between times of precipitation and cloud occurrence are considered (Figure 4.16), clear spatial patterns appear. On average, precipitation occurs

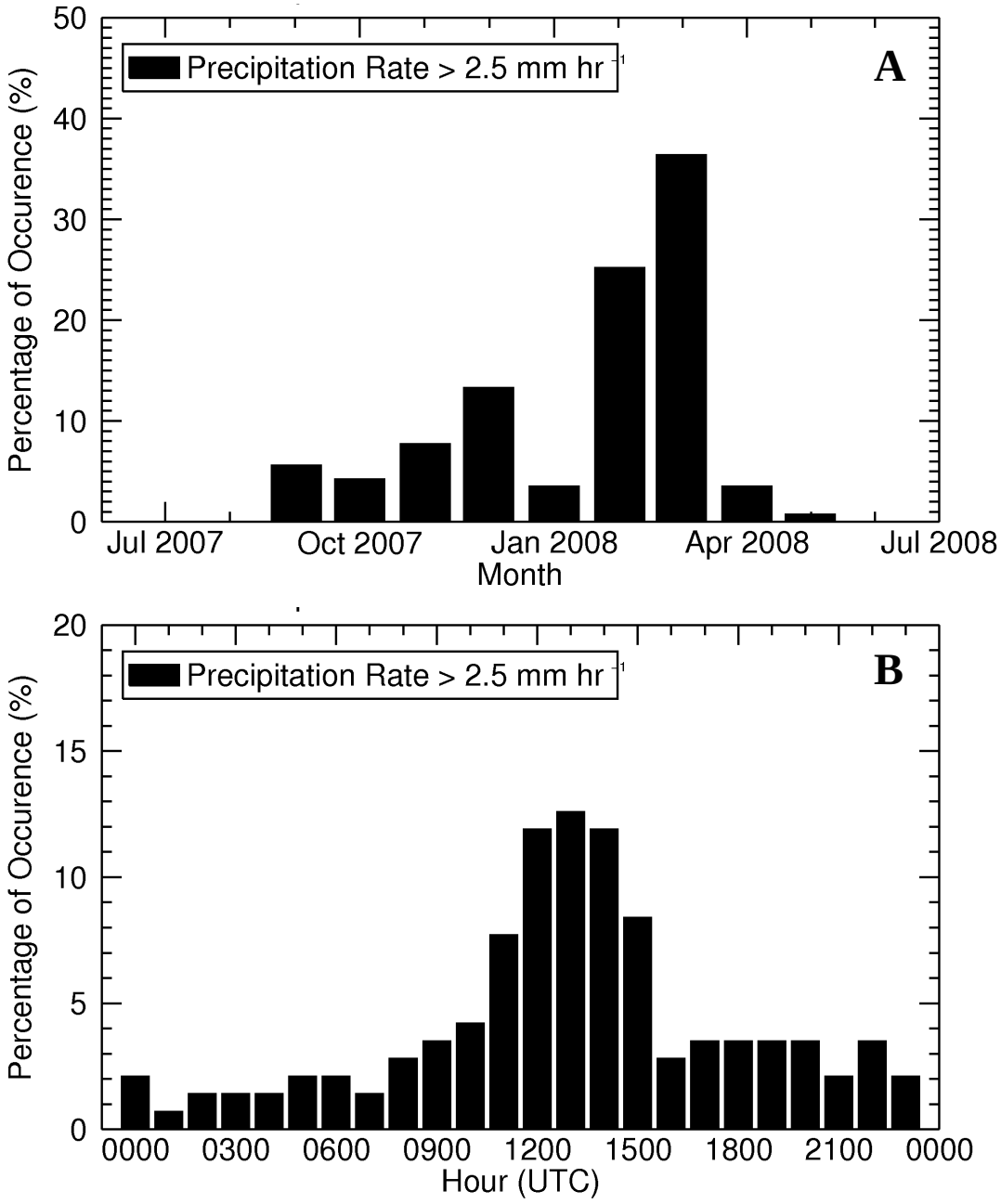

Figure 4.15 Frequency of occurrence of precipitation at points greater than 5000 m for (a) a monthly basis and (b) a diurnal basis. Kilimanjaro local time is UTC + 3, so the majority of the precipitation occurs between 1400 and 1800 local.

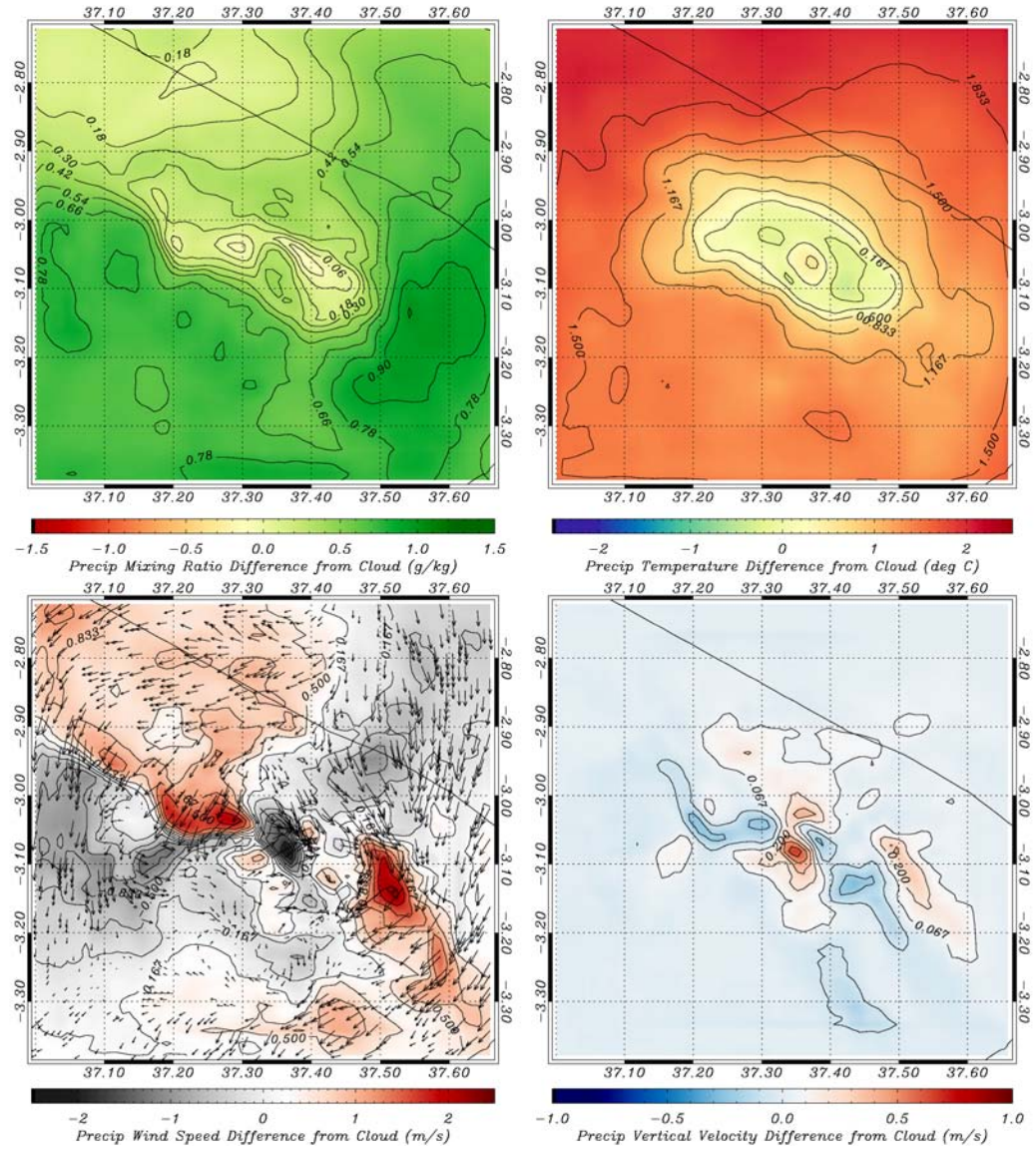

Figure 4.16 Differences in mixing ratio (a) temperature (b), wind speed (c) and vertical velocity (d) between simulation times where there the precipitation rate is greater than 2.5 mm hr^{-1} versus when there is a cloud with a liquid water path exceeding 35 gm^{-2} at elevations greater than 5000 m.

at high elevations when the mixing ratios (Figure 4.16a) are 0.60 – 0.80 gm^{-2} higher and temperature (Figure 4.16b) is ~1.5° C higher and more than when clouds occur. There is much spatial variation in the wind field (Figure 4.16c) for those times precipitation and clouds occur, but in general, it is an exacerbation of what happens to form clouds, with a much higher northerly component of the wind, which is most likely related to the seasonal distribution of rainfall versus the more even seasonal distribution of precipitation. Vertical velocities (Figure 4.16d) show that the only real increase is close to the peak, on the south side, which can be related to the flow regimes during the rainy seasons.

4.7 Terrain Effects on Regional Climate

This section is concerned with the amount of impact that the terrain presents in the regional climate of Kilimanjaro. Flow regimes and generation of precipitation via orographic processes is discussed, with the effects quantified by comparison to the NOTOPO simulation.

4.7.1 Flow diversion of the mountain

Since the terrain is nonuniform in each direction (as shown in Figure 3.1a), there are differing responses to the deflection upwards caused by interaction of the low-level flow with the topography. From the northeast, as the average surface wind is in DJF, the mountain presents a convex shape, easing in the flow around the mountain, whereas the mountain presents a concave shape from the south side, with the southwestern corner most concave. The greatest cross-section presented by the terrain is also during JJA and DJF, with the equivalent cross section presented by the mountain from the southeast being much less.

Spatial patterns of this blocking are clearly visible in Figure 4.17, which demonstrates the difference in wind speed and direction caused by the topography of Kilimanjaro by comparing the wind speeds and directions from the CTL run as previously shown in Figure 4.6 to the NOTOPO run, which uses the topography as specified in Figure 3.1b. The highest differences in wind speed are found in the "blocked" areas, which in JJA is to the north of the mountain, DJF to the southwest, and in the patches seen as areas of low wind speed during SON and MAM. This helps give a magnitude to the amount of blocking actually present in different seasons, something that can be inferred by analysis of Figure 4.6, but not quantified.

Since the wind direction changes with season, the flow diversion calculations found in *Fairman et al.* [2011] are difficult to compute on a consistent basis due to the changes of the prevailing wind. However, considering the uniformity in wind speed presented in the NOTOPO simulation, the variation in the blocking caused by terrain over the course of the year can be summarized by examining the amount of grid points that have low wind speeds over the course of differing months, as shown in Figure 4.18. With an increase in blocking caused by the mountain, there should be a higher percentage of grid points with lower wind speeds. If we consider the percentage of grid points with an average low-level wind speed of less than 3.5 ms^{-1}, we find that during June and July over 33% of the grid falls within this threshold, whereas less than 8% of the grid has wind speeds this low during October, November, and April. During DJF, approximately

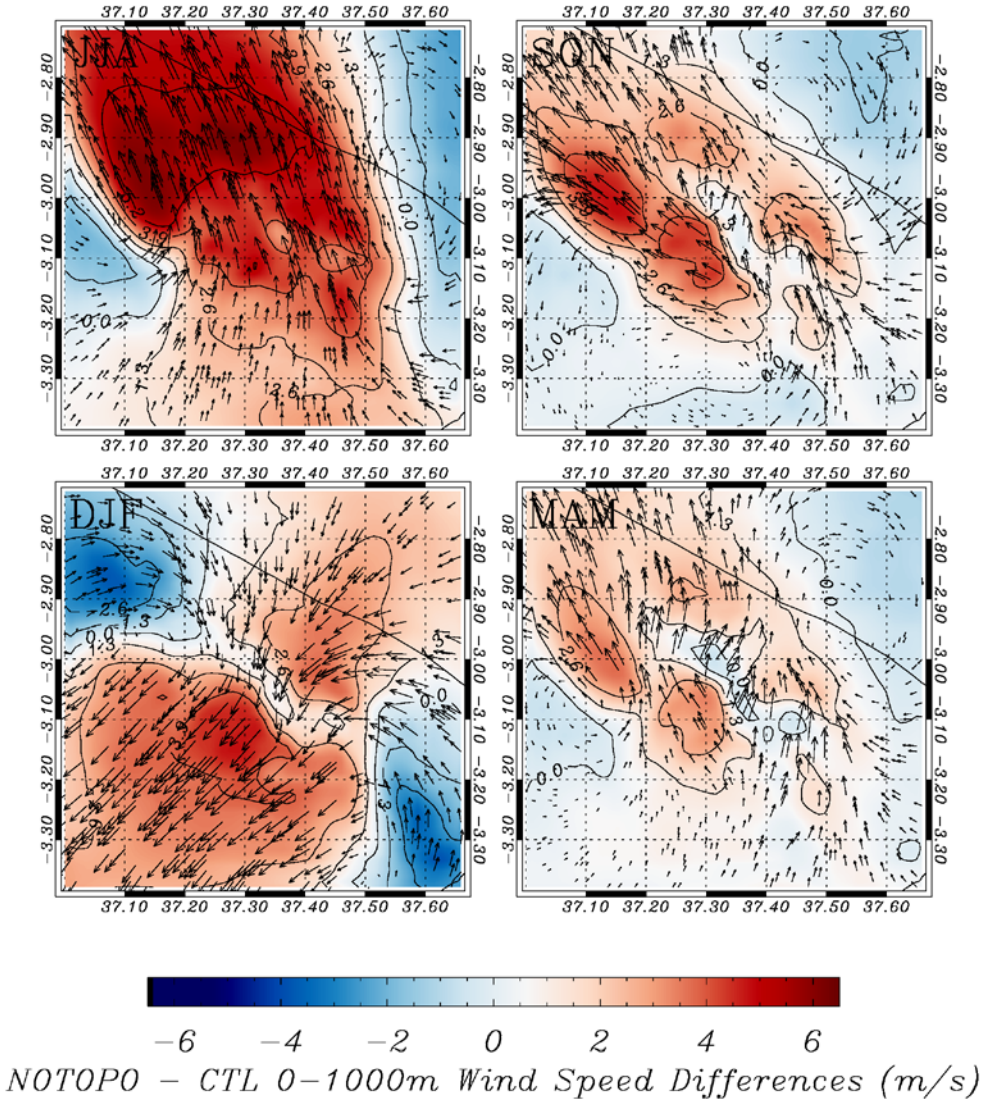

Figure 4.17 0-1000 m average wind speed and vector differences between the NOTOPO and CTL (Figure 4.7) simulations. This gives a measure of the blocking as well as the spatial locations of where the blocking takes place.

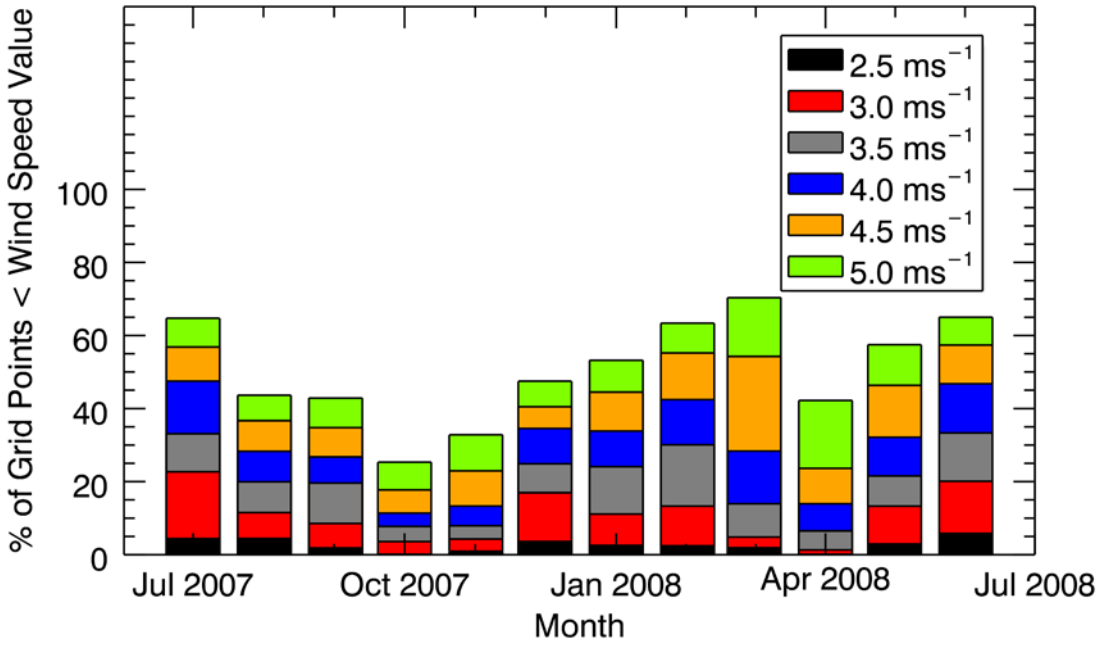

Figure 4.18 Percentage of grid points with the 0-1000m wind speed less than a threshold value over the course of the year. This indicates higher blocking during certain months (July, January) than during the rainy season months (October, April). Of interest is the difference in the number of points below 3.5 ms^{-1} to ascertain the seasonal progression of the blocking as well as the changes in the wind speeds in the transition months (particularly March).

25% of the grid has wind speeds lower than 3.5 ms^{-1}. This blocking leads to acceleration as well, with 14.5% of the grid points having wind speed greater than 8 ms^{-1} during July, whereas none of the grid has an average wind speed greater than 8 ms^{-1} during March. The rainy seasons generally lead to more uniform wind speeds in the CTL simulation because the wind direction and the cross section of the mountain facing the prevailing winds lead to a more "flow-over" situation than the "flow around" regime present in JJA and DJF.

With all of these topographic effects, it is useful to quantify the amount of precipitation generated via these local processes. When we compare the NOTOPO total accumulated precipitation (Figure 4.19a) to the CTL accumulated precipitation (Figure 19b), we can see that there are stark differences. The NOTOPO precipitation is fairly evenly distributed, with an enhancement of the precipitation amounts near the southwest corner of the domain as the air approaches Mount Meru. However, the large deficits are seen in the areas of orographic precipitation surround the south and east sides. We define the percentage of locally generated precipitation via this Equation 4.2:

$$P_{local} = \frac{P_{CTL} - P_{NOTOPO}}{P_{CTL}} \times 100, \tag{4.2}$$

where P_{local} is the percentage of locally generated precipitation due to orographic features, P_{CTL} is the precipitation from the CTL simulation using real topography, and P_{NOTOPO} is the precipitation from the NOTOPO simulation. When plotted against the CTL surface elevation (Figure 4.19c), we can see that the orographic effects account for

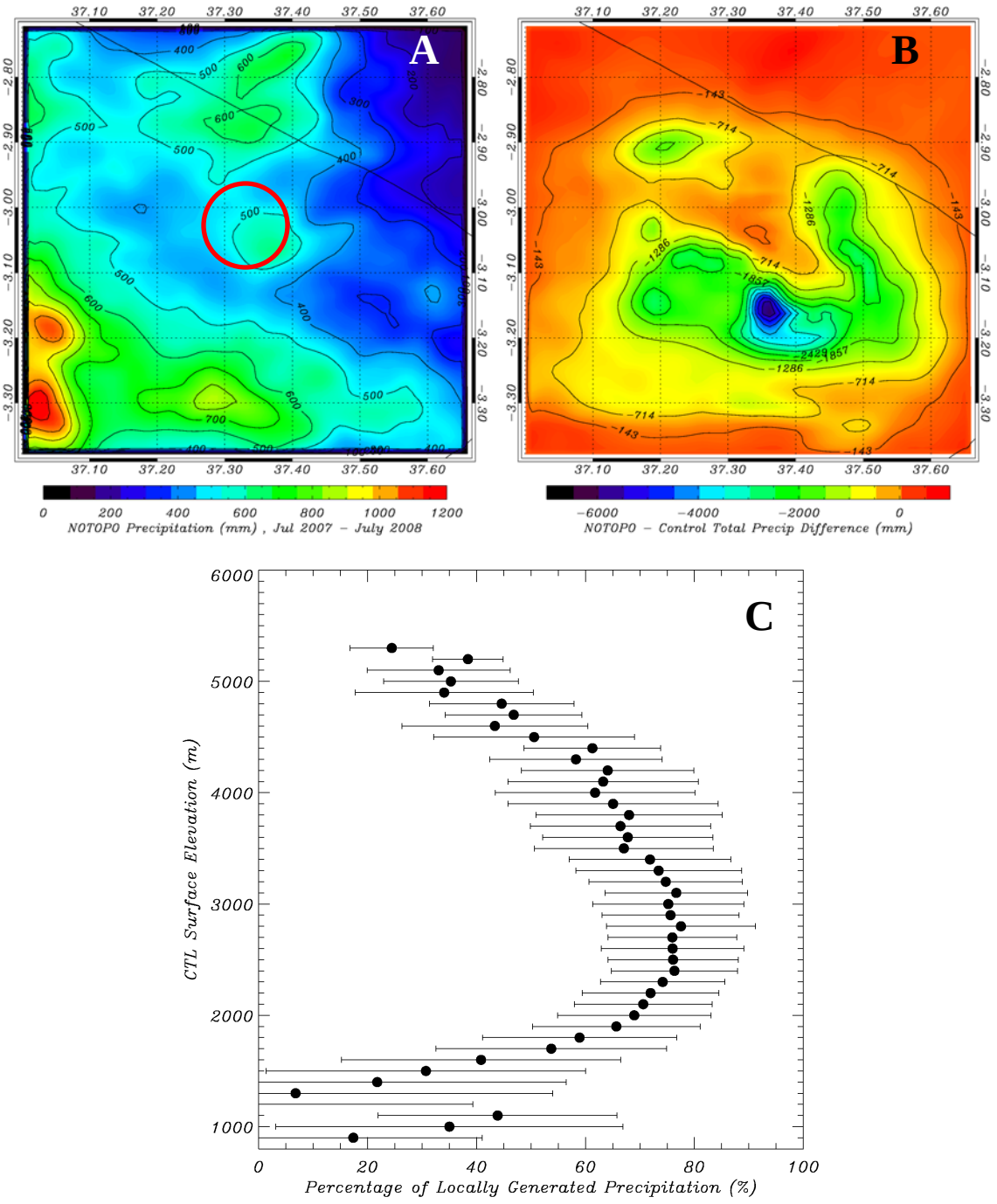

Figure 4.19 NOTOPO precipitation (a), the difference (NOTOPO-CTL) between the NOTOPO and CTL annual total accumulated precipitation (b), and the percentage of locally derived precipitation (c) with respect to the CTL surface elevation. The red circle denotes the peak of Kilimanjaro.

nearly 80% of the precipitation in the maximum elevation areas of rainfall as shown in Figure 4.13. At the peak, however, local effects contribute around 25% of the total precipitation.

4.7.2 Overview of the thermal circulation

Development of the thermal circulation throughout the day is caused by a difference between the free-air temperature and the surface temperature at the same horizontal level, prompting a drop in the pressure at the surface [*Barry,* 2008]. This causes air to flow from the free air to the surface, setting up a localized circulation. In our analysis of the formation of the thermal circulation of Kilimanjaro, we focus on two months at two times: January and July, at 0600 and 1200 UTC (0900 and 1500 East African time) which have been examined in the past for consideration of the thermal circulation in other studies. We compare to the data of *Pepin et al.* [2010] for surface temperature variations as well as the conceptual model of the thermal circulation present in that study, as well as look into the physical reasoning behind the differences in the strength of the thermal circulation.

4.7.2.1 Comparison with conceptual model of *Pepin et al.* [2010]

Pepin et al. [2010] also describes an observational conceptual model of the thermal circulation along a transect on the southwest corner of Kilimanjaro, describing the differences that occur over the course of the day during two different months: July and January. By using our data and comparing to the conceptual model (Figure 11 from *Pepin et al.* [2010]), we can see the similarities in the development of the thermal circulation on Kilimanjaro. These variations are shown in Figure 4.20.

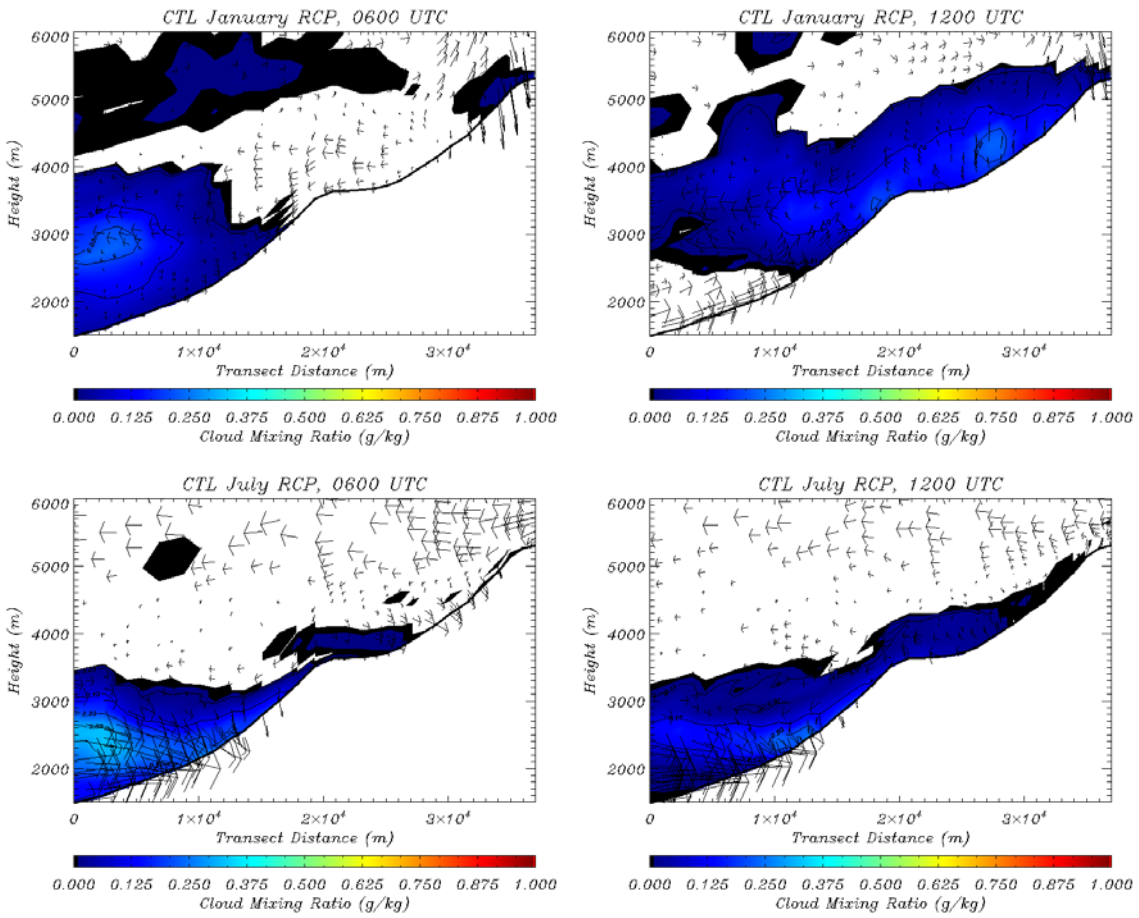

Figure 4.20 Cloud mixing ratio along the transect defined by *Pepin et al.* (2010), comparable to *Pepin et al.* [2010] Figure 11.

During the morning hours, there is persistent cloud cover over the lower elevations of Kilimanjaro, with cloud tops of ~4000 m during January (Figure 4.20a) and ~3500 m during July (Figure 4.20c). However, the clouds extend over the surface to elevations exceeding 3000 m (up to 4000 m) on average during July, versus cutting off at ~3000 m during January. Because of the solar position during January (during austral summer and perihelion), there is additional solar radiation present at upper slopes, causing the temperature to rise and exciting the thermal circulation. This causes the cloud tops to rise over the course of the day, as seen by the clouds present at 1200 UTC.

Pepin et al. [2010] describe the ability of the thermal circulation to be able to tap into the moisture source of the downslope vegetation as the primary factor between the thermal circulation present during July versus January. With the downslope vegetation being thermally limited due to cloud cover, the extent of the thermal circulation is limited to areas that warm due to solar heating. Since during July, the cloud cover extends further upslope than in January during the morning hours, there is less heating taking place over the higher elevation vegetation. In January, where the overnight clouds exist in a smaller location, there can be additional moisture flux from the vegetated areas from ~3000-4000 m as the thermal circulation develops throughout the day.

However, in July, there are differing factors. The solar angle will be to the north of the southwestern transect, limiting early morning shortwave radiation due to the shadowing of the mountain (versus the direct aspect present during January). The clouds cover the vegetated areas during the morning, limiting the vertical extent of the thermal circulation as the solar energy goes to evaporation of the clouds (therefore limiting their

vertical extent, as seen in the diagrams of the cloud mixing ratio) versus heating the surface as in January.

4.7.2.2 Diurnal variation in model derived fields

The thermal circulation peaks at 1200 UTC (1500 East African time), which is visible in the peaks of high elevation cloudiness (Figure 4.11) and precipitation (Figure 4.15). If we compare the change in temperature between 1200 UTC and 0600 UTC for the free air near Kilimanjaro, we see that during January (Figure 4.21a,b) there is a decrease in the free air temperature of up to 0.5° on the southern and western sides of Kilimanjaro, with an increase of 0.25° on the northern side. There is also an increase in moisture (Figure 4.21c,d) exceeding 2.0 g/kg. This can be directly contrasted to the changes that are found in July (Figure 4.22), where there is a fairly uniform rise in the free air temperature. With this temperature rise in the free air temperature over the course of the day, the difference between the free air temperature shown in Figure 4.22 and the surface will not be as elevated, therefore lessening the generation of the pressure gradients.

When we examine the change in pressure gradient from 0600 UTC to 1200 UTC in January (Figure 4.23a,b) and July (Figure 4.23c,d), we can se that the pressure gradient becomes stronger in July, with an increase in the magnitude of the pressure gradient force on the southwest side due to the temperature difference from the free air to the surface. In July, there is not a uniform signal in the generation of the pressure gradient force, with the magnitudes of the change between 1200 UTC and 0600 UTC being much smaller. This gives the physical reasoning behind the conceptual model given by *Pepin et al.* [2010], as the free air surface temperature difference does not

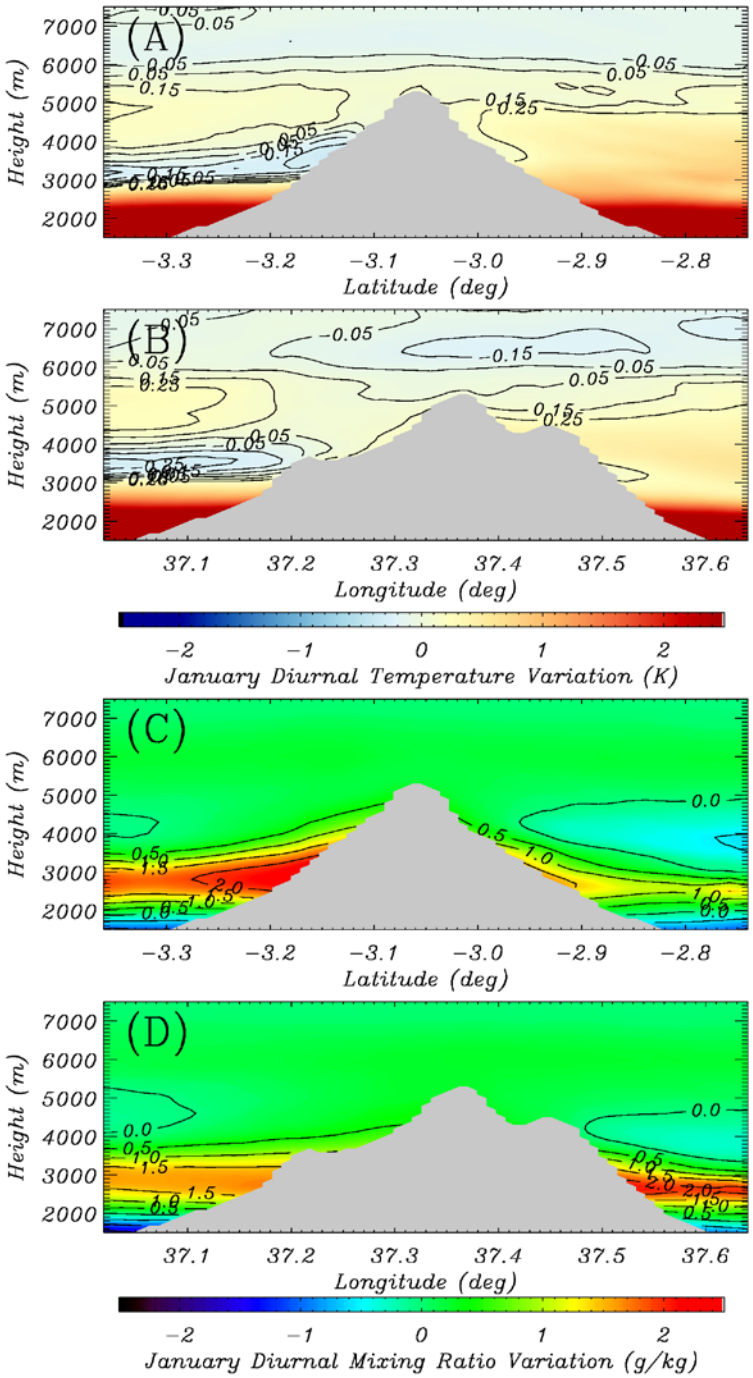

Figure 4.21 Zonal (a,c) and meridional (b,d) means of 1200 UTC – 0600 UTC temperature (a,b) and mixing ratio (c,d) during January.

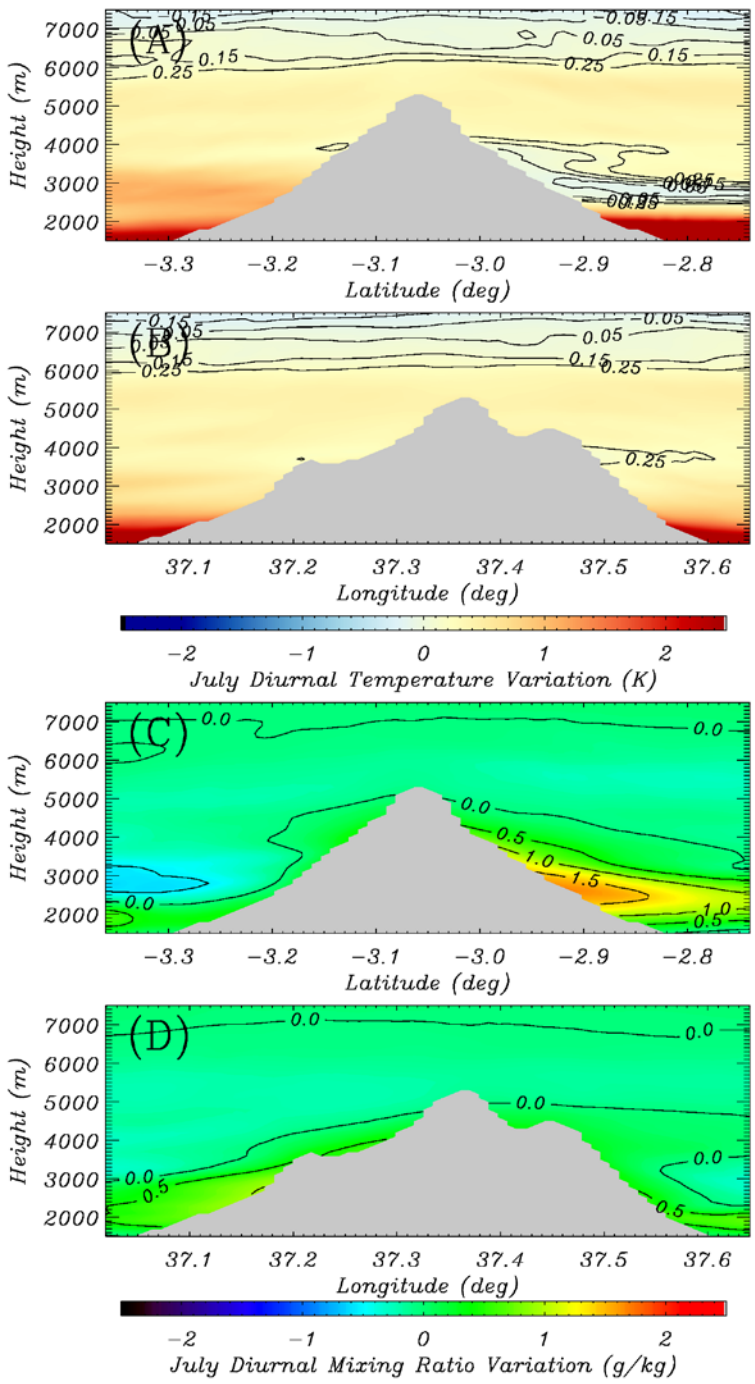

Figure 4.22 Same as Figure 4.21, but for July.

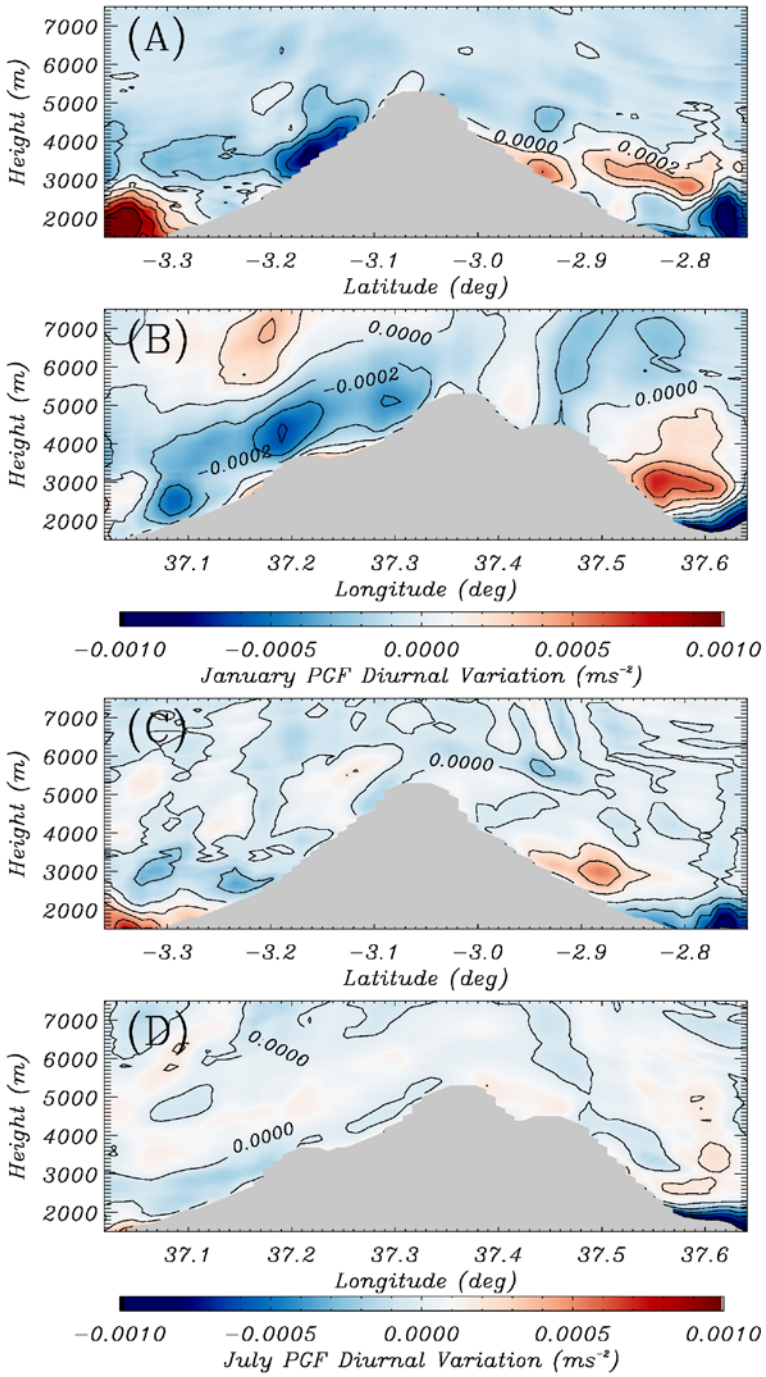

Figure 4.23 Zonal (a,c) and meridional (b,d) mean differences in pressure gradient force during January (a,b) and July (c,d). The strong negative values present in January indicate a stronger pressure gradient during January on the southwestern side than during July, and a more vigorous thermal circulation.

develop over the course of the day in July when compared to January, and the transport of moisture upslope is more limited.

4.8 Discussion

In the course of the analysis, there are several interesting results as well as issues to discuss. High resolution model runs have been performed of Kilimanjaro using a standardized Witch of Agnesi function in order to simulate model topography. While in the north-south direction, this is generally true, this is not representative of the topography as a whole, which has significant variations as well as marked concavity on the southwestern side. When faced with differing wind patterns, a Witch of Agnesi will show that Kilimanjaro would block winds from all directions uniformly, as was found in *Molg et al.* [2008], where Froude number did not vary with season. However, our results show that the amount of blocking caused by the mountain can be related to the shape of the topography, and that the blocked areas are much less during the seasons where the mountain presents the smallest cross section into the leading wind (such as is the case in DJF and MAM).

The "wet" and "dry" seasons of Kilimanjaro have typically been broken up into the "short rains" of October-December and "long rains" of March-May. These do vary on an annual basis, and we find that there is significant differences in what can be considered a "rainy" and "dry" season during our study year. For ease of understanding, we have grouped the seasons into the standard meteorological conventions of JJA, SON, DJF and MAM. This takes into account that we are grouping our first two months of model operation (July and August) with our last month of calculations (June), and are therefore grouping non-continuous time periods in the JJA analysis. Since the "short

rains" of October-December are split into two seasons, there will be incomplete cross-over and characteristics of the rainy seasons will be intermixed with the dry.

What we did notice this year, however, is that the secondary dry season between the "long rains" and "short rains" for our time period is very short, spanning a few weeks at the end of December until the middle of February. Monthly analysis of January shows far less rainfall than December or February, but the secondary dry season in this case is fairly short. The rain near Kilimanjaro also subsides near the middle of April, leading to the drying trend that is visible on the plots of dewpoint bias. Therefore, these characterizations of the rainy seasons are not all-encompassing for this analysis.

While our precipitation followed the approximate shape as derived from *Rohr and Killingveit* [2003], the shape required a tweak of 800m in the vertical in order to match the modeled precipitation. While the precipitation at the peak of Kilimanjaro will be overestimated to the data of *Molg et al.* [2009] due to the fact that it is a 1 km average with a maximum elevation of 5308 m, the amount of averaging of surface elevation most likely does not account for all of the adjustment to the derived function of precipitation. It is possible that the areas of maximum precipitation were moved upslope during this year due to either less moisture or higher wind speeds than those present during the analysis of *Rohr and Killingveit* [2003], which needs to be evaluated to see if this is a model bias or interannual variation.

Over the course of this year, an interesting feature became known. When the winds were generally calm, originating from the northeast during the months of February (Figure 4.24), the diversion caused by the mountain would set up a gyre that would lead

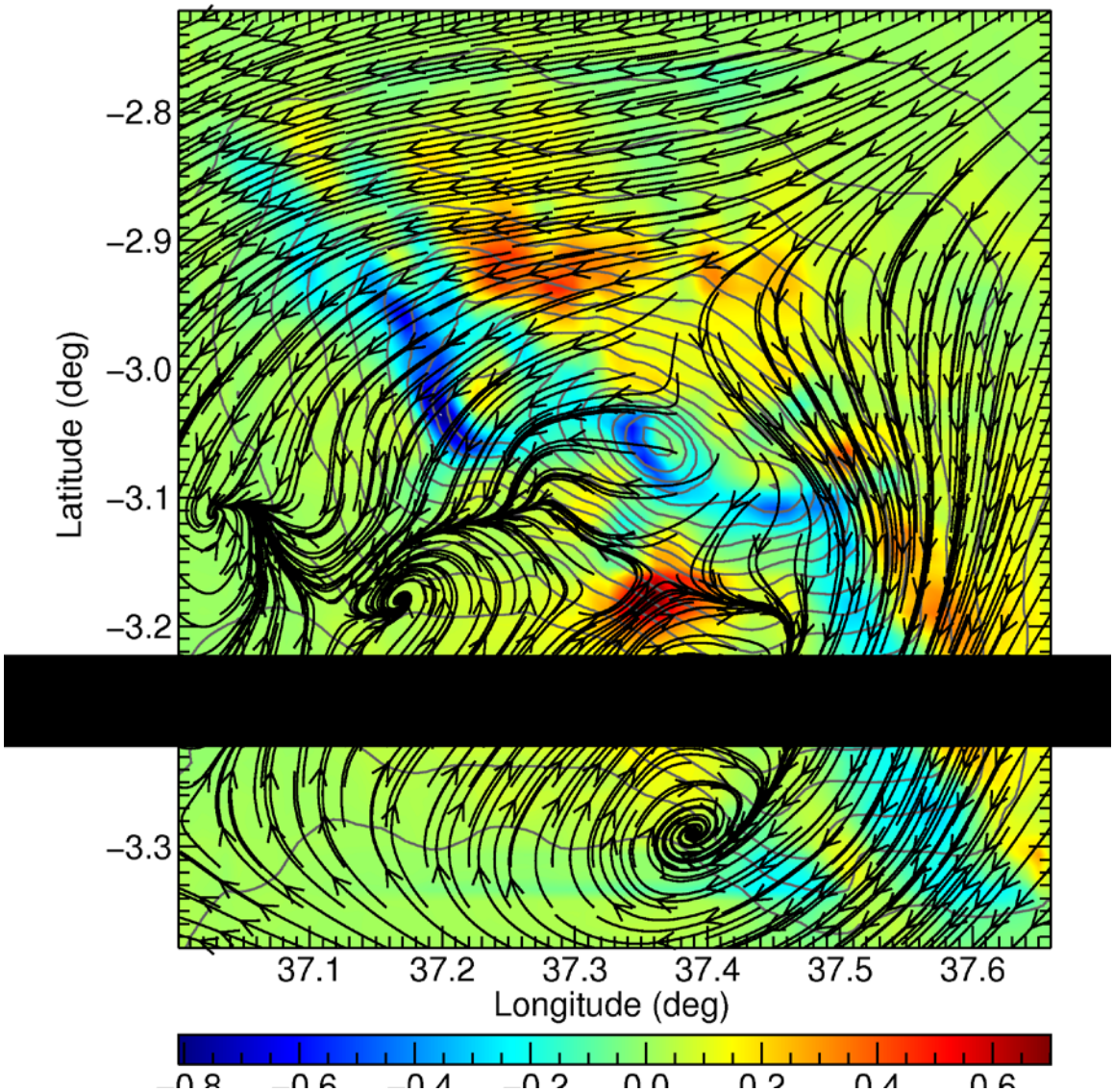

Figure 4.24 February average vertical velocity and 0-1000m horizontal wind streamlines, over contours of topography (250 m contours). This shows the flow reversal as discussed in *Molg et al.* [2008a], with characteristic flows originating from the northeast but the convection occurring on the south side of the mountain.

to an area of high precipitation on the leeward side. The mountain presents a convex shape to the northeast, leading to the winds to go to the outside areas, whereas the gyre would set up a strong updraft in the concave side of the mountain on the south side, leading to large (> 250 mm) amounts of precipitation falling. This feature was very localized and only appeared on certain days of the year with a certain synoptic wind pattern. There have been reports of strong storms to the south side of Kilimanjaro during these seasons, with isolated cloudbursts occurring [T. Molg and N. Pepin, personal communication], but it is a persistent, physically consistent feature that appears certain days of the year that may lead to this upward shift in elevation of maximum precipitation.

The quantification of what causes precipitation to occur at the peak of Kilimanjaro shows that there is a strong dependence on the thermodynamic variables present in upslope locations. Increases in mixing ratio and temperature at lower elevations were consistently found to be occurring when clouds or precipitation occurred at the peak. This indicates that the primary formation mechanism of high-elevation precipitation is a thermodynamic one versus mechanical formation of precipitation due to high wind speeds causing enhanced vertical velocity. While it is possible that wind speeds do have an impact, during cloud and precipitation times, there is generally less of an emphasis on the wind fields on a grid-averaged basis, with the main part being wind interacting with high topographic gradients. This caused increases in vertical velocity at certain points that when provided with a moist atmosphere allowed for convection to occur over the high elevations.

4.9 Conclusions

We have modeled the meteorology of Kilimanjaro at one kilometer grid spacing for the course of one year, examining the seasonal progression of meteorological fields as well as the impact that the topography had on the weather. Our conclusions are as follows:

1. The model results verify reasonably well for fields of temperature, dewpoint, and wind speed on the large scale, and temperature, vapor pressure, and cloud formation on the small scale, indicating adequate model characterization of the actual weather patterns and seasonal progression.

2. The model underestimates much of the large-scale precipitation over central east Africa, leading to a dry bias appearing in the dewpoint statistics after the departure of the ITCZ to the north. The broad circulation of Mount Kenya is not resolved on the large scale, with consistent underestimation of precipitation found in central Kenya. Comparison of the patterns shows agreement on a broad sense with TRMM for areas of high precipitation, excluding the area near Mount Kenya.

3. The amount of blocking caused by the topography varies by season, with JJA and DJF resulting in the most blocked area and therefore have the most variation in wind speed, accelerating the winds on the periphery of the mountain. This pattern of blocking would not be simulated via a uniform distribution of topography in two dimensions, and the areas of maximum vertical velocity would be in the wrong place.

4. The areas of the highest cloud frequency are found on the windward slopes of the mountain, which changes by season. The concavity of the mountain on the southeast corner leads to a very consistent cloud bank where the thickest clouds exist.

5. 50% of clouds at high elevations occur during the afternoon hours, with 60% of the precipitation occurring during the same time period. This shows the strong effects that the thermal circulation has on Mount Kilimanjaro.

6. There is little seasonal variation in cloud occurrence at high elevations, but much seasonal variation of precipitation occurrence, with the majority of precipitation times occurring during February and March of 2008.

7. Clouds occur at the peak during conditions of warmer low-elevation temperatures of around 1.5-1.7° and moister conditions of 0.80 gm^{-2} compared to when clouds do not occur. Precipitation exacerbates these patterns, with low elevation temperatures being around 3-3.5° warmer and surface mixing ratios being 1.5-1.7 gm^{-2} moister compared to when precipitation does not occur. This is double the difference needed for clouds to form.

8. Wind fields are variable during cloud and precipitation formation, but are tied to higher winds aloft leading to elevated areas of higher vertical velocity. The locations of enhanced vertical velocities are important to generate enough uplift for convection to reach the peak.

9. The altitude of maximum precipitation found in the model simulations is around ~600-800 m higher than shown in previous studies. By adjusting the function fit to the altitude of maximum precipitation shown by the model results, the function of precipitation with elevation follows the general pattern found through our one-year analysis.

10. 25% of the precipitation that falls at the peak is due to local effects caused by the orography interacting with the atmosphere. For the places on the mountain with the highest amount of precipitation, up to 80% of the precipitation is generated via orographic and other local processes.

11. The thermal circulation induces cloud formation that peaks over the afternoon. This is caused by a cooling in the free air compared to warming on the slope, inducing a horizontal pressure gradient directed towards the mountain. This leads to additional moisture transport up the mountain. On the southwest side of the mountain in January, the free air cools while the surface warms, whereas in July the free air warms while the surface does not.

12. February precipitation occurs mainly on the south slopes of Kilimanjaro due to a flow reversal on the leeward side of the mountain that forms a persistent updraft due to the reversed flow diverging after hitting the mountain. This, combined with the enhanced thermal circulation due to the solar position on the south side of the mountain, leads to enhanced precipitation formation.

We have shown the model results for one year of high-resolution atmospheric modeling, concentrating on factors that produce convection on the peak of Kilimanjaro, both in a diurnal and seasonal sense. The next chapter will discuss the differences caused by changing the land cover scenarios described in Chapter 3, focusing on the dry season month of July, presenting the results of *Fairman et al.* [2011]. Following analysis of the dry season, we will discuss the modifications of land cover situations with similar analysis to this chapter in Chapter 6, focusing on a full year of model results.

CHAPTER 5

LAND USE CHANGE IMPACTS ON REGIONAL CLIMATE OF KILIMANJARO (DRY SEASON)

5.1 Introduction

Orographic effects on regional weather and climate are significant [*Barry*, 2008; *Pielke*, 2002; *Whiteman*, 2000] with the modification of the background flow by the terrain being the dominant effect. Direct orographic uplift and formation of orographic cloud systems often leads to enhanced precipitation on the windward slopes and, at times, rain shadow regions on the lee slopes, depending on the nature of the terrain and geographic location. Thermal circulations forced by the terrain also enhance convection over orographic features. Relatively strong variations in temperature, moisture and wind in the vertical combined with terrain driven precipitation inhomogeneities and orographic cloud cover create significant climatic variations and provide the environment for high levels of biological endemism. Extreme examples of species which are unique to a single geographic zone include the golden toad, an amphibian endemic to Monteverde region of Costa Rica. Recent studies show that mountain weather and climate is disproportionately impacted by climate variability and change which is effected by both natural and

anthropogenic forcing [*Pounds et al.,* 1999; *Still et al.,* 1999; *Nair et al.,* 2003; *Ray et al.,* 2006; *Nair et al.,* 2010]. Since modification of mountain weather and climate has significant implications for regional water resources and ecological sustainability, there is a need to understand the impact of different anthropogenic and natural climate forcings and also their interactions.

Prior research [*Lawton et al.,* 2001; *Nair et al.,* 2003; *Ray et al.,* 2006; *Nair et al.,* 2010; *Van der Molen,* 2002; *Bruijnzeel,* 2004; *Van der Molen et al.,* 2009, *Chase et al.,* 1999] shows that land use change in the vicinity of montane regions alters topographically generated circulation patterns as well as temperature and moisture of lowland air masses that ultimately impact orographic cloud formation. However, atmospheric response of deforestation in montane areas is very dependent on the geographical setting. In Costa Rica, modeling studies [*Lawton et al.,* 2001; *Nair et al.,* 2003; *Ray et al.,* 2006; *Nair et al.,* 2010] as well as radiosonde observational analysis [*Nair et al.,* 2008] show that deforestation results in increase in cloud base height of boundary layer clouds. However, *Van der Molen* [2002] found that coastal deforestation in an island setting in Puerto Rico resulted in enhanced slope circulations leading to invigoration of montane cloud formation.

Land use may also impact the regional climate of Kilimanjaro in East Africa, where retreating glaciers on the peak of Kibo are one apparent phenomenon of large-scale climate variability and change [*Thompson et al.,* 2002; *Cullen et al.,* 2006]. The regional manifestation of the large-scale changes is characterized by drying, which might have its origin in the late 19th century and clearly appears in modern observations over the past

decades [*Mölg et al.*, 2009b]. Aside from glacier shrinkage this drying has affected regional life forms, agriculture, and vegetation, which is also summarized in *Mölg et al.* [2009b]. The manner in which regional climate of Kilimanjaro responds to land use change, however, may be significantly different compared to other areas since Kilimanjaro, as an isolated terrain feature in an inland area, occupies a very different geographical setting. Initial, idealized mesoscale numerical modeling experiments conducted by *Mölg et al.* [2009a] suggest that on Kilimanjaro a "flow-around-regime" may occur frequently, as opposed to a "flow-over-regime." Thus, topographically generated convection may be as or more relevant than cloud formation due to direct topographical lifting of air. In this context, land use change has the potential to impact the regional climate of Kilimanjaro. *Mölg et al.* [2008a] hypothesized that for Kilimanjaro, the local anthropogenic forcing due to land use change is potentially being superimposed on larger scale climate forcing. However, the magnitude and exact nature of this forcing is unknown.

The overall goal of the present study is to examine the impact of land use change on the regional climate of Kilimanjaro through a month-long regional atmospheric model simulations using the Regional Atmospheric Modeling System [*Cotton et al.*, 2003] (referred to from now on as RAMS) driven by larger scale observed atmospheric flow features. The study area was previously described in Chapter 2. Datasets used were described in Chapter 3, along with methodology for the land use classifications. Results are detailed for the dry season in Section 5.2. Section 5.3 includes discussion of the results, while Section 5.4 concludes.

5.2 Results

We use three different numerical modeling experiments, assuming land use scenarios in which 1) the current vegetation coverage persists; 2) the area is completely deforested; and 3) the area is completely reforested. The RAMS simulation assuming current vegetation coverage (referred as CTL from hereon) is used as the point of comparison for the other vegetation scenarios, as well as to evaluate the performance of RAMS over the study time by comparing it against surface observations and satellite observations of cloudiness. The model experiment is than repeated for deforested and reforested land use scenarios (referred from hereon as DEF and REF).

RAMS experiments for the land use scenarios described in Chapter 3 are used to examine the impact of land use on surface energy budgets, circulation patterns and cloud formation for the month of July 2007. Note that except for surface meteorology and rainfall comparisons (Sections 5.2.1.1 and 5.2.1.2), analysis discussed in the study are for grid 4.

5.2.1 Evaluation of the RAMS simulations

The RAMS simulation for the current land use conditions is evaluated by 1) Comparing the model simulated surface meteorology and observations at meteorological stations; 2) comparing the model simulated precipitation to surface observations and satellite observations; and 3) comparing the model simulated cloud fields against satellite observations.

5.2.1.1 Surface temperature, dew point and wind comparisons

This study utilizes a statistical approach similar to that of *Zhong and Fast* [2003] for evaluation of RAMS simulated 2 m temperature, dew point and winds against corresponding observations (Table 5.1, Figures 5.1a,b, and c). Since East Africa is a relatively observation-poor area [*Christy et al,*, 2009], only a few stations with observational fidelity sufficient for statistical analysis exist within the domain covered by the model grids. Therefore, the statistical approach compares hourly surface meteorological observations (NCDC DS-3505) from grid G2 (16 km grid spacing, Figure 3.1b) to maximize the number of observations available for the analysis. The statistical analysis (Figure 5.1a, b) show the magnitudes of root mean square error (RMSE) and bias for surface temperature and dew point comparisons show a pattern where a decreasing trend is observed, with lowest values of RMSE and bias occurring toward the end of the simulation. For example, the daytime temperature bias, which was often in excess of -1° C during the early part of the experiment, approaches zero towards the end of the simulation (Figure 5.1a, b). Table 5.2 shows the mean RMSE, bias, and error standard deviation for the entire month for two meter temperature, surface dewpoint, and surface wind speed. The comparisons indicate that the computed values of RMSE, BIAS, and ESD all fall within ranges reported by modeling studies over other regions [*Zhong and Fast* 2003; *Miao et al.* 2007; *Mölders* 2008; *Ray et al.*, 2010], demonstrating adequate performance of RAMS over the study area.

Table 5.1 The 24 stations used in the analysis of RMSE, bias, and error standard deviation. The table gives WMO identification number, station name, country, and latitude/longitude location. These 24 sites are indicated as red dots in Figure 5.1c. Asterisks indicate the site was also used for precipitation verification in Figure 5.5c.

WMO ID	Station Name	Country	Latitude	Longitude
637330	Musoma*	Tanzania	1.50	33.80
637890	Arusha	Tanzania	-3.33	36.61
637900	Moshi	Tanzania	-3.35	37.33
637910	Kilimanjaro Airport*	Tanzania	-3.41	37.06
638160	Same	Tanzania	-4.08	37.71
638440	Tanga	Tanzania	-5.08	39.06
638450	Pemba / Karume Airport	Tanzania	-5.25	39.81
638620	Dodoma	Tanzania	-6.16	35.76
638660	Morogoro*	Tanzania	-6.83	37.65
638700	Zanzibar*	Tanzania	-6.21	39.21
638940	Dar Es Salaam Airport*	Tanzania	-6.86	39.20
636610	Kitale*	Kenya	1.01	35.00
636710	Wajir	Kenya	1.75	40.06
636860	Eldoret	Kenya	0.53	35.28
636950	Meru	Kenya	0.08	37.65
637080	Kisumu*	Kenya	-0.10	34.75
637140	Nakuru*	Kenya	-0.26	36.10
637170	Nyeri*	Kenya	-0.50	36.96
637200	Embu*	Kenya	-0.50	37.45
637230	Garissa	Kenya	-0.46	39.63
637400	Nairobi*	Kenya	-1.31	36.93
637720	Lamu*	Kenya	-2.26	40.83
637930	Voi*	Kenya	-3.40	38.56
638200	Mombasa*	Kenya	-4.03	39.61

This trend observed in the simulation is potentially related to adjustment of the coarse grid spacing soil moisture field from the GFS-ANL analysis that is used to initialize the RAMS simulations. Comparison to observations over other geographical regions show that the GFS-ANL soil moisture fields have a wet bias, and the improvements in the day time RAMS simulated surface temperature is related to the soil moisture field adjusting to the atmospheric conditions at scales finer than those resolved in the NCEP global model used to generate the GFS analysis. The substantial biases in nocturnal temperatures found in the numerical simulation are due to the enhanced sensitivity of nocturnal boundary layer to local differences in surface characteristics between the land use scenarios [*Nair et al.,* 2010], which is not reflected in the coarse grid spacing experiment.

Table 5.2 Monthly mean values of root mean square error, bias, and error standard deviation for temperature, dewpoint, and wind speed.

	2m Temperature	**Dewpoint**	**Wind Speed**
RMSE	1.99 K	0.92 K	1.52 m/s
Bias	-1.49 K	-0.18 K	0.27 m/s
Error SD	2.51 K	1.34 K	2.17 m/s

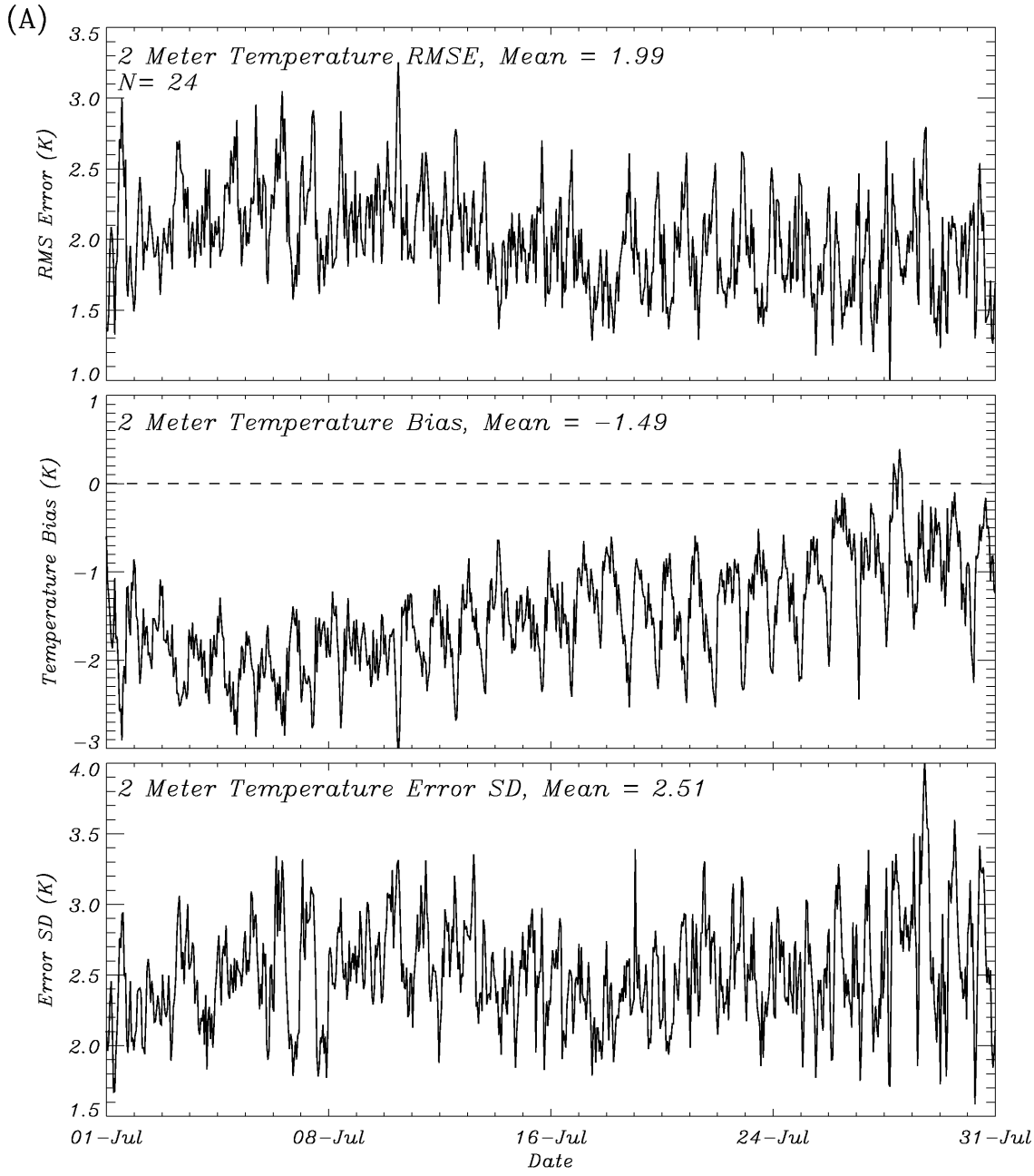

Figure 5.1 Root-mean-square errors for a) 2-meter temperature, b) dewpoint and c) wind speed following methods of *Zhong and Fast* [2003]. The 24 sites used in this analysis are shown in Table 5.1, and average values are given in Table 5.2.

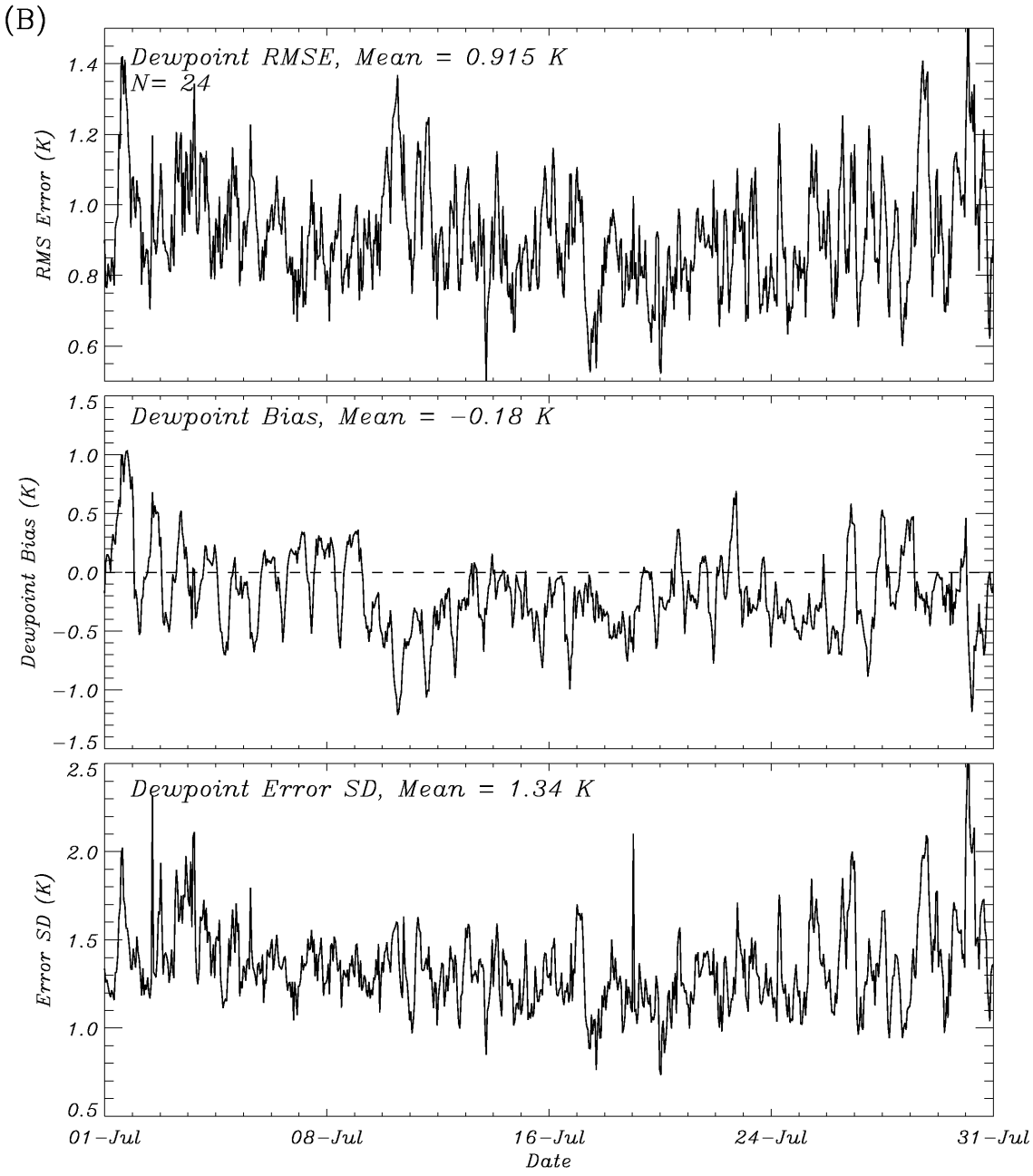

Figure 5.1 (continued).

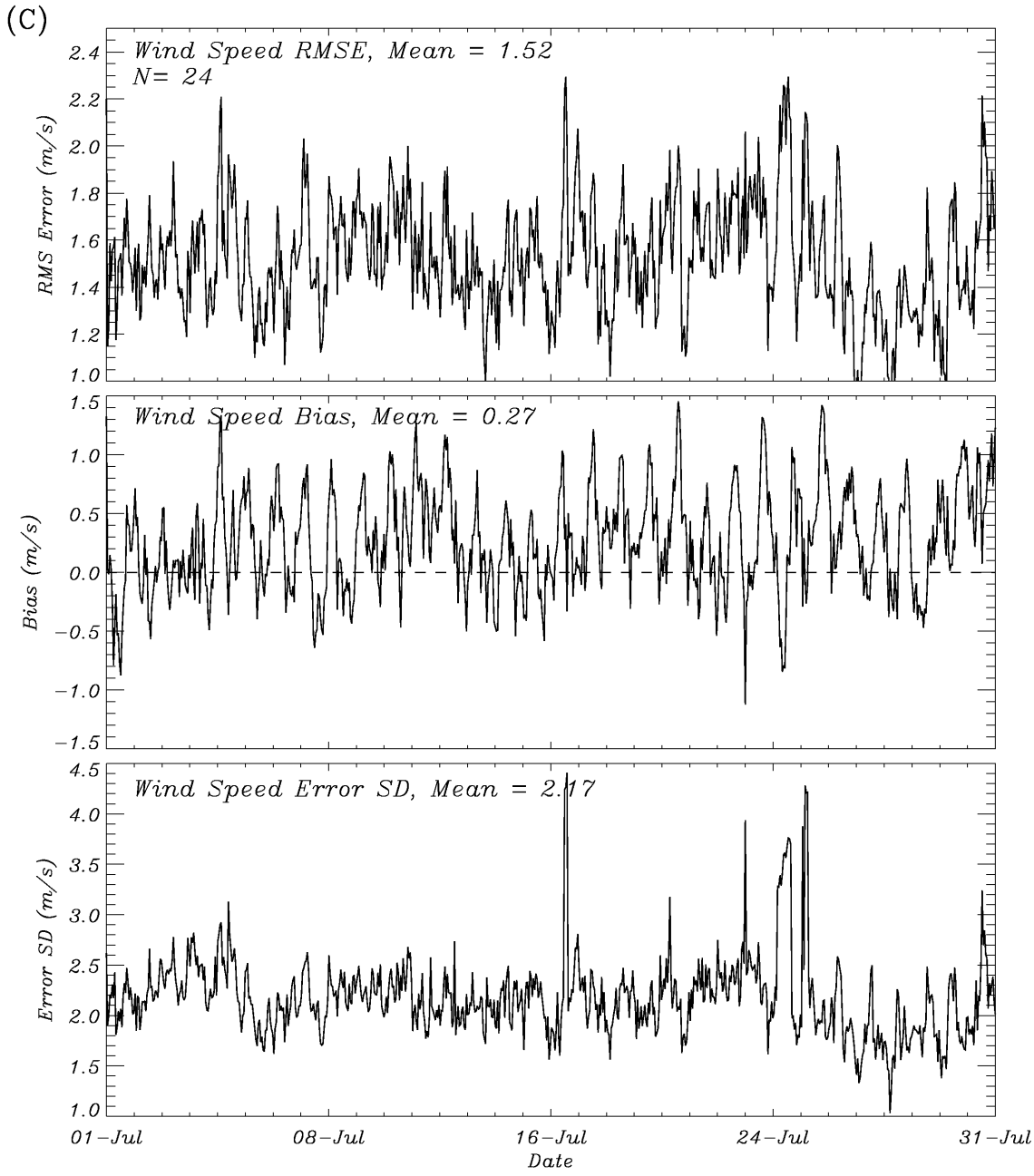

Figure 5.1 (continued).

In addition to the statistical approach, point comparisons are conducted against observations from Kilimanjaro International Airport and Nairobi for which simulated values from the grid G3 (4 km grid spacing) are used. There is good agreement between the RAMS simulated 2 m temperature and surface observations from Kilimanjaro International Airport, Tanzania and the Nairobi, Kenya Air Force base (Figures 5.2a, 5.2b) for the current land use condition with correlations of 0.76 and 0.84, respectively. The agreement between the RAMS simulated dew point temperature and observations is substantially less, with the correlations of 0.56 and 0.41 found for the Kilimanjaro Airport and Nairobi Air Force base stations, respectively (Figures 5.2c and 5.2d). However, this decrease in correlation coefficient may be more due to the lack of diurnal signal in the model as compared to the observations, as the average root mean square error is a lot less.

5.2.1.2 Surface rainfall comparison

The number of stations in the study area that report rainfall observations (Table 5.1, Figure 5.3c) are substantially less (14) compared to those that report temperature, dew point and wind speed observations (24). Therefore, numerical model simulated precipitation (Figure 5.3a) is also compared to the Tropical Rainfall Measuring Mission(TRMM) [*Kummerow et al.,* 1998] measurements over the study area (Figure 5.5b). However, note that while the 0.25° x 0.25° gridded TRMM 3B43 monthly total precipitation product (Figure 5.5b) does not adequately resolve the fine scale patterns of orographic precipitation over Kilimanjaro, it provides information on larger scale spatial patterns and complements the coarser scale surface observations.

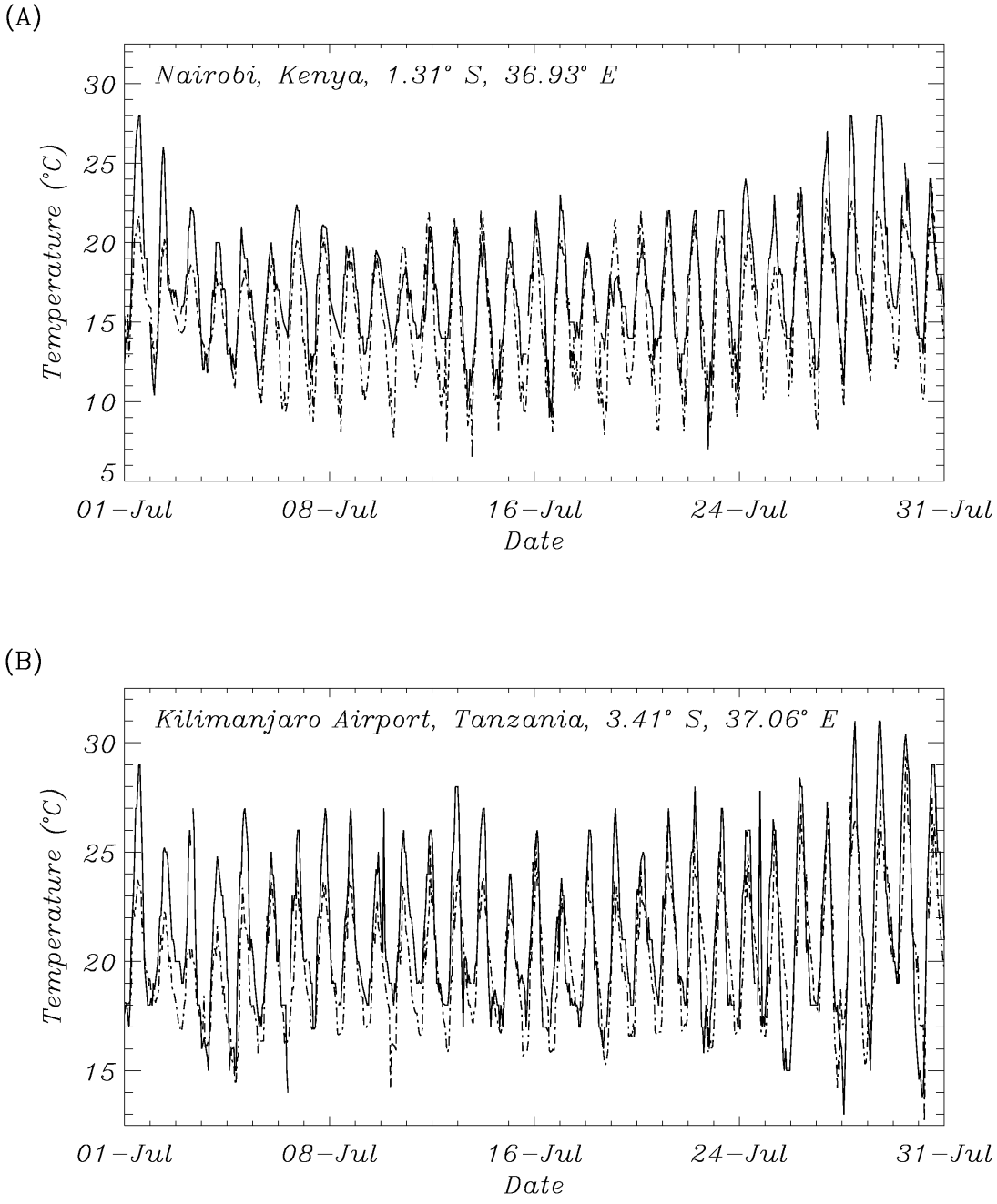

Figure 5.2 Month-long comparisons of temperature (a and b) and dewpoint (c and d) for Nairobi, Kenya, and Kilimanjaro International Airport between the model (dashed line) and observations (solid line).

(C)

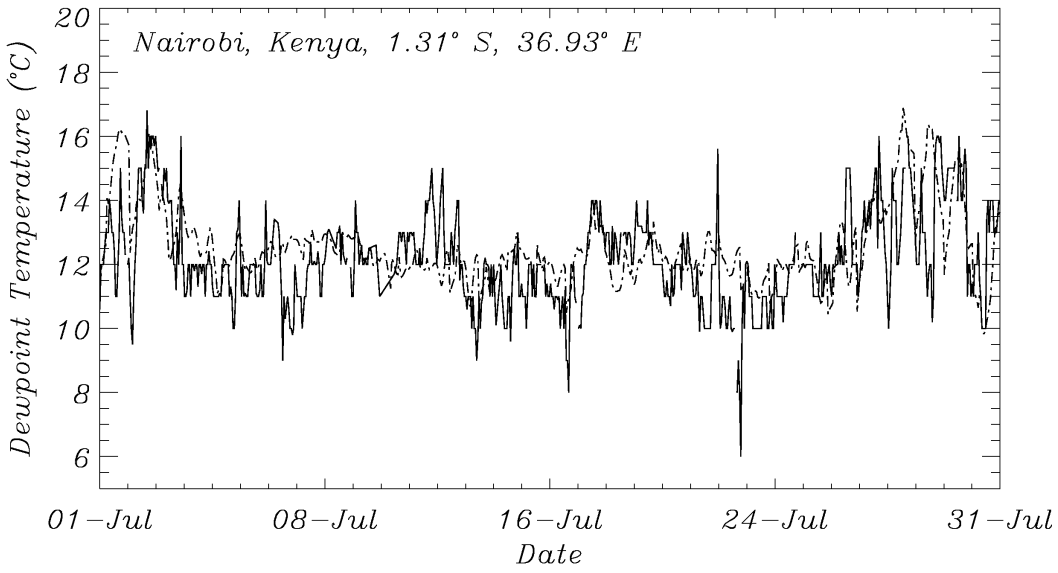

(D)

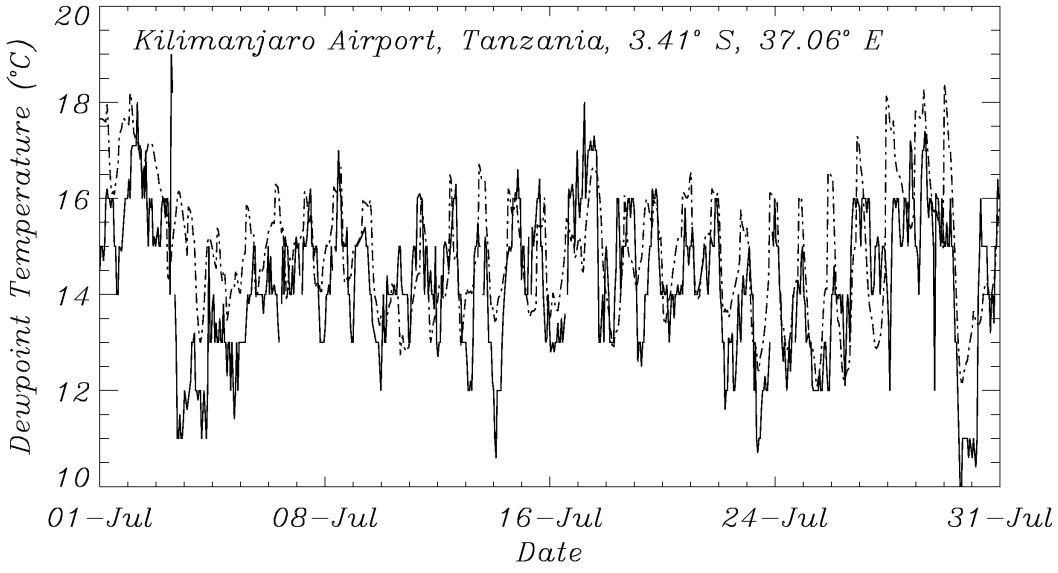

Figure 5.2 (continued).

Comparison of the RAMS simulated accumulated precipitation to TRMM and surface observations (Figure 5.3) in the second grid (G2) show that the spatial extent of local maximum on precipitation to in the vicinity of Lake Victoria is substantially less in the numerical simulation compared to satellite estimates and ground observations. Similar trends were also found in the numerical modeling study of *Ge et al*. [2007] over the same region using RAMS. However, in the vicinity of Kilimanjaro, numerical model simulation overestimates precipitation in comparison to surface observations and also satellite estimates. At Kilimanjaro International Airport, surface observations show 4 mm of accumulation for the study period while numerical model simulated value is ~8 mm. Satellite derived estimates show a maximum of less than 50 mm at Kilimanjaro while numerical model simulated values are in excess of 100 mm. Note that due to the two way interactive feature of nested grids, the vertical velocity field in the vicinity of Kilimanjaro in grid G2 is enhanced compared to the rest of the grid and resulting in the tendency of overestimating rainfall. While the two-way interactive nested grid leads to better representation of orographic effects on coarser grid G2, the grid spacing is still not adequate to properly resolve the spatial variability of such effects.

Comparison against ground based observations and TRMM derived estimates both show that over the entire grid (G2), RAMS underestimates precipitation. In comparison to TRMM derived estimates, model simulation (averaged to 0.25° x 0.25° TRMM grid) exhibits a root mean square error (RMSE) of ~ 23.1 mm and bias of -17.9 mm. The RMSE and bias for model simulated rainfall in comparison to ground based rainfall observations are 37.5 mm and -34.3 mm. Inter comparison of TRMM

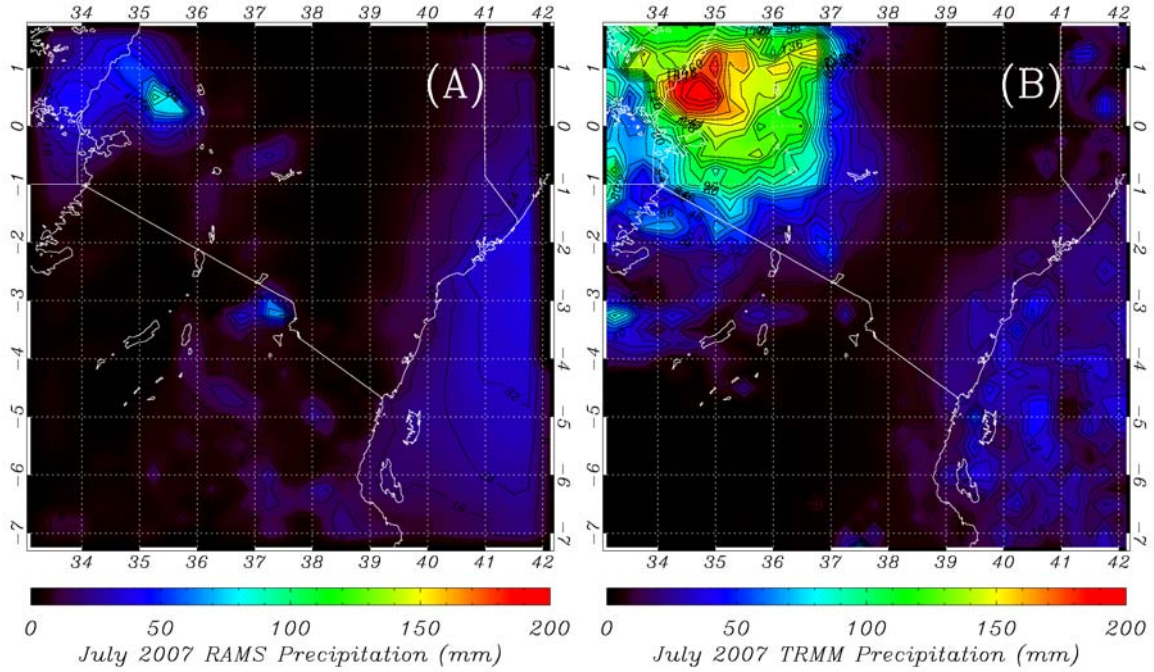

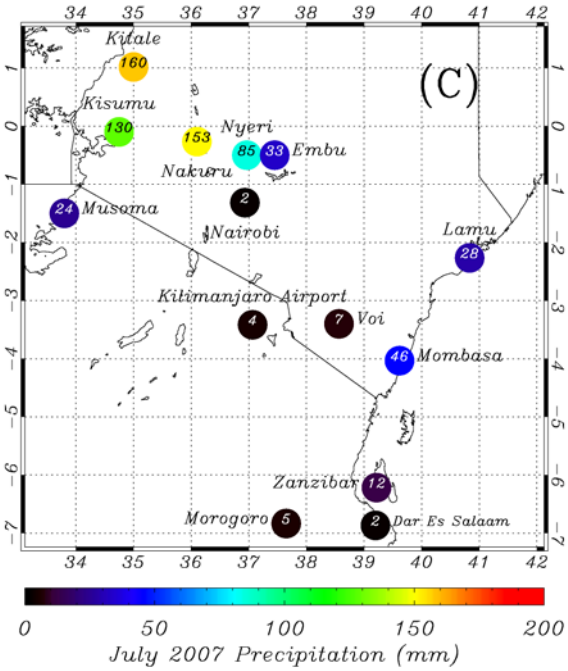

Figure 5.3 a) RAMS G2 (16 kilometer spacing) total monthly precipitation. b) Total monthly precipitation from the TRMM sensor (0.25° resolution) over Kenya and Tanzania for July of 2007. c) Monthly total precipitation at 14 observation sites within the G2 domain. Numbers listed are total monthly precipitation (mm) and the color of the dots is on the same scale as 5.5a and 5.5b.

rainfall estimates and ground observations show an RMSE of 18.11 mm and bias of -5.0 mm. Ground based observations or satellite derived rainfall estimates with adequate spatial resolution for evaluating the simulated orographic precipitation patterns in the innermost grid (G4) of 1 km grid spacing are not readily available. However, the simulated altitudinal structure of precipitation compares favorably with those reported in the literature and will be discussed further in Section 5.2.6.

5.2.1.3 Cloud frequency comparison

Due to the low density of surface observations, this study also employs a spatially distributed strategy of comparing the simulated cloud fields in grid 4 against MODIS satellite observations of cloud cover. The 1 km spatial resolution cloud mask derived from daily MODIS observations [*Ackerman et al.*, 1998], made approximately at 1100 local standard time (LST) (Terra platform) and 1400 LST (Aqua platform), and re-projected to the RAMS polar stereographic grid (G4) was used for this purpose. To compare the satellite derived cloud mask to the numerical model simulated cloud fields, we used the same methodology for evaluating cloud occurrence as described in Chapter 4, Section 4.1.4.

Spatial distribution of frequency of occurrence of clouds (FOC) computed from all the available MODIS overpasses for the study period shows two arcs of orographic cloudiness one on the windward side (south side) and other on the lee side (north side) of Kilimanjaro (Figure 5.4a). The FOC sharply decreases towards the peak of the mountain, with highest values around 2500m in elevation and tailing off to near zero values at high elevations. The spatial distribution of percentage accuracy (*A*) show 70-80% accuracy

over the core regions of arc of cloudiness on the windward side (Figure 5.6b), comparable to *Ray et al.* [2006]. Similar percentage accuracy is found for the leeward cloud bank, except along the western and eastern flanks, where lower values ranging from 40-50% are found. The percentage accuracy in the upwind slopes shows a decrease near the upper boundary of the orographic cloud bank, but above this region the accuracy increase to 90-95%. The spatial distribution of percentage false positive comparisons (*O*) show higher values along the upper boundary region of the windward orographic cloud bank (Figure 5.6c) indicating that the model over predicts the occurrence of clouds in this area. Thus, compared to observations, RAMS predicts the upper bounds of the windward orographic cloud banks to be located at slightly higher elevations compared to observations. The spatial distribution of percentage false negative comparisons show that the smaller accuracy values along the eastern and western flanks of the leeward cloud bank is due to under prediction of clouds in this area (Figure 5.4d).

Table 5.3 Model accuracy, overprediction, and underprediction of cloud occurrence at MODIS-Terra and MODIS-Aqua overpasses for the one kilometer spacing domain.

	Accuracy	**Overprediction**	**Underprediction**
MODIS-Terra	57.3%	8.9%	33.8%
MODIS-Aqua	58.4%	10.0%	31.6%

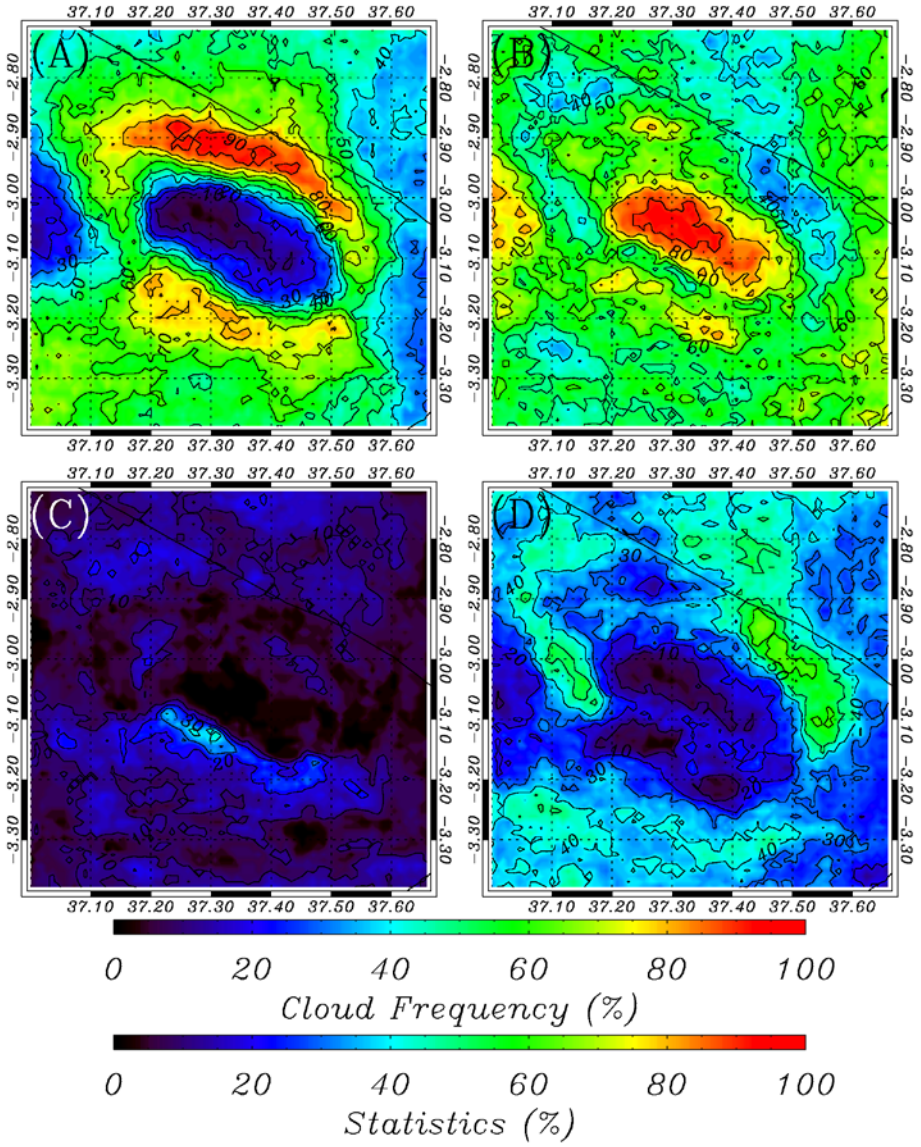

Figure 5.4 Spatial plots of accuracy of prediction of FOC from collocated MODIS and RAMS data for both MODIS-Aqua and MODIS-Terra time steps. a) Average FOC (%) for all observations. b) Model accuracy (%, see Expression 1). c) Model overprediction (%). d) Model underprediction (%). Domain average statistics are found in Table 5.3.

5.2.2 Response of cloud formation to land use change

Prior investigations of land use change impact on montane environments [*Lawton et al.*, 2001; *Ray et al.*, 2006; *Nair et al.*, 2010] show changes to orographic cloudiness. In order to examine changes to orographic cloudiness, spatially averaged FOC as a function of altitude is utilized. FOC initially increases with elevation reaching a maximum at altitudes of ~2200 m (Figure 5.5a) and than steadily decreases above this altitude. Comparison between the CTL and DEF simulations (Figure 5.5b) shows that the impact of deforestation is to decrease spatially average FOC at all elevations. The impact of reforestation is the opposite, an increase in spatially average FOC at all elevations (Figure 5.5c). The maximum decreases in FOC are found between the DEF and REF simulations (Figure 5.5d). Note that the differences in orographic cloudiness between the three experiments are statistically significant (Student's t-test, 95% confidence) at most elevations (Figure 5.5).

Variations in the integrated liquid water path (LWP) among the CTL, DEF, and REF simulations (Figure 5.6) are more substantial compared to differences in FOC. Average LWP shows a band of convection to the south of the mountain, which is consistent with the average wind patterns for this season, and a smaller leeward area of higher liquid water path on the north side of the mountain (Figure 5.6a). In general, deforestation results in a decrease of LWP in the lower half of the windward cloudbank while causing an increase in upper half (Figure 5.6b-d). The leeward cloudbank experiences a decrease in LWP in response to deforestation. Note that the magnitude of

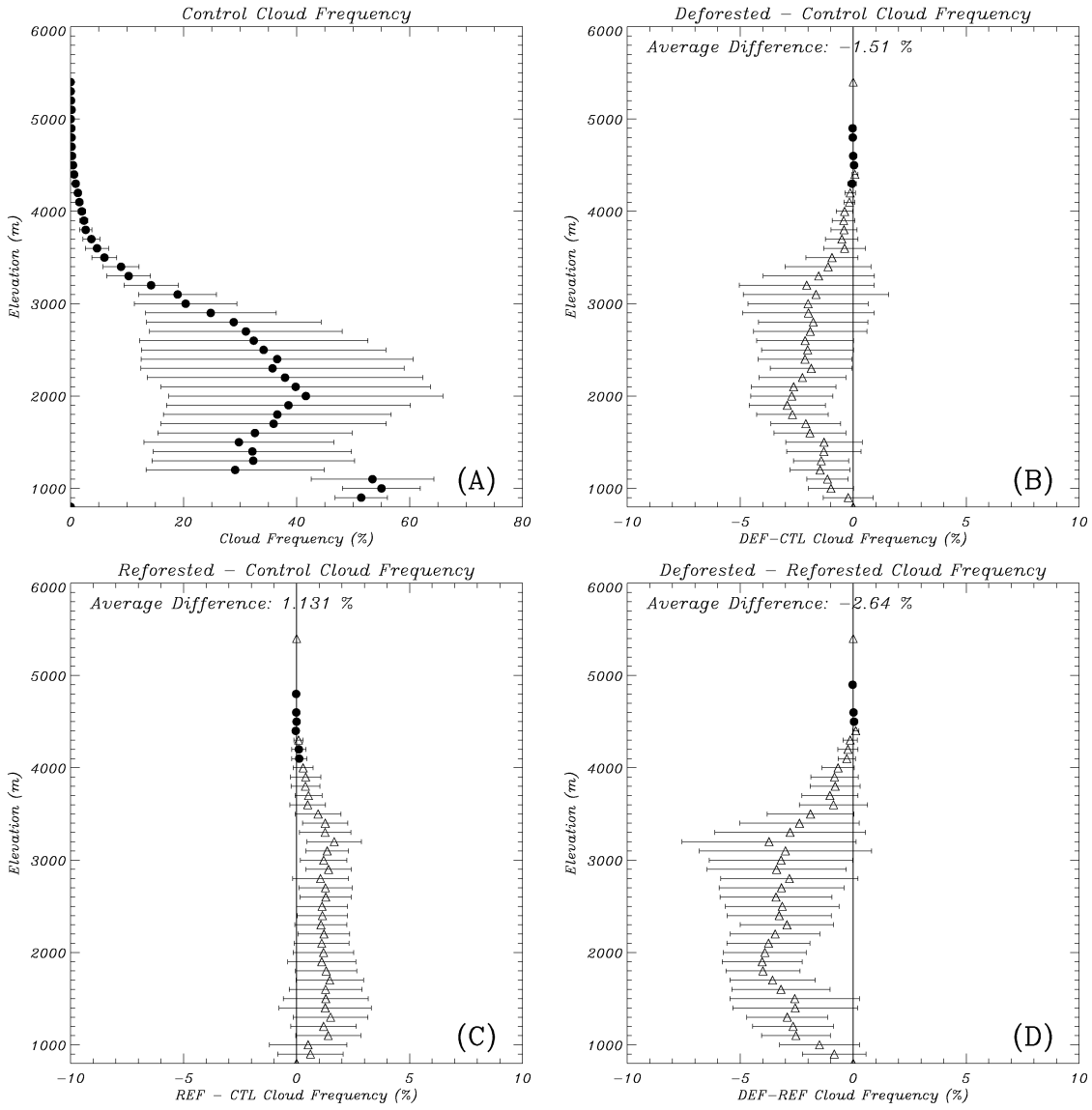

Figure 5.5 Cloud frequency differences binned to 100 m elevation increments for the one kilometer spacing model grid. Dots and triangles indicate mean values and bars indicate plus or minus one standard deviation. Triangles indicate the differences between the simulations are at greater than 95% statistical significance via t-means tests.

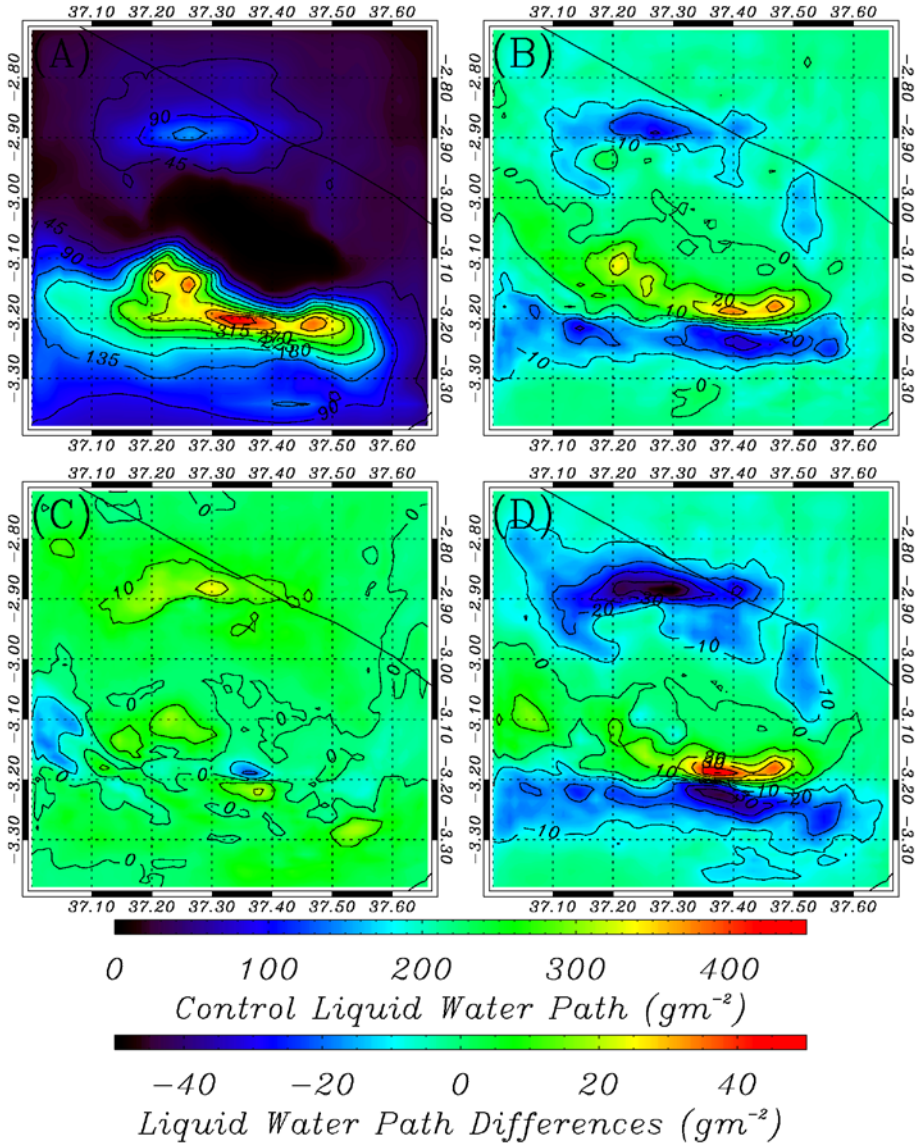

Figure 5.6 Comparisons of cloud liquid water path for the model simulations. Figure 5.6a uses the top color bar, all others the bottom. a) Average cloud liquid water path for July of 2007. b) Differences between the DEF and CTL simulations. c) Differences between the REF and CTL simulations. d) Differences between the DEF and REF simulations.

changes in LWP increases with the severity of deforestation. Magnitude of differences exceeding 40 gm^{-2}, 30 gm^{-2}, and 10 gm^{-2} are found between DEF and REF (Figure 5.6d), DEF and CTL (Figure 5.6b), REF and CTL (Figure 5.6c) simulations respectively. Thus while the general decrease in frequency of occurrence in orographic cloudiness in response to deforestation is accompanied by reduction in LWP at lower elevations, at higher elevations on the windward side it is associated with increased LWP. Averaged over the entire grid, there is a decrease in LWP of 4.13 gm^{-2} in the DEF simulation compared to CTL, and an increase of 2.6 gm^{-2} in REF simulation compared to the CTL simulation.

5.2.3 Horizontal and vertical wind field differences

The CTL, DEF and REF simulations also show differences in wind patterns, averaged over the lowest 1 km of the atmosphere (Figure 5.7). The average pattern of low-level flow (Figure 5.7a) is a predominantly southerly flow forced to diverge around Kilimanjaro, accelerating as it flows along the eastern and western slopes. The average wind speeds are highest in the DEF simulation followed by the CTL and REF simulations. Increased average wind speeds in DEF and CTL (Figures 5.7b, 5.7c) simulations are primarily due to smaller roughness length associated with deforestation. In the DEF simulation, decrease in surface roughness, and thus frictional effects, leads to an increase in wind speeds along the windward and leeward slopes (see regions R1 and R2 in Figure 5.7b) approximately directed along the topographical gradient, and also along the western and eastern slopes of Kilimanjaro (see regions R3 and R4 in

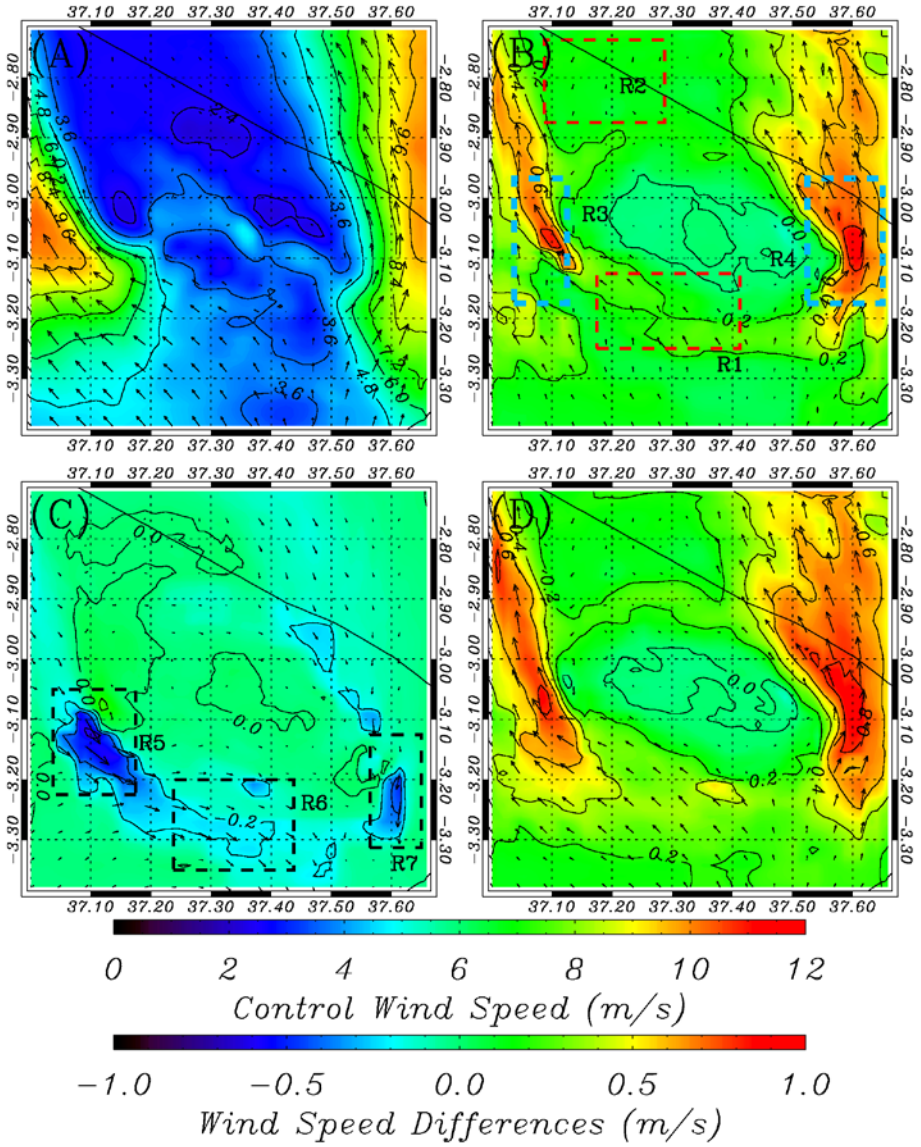

Figure 5.7 Average of layer mean (0-1 km) horizontal wind speed and wind vector for CTL simulation. b) Average difference of layer mean (0-1 km) horizontal wind speed between the DEF and CTL simulations. R1 and R2 indicate areas of increased flow towards the mountain, R3 and R4 areas of increased flow around the mountain. c) Same as b except for REF and CTL simulations. R5, R6, and R7 indicate areas of maximum change.) Same as b except for DEF and REF simulations.

Figure 5.7b) with significant component of the difference vector also directed along the topographical gradient. Note that the areas of significant wind differences in the DEF simulation (Figure 5.7b) correlate well with areas of deforestation (Figures 3.2a, 3.2b). In the REF simulation, the most substantial decreases in wind speeds and direction (see regions R5, R6 and R7 in Figure 5.7c) occur along the regions of reforestation in the windward side of Kilimanjaro (Figure 3.2c), as well as at the interface of the cropland and forested areas in the CTL land use scenario (Figure 5.2a). The pattern of wind speed differences between the DEF and REF simulations (Figure 5.7d) is very similar to that between CTL and DEF simulations, but with magnitude of differences being much higher in the former.

The average vertical velocity field for the CTL experiment (Figure 5.8a) shows regions of positive vertical velocity on the windward and leeward slopes, coinciding with location of orographic cloud banks in these regions. The impact of deforestation is an altitudinal shift in regions of convergence, with the increase in wind speed in the direction of the topographical gradient within region R1, R2, R3 and R4 (Figure 5.7b) resulting in enhanced vertical velocities in these regions (Figure 5.7b). A similar trend is found when the differences in average vertical velocities between the REF and CTL simulations are examined (Figure 5.8c). The differences in average vertical velocities between the DEF and REF simulations (Figure 5.8d) show a pattern very similar to the differences found between DEF and CTL simulations, except that the regions of enhanced vertical velocities are enlarged (compare to Figure 5.8b). Deforestation also enhances subsidence, in regions where it is already pronounced (S1, S2 in Figure 5.8a) found in the CTL simulation, along the eastern and western slopes south of these regions.

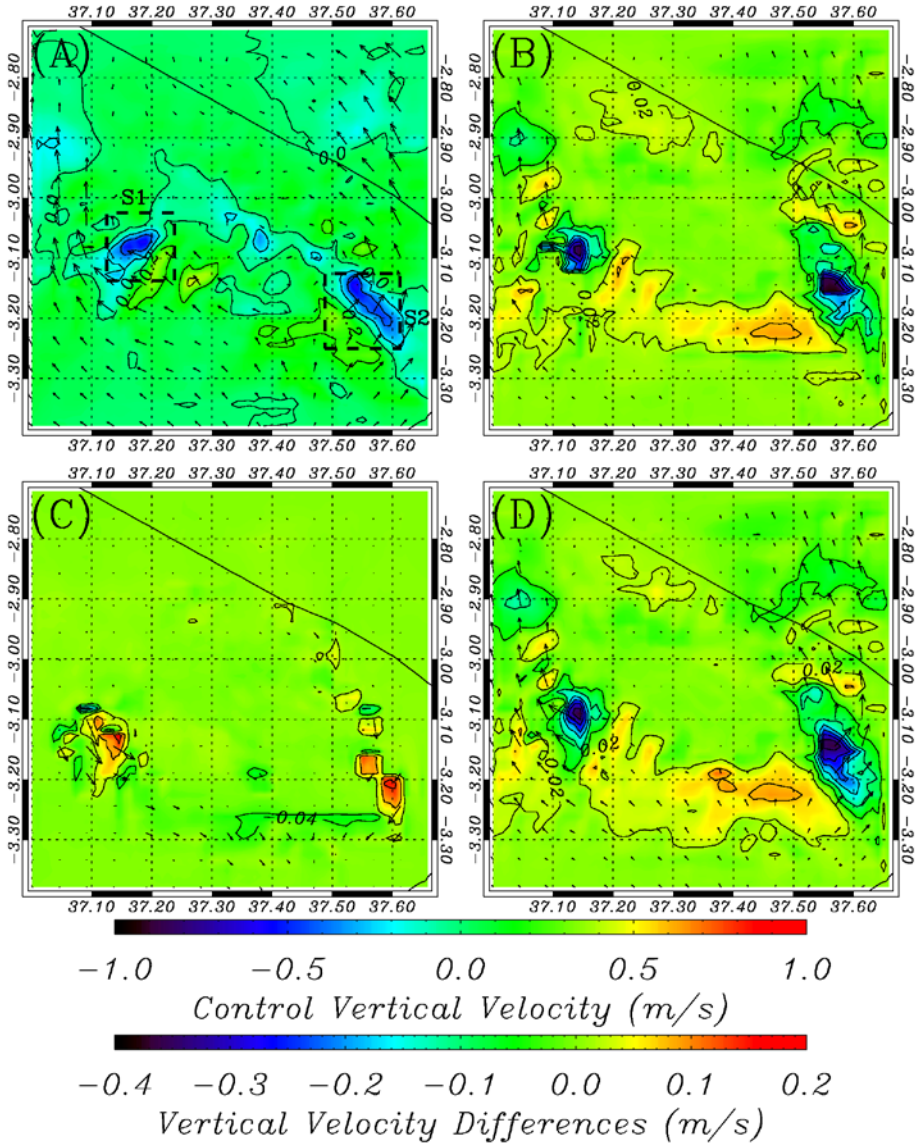

Figure 5.8 Analysis of vertical velocity overlaid with surface horizontal wind vectors. Figure 5.8a uses the top color bar, all others the bottom. a) Average CTL surface vertical velocity with horizontal wind vectors. S1 and S2 indicate areas of subsidence. b) Vertical velocity differences (contoured) and horizontal wind vector differences between the DEF and CTL simulations. c) Differences between REF and CTL simulations. d) Differences between DEF and REF simulations. Note the unbalanced color bars in Figures 5.8b-d.R3 and R4. The difference between REF and CTL simulations show that subsidence in the S1 and S2 regions are further enhanced in comparison to differences between DEF and CTL simulations.

The localized increases in LWP and precipitation at higher elevations and decreases at lower elevations following simulated deforestation (Figure 5.5) is consistent with the above discussed patterns of differences in horizontal and vertical wind speeds between DEF and CTL, REF and CTL, and DEF and REF simulations.

5.2.4 Impact of deforestation on flow modification of terrain

To quantify the modification of orographic flow pattern due to land cover changes, the flow diversion ratio (FD) was computed following the approach of *Rienecke and Durran* [2008]. The flow diversion ratio is computed based on a control volume that is parallel to the direction of the large scale flow. Of the two faces perpendicular to the direction of the large scale flow, one is located upwind of the mountain where the terrain gradient is minimal. The other face is formed by the cross-section of the mountain along the central ridge line. For the idealized mountain geometry (triangular-prism) considered by *Rienecke and Durran* [2008], such a control volume is a cuboid. Assuming that the large scale flow direction is southerly, the cuboid control volume is oriented south to north, with the northern face being defined by the mid cross-section of the triangular-prism shaped terrain with west-east orientation. Of the faces parallel to the flow direction, the bottom face is co-planar to the surface of zero elevation (mean sea level). The flow obstruction due to terrain is quantified as Equation 5.1:

$$FD = \frac{\phi_W - \phi_E}{\phi_S} \quad , \qquad (5.1)$$

where *FD* is the flow diversion ratio given by the ratio of the difference in mass flux in through the walls on the west side of the cuboid (φ_W), east side of the cuboid (φ_E) and south side (φ_S) respectively (Equation 5.1). In the situation of no flow obstruction, the incoming flow from the south is deflected in the vertical direction and thus the mass flux along the east and west faces will be zero, yielding a FD value of zero. However, if the terrain offers complete obstruction to the flow, there will be no mass flux through the top face and the net mass flux in the north-south direction will be same as that in the east-west direction, resulting in the FD ratio to be unity.

Computation of FD ratio for Kilimanjaro, whose terrain is more complex (Figure 5.9b) compared to idealized topography assumed by *Rienecke and Durran* [2008], requires the use a irregular control volume instead of a cuboid (Figure 5.9c). The surface of the irregular control volume is a southward extrusion of the east-west cross section of Kilimanjaro through highest peak. The mass flux in the east-west direction is computed using the vertical surfaces that are normal and the velocity component parallel to this direction. Similarly, the net mass flux in the north-south direction is computed by considering the control volume surfaces normal to and the velocity component parallel to this direction. The equation used for this computation is given in Equation 5.2:

$$FD = \frac{\int_{E}^{W} \phi_{E-W}}{\phi_{N-S}}, \tag{5.2}$$

where FD is the flow diversion ratio given by the ratio of net mass flux in the east-west ($\varphi_{\text{E-W}}$) and north-south ($\varphi_{\text{N-S}}$) directions, respectively.

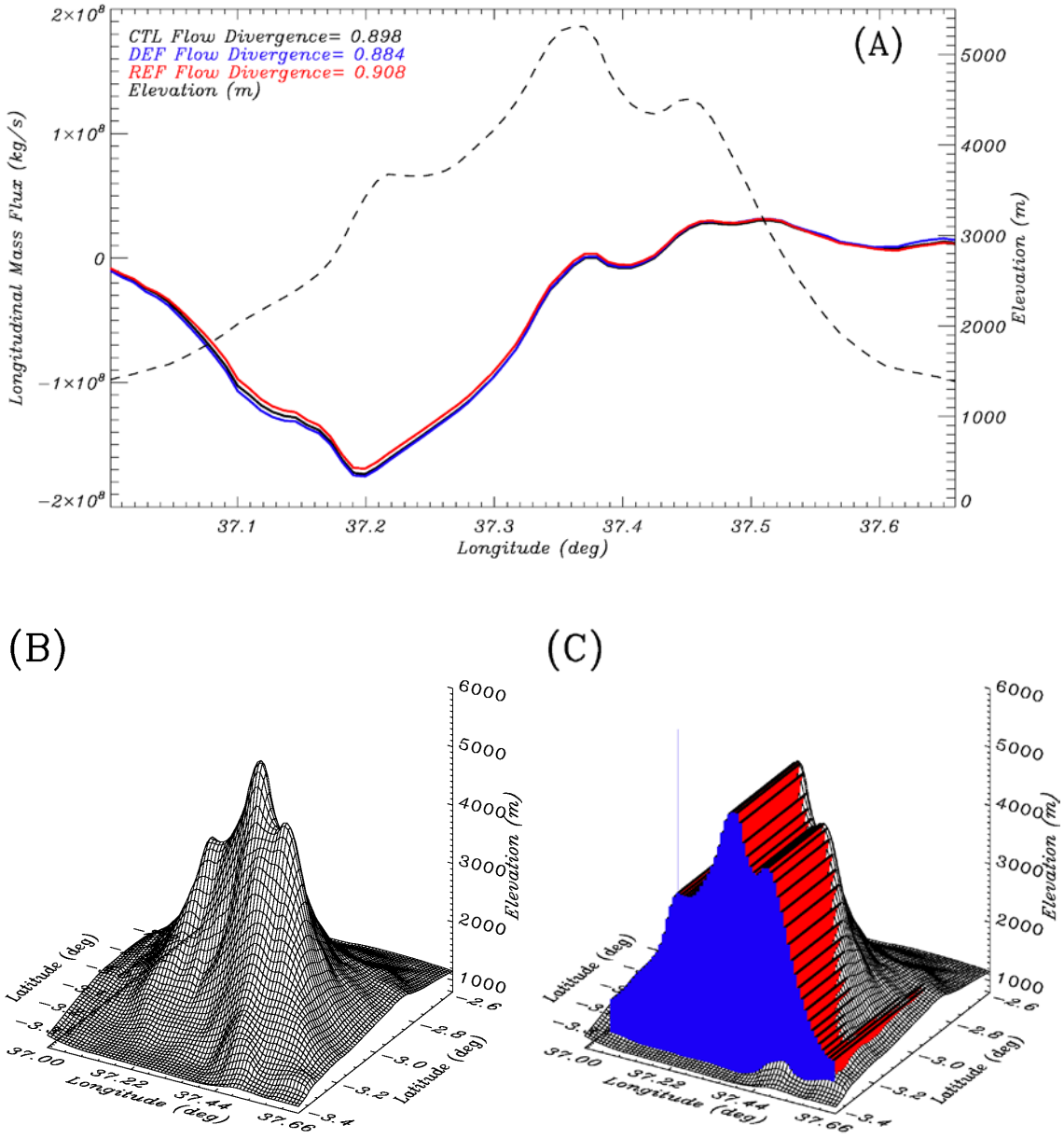

Figure 5.9 a) Plot of longitudinal mass flux for all three simulations with flow diversion numbers. b) Surface plot of model elevation for Model Grid 4, used in the flow diversion calculations. c) Volume used to compute flow diversion. The incoming latitudinal mass flux for the blue wall to the south of the mountain was used as the denominator, whereas integration of the mass flux through the red faces was the numerator in the flow divergence calculations.

The average control volume mass flux in the east-west direction, as a function of the longitude, show differences between the three simulations, especially in the west half of the control volume (Figure 5.9a). The magnitude of mass flux on the western half of the mountain increases as deforested land cover increases. The average FD ratio for the CTL, DEF and REF simulation are 0.898, 0.884 and 0.908 respectively. These values show that, for the flow conditions characteristic of the study period, Kilimanjaro does offer substantial obstruction to the large scale flow, with values indicating a mountain top inversion [*Reinecke and Durran*, 2008]. However, the land cover change does indeed impact the FD ratio, with the FD ratio increasing by 2.4% as forest cover increases. Thus, reforestation results in an increase in the ability of the mountain to obstruct the flow, and deforestation leads to a greater proportion of flow upslope and over the mountain. Although the flow rate around the mountain increases with deforestation, so does the flow up the windward slopes. The result is an increased vertical velocity in the deforested setting, and therefore a greater proportion of the air rising over the mountain, versus diverging around it, relative to the CTL and REF simulations. The regions of enhanced vertical velocity correlate to regions of increased horizontal winds (Figure 5.7).

5.2.5 Surface temperature, moisture and latent heat

Although consistent differences in model simulated cloud, precipitation and wind patterns are found in response to deforestation, these changes make it difficult discern the direct impact of deforestation on surface temperature (not shown). The DEF simulation shows that the surface air is generally warmer (not shown) and drier (Figure 5.10b) over deforested regions, while REF simulations show cooler (not shown) and moister air (Figure 5.10c) over forested regions in the windward side. Drier surface air is found on

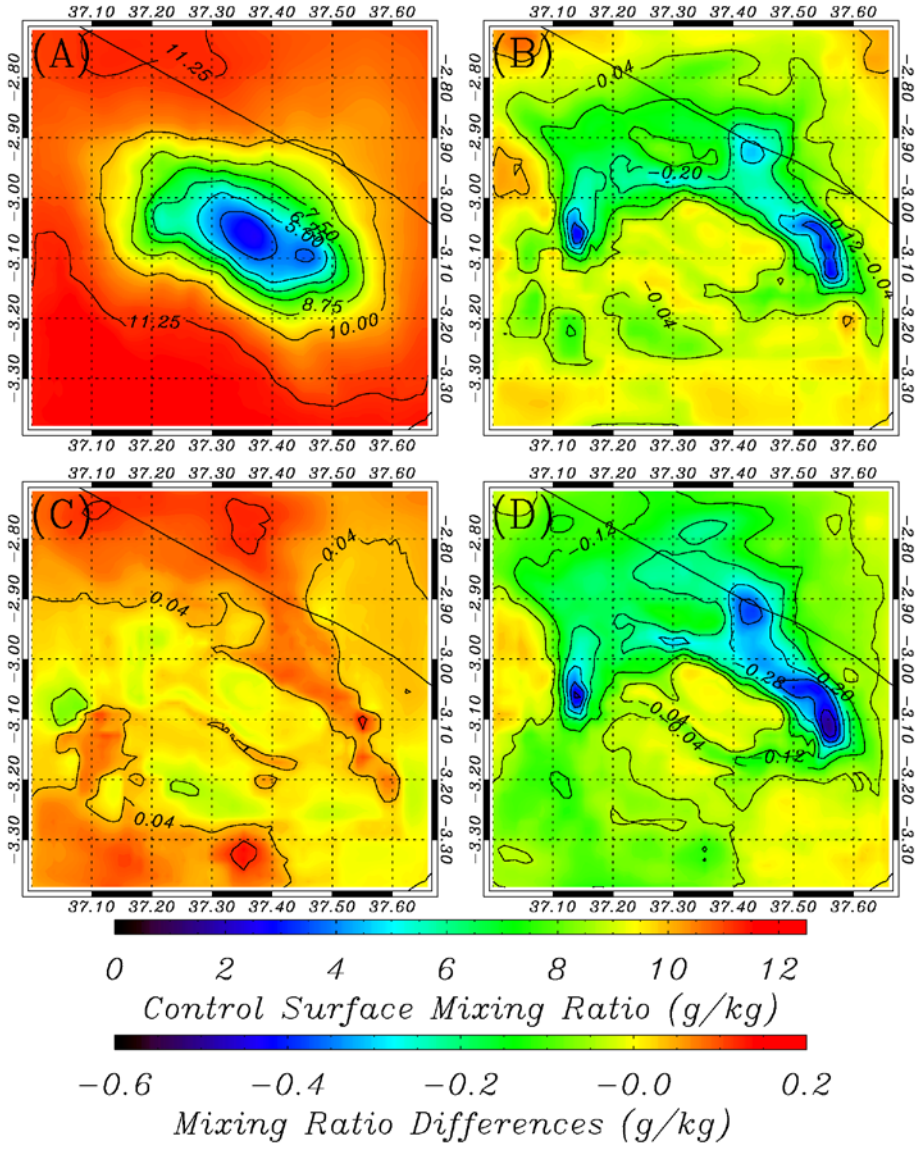

Figure 5.10 Comparison of monthly mean surface mixing ratio for the three differing simulations. Figure 5.10a uses the top color bar, all others the bottom. a) Average CTL liquid water mixing ratio for July 2007. b) Difference between DEF and CTL mixing ratios. c) Difference between REF and CTL mixing ratios. d) Difference between DEF and REF mixing ratios. Note the unbalanced color bar in Figures 5.10b-d.

the leeward side of Kilimanjaro when comparing the DEF simulation to the CTL and REF simulations (Figures 5.10b, 5.10c, 5.10d). Deforestation results in a decrease of water vapor mixing ratio on average, but increases in near surface wind speed result in very small positive changes to the mixing ratio in localized areas, including the peak. The impact of reforestation is to enhance surface moisture at lower elevations along the windward slopes, which coupled with changes to flow patterns increases moisture also on the lee side of the Kilimanjaro (Figures 5.10c, 5.10d). This is evident in the patterns of monthly averaged water vapor flux along the east-west cross section through the peak of Kilimanjaro (center of grid domain 4), which shows enhanced northerly water vapor flux in both CTL and REF simulations compared to DEF simulation (Figure 5.11) above the surface layer. These produce decreases in water vapor mixing ratio on the lee slopes and the areas on the side of the mountain which roughly coincide with regions of enhanced wind speed. Changes in the land cover do not show significant changes in average moisture or temperature at high elevation areas downwind of the land use changes, instead occurring on the leeward side which is consistent with the lack of changes at high elevations.

Only small differences in domain averaged latent heat fluxes were found between the three experiments, with Grid 4 average values of 36.6 Wm^{-2}, 34.7 Wm^{-2} and 35.4 Wm^{-2} respectively for CTL, DEF and REF experiments. The domain averaged latent heat fluxes are least in the DEF experiment due to reduced evaporation and transpiration over deforested regions. In the REF experiment, latent heat fluxes are indeed higher over reforested regions (not shown), but the domain averaged value is lower compared to CTL experiment. Higher domain averaged latent heat fluxes in the

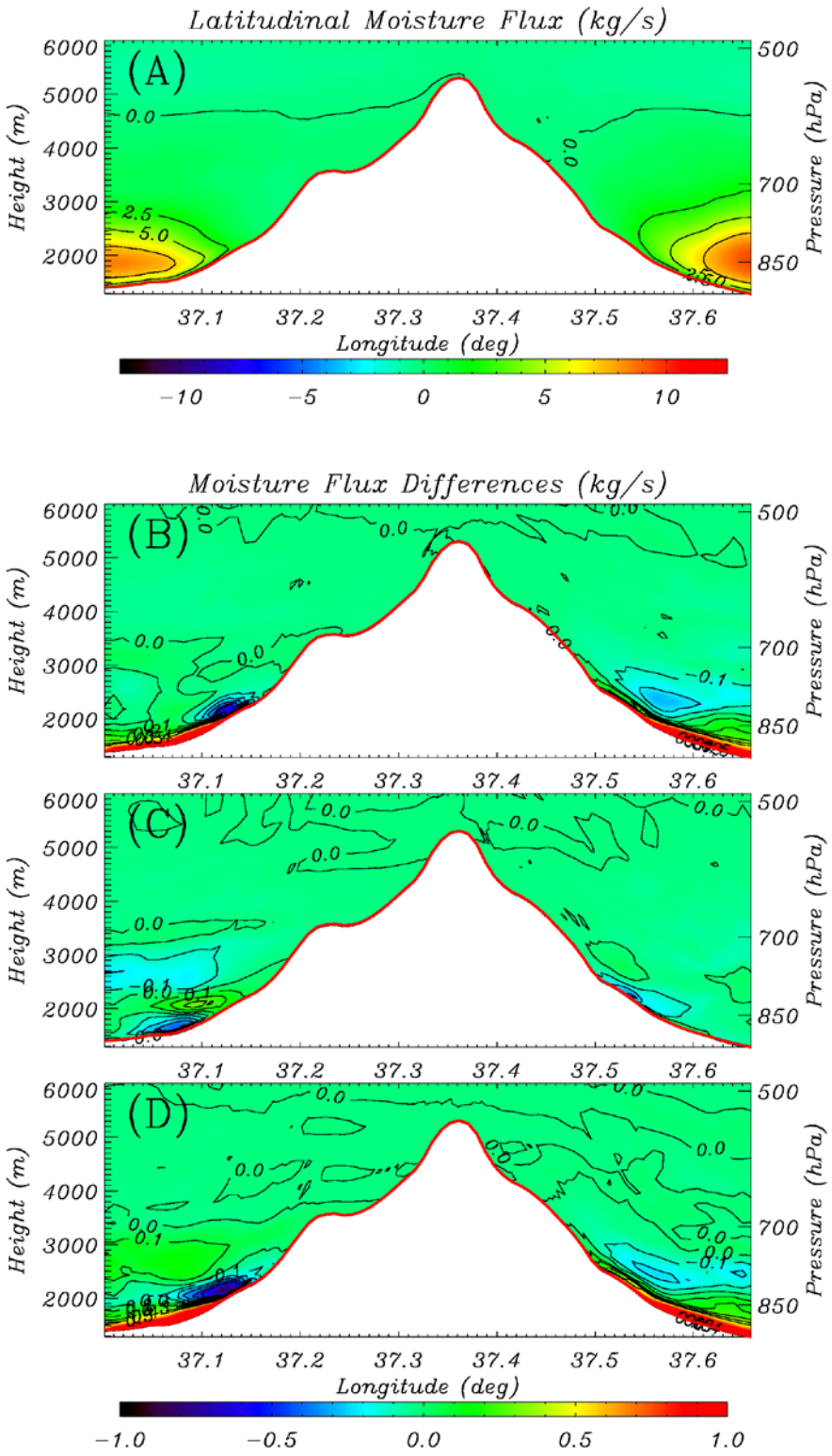

Figure 5.11 Cross section of latitudinal moisture flux for the three simulations and differences at the highest elevation. a) CTL latitudinal moisture flux. b) Differences between DEF and CTL simulations. c) Differences between REF and CTL simulations. d) Differences between DEF and REF simulations.

CTL experiment could be potentially related to enhanced rainfall on the windward slopes. Relatively small differences in domain averaged latent heat fluxes also suggest that changes in flow diversion (see Section 5.4.4) is the main contributor to differences in orographic cloudiness found between the three simulations.

5.2.6 Precipitation differences

Averaged monthly accumulated precipitation, as a function of surface elevation (100 m bins) increases up to an altitude of ~2400 m and than decreases with altitudes up to ~4000 m (Figure 5.12). This pattern is consistent with elevational profiles of precipitation reported for Kilimanjaro [*Røhr and Killingtveit*, 2003; *Barry*, 2008]. Spatial average precipitation differences between DEF and CTL simulations on the windward areas (the southern half of the fourth grid) is negative in the elevation ranges of 1000-2200m (Figure 5.13a) and is positive between 2200-4000m. However, pattern for leeward areas (the northern half of the fourth grid), show negative differences at all elevations expect between 1300-1800m, where a small positive difference is found (Figure 5.13b). The windward differences between REF and CTL simulations are slightly negative below elevations of 1300m and positive between 1300-4000m (Figure 5.13c). Other than slightly positive differences between 1400-1800m, very little leeward differences are found between REF and CTL simulations (Figure 5.13d). The differences between DEF and REF simulations are negative at elevation below 1800 m and are positive between 1800-4000m on the windward areas (Figure 5.13e). On leeward areas, the differences are positive below 1700m while it is negative between 1700-4000m (Figure 5.13f). Note that the differences in orographic precipitation between the

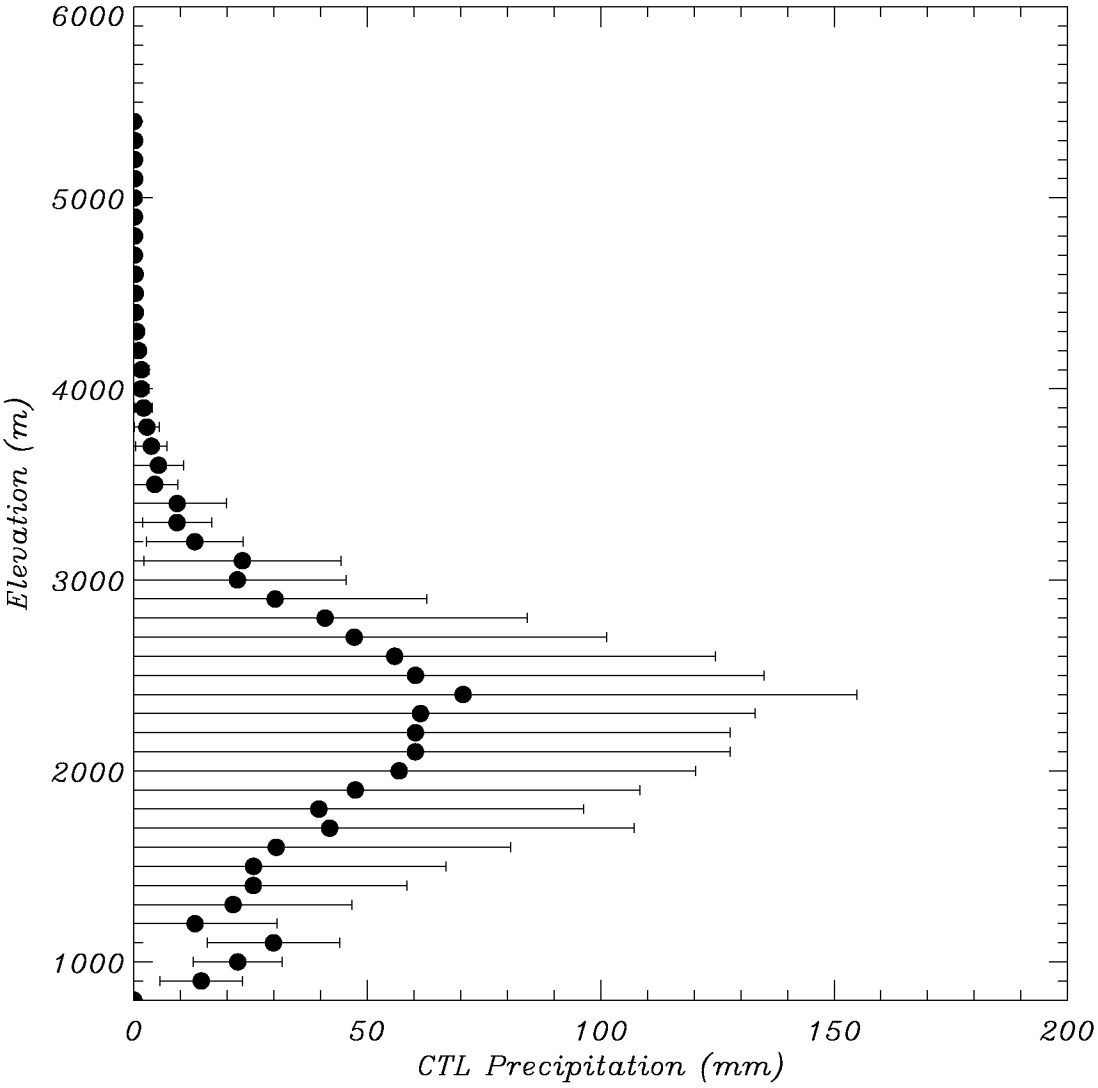

Figure 5.12 Average accumulated precipitation for July 2007 as a function of elevation. Averages are for 100m elevation bins. The bars indicate a one standard deviation difference from the mean.

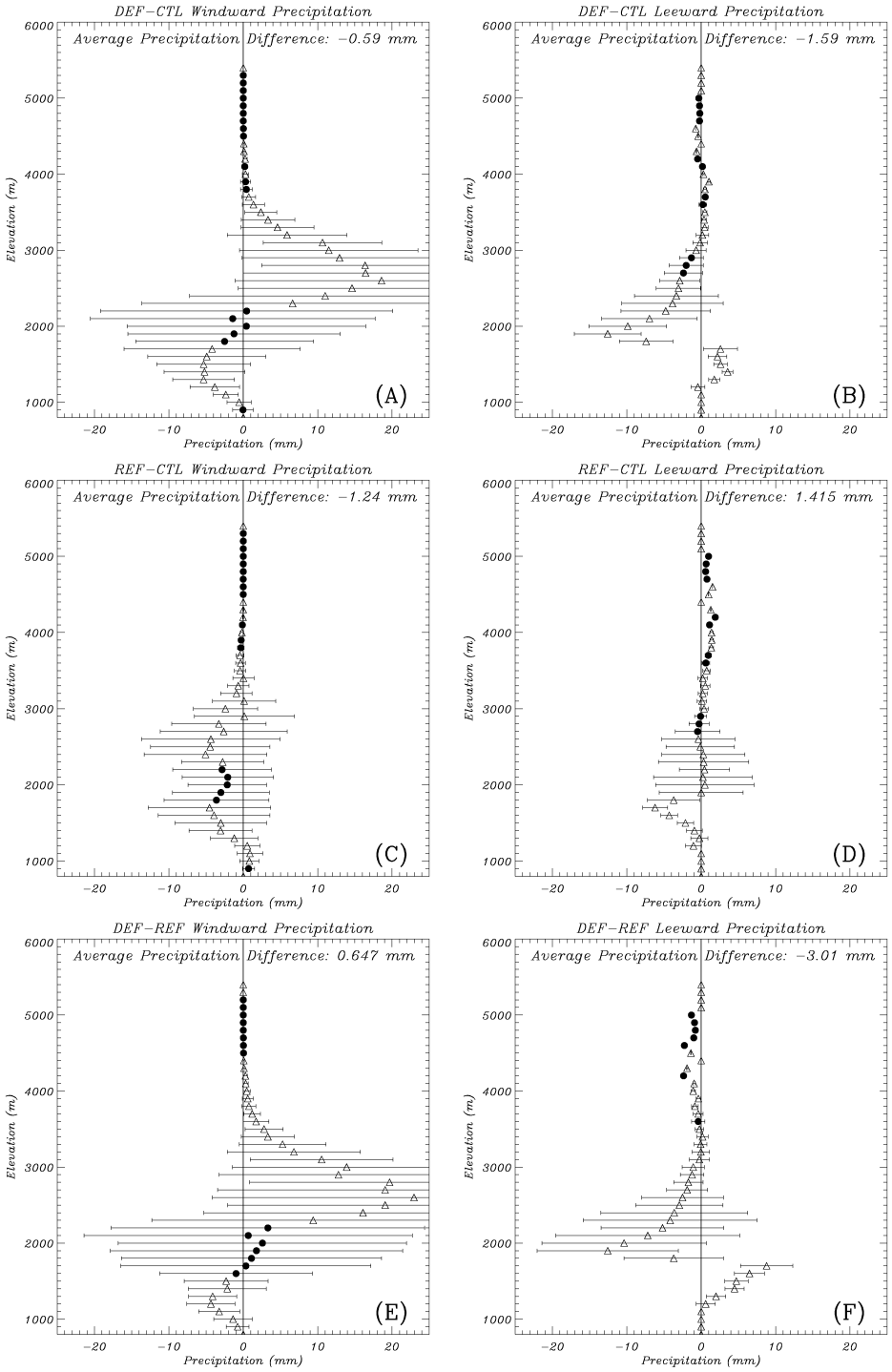

Figure 5.13 Comparison of July 2007 total surface precipitation with respect to elevation, binned at 100m intervals for windward (a,c,e) and leeward (b,d,f) sides. The bars indicate a one standard deviation difference from the mean values. Statistical significance greater than 95% is denoted by triangles.

three experiments are statistically significant (Student's t-test, 95% confidence) at most elevations (Figure 5.13).

The simulations thus show that the impact of deforestation is to cause decrease in precipitation at lower elevations and increase at higher elevations on the windward areas. On the lee region, there is precipitation decreases at higher elevations while there is some increase at lower elevations. Spatial pattern of precipitation differences (not shown) show that areas of increased precipitation coincide with regions of enhanced LWP (Figure 5.6) which in turn coincides with patterns of vertical velocity enhancements (Figure 5.8). Areas of reduced precipitation on the lee regions also coincide with patterns of moisture deficits (Figure 5.10).

5.3 Discussion

The total deforestation of Kilimanjaro as given in this experiment is the upper bound of possible land use change. While such deforestation is a hypothetical end-member scenario, the reforested simulation, where anthropogenic land cover is replaced by tropical montane forests, is reflective of past land use scenarios documented by *Hemp* [2009] and *Soini* [2005]. Note that the differences between the reforested and current land use scenarios do show a consistent signal that is amplified when the extent of deforestation increases.

While land cover change does indeed impact cloudiness at Kilimanjaro, physical mechanisms through which the changes are effected are different than those found in prior studies [*Lawton et al.*, 2001; *Nair et al.*, 2003; *Ray et al.*, 2006; *Bruijnzeel*, 2004]. At Monteverde, Costa Rica, lowland deforestation impacted orographic cloud formation

by causing the air mass to be warmer and drier, elevating the lifting condensation level and the height of formation of the orographic cloud bank. In an island setting in Puerto Rico, both changes in air mass and sea-breeze circulation patterns caused by deforestation was found to alter orographic cloudiness [*Bruijnzeel*, 2004]. In the present study for an inland site, while the changes in moisture at the surface potentially contribute to decreased cloudiness in deforested scenarios, altered flow patterns caused by reduced aerodynamic roughness and associated increase in the strength of thermally driven winds appear to play a dominant role. The pattern of increased LWP in the upper half of the windward cloud bank (Figure 5.6) correlates well with regions of enhanced vertical velocity (Figure 5.8). The increase in vertical velocity in turn is higher horizontal wind speeds in the direction of the topographical gradient. Note that vertical velocity component (w_s) relative to slopes is related to topographical gradient (∇h) and horizontal wind ($\vec{V}_s$) at the surface in the following manner [*Barry et al., 2008*]:

$$w_s = \vec{V}_s \bullet \nabla h \quad . \tag{5.3}$$

During the time period considered in the study, flow characteristics are such that, obstruction caused by Kilimanjaro to the background flow decreases with the amount of deforestation, increasing near surface wind speeds along the windward slopes at higher elevations where the topographical gradient is also higher.

The above discussed differences in flow patterns lead to increase in cloud thickness and precipitation at higher elevations in response to deforestation. Decrease in cloud cover and precipitation, due to large scale changes in tropical climate and associated

increase in absorbed shortwave radiation is one of the mechanisms that has been shown to impact glacier mass loss on the peak of Kilimanjaro significantly [*Mölg et al.*, 2003, 2006, 2008b, 2009b; *Mölg and Hardy*, 2004; *Hastenrath*, 2006]. The present study did not find substantial changes in cloudiness and precipitation at the peak of Kilimanjaro in response to deforestation during the dry season month of July, indicating minimal local forcing in this zone. However, this does not rule out the possibility of such impacts occurring in other seasons. The decrease in precipitation in response to deforestation at lower elevations complements the drying trend in the region associated with larger scale changes in tropical climate, while increases at mid elevations potentially mitigates such effects.

Note that, while the comparison of RAMS simulations for the current land use conditions against observations show adequate performance, there are also systematic biases exhibited by RAMS, especially in the simulation of precipitation. Since the magnitude of the biases itself could be impacted by land use [*Ge et al.*, 2007], caution should be exercised when interpreting quantification of changes in cloudiness, precipitation and surface thermodynamics. Another factor to be considered in the interpretation of the results is the inability of the 1° by 1° Global Forecasting System analysis used for soil moisture initialization to adequately reflect small scale variation of soil moisture in the study area. In order to assess the impact of land use change on orographic cloud formation, the approach utilized in this study focuses on the differences between the three experiments, provided that the CTL simulation performs adequately in comparison to observations. However, the possibility of soil moisture heterogeneity

substantially modulating the differences between the experiments cannot be ruled out and the results from this study should be viewed in the context of the initial soil moisture field utilized in the experiments.

5.4 Conclusions

This study utilized numerical model simulations to investigate the impact of land cover changes at lower elevations of Kilimanjaro on the regional climate of the area. The RAMS was used to simulate atmospheric conditions for July 2007, assuming current, deforested, and forested land cover scenarios. The findings from the comparison of these simulations can be summarized as follows:

1. Comparison of RAMS simulations for the current land use conditions against surface meteorological observations and satellite observations of cloudiness show satisfactory performance of RAMS over the study region.
2. The RAMS simulations show that deforestation at lower elevations of Kilimanjaro leads to decrease in frequency of occurrence of clouds at all elevations. Cloud liquid water path decreases in response to deforestation except at higher elevations on the windward side where it increases. Reforestation has the opposite effect, increasing frequency of occurrence of clouds at all elevations, increases in cloud liquid water path except at higher elevation on the windward side where it decreases.
3. Precipitation decreases at low elevations and increases at mid elevations on the windward side in response to deforestation. On the leeward side precipitation decreases at mid elevations while there is a very small increase at lower

elevations. The magnitude of differences increase with the extent of deforestation.

4. Flow diversion values computed for the different scenarios also show that obstruction caused by Kilimanjaro is enhanced when the lower elevations areas are reforested.
5. Surface moisture patterns are also altered due to changes in terrain flow, with reforestation increasing moisture transport to the lee side of the mountain in comparison to current vegetation and deforestation.
6. While differences in surface moisture contributes to decrease in frequency of occurrence in cloudiness, changes in flow pattern caused by reduced aerodynamic roughness play an important role. When the lower elevation regions are deforested, Kilimanjaro offer less obstruction to background flow and resulting increase in flow around the mountain causes reduced moisture transport to the lee side, causing reduced cloud liquid water path and precipitation. On the windward side, increase in wind speed directed parallel to the topographic gradient at higher elevations, caused by reduced aerodynamic roughness in upwind areas lead to enhanced surface convergence, cloud liquid water path and precipitation.
7. Lack of precipitation at the peak during the period of study prevents making conclusions about potential impacts on precipitation at that level. Further study is required to investigate the possibility of such effects occurring during other seasons.

This study addresses only the impact of deforestation on one dry season month. There are no compelling reasons for expecting the physical processes that cause the changes in clouds and precipitation to be substantially different if the analysis is extended to include dry season month of July from other years. However, further study that extends the analysis to other seasons is required to establish the overall impact of land use change on the higher elevation climate of Kilimanjaro. The next chapter extends this analysis, and discusses annual effects of these land cover change experiments, extending the analysis present in this chapter to an entire year, comprising of 366 days, from July 1, 2007 through June 30, 2008, examining several of the same meteorological fields in order to analyze the impact on the wet seasons and the overarching ties in the local circulation patterns to the upwind land cover classifications.

CHAPTER 6

ANNUAL IMPACT OF LAND COVER CHANGE ON THE REGIONAL CLIMATE OF MOUNT KILIMANJARO (TANZANIA)

In this chapter, results from the RAMS experiments for the land cover scenarios described in Chapter 3 are used to examine the impact of land use on flow patterns, cloud and precipitation formation, and local terrain-circulation generation for a total of 366 days, starting from July 1, 2007 through June 30, 2008. This is an extension of the analysis present in the previous chapter, which comprised only for one month (July) during the dry season. Verification for this simulation is present in Chapter 4, where the meteorological patterns for the CTL simulation and their seasonal progression were discussed. Therefore, we will purely discuss the differences caused by the alterations in land use classification.

6.1 Average Differences in Meteorological Fields

The primary mechanisms in which land cover change can affect regional climate are through reduced envirotranspiration caused by the loss of plant matter, impacting the surface moisture levels; changes in temperature due to repartitioning of fluxes from

sensible to latent heating related to the changes in Bowen ratio; and alteration of the wind fields due to differences in surface roughness. Therefore, before discussing the integrated effects of the land use change on complex variables such as cloud and precipitation formation, it is important to look at the average differences in these three fields: mixing ratio, temperature, and wind speed, as well as the resulting vertical velocity changes that come by changing the buoyant (mixing ratio and temperature fields) as well as the mechanical (wind speed and direction) inputs into the vertical velocity equations.

Differences in surface moisture content (Figure 6.1) show that the deforested simulation (Figure 6.1b) has a deficit in moisture along the slopes of Kilimanjaro, with the strongest areas of this deficit existing on the northwestern side at values exceeding 0.2 g/kg. The REF simulation shows an increase in grid-averaged mixing ratio at the surface of 0.05 g/kg on average, with the majority of the mixing ratio increase occurring over the added forest areas on the south side of the mountain. The difference is exacerbated when comparing the DEF and REF simulations (Figure 6.1d), showing an overall deficit on the grid with similar synoptic input, indicating the effects of the envirotranspiration from the montane forests. There is little difference at the peak in the moisture fields, but the REF simulation has a slight increase in average surface mixing ratio and the DEF simulation showing a slight decrease. Both of these are less than 0.08 g/kg in magnitude.

Spatial patterns of temperature (Figure 6.2) show similar patterns in changes on average to the changes in moisture. There is an increase in temperature on the slopes of Kilimanjaro, of around 0.1° C between the DEF and CTL simulations as well as the DEF

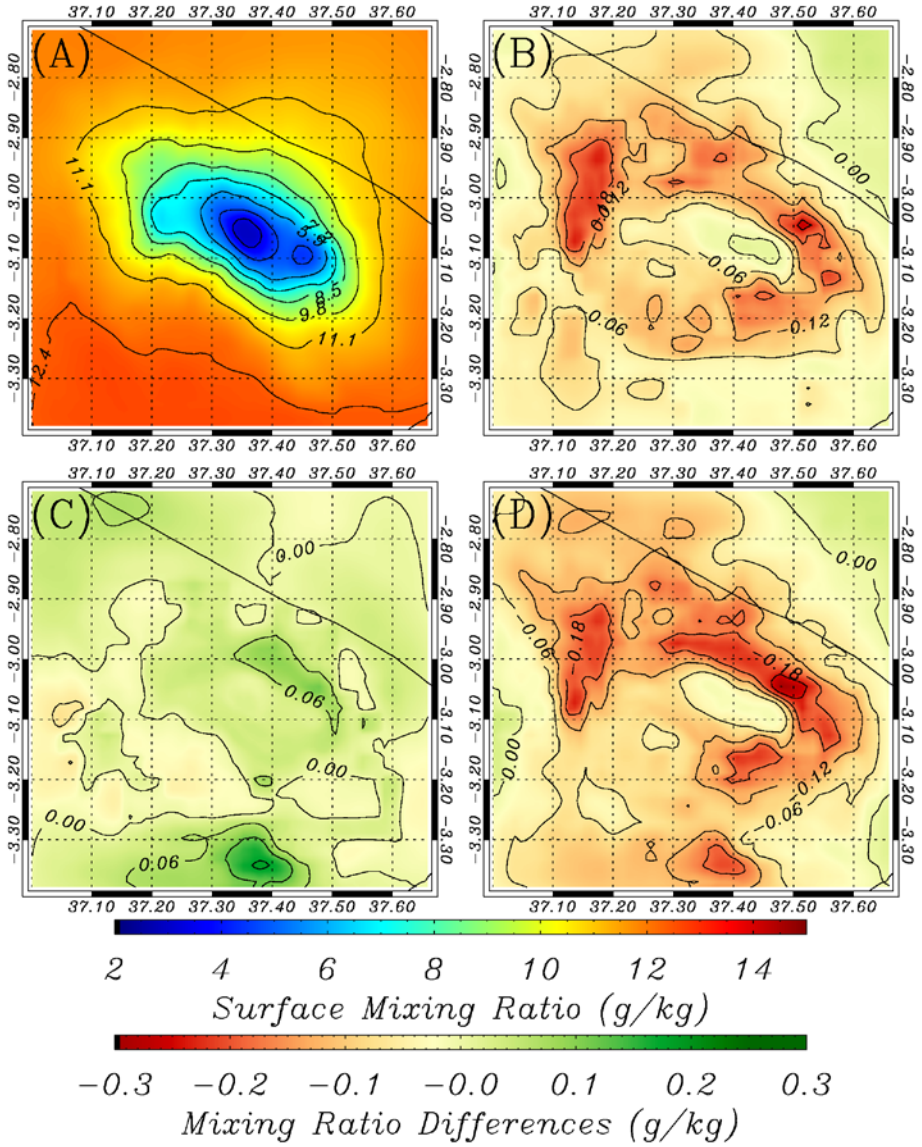

Figure 6.1 CTL surface level mixing ratio (a) and differences [(b) DEF-CTL, (c) REF-CTL, (d) DEF-REF] between the different simulations . Deforestation produces a deficit in moisture over the forested areas and in upslope locations with little change to the boundary conditions, whereas afforestation increases moisture on the mountain.

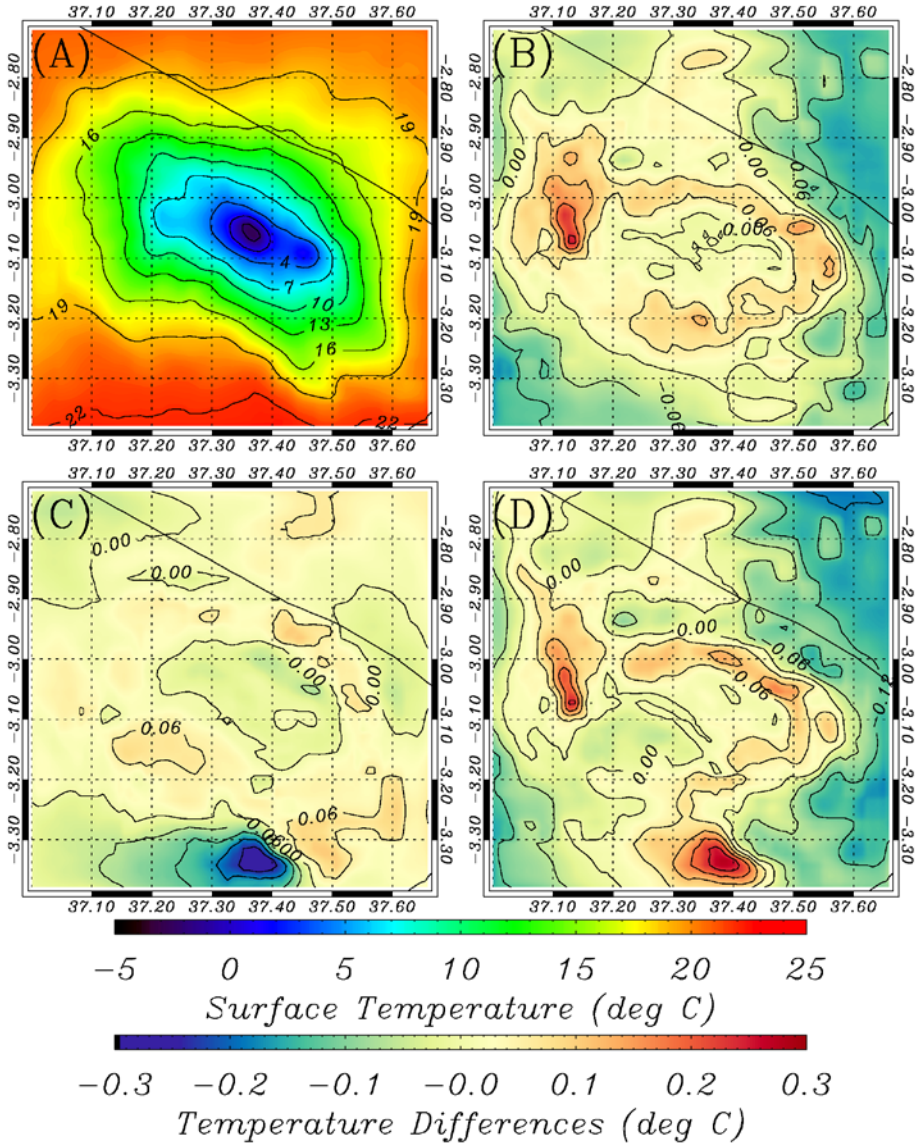

Figure 6.2 CTL surface level temperature (a) and differences [(b) DEF-CTL, (c) REF-CTL, (d) DEF-REF] between the different simulations. Temperature in the DEF simulations is higher further up the slope than in the REF simulations, while the DEF simulation is cooler on the periphery of the grid. There is little difference between the REF and CTL simulations.

and REF simulations. There are some differences between the REF and CTL simulations, mainly on the south side of the mountain where there is also the large increase in moisture. While there are increases in temperature on the slopes of Kilimanjaro, there is little difference at the peak. Of interest is the decrease in the temperature on the outskirts of the DEF simulation, since there is no synoptic-level change between these three simulations.

Differences in wind speed between these three simulations (Figure 6.3) show patterns of wind speed increases in the DEF simulation and decreases in the REF simulation. These patterns of increase show that the average wind speed and direction is enhanced around Kilimanjaro in the DEF simulation with compared to the CTL simulation, with enhancements in wind speed on the artificially deforested areas on the south side of the mountain. The REF simulation shows wind speed deficits to the opposite direction of the general flow than the CTL simulation, with values on average being fairly small, below 0.5 ms^{-1}. When comparing the DEF and REF simulations, it is clear that the average wind speeds at all elevations below 3000 m are increased, with the flow pattern present in the CTL simulation being enhanced at all times. Maximum differences exceeding 0.6 ms^{-1} on average are clearly visible on the eastern side of the mountain. These differences in wind speed lead to changes in vertical velocity (Figure 6.4), as enhanced convergence in the DEF simulation due to higher wind speeds causes more positive vertical velocity formation. The main convective areas, as shown in Figure 6.4a, are generally to the southwestern and northern side of the peak (located in the center). Deforestation enhances the southwestern vertical velocity compared to the CTL or REF simulations on average.

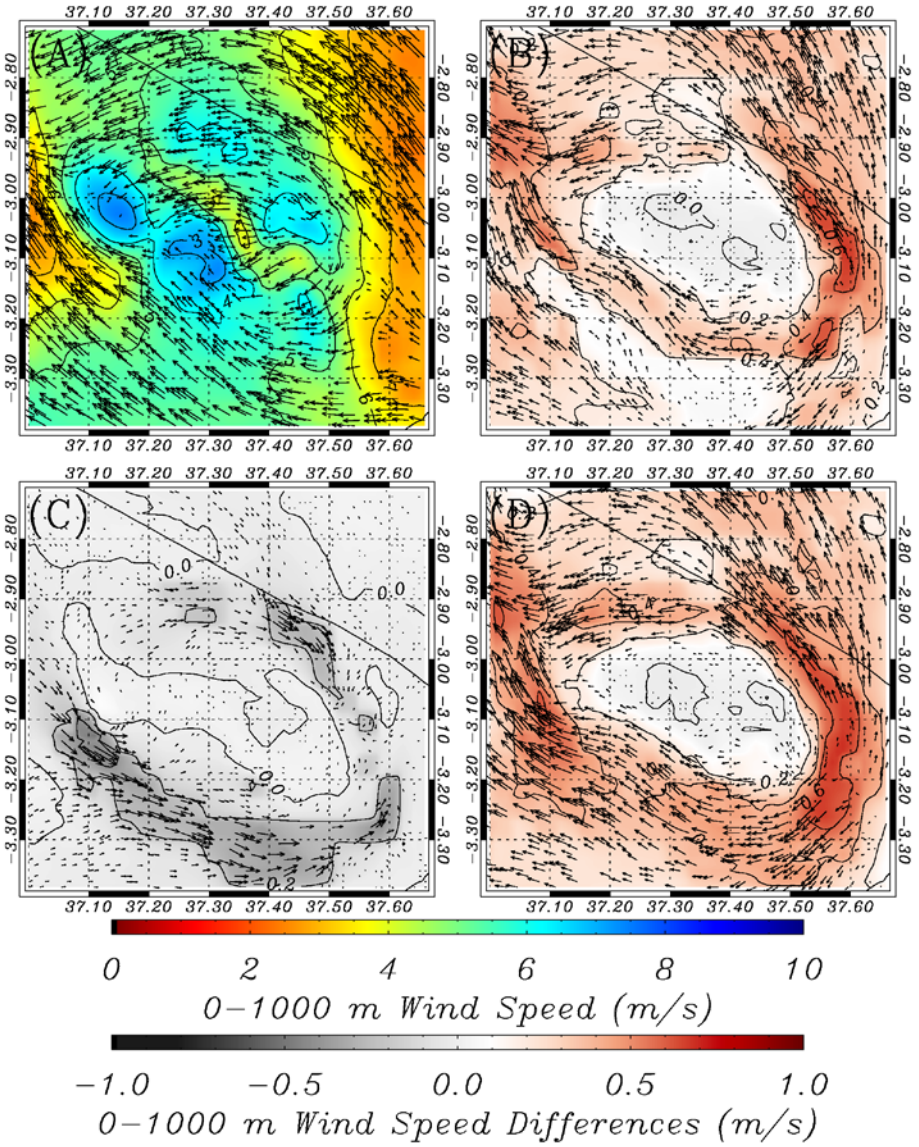

Figure 6.3 CTL annual average wind speed and direction (a) and differences [(b) DEF-CTL, (c) REF-CTL, (d) DEF-REF] between the differing simulations. Deforestation causes increases in wind speeds at elevations below 3000 m, whereas additional forested area slows the wind due to frictional effects.

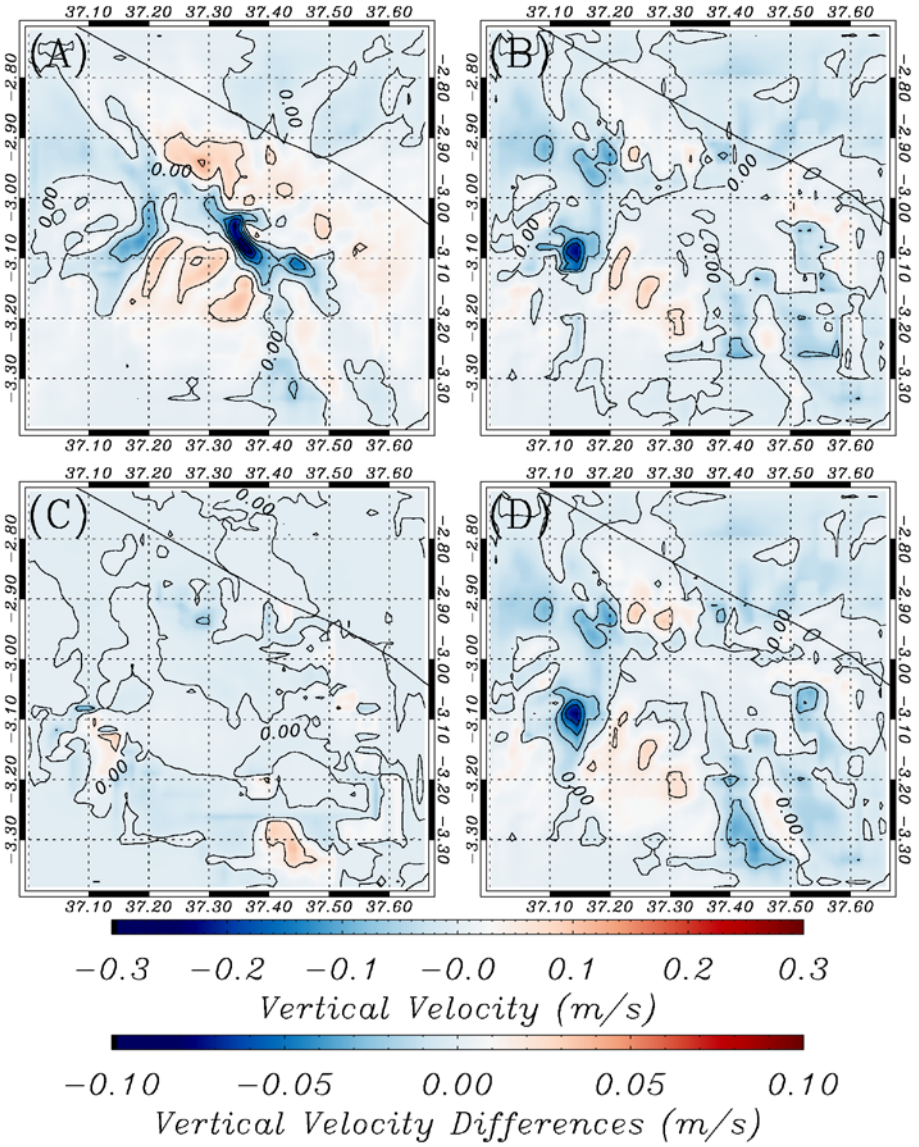

Figure 6.4 CTL annual average surface vertical velocity (a) and differences [(b) DEF-CTL, (c) REF-CTL, (d) DEF-REF] between the three differing simulations. The areas of positive vertical velocity for the CTL simulation (Figure 6a) are increased in the DEF simulation on the southern side.

6.2 Land Use Effects on Orographic Clouds

This section details the effects that the differing land use scenarios have on cloud frequency of occurrence, cloud liquid water path, the meteorological factors that govern cloud formation at high elevations, as discussed in the previous chapter for the CTL run, as well as examining the timing of cloud formation at high elevations with regards to both the diurnal cycle as well as the seasonal differences.

6.2.1 Cloud frequency of occurrence and liquid water path

Fairman et al. [2011] (Chapter 5) demonstrated that for the dry season month of July, there was no difference between the deforested, reforested and control simulations with cloud frequency at the peak of Kilimanjaro, due to the fact that there were no clouds formed. However, when extended to an annual basis, we find that there are some changes in the frequency of cloudiness with elevation (Figure 6.5). The differences between the three runs have similar magnitudes for the analysis over July 2007. On average, there is a deficit in frequency of cloudiness 1.62% between the deforested and control simulation, and an excess of 0.55% between the reforested and control simulation. This compares similarly to the numbers from July, which were a deficit of 1.51% between the deforested and control simulation and an excess of 1.13% between the reforested and control simulation. The patterns of the differences with regards to elevation are fairly similar as well, with the deforested simulation having less frequent cloud formation for elevations < 4000 m compared to the control and reforested simulations, and the reforested simulation having more clouds form between 3000 and 4000 m than the control simulation.

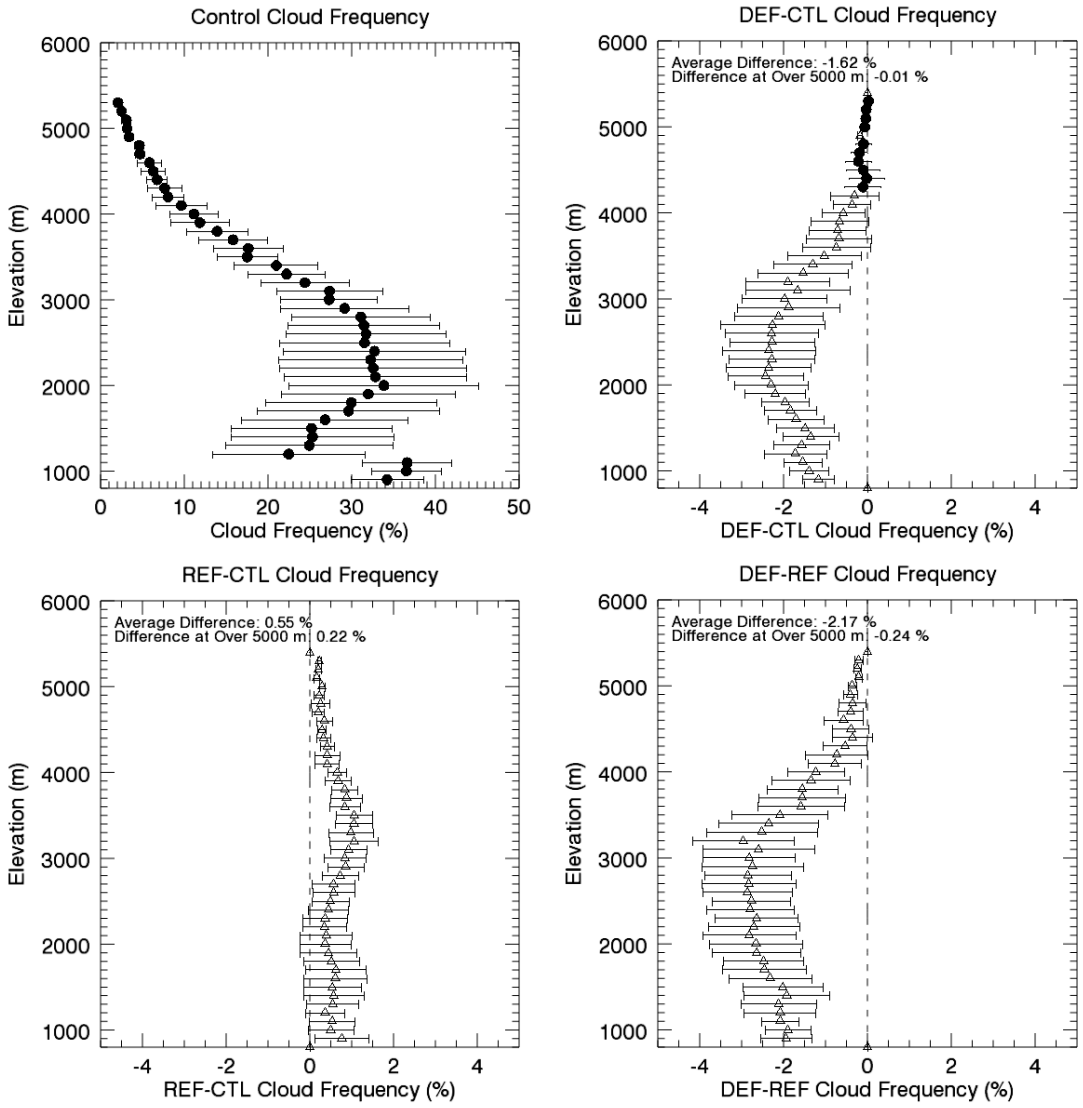

Figure 6.5 Plots of annual average cloud frequency for the three model simulations, binned to 100 m elevation increments. There is little difference between the three runs at higher elevations.

Of interest are the effects at the high elevations, where the frequency of cloudiness will impact the amount of shortwave radiation present at the peak, which is a primary control in the mass balance calculations of the glacier. There is minimal difference in cloud frequency between the deforested and control simulations at the peak, with no statistical significance. The reforested simulation has statistically significant results (> 95% from t-test) but the average magnitude of the difference at elevations exceeding 5000 m is 0.22%. Over the 8784 hours of model operation, the deforested run had 714 hours where clouds were detected above 5000 m, the control simulation had 724 hours of where clouds were detected above 5000 m, and the reforested simulation had 753 hours of clouds detected over 5000 m, showing an increase of 4% from the CTL.

There are also effects on the thickness of the clouds that result from orographic processes on the mountain, demonstrated by Figure 6.6, which shows the spatial patterns of the cloud liquid water path (LWP). In general, the deforested simulation shows thinner clouds over most of the regions in comparison to the control simulation, particularly on the south side of the mountain. However, over the peak, the average cloud liquid water path when clouds occur is higher for the deforested run than either the control or reforested case, with the average liquid water path for the DEF simulation being 68.43 gm^{-2} over elevations exceeding 5000 m while for the REF simulation it is 63.99 gm^{-2} and is 60.6 gm^{-2} for the CTL simulation. This is an increase in liquid water path of 13% for the DEF simulation and 6.6% for the REF simulation in comparison to the CTL simulation at high elevations. However, the general pattern is that clouds that form on the south side of the mountain under deforestation are thinner by ~30 gm^{-2} compared to the CTL or REF simulations.

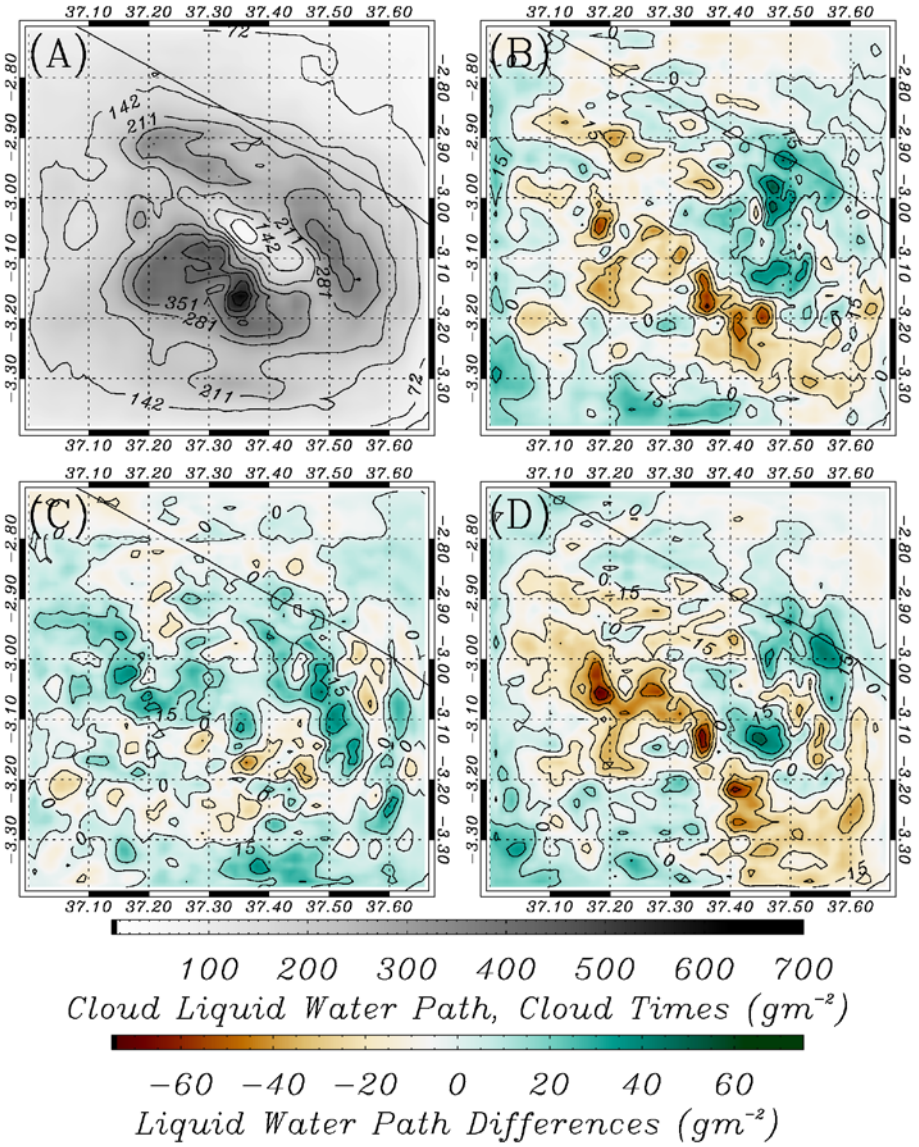

Figure 6.6 Annual average difference in cloud liquid water path at times of cloud occurrence. Figure 6.6a shows the control run average, Figure 6.6b shows the difference between the deforested and control simulations (DEF-CTL), 6.6c shows the differences between the reforested and control (REF-CTL), and 6.6d shows the differences between the deforested and reforested (DEF-REF). The most significant differences are found at low elevations, where the deforested simulation produces thinner clouds. However, the clouds are very similar at higher elevations.

6.2.2 Differences in factors governing orographic cloud formation

In the previous chapter, we discussed the meteorological parameters of mixing ratio, temperature, wind speed, and vertical velocity at the surface and related these to times where orographic clouds existed at high elevations. Average values from the CTL simulation for these 4 fields at times of cloud occurrence are shown in Figure 6.7. However, land cover differences can have influences in all four of these fields, with differences in temperature, moisture, and wind speed at the surface all leading to changes in the vertical velocity due to buoyant or mechanical effects. Therefore, it is important to quantify changes in these fields for times that clouds occur at high elevations between the differing simulations, in order to gain knowledge of the processes that dominate in different vegetation scenarios.

The differences in these surface meteorological parameters are demonstrated in Figures 6.8-6.10. When considering the differences between the deforested and control simulations (Figure 6.8), it is clear to see that there is a general deficit in mixing ratio of around 0.12 g/kg on the south side of the mountain during times of cloud occurrence when compared to the CTL simulation. However, the moisture in the northeast corner of the map is enhanced by around the same magnitude. Since the surface roughness in the deforested case is much lower, it is of no surprise that the average wind velocity is higher across the vast majority of the grid, but there is little difference in vertical velocity at the center of the domain.

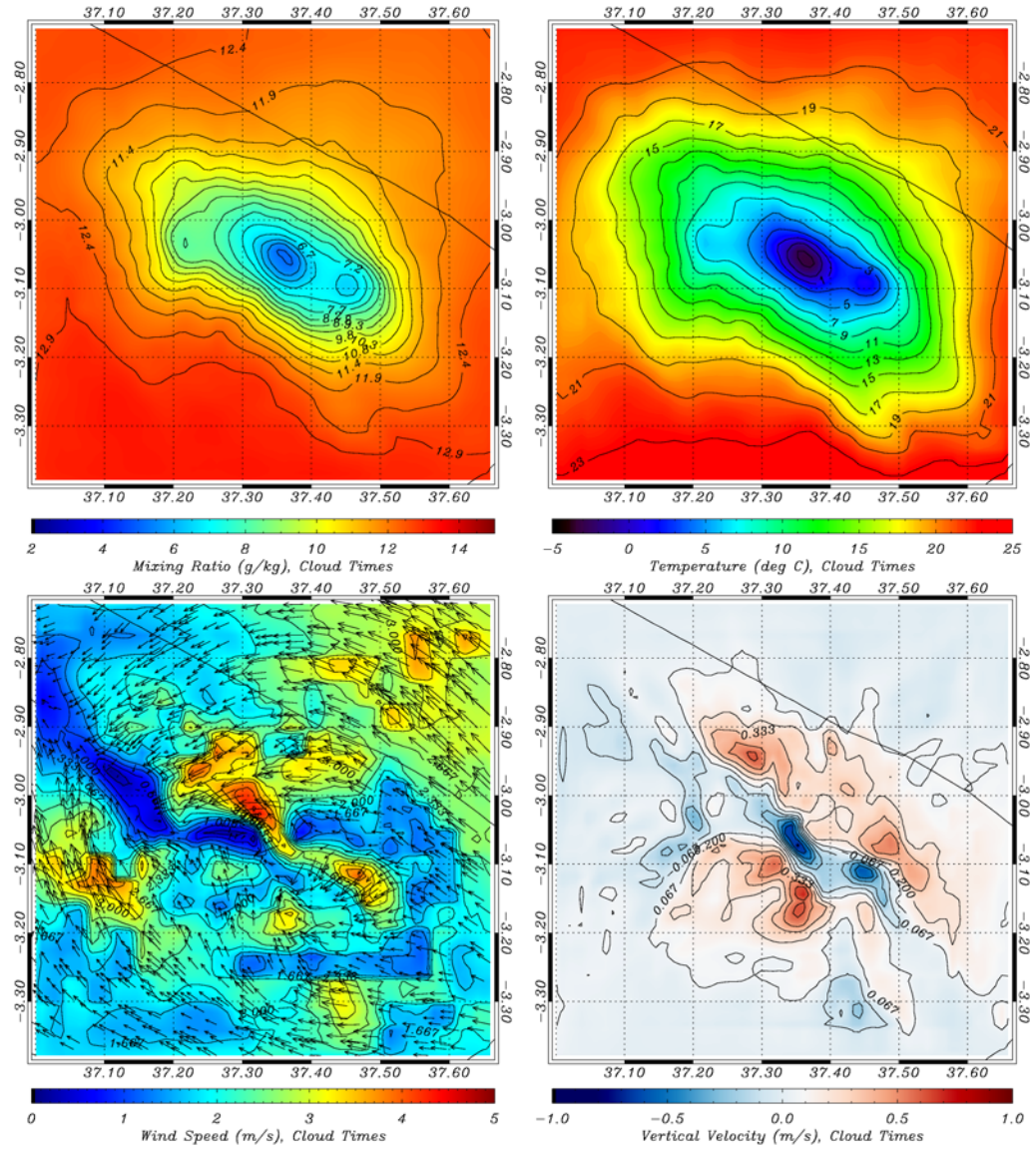

Figure 6.7 Average meteorological parameters of mixing ratio, temperature, wind speed, and vertical velocity at the surface level during times of cloud occurrence for the CTL simulation.

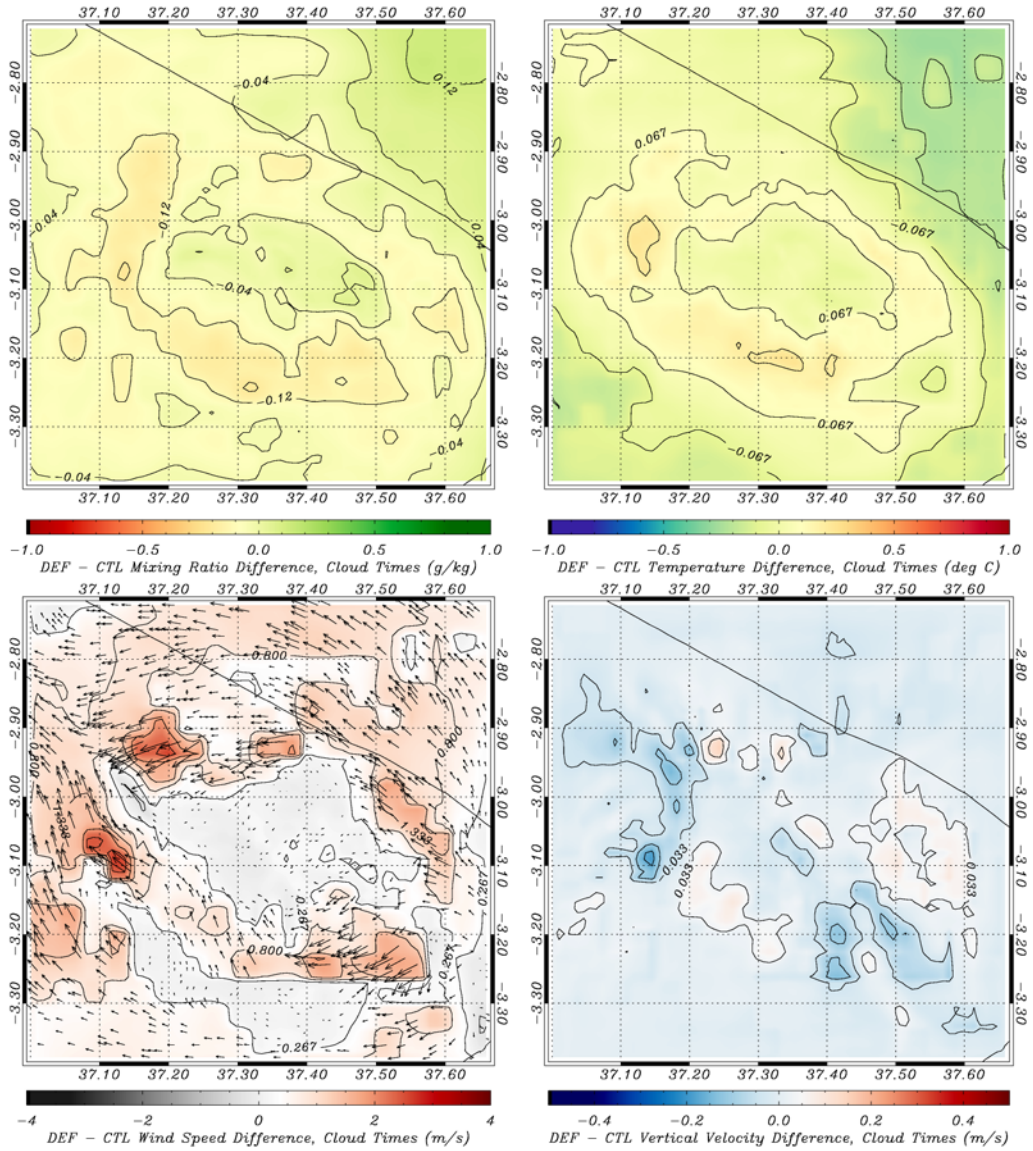

Figure 6.8 Difference in the average meteorological parameters at times of cloud occurrence between the DEF and CTL simulations.

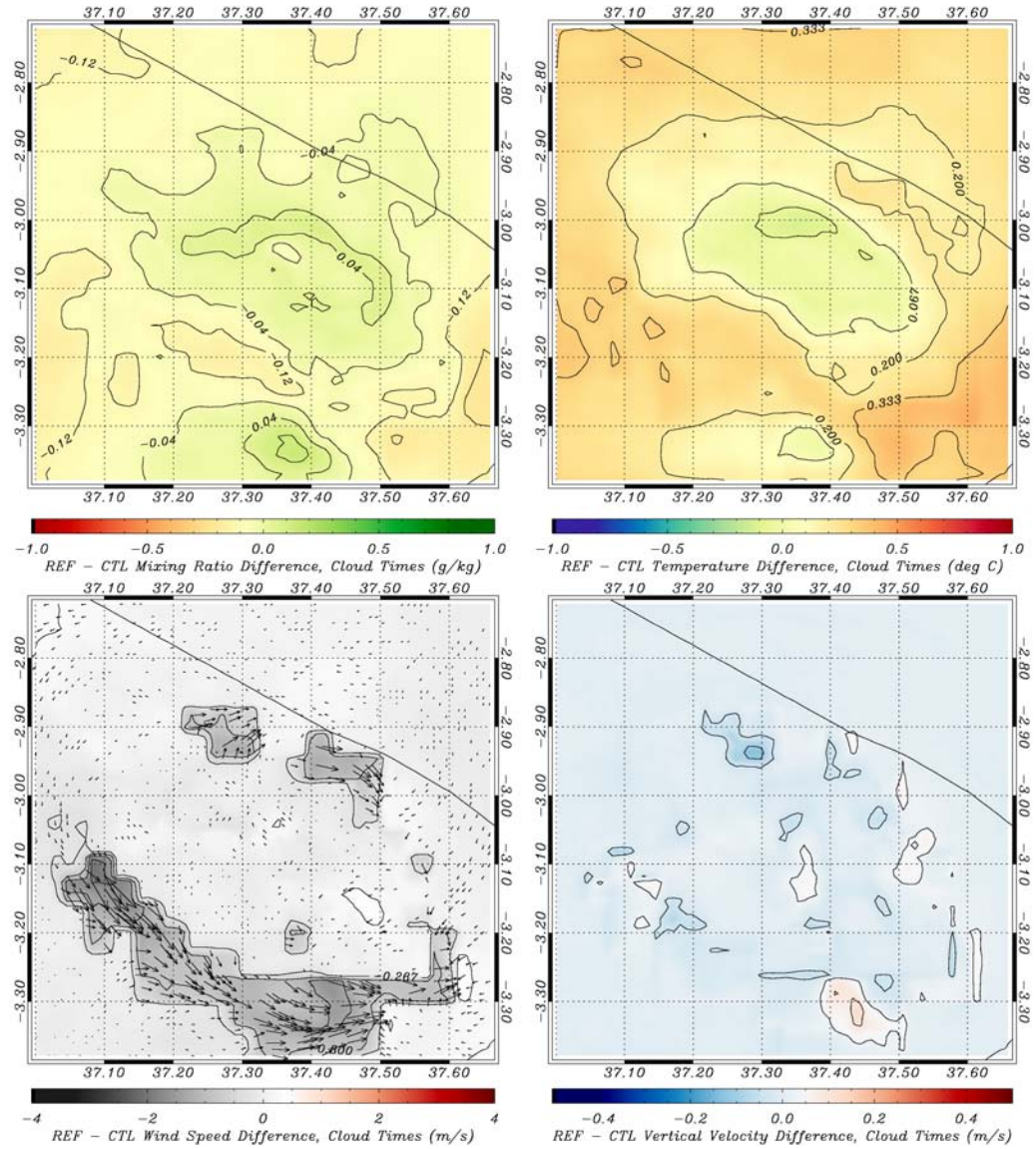

Figure 6.9 Difference in the average meteorological parameters at times of cloud occurrence between the reforested and control simulations.

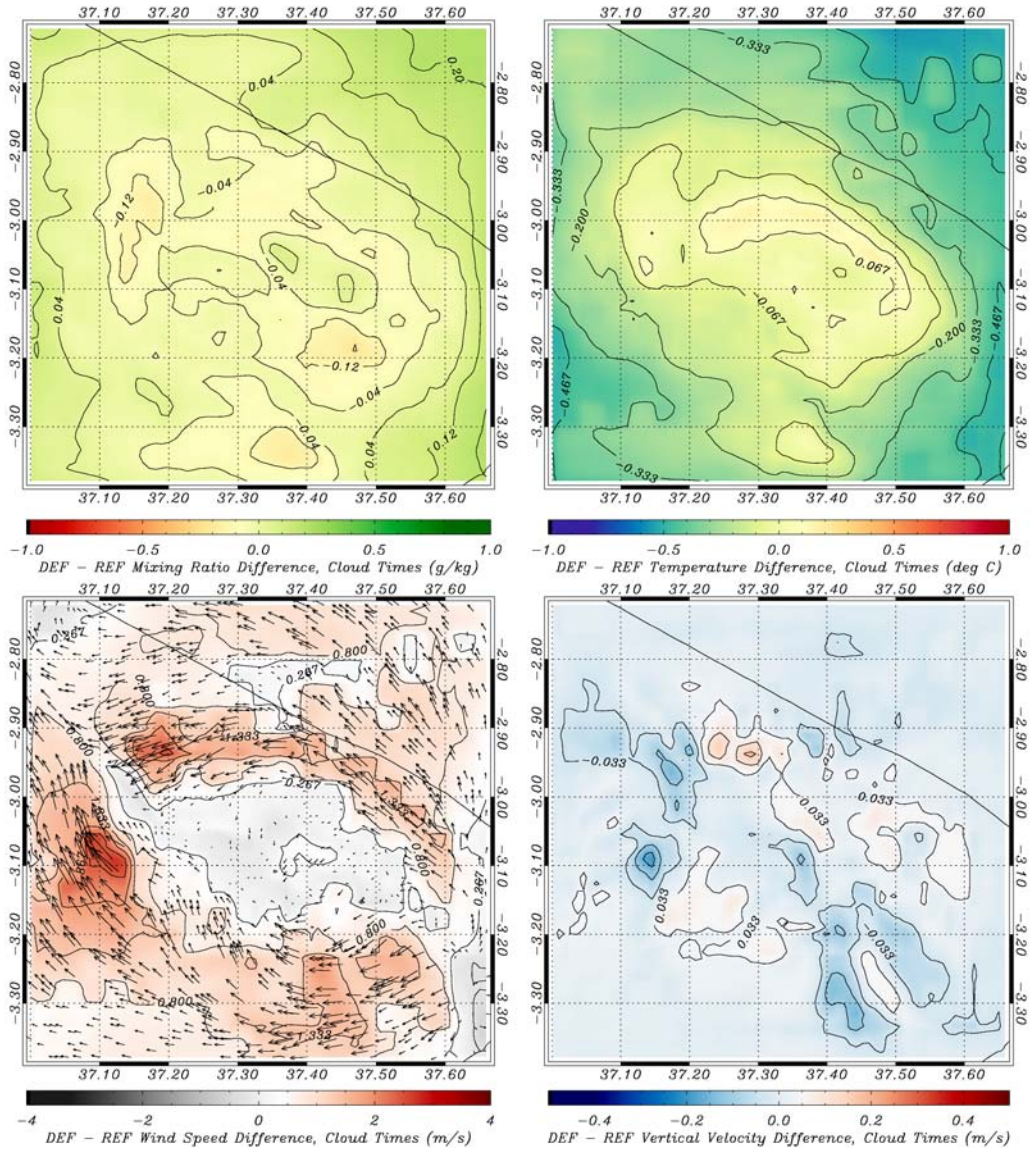

Figure 6.10 Difference in average meteorological parameters at times of cloud occurrence between the deforested and reforested simulations.

While the difference between the DEF and CTL simulations can be clearly seen, there is less of a clear picture between the REF and CTL simulations (Figure 6.9) at times of cloud occurrence. There is a general increase of surface mixing ratio over the center of the grid where clouds occur, and an excess in temperature on the outside of the grid. The wind speed differences at the surface are in the areas where there is additional forested area. There is a deficit at the surface level mixing ratio of -0.12 g/kg at the south side of the mountain, due to moisture excesses being transported up the mountain. When examining the differences between the DEF and REF simulations (Figure 6.10), we see the additive effects from both simulations. There is a moisture excess across most of the grid, with small areas where the REF simulation has higher surface moisture availability. The temperature in the REF simulation at times of high elevation cloud occurrence is consistently higher than the temperature at times of cloud occurrence in the DEF simulation. Wind speeds in the DEF simulation are uniformly higher, up to 3 ms^{-1}, which contributes to patchy areas of higher vertical velocity.

6.2.3 Differences in timing and seasonality of high elevation clouds

With the differences shown in the previous figures due to changes in the land use classifications, it is important to analyze any changes that occur via event occurrence in either a diurnal setting as well as a seasonal setting, as this will allow us to gain a better understanding of the processes that are important for the formation of clouds in these three simulations. Over a diurnal basis (Figure 6.11), there is a much less pronounced peak in cloud occurrence in the DEF simulation at 1200 UTC compared to the CTL and REF simulation. This implies that there is a greater dependence on the thermal circulation and other diurnal processes in the formation of clouds in the REF and CTL

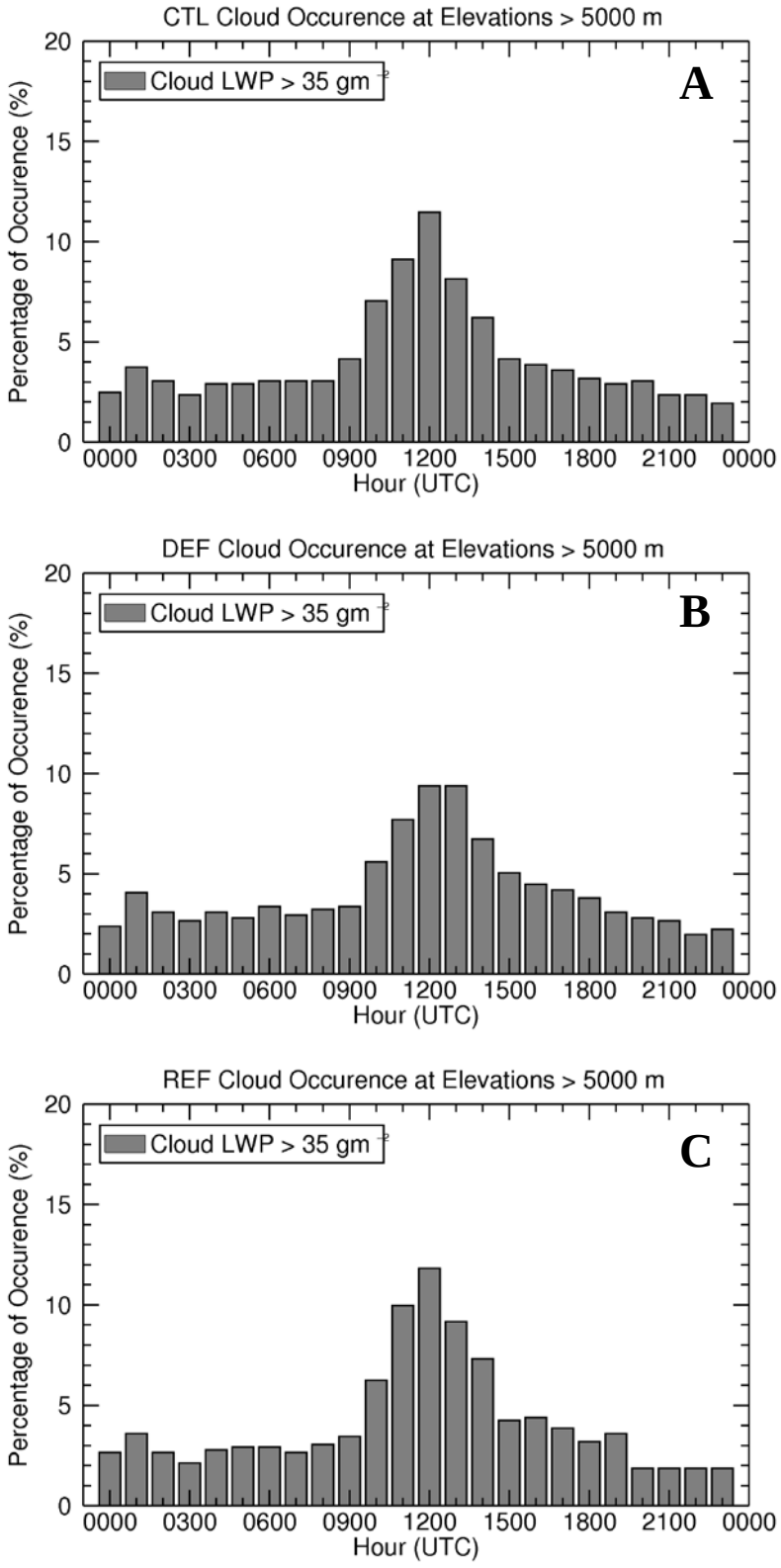

Figure 6.11 Histograms of the percentage of occurrence of clouds at high elevations for the three differing land use simulations. The CTL and REF simulations have higher peaks during the strongest times of the thermal circulation.

simulations compared to the CTL. If we add up the amount percentage of cloud occurrence for the three simulations between 1100 UTC and 1300 UTC (corresponding to 2:00 and 4:00 PM local time, the peak of the thermal circulation) we find that clouds occur 28.5% of the time for the CTL simulation, in comparison to 25% of the time in the DEF simulation and 31% of the time for the REF simulation. In comparison to the differences in cloud formation on a diurnal basis, there is little difference in the timing of clouds on a monthly basis (Figure 6.12). The highest months for cloud occurrence at high elevations in all three simulations in March, followed by September. The months of June, July, and August show no difference in cloud occurrence between all three simulations.

6.3 Land Use Effects on Precipitation

With changes in the diurnal circulations occurring due to differing land use scenarios, as well as factors governing orographic cloud formation, it makes sense to examine how these add up into changes in the precipitation fields. In the previous chapter, we discussed the absolute differences in what occurred for the CTL simulations in cases where precipitation did or did not occur at high elevations, and this section discusses changes in the spatial patterns, elevational distribution, and factors governing the formation of orographic precipitation for the three differing land use scenarios.

6.3.1 Changes in spatial patterns and distribution with elevation

There is considerable change in the spatial patterns of precipitation (Figure 6.13) between the three differing simulations. On average, there is less precipitation in the DEF simulation compared to the CTL and REF simulations, with a strong precipitation maximum noted on the south side of the mountain. The CTL and REF simulations have

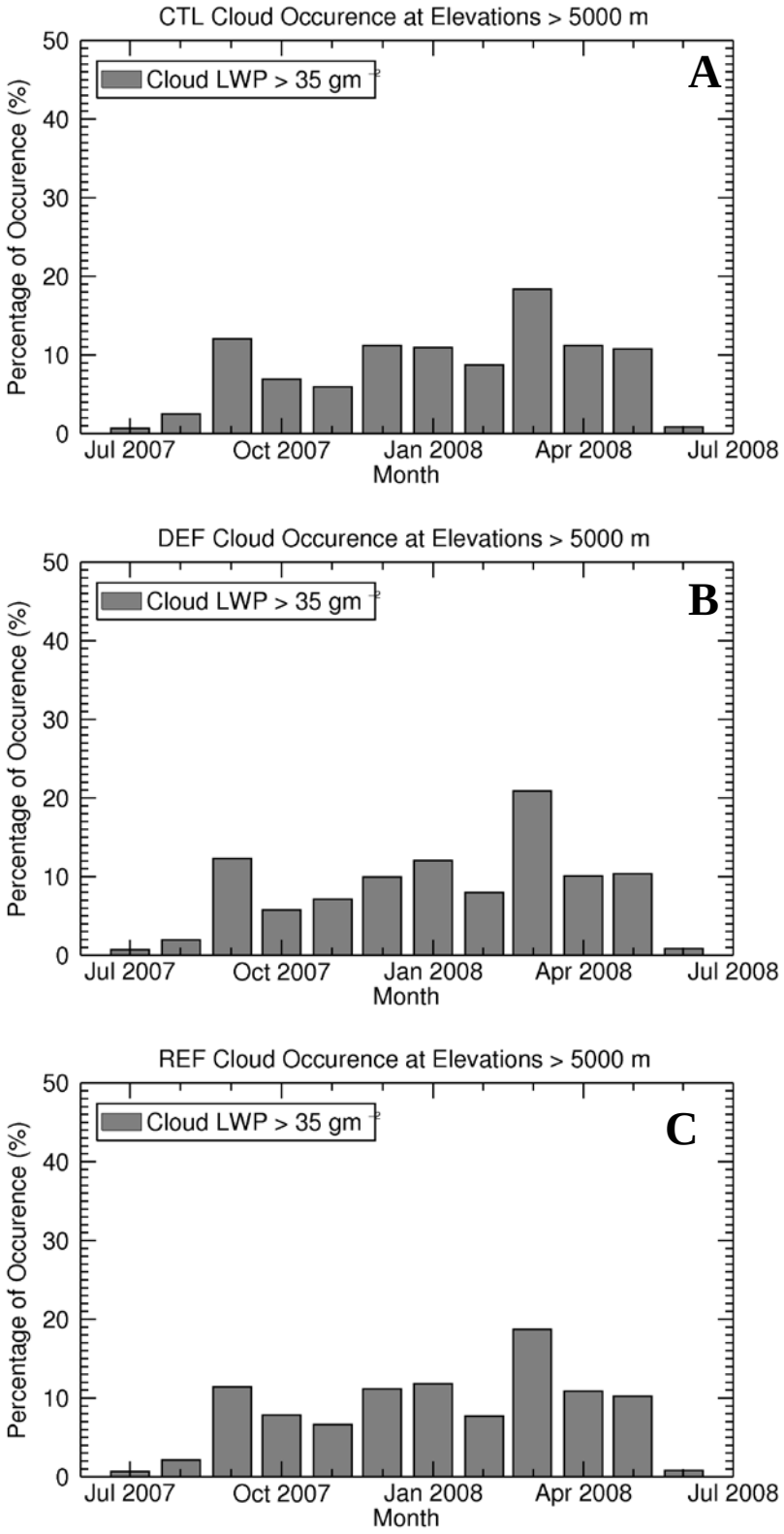

Figure 6.12 Monthly distribution of cloud occurrence at the peak of Kilimanjaro for the three differing land use simulations.

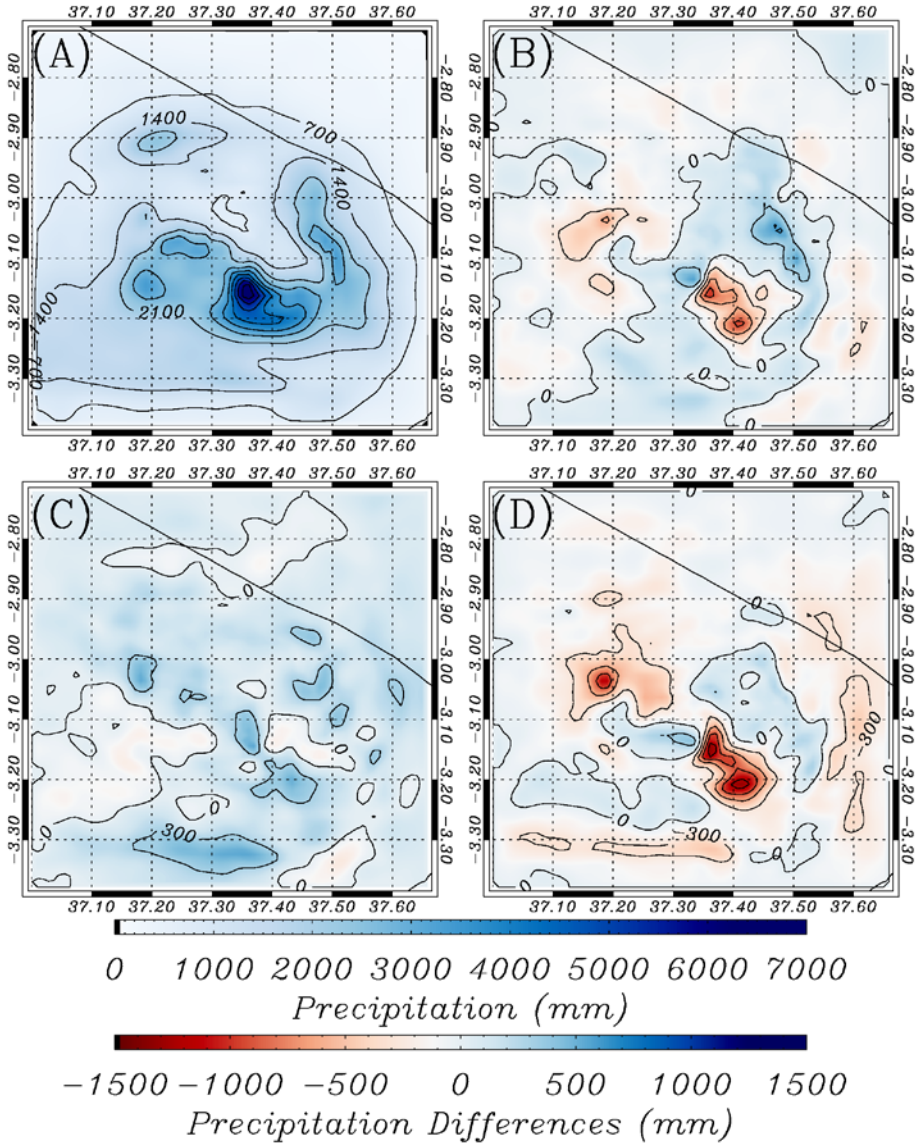

Figure 6.13 Spatial patterns and magnitudes of CTL precipitation (a) and precipitation differences [(b) DEF-CTL, (c) REF-CTL, (d) DEF-REF] between the differing simulations. The bullet point of convection present in the CTL simulation is exacerbated in the REF simulation, but does not appear as much in the DEF simulation.

a maximum precipitation exceeding 6500 mm in an area of high topographic gradients (see Chapter 4), which the DEF simulation does not. The DEF simulation shows precipitation enhancements across the center of the grid, with general declines elsewhere. The REF simulation shows precipitation enhancements across the entire grid, with increases being the strongest of ~300 mm near the areas that were changed into forested land use classifications on the south side of the grid. The largest differences are between the DEF and REF simulations, although the spatial patterns of the differences is complex, with less precipitation falling on the lower slopes of the mountain in the high topographic relief areas and more falling near the center of the domain.

These spatial patterns are complex, but when binned and compared against surface elevation (Figure 6.14), a consistent pattern becomes evident. Figure 6.14a shows the CTL precipitation in 100m binned increments plotted in accordance to surface elevation, showing the areas of maximum precipitation to be located between 2500 m and 3200 m of elevation. On average, the difference between the DEF and CTL simulation (Figure 6.14b) has a deficit of 39.3 mm over the entire grid, whereas the REF simulation has a precipitation excess of 85.35 mm. The majority of the difference in the precipitation in the DEF simulation occurs at points of elevation < 2500 mm, with statistically significant precipitation differences present under this elevation. Between 2500 m and 4200 m, there is not a statistically significant difference between the DEF and CTL simulations, with a precipitation enhancements being found in the DEF simulation over ~4500 m, leading to an average precipitation enhancement of 176.3 mm at high elevations. The REF simulation shows a general enhancement of precipitation

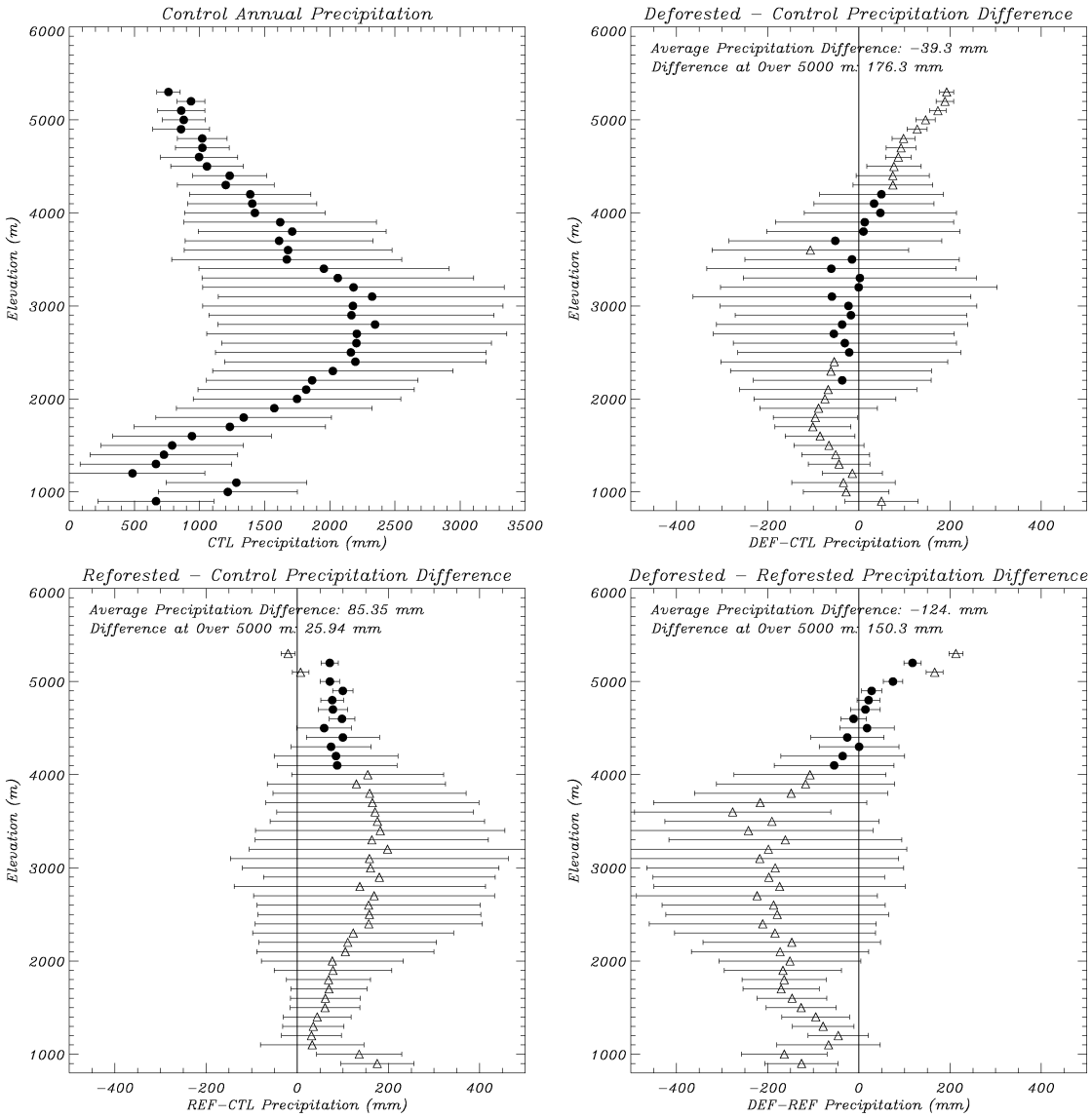

Figure 6.14 Precipitation distribution and differences binned in 100m increments dependent on surface elevation. Triangles denote statistical significance greater than 95% via t-test. The deforested simulation decreases precipitation overall but causes higher precipitation at the high elevations (exceeding 4000 m) compared to the reforested and control simulations.

(Figure 6.14c) across all elevation bands, with the highest enhancements compared to the CTL simulation occurring between 2500 and 4000 m in elevation. Above this point, there is not statistically significant difference in precipitation amounts, although there is a consistent positive signature, leading to a precipitation enhancement of 25.94 mm at the peak. These patterns add together to show that there is a strong deficit in the DEF simulation compared to the REF simulation (Figure 6.14d), with nearly all points having statistical significance up to 4000 m in elevation, after which there is a decided increase in precipitation of 150.3 mm above 5000 m.

6.3.2 Differences in factors governing precipitation formation

As we previously discussed the meteorological factors that govern cloud formation between the three differing simulations, we will consider the factors governing precipitation formation in the same manner. We define times of precipitation occurrence as when hourly rain rates exceed 2.5 mm hr^{-1} at elevations exceeding 5000 m, and analyze the meteorological fields at that point that can show a signal due to upwind land cover change. Figure 6.15 shows the average values of mixing ratio, temperature, surface wind speed, and vertical velocity for times where precipitation occurs at high elevations for the CTL simulation. This indicates strong moisture presence on the southern side, with mixing ratio values exceeding 14 g/kg and temperatures of 23-25° C. This forms a convective response, as indicated by the areas of high vertical velocity, with values of vertical velocity exceeding 0.75 ms^{-1}.

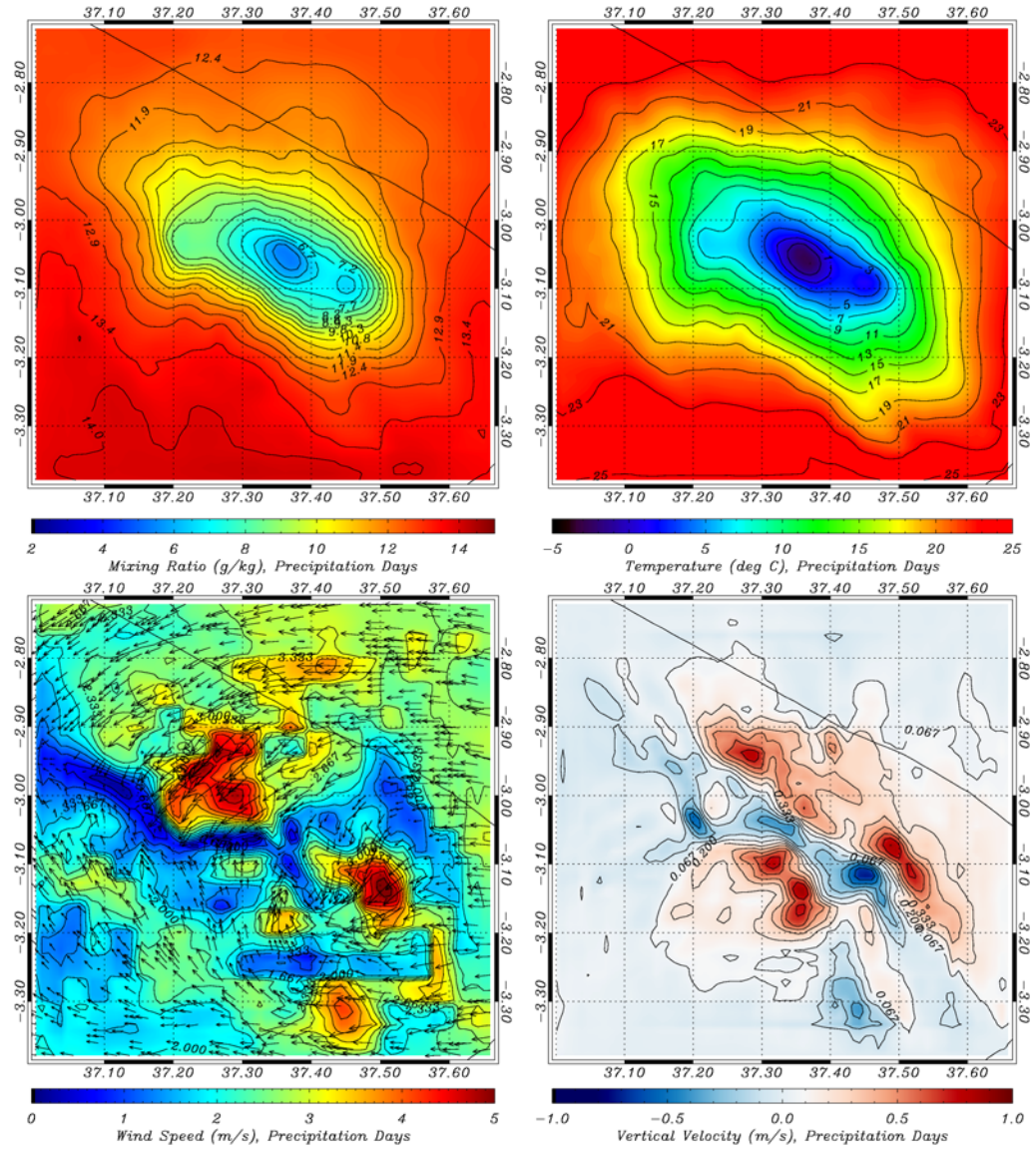

Figure 6.15 Average meteorological parameters for the CTL simulation when precipitation occurs at elevations > 5000 m. Similar to Figure 6.7, except for times of precipitation occurrence.

The differences between the DEF and CTL simulations at times of high elevation precipitation occurrence (Figure 6.16) have a strong signal in moisture, temperature, wind speed, and vertical velocity with differing spatial patterns. Moisture availability is in general much higher when precipitation occurs in the DEF simulation, with enhancements approaching 0.5 g/kg in the northeast corner. However, there is a moisture deficit over the southwestern area, as moisture is not provided from the forests. In general, temperatures are lower across the grid, with minor enhancements occurring over the center of the grid. Wind speeds are uniformly higher, with more of an easterly component to them. These three factors lead to an enhancement of vertical velocity on the eastern side of the compared to the CTL simulation.

While there are clear signals again from the DEF simulation, the differences between the REF and CTL simulations (Figure 6.17) are a little more complex. The clearest difference between the REF and CTL simulations that can be seen is a moisture deficit on the south side of the mountain, with increases in moisture on the northern side. Temperature differences are fairly uniform across the entire grid, and the largest differences in surface wind speed are found in the forested areas, as demonstrated previously in Figure 6.4. This leads to slight changes in vertical velocity, with patches of vertical velocity increase on the eastern side and upslope on the southern side, but generally vertical velocities are smaller in the REF simulation than the CTL simulation.

The largest differences are found between the DEF and REF simulations at time of high precipitation occurrence (Figure 6.18). There is significantly more grid-averaged moisture in the DEF simulation at times of precipitation occurrence than the REF simulation, with excesses approaching 0.5 g/kg. On the south side of the mountain, there

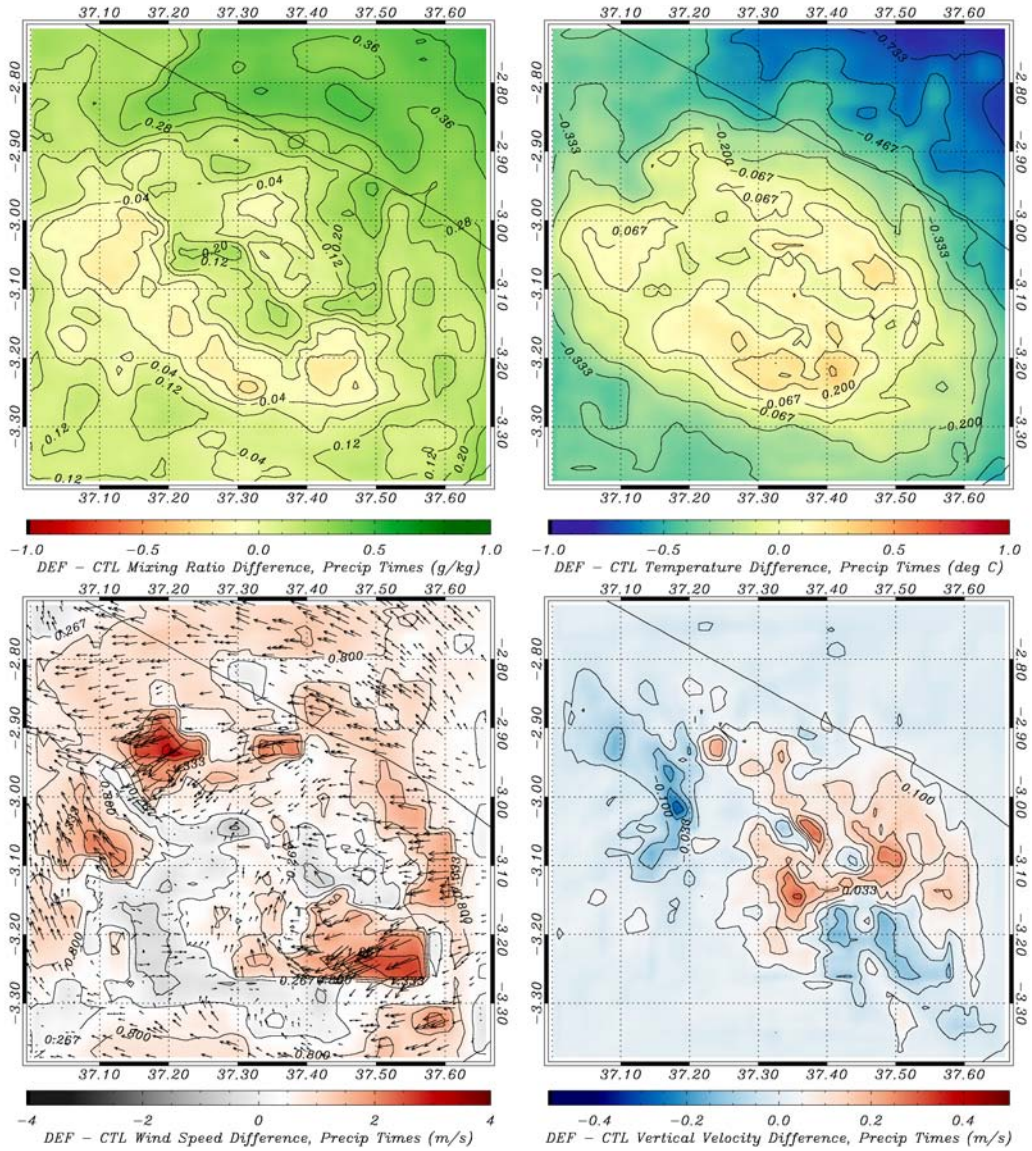

Figure 6.16 Differences between meteorological parameters of the DEF and CTL simulations at times of precipitation occurrence at high elevations.

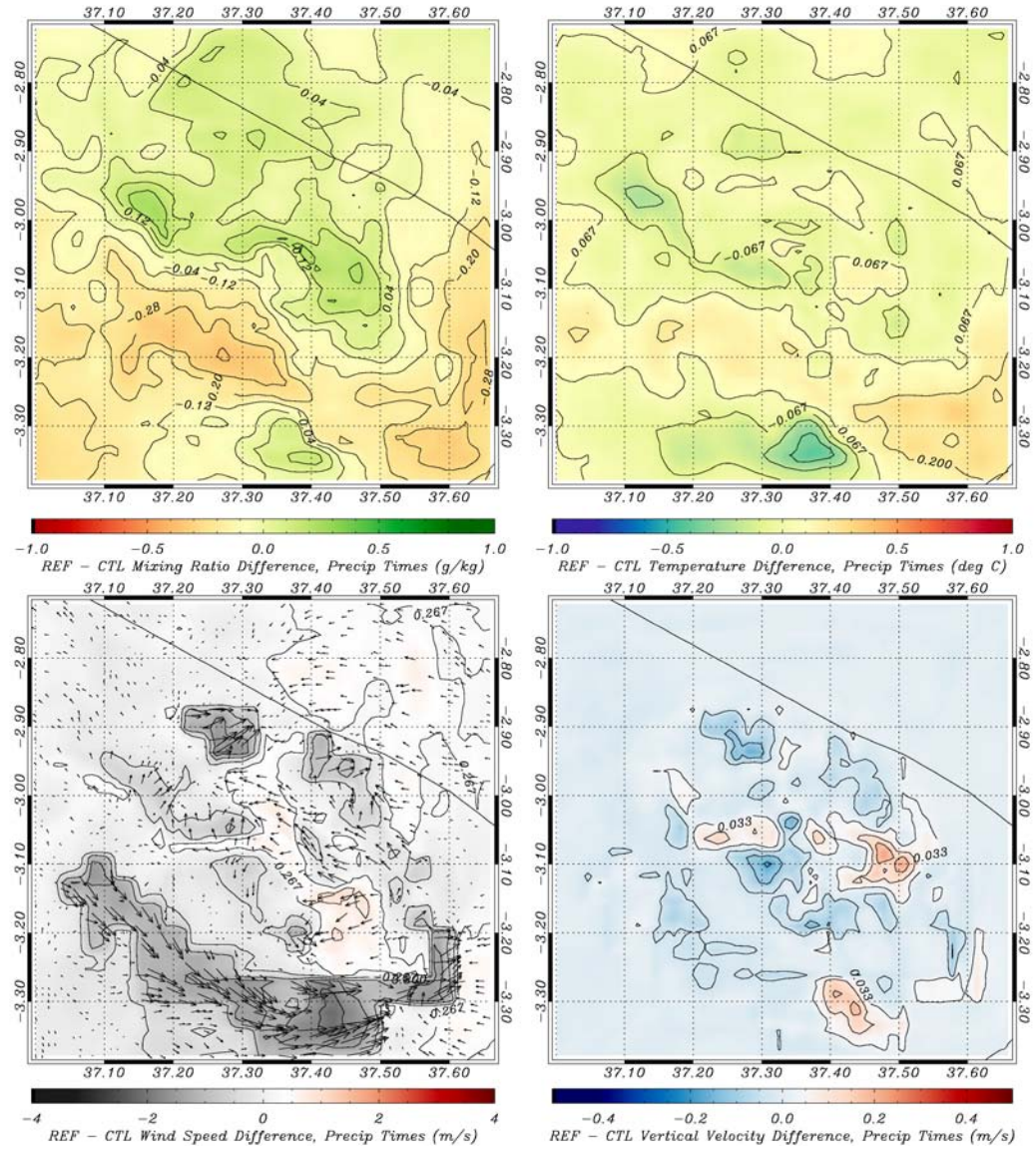

Figure 6.17 Differences in average meteorological parameters at the surface for the REF and CTL simulations during times of precipitation occurrence at high elevations.

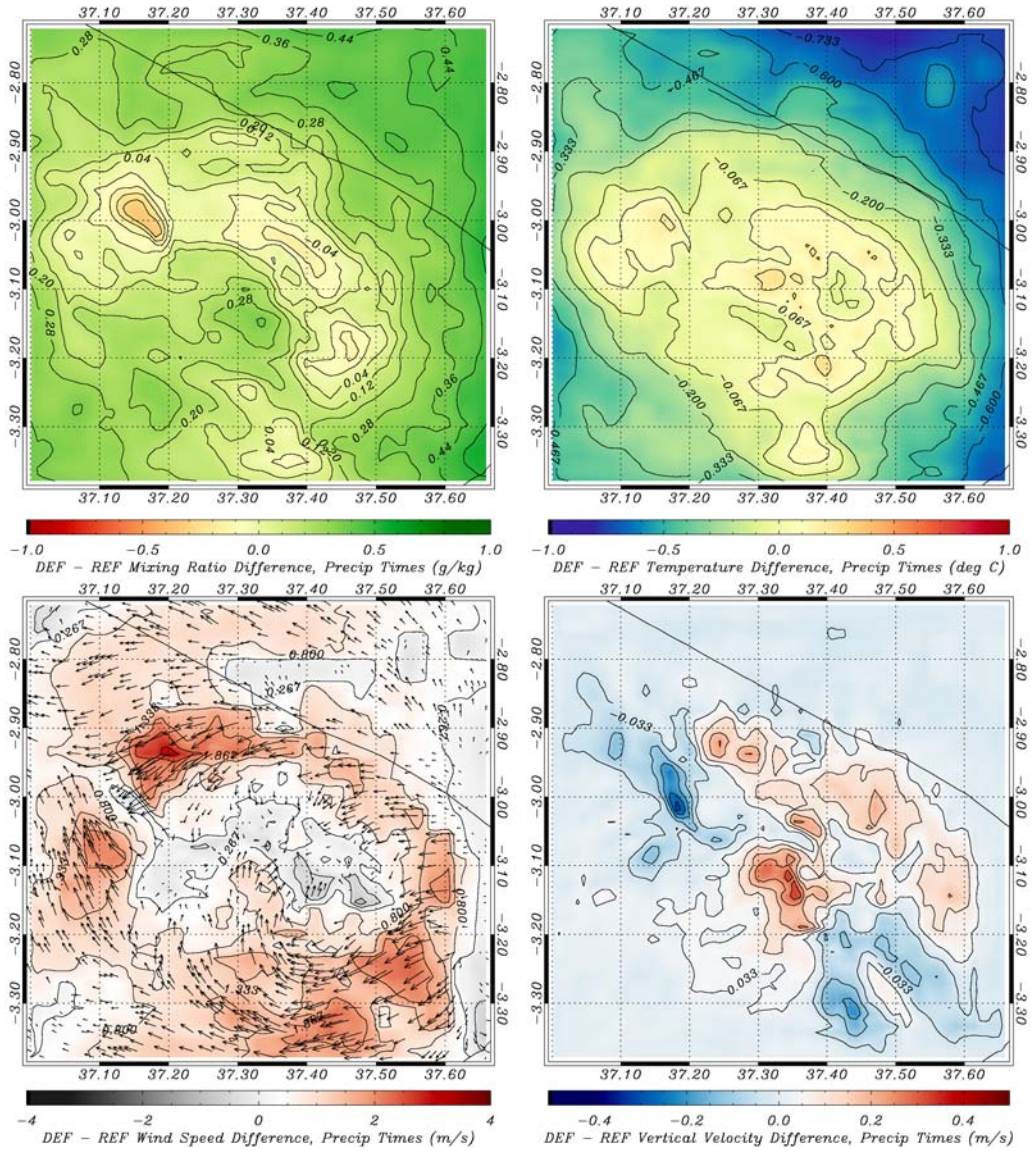

Figure 6.18: Difference in meteorological parameters during times of precipitation occurrence between the DEF and REF simulations.

is an enhancement of moisture close to 0.3 g/kg, whereas the moisture availability is lower in an arc spanning the center of the grid. The temperature in the DEF simulation is nearly uniformly lower at times of precipitation occurrence compared the REF simulation, with the highest differences being found near the periphery of the model grid. Wind speeds are consistently higher, showing a stronger upslope flow and a more distinct circulation from the south, as more flow is directed upslope on the southern side. This leads to enhancements of vertical velocity that are strongest on the southern side of the mountain, but are mainly located on the northeastern side.

6.3.3 Differences in timing and seasonality of high elevation precipitation events

If there are changes in the meteorological fields due to land use, there should be a diurnal effect that is manifested by changes in the precipitation at high elevations caused by the thermal circulation. Figure 6.19 shows the timing of precipitation events at high elevations for the three differing simulations. In general, there is a peak of precipitation occurrence between 1100 UTC and 1500 UTC (corresponding to 2:00 PM and 6:00 PM locally). However, there are significant differences in the magnitudes of these peaks between the three differing simulations. For example, by adding up the precipitation occurring at 1200 UTC to 1400 UTC, we find that precipitation during these three times accounts for 36.5% of the total times of precipitation occurrence. However, for the DEF simulation, these three hours only account for 29% of the precipitation occurrence. A

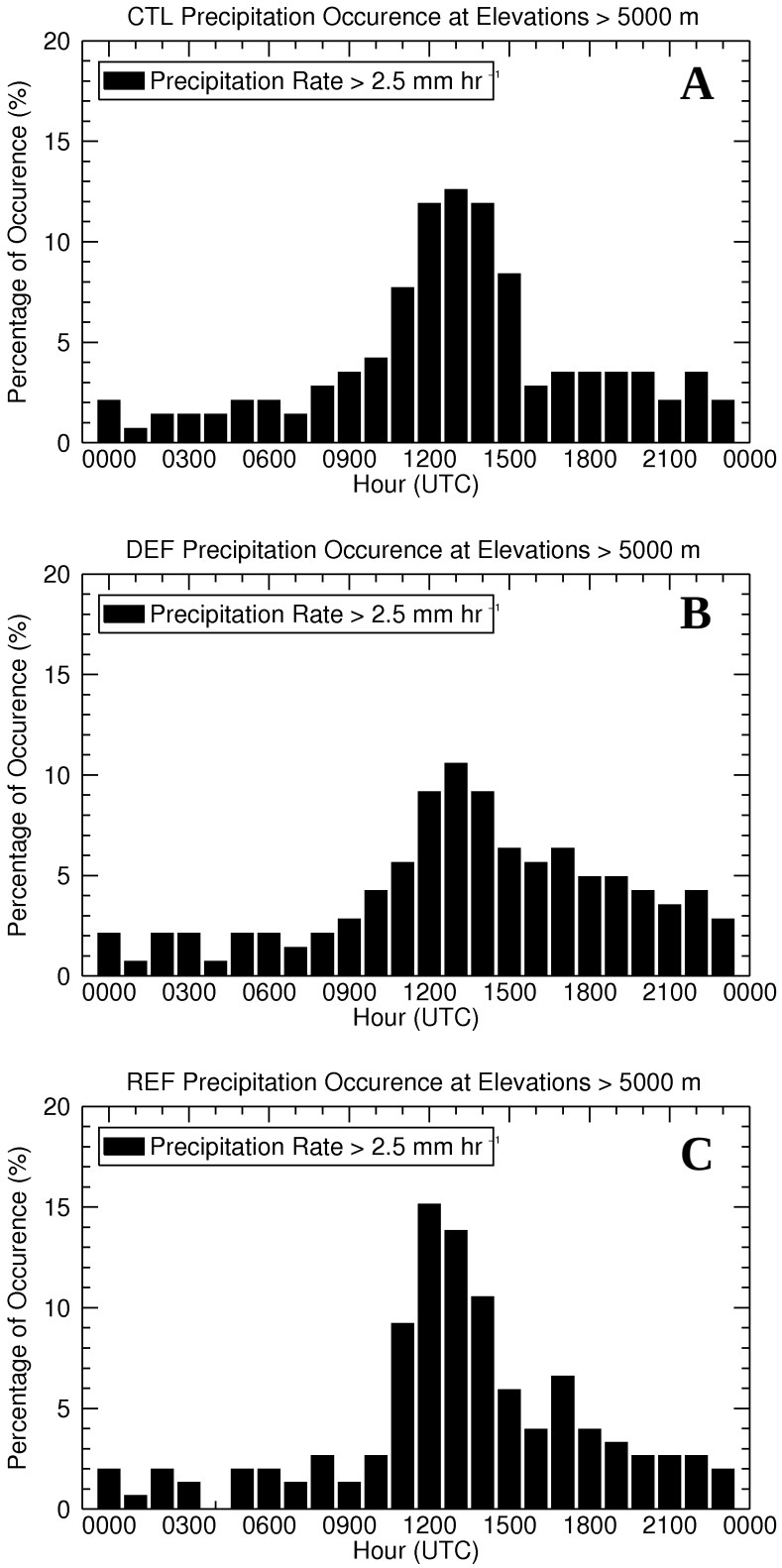

Figure 6.19 Histogram of the times of precipitation occurrence for the three differing simulations. The REF and CTL simulations have a very strong peak at 1200/1300 UTC.

stronger response is seen in the REF simulation, where over 40% of the precipitation falls within these three hours, and over 50% of the precipitation falls between 1000 UTC and 1500 UTC.

Monthly distributions of high elevation precipitation occurrence (Figure 6.20) show a larger difference compared to the monthly differences of cloud occurrence at high elevations, with more seasonal dependency for differing model simulations. For example, the highest month of precipitation occurrence for all three simulations is March, with 37% of the CTL precipitation falling within this month. However, the DEF run has 43% of the times of precipitation occurrence falling within March. There are similar patterns in the seasonality of high-elevation precipitation between the REF and CTL simulations, with the main difference being the CTL simulation having higher occurrence of precipitation in February than the REF simulation, and the REF simulation having higher precipitation occurrence in December than the DEF simulation. The changes in precipitation are mainly evident in the distribution in the wet season months, as the dry season months of June, July, and August are not effected at all. No precipitation falls at high elevation until September, and little falls after April.

6.4 Differences in Generation and Maintenance of the Thermal Circulation

In order to go back to the basic physics concerning the generation of the diurnal circulation, it is useful to look at differences at various hours of the day and examine fields that contribute to the formation of the pressure gradient that forms the thermal circulation. Since the thermal circulation is based off the surface air heating more than the free air at a given point, we can examine the differences in temperature at the peak of

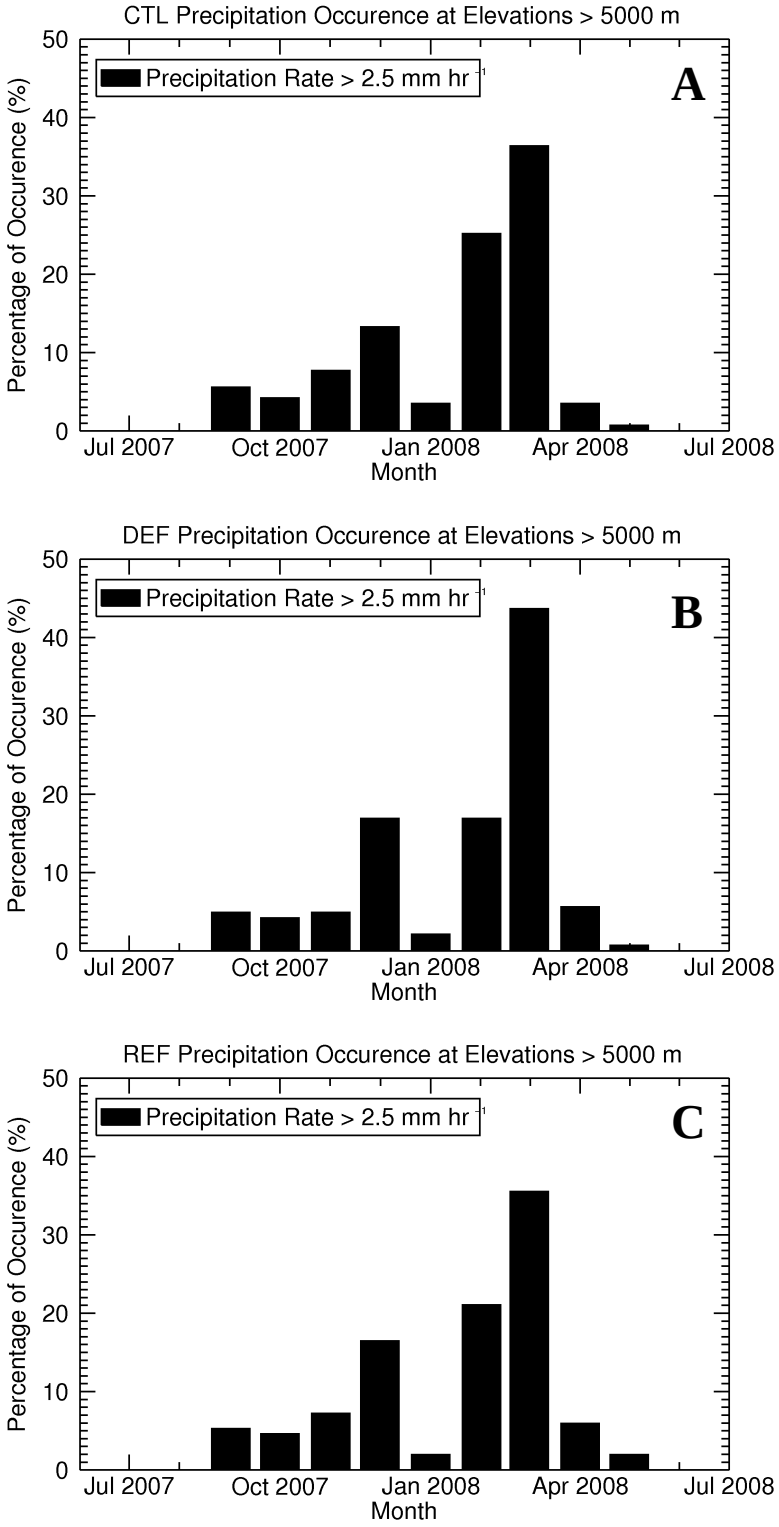

Figure 6.20 Histograms of times of precipitation occurrence at high elevations for each month of the model operation. The DEF simulation has the highest peak in March compared to the REF and CTL simulations.

the thermal circulation, which is at 1500 local time (1200 UTC), and compare it to the circulation patterns present at 0900 local time (0600 UTC) in order to see the differences that the change in low-elevation land cover has throughout the atmosphere. Figure 6.21 shows the zonal mean difference in the 1200 UTC – 0600 UTC temperature, averaged over the entire year for the CTL simulation, as well as the differences in this ΔT throughout the day, whereas Figure 6.22 shows the same field but for the meridional mean. Over these six hours, the average temperature difference is ~0.1 – 0.2 degrees over the elevations that comprise the high-level thermal circulation, which are from 3000-5000 m. However, the differences in temperature are higher in the deforested simulation by 0.1 degrees, indicating that the free air heats up more than in CTL or REF scenarios. With the additional heating in the free air at these elevations, there would be less of a temperature difference between the free air and the surface.

This difference in temperature changes the thermal circulation by altering the horizontal pressure gradient force, which is shown in zonal mean form in Figure 6.23 and meridional mean form in Figure 6.24. In order to compute the pressure gradient force at each point, it is first necessary to reform the sigma-z model grid to a true horizontal coordinate, than compute the gradient along this true horizontal level. Figures 6.23 and 6.24 show the difference in the pressure gradient force at 1200 UTC and 0600 UTC for the CTL simulation (Figures 6.23a and 6.24a) as well as the differences between this diurnal variation from the DEF and CTL simulations (Figures 6.23b and 6.24b), REF and CTL simulations (Figures 6.23c and 6.24c), and DEF and REF scenarios

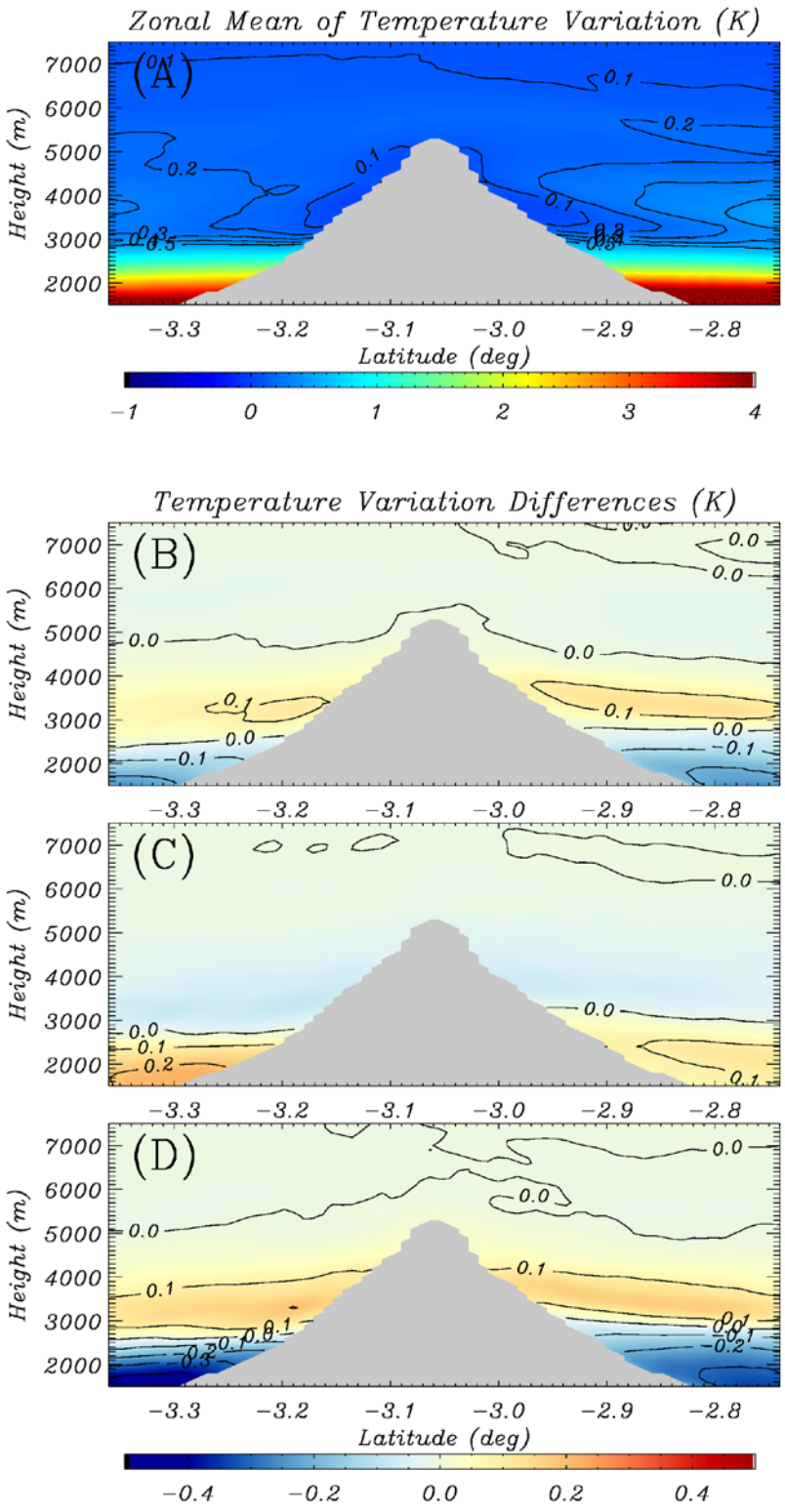

Figure 6.21 a) CTL Zonal mean difference in temperature variation between 1200 UTC and 0600 UTC. b) DEF-CTL variation difference. c) REF-CTL variation difference d) DEF-REF variation difference. Enhanced variations lead to enhanced circulations.

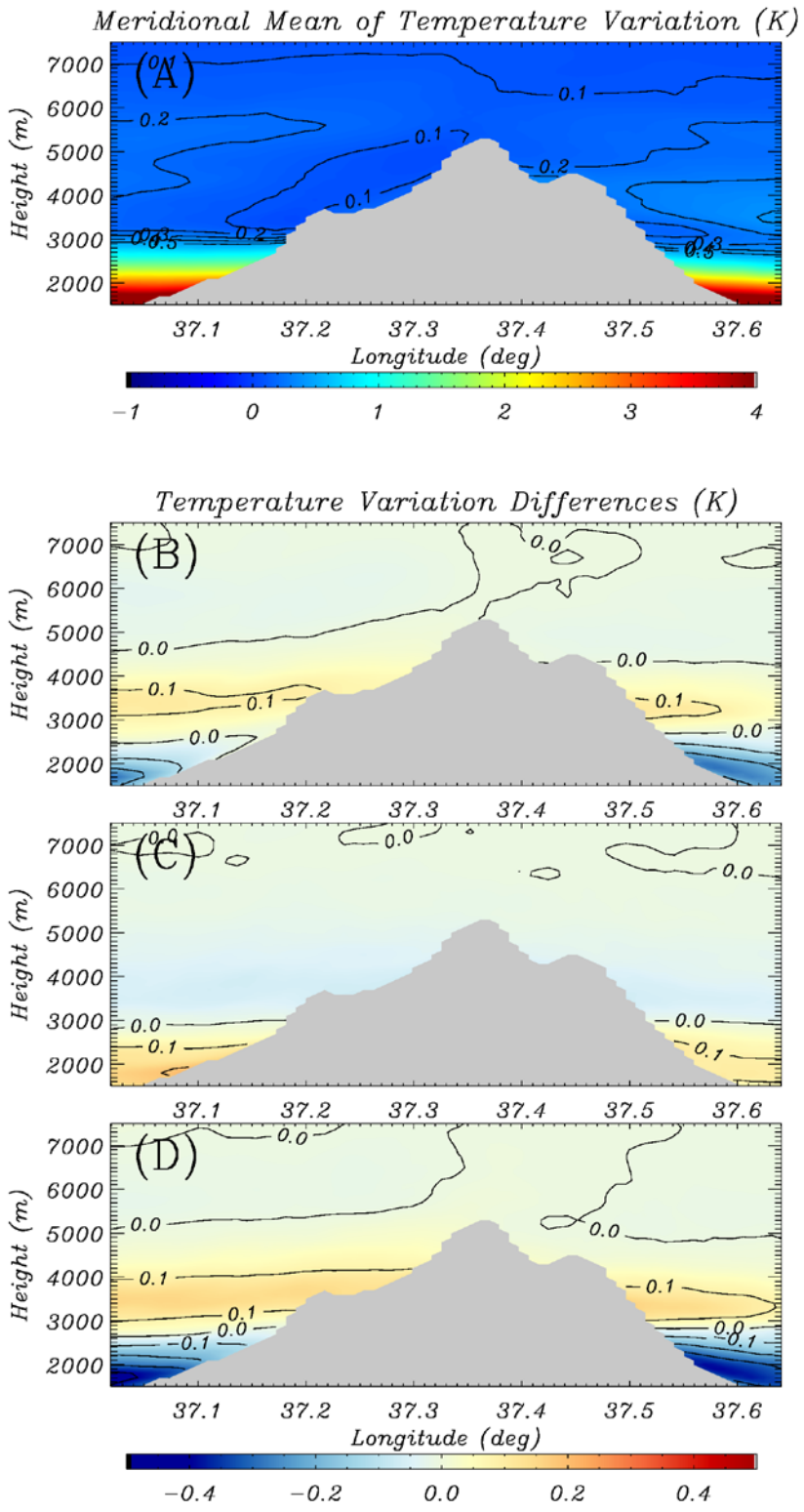

Figure 6.22 The same as Figure 6.21, but for the meridional mean.

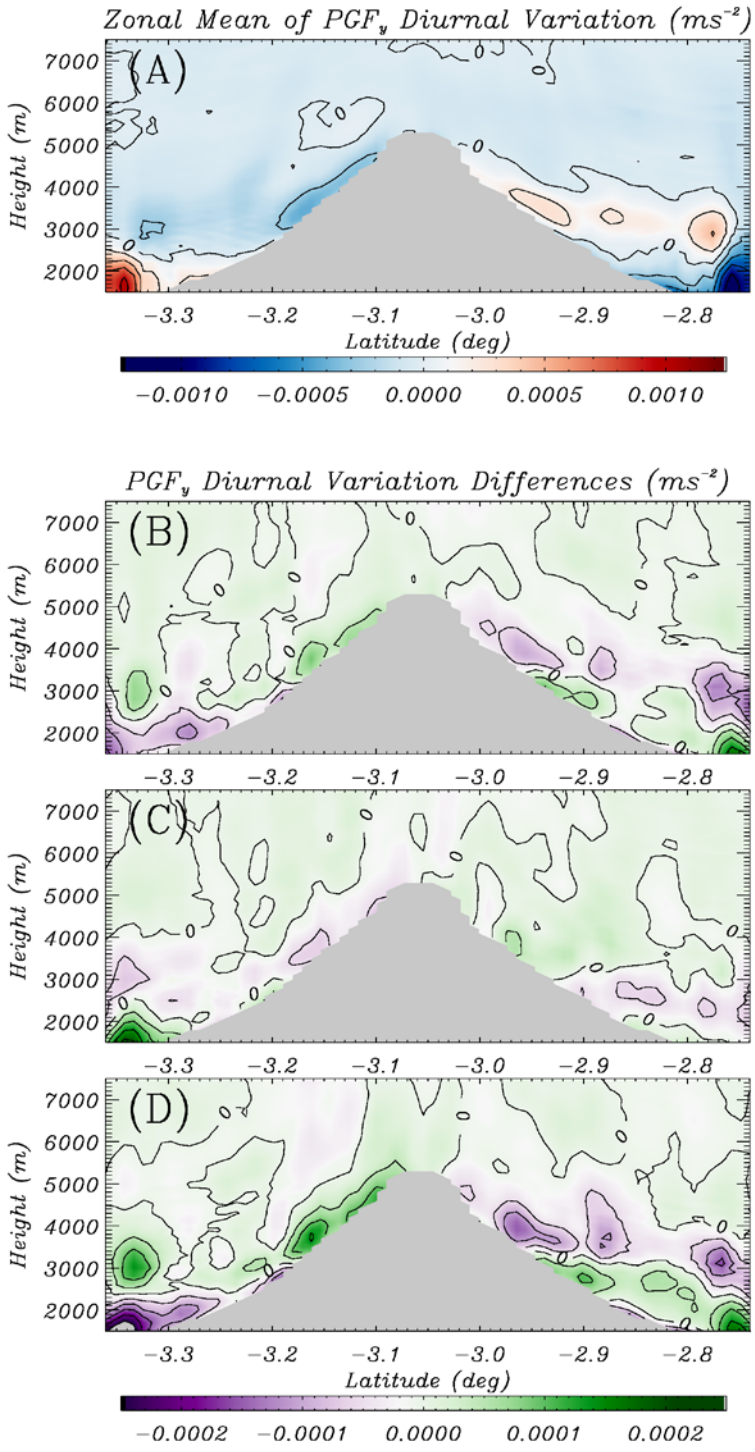

Figure 6.23 Zonal means of a) Differences in variations of horizontal pressure gradient force. b)DEF-CTL differences c) REF-CTL differences d) DEF-REF differences.

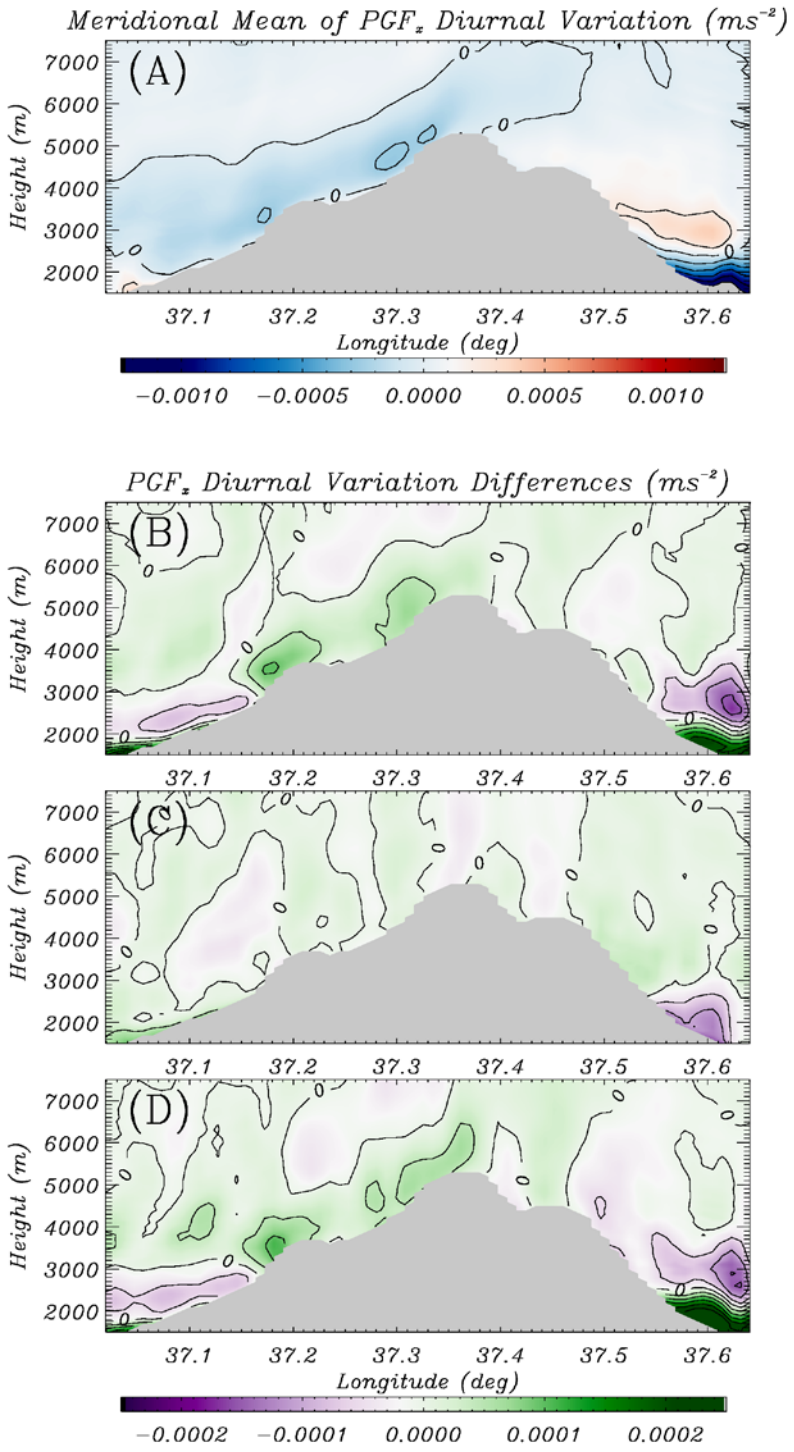

Figure 6.24 Same as Figure 6.23, but meridional mean values.

(Figures 6.23d and 6.24d). What this indicates is that there is less pressure gradient force manifested at the surface at 1200 UTC with decreasing amounts of forested cover, with increasing amounts of forested cover (such as the REF simulation) causing enhanced formation of the thermal circulation. This is a direct result of the difference in temperature shown in Figures 6.21 and 6.22. The locations of enhanced pressure gradient force also coincide with the thermal circulation transect presented in *Pepin et al.* [2010] as well as the previous chapter. The enhanced circulation is mainly on the southwest side of the mountain, which is due to enhanced solar radiation on that side during the afternoon, with a decreased pressure gradient force on the east and north sides of the mountain due to solar positioning and shading.

This change in the diurnal evolution of the thermal circulation leads to moisture differences at various elevations, with the reforested scenario transporting more moisture upslope on a daily basis. Figures 6.25 (zonal mean) and 6.26 (meridional mean) show the differences in the atmospheric mixing ratio between 1200 UTC and 0600 UTC. What we find is from elevations over where the peak of the thermal circulation is (from ~2500 m in elevation to ~4000m in elevation), there is up to 1.2 g/kg of a mixing ratio increase in between these two times. However, if we consider the differences between the three simulations, we find that there are significant decreases in upslope moisture transport. The DEF simulations transports up to 0.4 g/kg less moisture upslope than the CTL does between 2500m and 4000m in elevation, which constitutes 25-50% of the total moisture transported. There is a slight increase in the REF simulation, with increases exceeding 0.1 g/kg from 2500 m to 4000 m, which constitutes a 10-25% increase in the amount of moisture transported. This would indicate that there is enhanced moisture

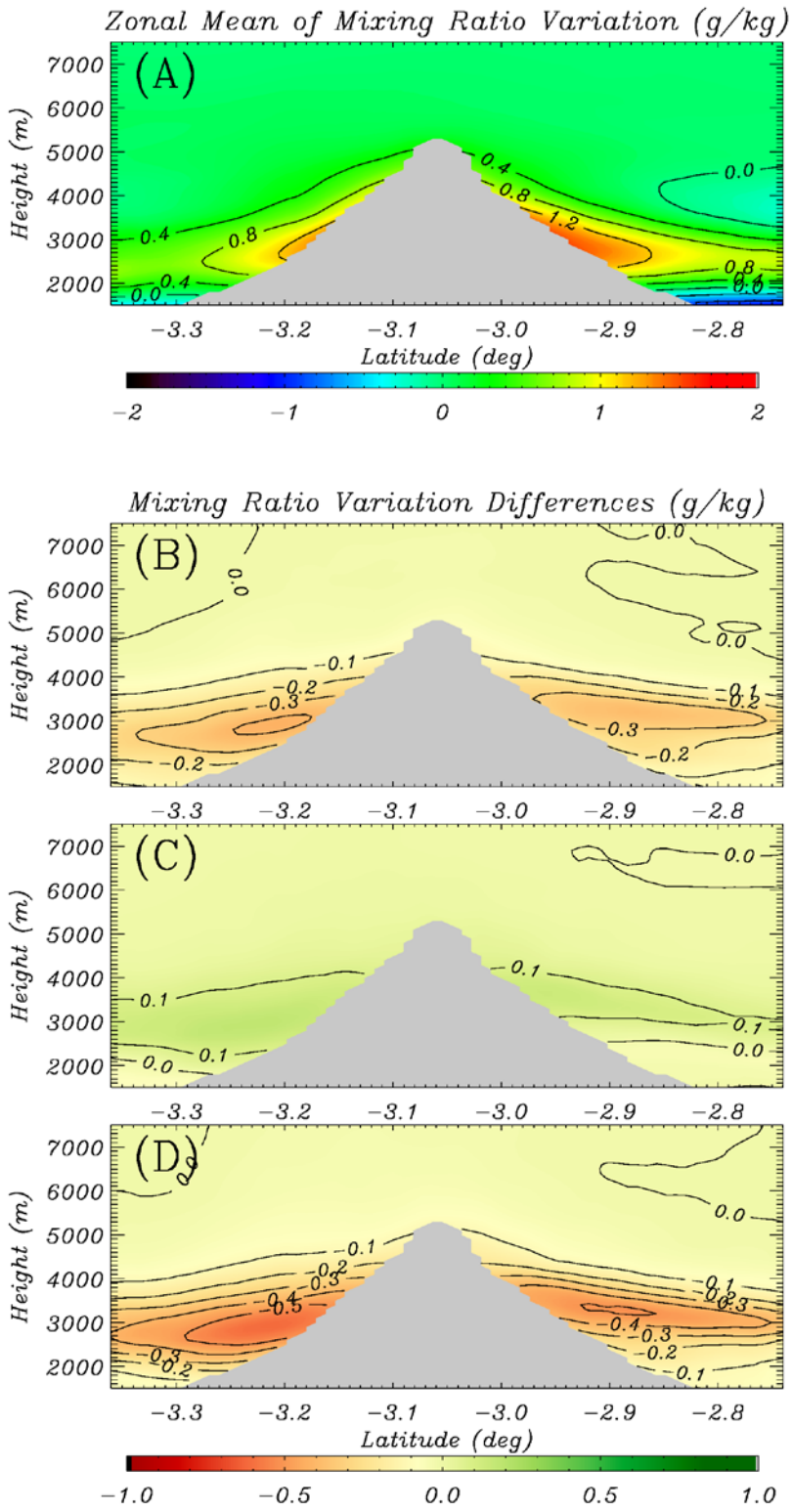

Figure 6.25 CTL zonal mean moisture differences between 1200 UTC and 0600 UTC (a) and the differences [(b) DEF-CTL, (c) REF-CTL, (d) DEF-REF] of the diurnal variation between the three simulations.

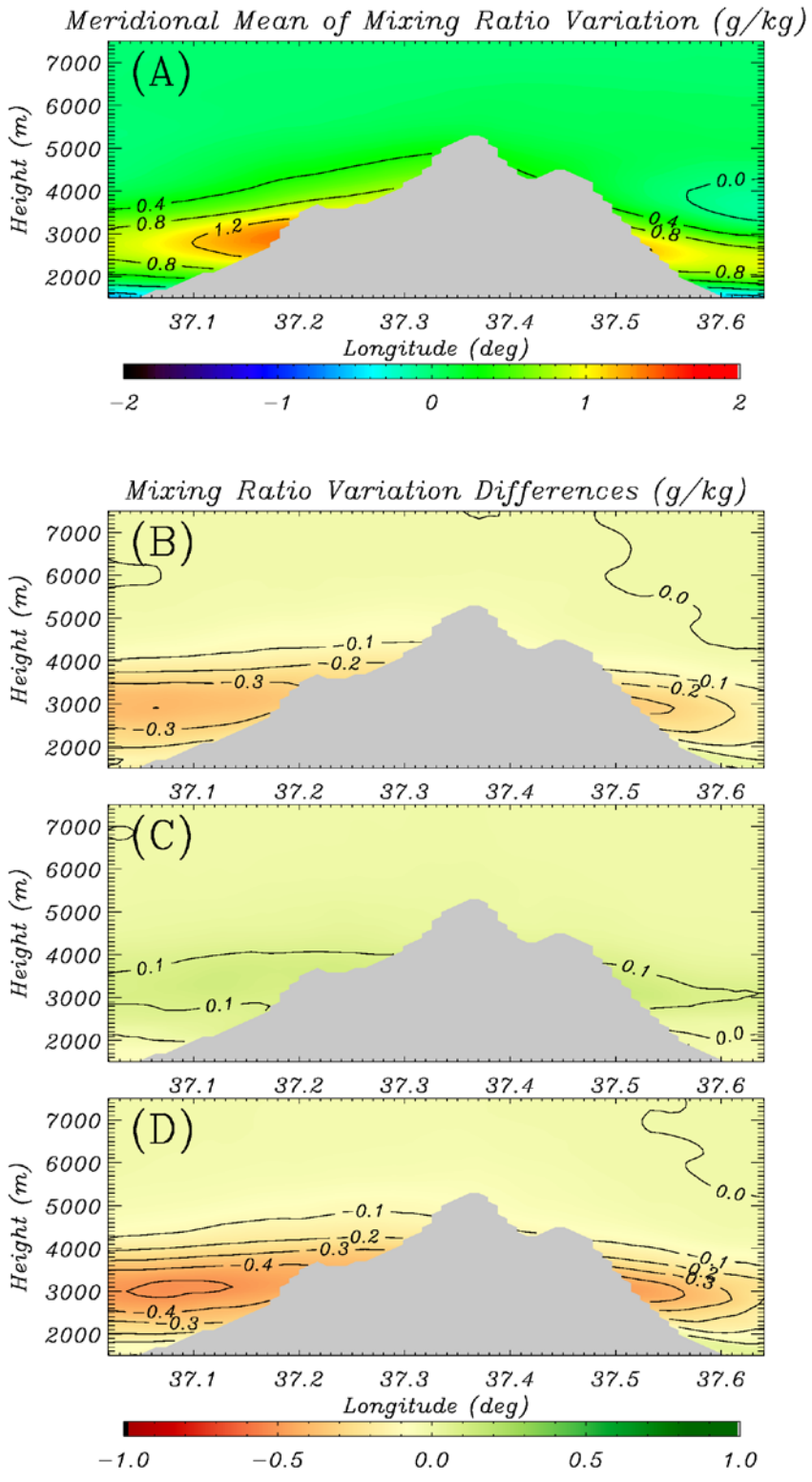

Figure 6.26 Same as Figure 6.25, except the meridional mean.

transport upslope, indicating that the DEF simulation transports air that is both drier and at a higher temperature than in the REF simulation.

This difference in upstream moisture content along with the temperature leads to examining the differences in vertical velocity throughout the day. Figures 6.27 and 6.28 look at the zonal and meridional means of the change vertical velocity from 0600 UTC to 1200 UTC. What is evident is that even though the average vertical velocity is higher (as seen in Figure 6.4, the DEF simulation (Figures 6.27b and 6.28b) leads to much less increase in vertical velocity throughout the day, while the REF simulation (Figures 6.27c and 6.28c) leads to an invigoration and increase in the vertical velocity at 1200 UTC in comparison with 0600 UTC. This is consistent with the enhanced transport of moisture along the slope, and the enhanced strength of the thermal circulation in the REF simulation compared to the DEF simulation.

6.5 Discussion

These model results show several confounding factors compared to average results. A deficit in moisture exists on the slopes of the mountain during times of precipitation and cloud occurrence when comparing the REF and CTL simulations, where a moisture excess would be expected due to higher envirotranspiration rates over forested areas than farmland. There is also an excess of moisture present in the DEF simulation at times of precipitation occurrence in comparison to the REF and CTL simulations. Finally, the amount of precipitation at high elevation increases for both the DEF and REF simulations with regards to the CTL simulation, and the DEF simulation increases high level precipitation more than 6 times what the REF simulation does in comparison to the

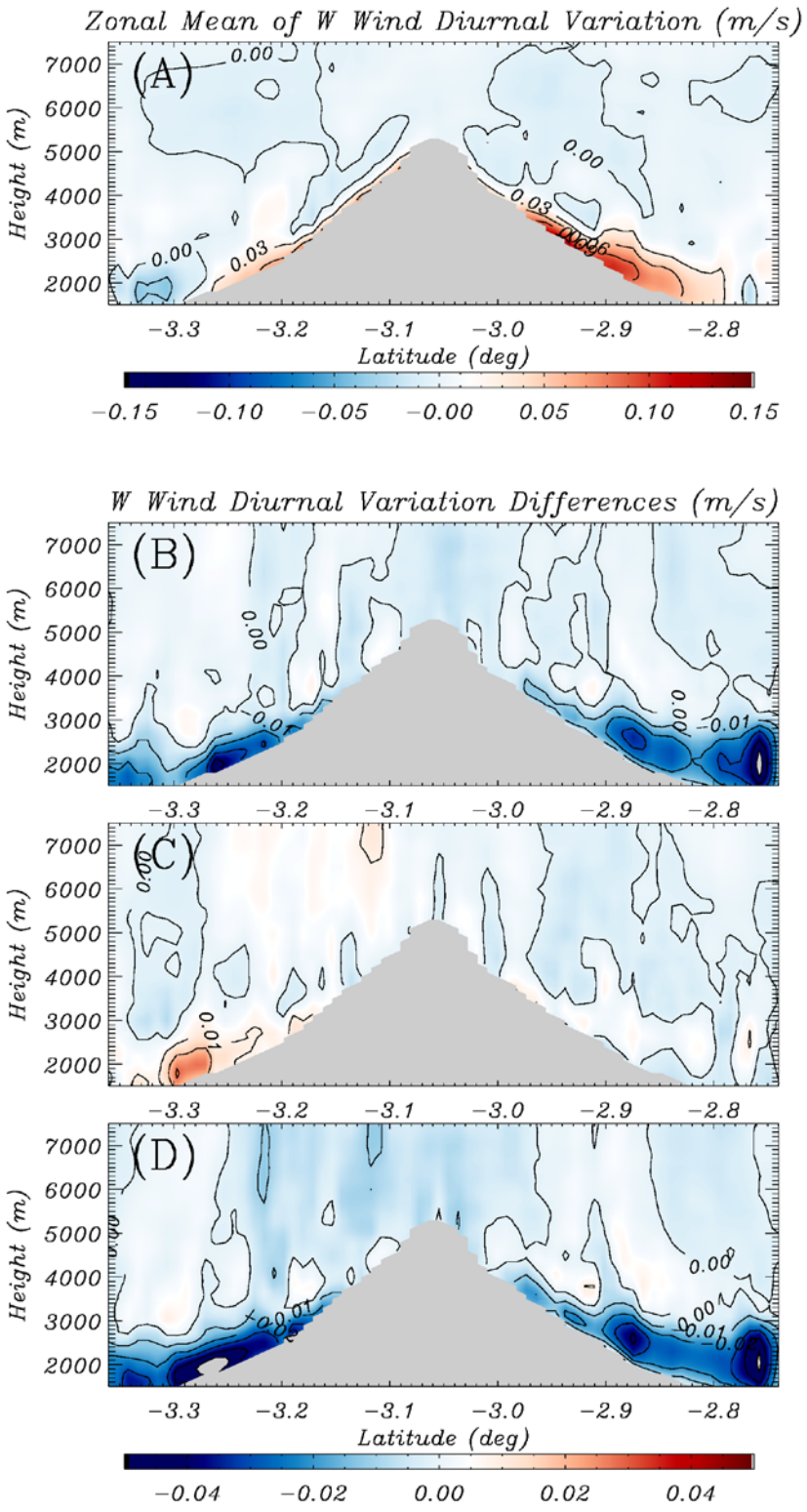

Figure 6.27 Zonal means of a) Diurnal variation of vertical velocity. b) DEF-CTL differences. c) REF-CTL differences. d) DEF-REF differences.

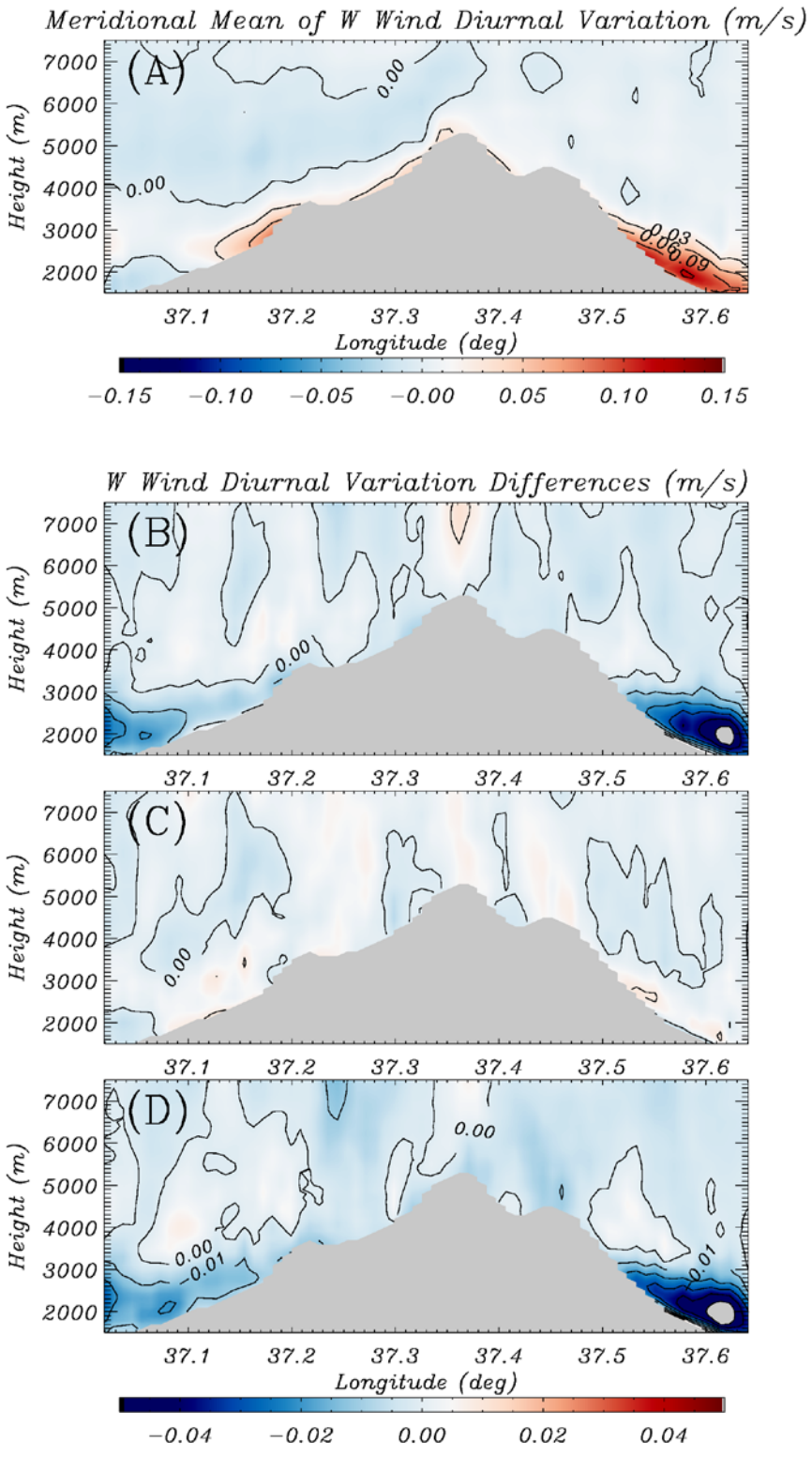

Figure 6.28 The same as Figure 6.27, but for meridional means.

CTL simulation, and does this with little change in the frequency of cloudiness between all three model simulations. This section will try to address these confounding factors that exist from these past model results.

The deficit of moisture on the southern slopes of Kilimanjaro as shown in Figures 6.9 and 6.17 between the REF and CTL simulations is due to excess moisture being transported upslope prior to the initiation of clouds and precipitation at the peak. Since these averages are concerned with the whole time that clouds exist, the upslope transport of moisture is not present, instead focusing on the increases in moisture in downstream areas. Figures 6.29 and 6.30 show the average meteorological fields 1 hour before the occurrence of clouds and precipitation, respectively. Present in Figures 6.29a and 6.30a is a moisture excess in the REF simulation compared to the CTL simulation, which propagates up the mountain in a three-hour period before precipitation or clouds exist at the peak. This moisture excess is transported due to enhanced strength of the thermal circulation, which can also be demonstrated by the strong peak in precipitation and cloud occurrence from 1100 – 1300 UTC (as shown in Figures 6.11c and 6.20c), when the thermal circulation will be the strongest. There is less of a dependence on the thermal circulation for the DEF simulation, as indicated by a much less pronounced peak in Figures 6.9b and 6.19b. This agrees with the conceptual model of the thermal circulation as discussed by *Pepin et al.* [2010] and the previous chapter.

The excess moisture present at times of cloud and precipitation occurrence in the DEF simulation in comparison to the CTL and REF simulations as shown in Figure 6.9 and Figure 6.17 is mainly due to the monthly frequency of occurrence of clouds and precipitation and the averaging over those months. There is a very pronounced peak in

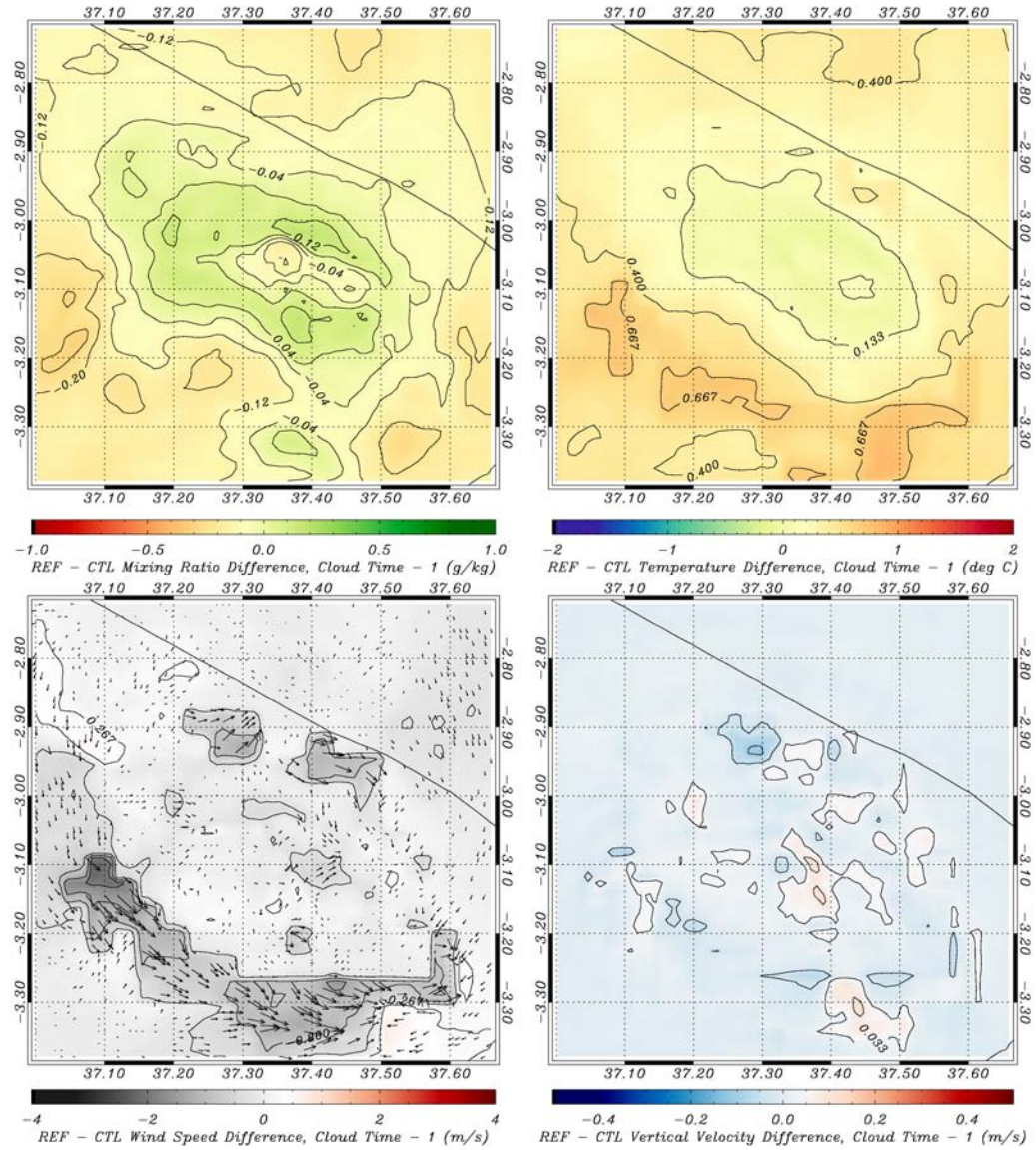

Figure 6.29 Difference in meteorological parameters 1 hour before cloud occurrence at the peak between the REF and CTL simulations. Of interest is the higher temperature to the south side of the mountain and the areas of moisture enhancement on the slopes of Kilimanjaro.

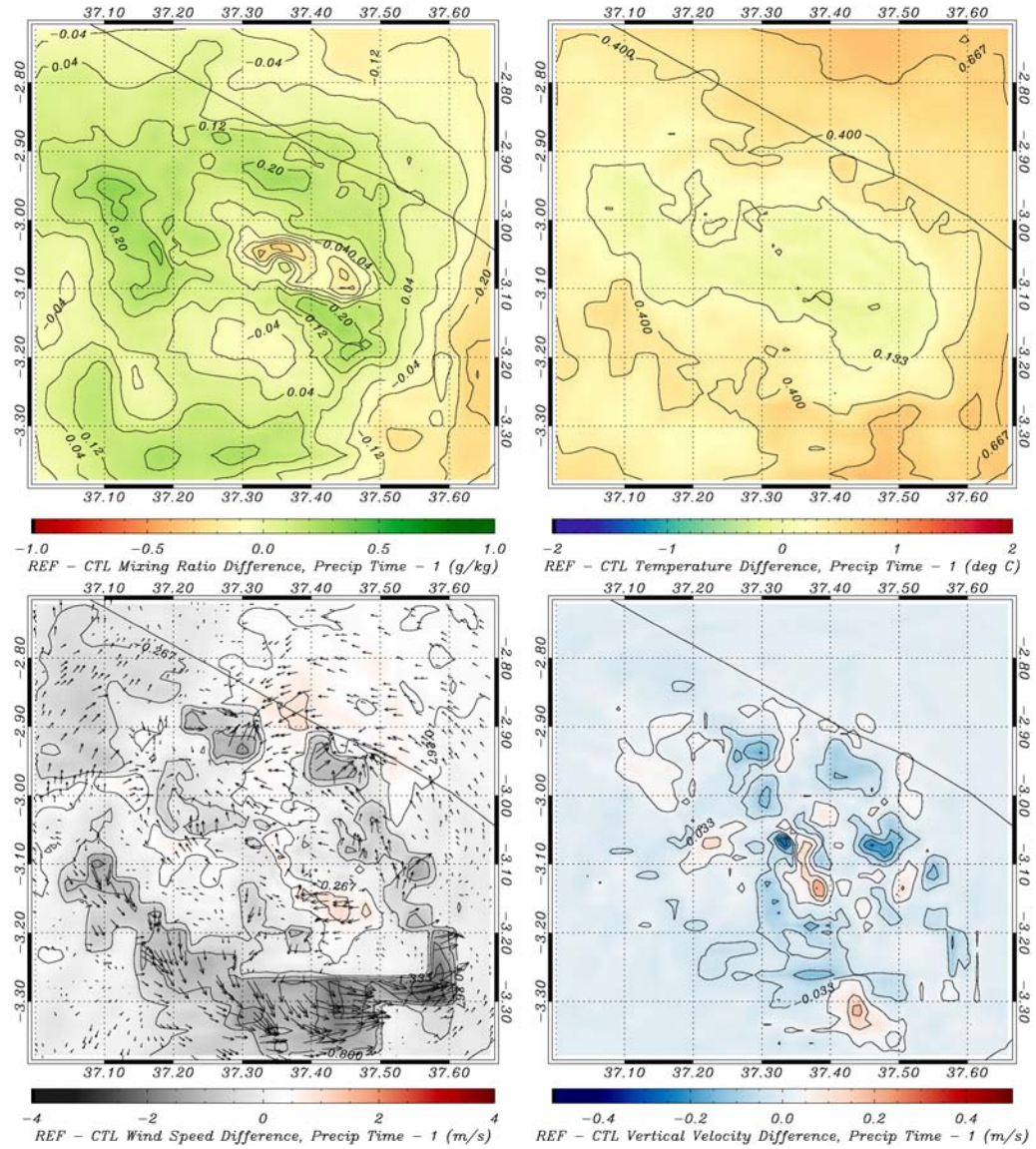

Figure 6.30 Same as Figure 6.29, except for precipitation occurrence.

precipitation occurrence in March for the DEF simulation, when synoptically there is an excess in moisture availability due to passage of the ITCZ. Since more precipitation at high elevation occurs during this month, the synoptic moisture input dominates. There also is less of a reliance on the thermal circulation in order for precipitation to occur, as the moisture is not generated locally due to transpiration from the forested areas as the cases are for the REF and CTL simulations, as is shown in Figures 6.27 and 6.28.

The most interesting aspect of these simulations is the high increase of precipitation at the peak in the DEF simulation when comparing to the REF and CTL simulations. While there is on average less precipitation over the entire grid of 39.3 mm per point, there is an increase of 176 mm at high elevations when compared to the CTL simulation and 150 mm when compared to the REF simulation. This happens because of enhanced vertical velocities present during precipitation occurrence, as well as the high amounts of moisture available due to synoptic inputs. While the REF and CTL simulations have more times of precipitation at the peak in comparison to the DEF simulation, more precipitation falls at higher elevations in the DEF simulation, increasing the amount of extreme events. Since the moisture availability is much higher in the DEF simulation than the REF or CTL, there can be more moisture transported into rain and more towering cumulus occurring due to enhanced vertical velocity caused by higher mechanical forcing due to the higher wind speeds caused by lower surface roughness. Without the additional roughness of the forested areas, there are higher mechanically-driven vertical velocities to transport the additional moisture present in the atmosphere to high elevations at the surface to fall as precipitation.

Since we have focused on cloud and precipitation occurrence at high elevations, it begs the question about the effects that would be felt from these differing land use scenarios on the mountain glacier, and the impacts that can be felt due to these local changes. The primary inputs in a mass balance model for a tropical glacier are solar radiation and solid precipitation. Since all three simulations show a consistent below-freezing temperature at the peak, there is little difference in the amount of temperature-driven melt that would occur. There is also little difference in the frequency of clouds at high elevation, therefore leaving the amount of precipitation to be the primary difference. What is interesting based on these results is that complete deforestation would provide more solid precipitation to the glacier, but less frequently than the CTL or REF simulation. Since there is little change in the solar radiation at the peak, there could be additional glacier loss due to the snow aging in the DEF simulation than in the CTL or REF simulation. The REF simulation increases the average amount of precipitation at elevations over 5000 m by 25 mm, but also has more frequent precipitation events. This would keep the snow albedo higher, as well as provide more input to the glacier surface than the CTL simulation.

The role of Kilimanjaro's forests, therefore, seems to act by insulating the mountain from synoptic-level atmospheric changes through enhancement of the local thermal circulation. With additional forested areas, there can be a deficit in the synoptically provided moisture fields that would cause more precipitation to occur at high elevations, as well as precipitation being more frequent than the current day scenario. With the partial loss of the forested areas as seen today, and the continuing loss due to additional farming on the slopes, there is less forested area to provide moisture excesses

and enhance the thermal circulation. However, with a complete loss of forested areas, there is a much stronger dependence on synoptic moisture levels. These findings are consistent with the findings of *Molg et al.* [2008a], which hypothesized the local anthropogenic forcing due to land use change could be super-imposed on a larger-scale climate forcing, as well as the importance of synoptic moisture input that could be related to a switch in the Indian Ocean dipole [*Molg et al.*, 2006].

6.6 Conclusions

This study used one year of numerical modeling simulations to investigate the impact of land cover changes on the regional climate of Kilimanjaro, with a particular focus on those parameters that would impact orographic convection and therefore the remnant glaciers on the peak. RAMS was used to simulate atmospheric conditions for a time period of 366 days ranging from July 1, 2007 through June 30, 2008 assuming current-day, deforested, and reforested land cover scenarios. The findings can be summarized as follows.

1. On average, deforestation causes increases in temperature and wind speed on the slopes of Kilimanjaro while causing a deficit of surface moisture. Additional forested areas decrease the wind speed due to higher surface roughness and increase average moisture availability.

2. Deforestation causes a deficit in cloud frequency at lower elevations, but little change occurs at high elevations. Additional forested areas increases cloud frequency, particularly at elevations around 4000 m.

3. Grid averaged precipitation decreases with deforestation and increases with additional forested area. However, precipitation at the peak increases the most in the deforested case due to high synoptic moisture availability and enhanced mechanical uplift due to higher wind speeds.

4. Reforestation increases the strength of the thermal circulation, with a higher percentage of cloud and precipitation occurrence during the afternoon hours than the current or deforested scenarios, with enhanced moisture transport on a diurnal basis and a higher free air to surface temperature gradient.

5. The additional forested areas transport moisture up the mountain prior to precipitation and cloud occurrence, requiring less synoptic moisture for convection to occur. The amount of synoptic moisture necessary for convection to occur increases with decreasing forest cover. In this way, the montane forests insulate the peak from synoptic change.

6. Deforestation causes differences in the seasonality of the precipitation at the peak, since there is a stronger dependence on the synoptic influence and less of a dependence on local processes. The warming of free-atmosphere air mitigates the temperature gradient between the surface and the air, causing less pressure gradient force to develop, thereby weakening the thermal circulation.

7. Land cover change effects are much more prevalent during the wet season months than the dry season months at high elevations for Mount Kilimanjaro as shown by distribution of the convective events over the course of the year.

8. The state of current-day deforestation impacts the glacier by weakening the thermal circulation, causing less moisture to be transported upslope. This decreases the annual average precipitation by 25 mm, but also decreases frequency of precipitation events, causing the ice to age more and lead to further melting. Deforestation also subjects the glacier to more synoptic input, making any synoptic change become more prevalent.

Future research would involve examining the effects of the El Niño-Southern Oscillation on the moisture patterns surrounding Mount Kilimanjaro by performing this analysis during positive and negative cycles and these land use classifications. Based on these results, the large-scale changes will have a much higher impact in the current and any further deforested land use classifications. We also plan to simulate the glaciers directly using our model output to look at the mass balance that would result from these scenarios, since it is unknown how much the aging of the snow caused by the less frequent snowfall present in the DEF scenario will impact the mass balance compared to the more frequent snowfall in the REF scenario.

CHAPTER 7

CONCLUSIONS AND FUTURE WORK

This study used the Regional Atmospheric Modeling System (RAMS) to characterize the annual progression of atmospheric flow, cloud and precipitation formation on Kilimanjaro. Analysis of these numerical simulations is used to quantify terrain forcing contributions to the regional climate as well as the modulation of the same by land cover change. Numerical modeling simulations are also used to understand processes through which the terrain forcing and land cover change effect regional climate. Review of literature suggests that one of the unique aspects of the present study is that this study utilizes dynamic downscaling over complex terrain at a spatial resolution and timescale that is unprecedented. This dissertation also presents the most detailed analysis of flow patterns, cloud and precipitation formation over Kilimanjaro available at present. This chapter provides an overall summary of the research findings as well as basic implications of our study and how this fits within a longer-term approach of modeling, remote sensing, and monitoring of the climate of Kilimanjaro.

This study analyzed the seasonal changes of meteorology at Kilimanjaro, significantly advancing the state of knowledge based on prior studies. Prior studies had

either concentrated on specific case days [*Molg et al.*, 2009] or was limited in time to one or two months [*Fairman et al.,* 2011; *Molg and Kaser,* 2011], or was not at a high enough resolution [*Ge et al.*, 2008]. The state of knowledge, prior to the present study, was based on extrapolations of these limited set of numerical simulations. This study quantifies the base meteorological parameters: mixing ratio, temperature, and wind speed/direction that are present while atmospheric convection is occurring at high elevations, and has quantified how much precipitation occurs based on diurnal processes and through seasonal progression. The study also examined exactly what caused a difference between formation of cloud and precipitation, noting the changes in wind speed and direction as well as mixing ratio in order to find the atmospheric states that are necessary for formation of orographic convection.

The results from this study is in agreement with prior modeling studies concerning the flow reversal present in February [*Molg et al.*, 2009] as well as conceptual descriptions of the thermal circulation [*Pepin et al.*, 2010]. Along with rigorous validation with satellite and in-situ observations, this study provides a one-year dataset at one kilometer grid spacing in a very high elevation area that is very much of interest to the meteorological community. Modeling runs conducted without the mountain (described as the NOTOPO simulation in Chapter 3) quantified the impact that the mountain has on the local wind field, with the rainy seasons of SON and MAM providing much less blocking than the "dry" seasons of DJF and JJA. Without the mountain, the winds are fairly uniform throughout the atmosphere in the 75 x 75 km area comprising grid G4 in this study. When comparing precipitation from the NOTOPO simulation to the CTL simulation, we can attribute differing numbers at differing elevations to account

for the precipitation that is generated via local processes compared to those directed from synoptic processes, with over 80% of the precipitation at the middle elevations being associated with local processes.

The analysis conduced in this study provides a basis for downscaling synoptic input from global circulation model simulations that do not resolve Kilimanjaro adequately. For example, for precipitation to occur at high elevation on Kilimanjaro, the mixing ratio is on average 13 g/kg, or 1.5 g/kg greater than the value where no precipitation occurs. Therefore, a drop of mixing ratio of 1.5 g/kg will severely limit the amount of precipitation that forms at the peak, assuming the current flow scenarios. If there was a decrease in mixing ratio of around this magnitude in a future climate scenario, we would be able to know that the precipitation on the peak would be greatly impacted and decline greatly.

Chapter 5 discusses land use change impacts during the dry season on Mount Kilimanjaro. Results from one month of analysis led to conclusions that the primary effect of land cover change during the dry season was mainly dynamic, (changing wind speeds and direction) versus thermodynamic (changing the air temperature and moisture patterns). The additional roughness present via the forested areas led to lower wind speeds with increasing forested cover; therefore, altering the flow patterns to cause more air to flow around the mountain versus flowing over the mountain. This led to changes in the upwind cloud cover and precipitation, with higher elevations of maximum precipitation present in the DEF simulation, but overall, total precipitation decreased with decreasing amounts of forested cover. During the dry season, there is little deep convection occurring on the slopes of Kilimanjaro, due to higher stability and much less

environmental moisture. There was no simulated cloud cover or precipitation that occurred at high elevations (>5000 m), leading to the conclusion that land cover change impact on the glacial environment at the peak is minimal during the dry season.

Land cover change impact on the regional climate over annual time scales was found to be significant, which extends the analysis of the dry season found in Chapter 5 [*Fairman et al.*, 2011]. In the dry season, there is minimal impact of the thermal circulation (as well as the thermal circulation being much more benign), whereas the impact of the thermal circulation is more prominent in other seasons. Since there are also changes in the flow patterns with this ITCZ transition, it is necessary to find out the impact that land cover change has in differing seasons as well, since the areas that are forested are mainly on the south side of the mountain.

The land cover scenarios described in this study were found to have strong impacts on the regional climate, particularly in the formation of orographic convection. Based on prior studies [*Lawton et al.*, 2001; *Ray et al.*, 2006] deforestation and reforestation were expected to be accompanied by effects such as raising the cloud base and maximum elevation of cloudiness with decreasing forested cover. However, the present study also found that the sensitivity of the thermal circulation to land cover change was particularly pronounced. In the reforested simulation, less upstream moisture is required for convection to occur at high elevations compared to the current-day, whereas in the deforested simulation, more is required. While there is a net average reduction in moisture availability with reducing forest cover, the strong precipitation days associated with the passage of the ITCZ enhance extreme precipitation at the peak. The forested areas function as a blanket to the high elevations, insulating the mountains from

synoptic change via invigoration of the thermal circulation. With the complete loss of forested area, there is a high reliance on synoptic weather parameters, particularly the moisture provided via transition of the ITCZ. Given the work that has been performed via *Molg et al.* [2006], linking the loss of the glaciers to a drying trend, this analysis implies that the current-day vegetation state has exacerbated the loss of the glacial surface.

However, the loss of forested area reduces the effects of the thermal circulation, due to changes in Bowen ratio causing the free-air temperatures to rise via additional sensible heating. This additional heating reduces the pressure gradient between the free air and the mountain surface, weakening the winds that would form towards the slope and therefore not allowing the thermal circulation to become as strong. As a corollary, this weakening of local circulations allows any larger scale climate changes to have more of an effect. Based on this analysis if deforestation increases in the future, the sensitivity of the glacial environment to synoptic-level climate change will increase. If the synoptic moisture increases in the tropics, than we could very well see an enhancement of precipitation at the peak with additional deforestation due to the maximization of upslope winds causing more extreme high-elevation precipitation; however, with replanting of the forested areas we should see a more immediate effect.

These model simulations have identified factors that are crucial to formation of clouds around Kilimanjaro, but there are still some interesting questions that these simulations raise. For example, the 0° C line is much lower than the peak, as the glaciers are typically well below freezing at all times. Snow falls on the slopes of Kilimanjaro, and will continue to fall in the future even though the permanent ice may not exist. What

is not currently quantified is the actual dwell time of the snow on the slopes of Kilimanjaro. The daily cloud extent is also not resolved to examine due to lack of observations on a diurnal basis. A network of digital cameras set up around Kilimanjaro aimed at the peak would be able to find out the frequency of snowfall on the slopes as well as being able to define the dwell time of that snow, as well as to give insight on the diurnal dependence of high elevation cloud formation.

The model results this study presents do not necessarily indicate the true impact on the glacier. What would be necessary in the future would be to incorporate a full snow model into an atmospheric model, with a two-way coupling in order to find out the daily snowfall on the peak as well as the loss due to sublimation (which would be the primary factor in glacier loss at these elevations). This could than be used with various atmospheric situations (El Niño and La Niña cycles, for example) as well as downscaling past climates in order to gain knowledge of what the atmospheric cases were that would support the formations of ice sheets on the peak of Kilimanjaro. In the future, it would be very interesting to take a paleoclimatic perspective on the Kilimanjaro situation by using a last glacial maximum climate analysis (such as CLIMAP) and using RAMS to downscale the climate to examine the thermal circulation with differing synoptic temperature and moisture conditions. Tying in the mass and energy balance for this past scenario would be quite interesting to see if we could match past glacial extents, such as those mapped by *Osmaston* [1965].

A simple first step would be to use these climate scenarios to drive an existing mass and energy balance model, such as that of *Plummer et al.* [2002], which was used in *Fairman* [2006] to examine tropical glaciers in the Cordillera Blanca. Initial simulations

using the RAMS-derived climate found in this study show permanent ice formation at the peak and do not simulate the current glacier locations. However, the model acts using monthly-mean data and reconstructs the ice sheet at equilibrium status, whereas the current ice features are in consistent decline.

These future paths show the impact that this type of analysis can have. Long term modeling at high grid spacing can have implications that relate back to global climate change as well as finding the local sensitivity to the current day. In this case, this study provides a unique look at the climate of Kilimanjaro, the impact of land cover change on the regional climate, and the dependence of the local processes on synoptic input. Currently, these simulations require supercomputing access to complete, whereas with future processing advances, the current short-term simulations will be able to be extended and the resolutions will be able to increase for current regional studies, which will greatly increase the studies of this type.

REFERENCES

Ackerman, S. A., K. I. Strabala, W. P. Menzel, R. A. Frey, C.C. Moeller, and L. E. Gumley (1998), Discriminating clear sky from clouds with MODIS, *J. Geophys. Res., 103*, D24, doi:10.1029/1998JD200032.

Ackerman, S.A., R. E. Holz, R. Frey, E. W. Eloranta, B. C. Maddux, and M. McGill (2008), Cloud detection with MODIS. Part II: Validation. *J. Atmos. Oceanic Technol., 25*, 1073-1086.

Barry, R.G. (2008), *Mountain Weather and Climate*, 3rd ed, Cambridge University Press, 512 pp.

Bruijnzeel, L. A. (2004), Hydrological functions of tropical forests: Not seeing the soil for the trees?, *Agric. Ecosyst. Environ., 104,* 185– 228.

Camberlin, P. and N. Philippon (2002), The east African March-May rainy season: Associated atmospheric dynamics and predictability over the 1968-97 period, *J. Clim., 15:9*, 1002-1019.

Castro, C.L., R. A. Pielke Sr., and G. Leoncini (2005), Dynamical downscaling: Assessment of value retained and added using the Regional Atmospheric Modeling System (RAMS), *J. Geophys. Res., 110*(D5), D05108, doi:10.1029/2004JD004721.

Chan, R.Y., M. Vuille, D.R. Hardy and R.S. Bradley (2008), Intraseasonal precipitation variability on Kilimanjaro and the East African region and its relationship to the large-scale circulation. *Theoret. Appl. Climatol., 93,* 149-165.

Chase, T.N., R.A. Pielke, Sr., T. G. F. Kittell, J. S. Baron, and T. J. Stohlgren, (1999) Potential impacts on Colorado Rocky Mountain weather due to land use changes on the adjacent Great Plains, *J. Geophys. Res., 104*, D14, doi:10.1029/1999JD90011

Chen, C. and W.R. Cotton (1983), A one-dimesional simulation of the stratocumulus-capped mixed layer, *Bound-Layer Meteor.*, *25*, 2889-321

Cullen, N. J., T. Mölg, G. Kaser, K. Hussein, K. Steffen, and D. R. Hardy (2006), Kilimanjaro glaciers: Recent areal extent from satellite data and new interpretation of observed 20th century retreat rates, *Geophys. Res. Lett., 33*, L16502, doi:10.1029/2006GL027084.

Christy, J.R., W.B. Norris, and R.T. McNider (2009), Surface temperature variations in East Africa and possible causes, *J. Clim.*, *22*, 3342-3356.

Cotton, W.R., et al. (2003), RAMS 2001: Current status and future directions, *Meteorol. Atmos. Phys.*, *82*, 5-29, doi:10.1007/s00703-001-0584-9.

Fairman, J.G., U.S. Nair, S.A. Christopher, and T. Molg (2011), Land use change impacts on regional climate over Kilimanjaro, *J. Geophys. Res.*, *116*, D03110, doi:10.1029/2010JD014712.

Food and Agriculture Organization (1971), Soil map of the world, scale 1:5,000,000, vol. II– X, U.N. Educ., Sci., and Cult. Organ., Paris.

Frey, R.A., S.A. Ackerman, Y. Liu, K. I. Strabala, H. Zhang, J.R. Key, and X. Wang (2008), Cloud detection with MODIS. Part I: Improvements in the MODIS cloud mask for Collection 5, *J. Atmos Oceanic Technol.*, *25*, 1057-1072.

Fuhrer, O. and C. Schar (2005), Embedded cellular convection in moist flow past topography, *J. Atmos. Sci*, *62*, 2810-2828, doi:10.1175/JAS3512.1.

Ge, J., J. Qi, B. M. Lofgren, N. Moore, N. Torbick, and J. M. Olson (2007), Impacts of land use/cover classification accuracy on regional climate simulations, *J. Geophys. Res.*, *112*, D05107, doi:10.1029/2006JD007404.

Gerakis, A., and B. Baer (1999), A computer program for soil textural classification, *Soil Sci. Soc. Am. J.*, *63*, 807– 808.

Harrington, J.Y. (1997), *The effects of radiative and microphysical processes on simulated warm and transition season Arctic stratus*, PhD Dissertation, Atmospheric Science paper No 637, Colorado State University, Department of Atmospheric Science, Fort Collins, CO.

Hastenrath, S. (1991), *Climate Dynamics of the Tropics*, Kluwer Academic Publishers, Norwell, MA.

Hastenrath, S. (2000), Zonal circulations over the equatorial Indian Ocean, *J. Clim., 13*, 2746– 2756.

Hastenrath, S. (2006), Diagnosing the decaying glaciers of equatorial East Africa, *Meteorol. Z., 15*, 265– 271, doi:10.1127/0941-2948/2006/0106.

Hastenrath, S. and L. Geischar (1997), Glacier recession on Kilimanjaro, East Africa, 1918-1989, *J. Glaciol, 43*, 145, 455-459.

Hemp, A. (2005), Climate change driven forest fires marginalizes the ice cap wasting on Mt. Kilimanjaro, *Glob. Change Biol. 11*, 1013-1023. doi: 10.1111/j.1365-2486.2005.00968.x

Hemp, A. (2009), Climate change and its impact on the forests of Kilimanjaro, *African J. Ecology, 47*, 3-10, DOI: 10.1111/j.1365-2028.2008.01043.x.

Intergovernmental Panel on Climate Change (IPCC) (2007), *Climate Change 2007: The Physical Science Basis. Contribution of Working Group I to the Fourth Assessment Report of the Intergovernmental Panel on Climate Change,* edited by S. Solomon et al., Cambridge University Press, Cambridge, United Kingdom and New York, NY, USA.

Jarvis, A., J. Rubiano, A. Nelson, A. Farrow, and M. Mulligan (2004). Practical use of SRTM data in the tropics—comparisons `with digital elevation models generated from cartographic data. *Working Document, 198*. Centro Internacional de Agricultura Tropical (CIAT), Cali, Colombia, 32 pp.

Jiang, Q. (2003), Moist dynamics and orographic precipitation, *Tellus, Ser. A, 55*, 301-316.

Justice, C., et al. (1998), The Moderate Resolution Imaging Spectroradiometer (MODIS): Land remote sensing for global change research, *IEEE Trans. Geosci. Remote Sens., 36,* 1228– 1249.

Kain, J.S. and J.M. Frisch, (1990), A one-dimensional entraining detraining plume model and its application in covective parameterization, *J. Atmos. Sci, 47,* 2784-2802.

Kaser, G. and H. Osmaston (2002), *Tropical Glaciers*, Cambridge Univ. Press, New York.

Kaser, G., D. R. Hardy, T. Mölg, R. S. Bradley, and T. M. Hyera (2004), Modern glacier retreat on Kilimanjaro as evidence of climate change: Observations and facts, *Int. J. Climatol., 24,* 329– 339.

Kirshbaum, D.J. and D.R. Durran (2004), Factors governing cellular convection in orographic precipitation, *J. Atmos. Sci., 61,* 682-698, doi:10.1175/1520-0469(2004)061<0682:FCCIO>2.02CO;2

Klemp, J.B and R.B. Wilhelmson (1978), The simulation of three-dimensional convective storm dynamics, *J. Atmos. Sci.* 35:1070-1096

Kummerow, C., W. Barnes, T. Kou, J. Shiue, and J. Simpson (1998), The Tropical Rainfall Measuring Mission (TRMM) sensor package, *J. Atm. Oc. Tech., 15,* 809-917.

Lambrechts, C., B. Woodley, A. Hemp, C. Hemp and P. Nnyiti (2002) *Aerial Survey of the Threats to Mt. Kilimanjaro Forests*. Dar es Salaam: UNDP, GEF Small Grants Programme.

Lawton, R. O., U. S. Nair, R. A. Pielke, and R. M. Welch (2001), Climatic impact of tropical lowland deforestation on nearby montane cloud forests, *Science, 294,* 584– 587.

Latif, M., et al. (1999), The role of Indian Ocean se surface temperature in forcing East African raingall anomalies during December-January 1997/1998, *J. Climate, 12*, 3497-3504.

Lilly, D.K (1962), On the numerical simulation of buoyant convection, *Tellus, XIV*, 148-172.

Loveland, T.R., et al. (2000), Development of a global land cover characteristics database and IGBP DISCover from 1 km AVHRR data, *Int. J. Remote Sensing, 21*, 6-7, 1303-1330.

Mahrer, Y. and R.A. Pielke (1977), A numerical study of the airflow over irregular terrain, *Beitrage zur Physic der Atmosphare*, 50, 98-113.

Mellor, G.L. and T. Yamada (1982), Development of a turbulence closure model for geophysical fluid problems, *Rev. Geophys. Space Phys., 20*, 851-875.

Mark, B.G. and H.A. Osmaston (2008), Quaternary glaciation in Africa: Key chronologies and climatic implications, *Journ. Quaternary Sci., 23* (6-7), 589-608, doi:10.1002/jqs.1222.

Miao, J.F., et al. (2007), Evaluation of MM5 mesoscale model at local scale for air quality applications of the Swedish west coast: Influence of PBL and LSM parameterizations, *Meteor. Atmos. Phys., 99*, 77-103.

Mölders, N. (2008), Suitability of the Weather Research and Forecasting (WRF) Model to predict the June 2005 fire weather for interior Alaska, *Weather and Forecasting, 23*, 953-973.

Mölg, T. and D.R. Hardy (2004), Ablation and associated energy balance of a horizontal glacier surface on Kilimanjaro. *J. Geophys. Res. 109*, D16104, doi: 10.1029/2003JD004338.

Mölg, T., D.R. Hardy, and G. Kaser (2003), Solar-radiation-maintained glacier recession on Kilimanjaro drawn from combined ice-radiation geometry modeling. *J. Geophys. Res., 108*, 4731, doi: 10.1029/2003JD003546.

Mölg, T., M. Renold, M. Vuille, N.J. Cullen, T.F. Stocker, and G. Kaser (2006), Indian ocean zonal mode activity in a multicentury-integration of a coupled AOGCM consistent with climate proxy data. *Geophys. Res. Let., 33*, L18710, DOI: 10.1029/2006GL026384.

Mölg, T., N. J. Cullen, D. R. Hardy, and G. Kaser, (2008a): Tropical glaciers in the context of climate change and society: Focus on Kilimanjaro (East Africa), *The Darkening Peaks: Glacial Retreat in Scientific and Social Context*, B. Orlove, E. Wiegandt, and B. Luckman, Eds., Univ. of Calif. Press, Berkeley, 168-184.

Mölg, T., N. J. Cullen, D. R. Hardy, G. Kaser, and L. Klok (2008b), Mass balance of a slope glacier on Kilimanjaro and its sensitivity to climate, *Int. J. Climatol., 28*, 881-892.

Mölg, T., J.H.C. Chiang, A. Gohm, and N.J. Cullen (2009a): Temporal precipitation variability versus altitude on a tropical high mountain: Observations and mesoscale atmospheric modeling, *Q. J. R. Meteorol. Soc., 135*, 1439-1455.

Mölg, T., N. J. Cullen, D. R. Hardy, M. Winkler, and G. Kaser (2009b), Quantifying climate change in the tropical midtroposhere over east Africa from glacier shrinkage on Kilimanjaro, *J. Clim., 22*, 4162-4181.

Mölg, T, and G. Kaser (2011), A new approach to resolving climate-cryosphere relations: Downscaling climate dynamics to glacier-scale mass and energy balance without statistical scale linking, *J. Geophys. Res., 116,* D16101, doi:10.1029/2011JD015669.

Mote, P.W., and G. Kaser (2007), The shrinking glaciers of Kilimanjaro: Can global warming be blamed? American Scientist, *95*, 318-325.

Mutai, C.C. and M.N. Ward (2000), East African rainfall and the tropical circulation/convection on intraseasonal to interannual timescales, *J. Climate, 13*, 3915-3939.

Nair, U. S., R. O. Lawton, R. M. Welch, and R. A. Pielke Sr. (2003), Impact of land use on Costa Rican tropical montane cloud forests: Sensitivity of cumulus cloud field characteristics to lowland deforestation, *J. Geophys. Res., 108*, D7, 4206, doi:10.1029/2001JD001135.

Nair, U. S., S. Asefi, R. M.Welch, D. K. Ray, R. O. Lawton,V. S. Manoharan, M. Mulligan, T. L. Sever, D. Irwin, and A. Pounds (2008), Biogeography of tropical montane cloud forests. Part II: Mapping of orographic cloud immersion, *J. Appl. Meteorol. Climatol., 47*, 2183 – 2197, doi:10.1175/2007JAMC1819.1.

Nair U. S., D. K. Ray, R. O. Lawton, R. M. Welch, R. A. Pielke Sr., and J. Calvo (2010), Impact of deforestation on orographic cloud formation in a complex tropical environment, *Mountains in the Mist, Science for conserving and managing Tropical Montane Cloud Forest*. L.A. Bruijnzeel, J.Juvik, F.N. Scatena, L.S. Hamilton and P. Bubb (Eds.), Cambridge University Press, 538-548.

Olson, J. S., (1994), Global Ecosystems Framework: Definitions. Internal Report, USGS EROS Data Center, Sioux Falls, SD, USA, 37p.

Osmaston, H.A (1965), *The Past and Present Climate and Vegetation of Ruwenzori and Its Neighbourhood*, DPhil thesis, University of Oxford, Oxford, UK.

Paegle, J. and J.E. Geisler (1986), The effect of East African topography on flow driven by zonally symmetric forcing, *J. Atmos. Sci., 43*, 1862-1872.

Pepin, N.C., W.J. Duane, and D.R. Hardy (2010), The montane circulation on Kilimanjaro, Tanzania, and its relevance for the summit ice fields: Comparison of surface mountain climate with equivalent reanalysis parameters, *Global Planetary Change, 74*(2), 61-75, doi:10.1016/jglobplacha.2010.08.001

Pielke Sr., R. A. (2002), *Mesoscale Meteorological Modeling*, International Geophysics Series 78, Academic Press, San Diego, CO.

Plummer, M.A. and F.M. Philips, A 2-D numerical model of snow/ice energy balance and ice flow for paleoclimatic interpretation of glacial geomorphic features, *Quaternary Sci. Rev., 22*, 14, 1389-1406, doi:10.1016/S0277-3791(03)00081-7

Pounds, A. J., M. P. L. Fogden, and J. H. Campbell (1999), Biological response to climate change on tropical mountain, *Nature, 389*, 611– 614.

Ray, D. K., U. S. Nair, R. O. Lawton, R. M. Welch, and R. A. Pielke Sr. (2006), Impact of land use on Costa Rican tropical montane cloud forests: Sensitivity of orographic cloud formation to deforestation in the plains, *J. Geophys. Res., 111*, D02108, doi:10.1029/2005JD006096.

Ray, D.K., R.A. Pielke, Sr., U.S. Nair, and D. Niyogi, (2010), Roles of atmospheric and land surface data in dynamic regional downscaling, *J. Geophys. Res., 115*, D05102, doi:10.1029/2009JD012218.

Rienecke, P.A. and D.R. Durran, (2008), Estimating the orographic blocking using a Froude number when the static stability is nonuniform, *J. Atmos. Sci, 65,* 1035-1048.

Røhr P.C. and Å. Killingtveit (2003): Rainfall distribution on the slopes of Mt. Kilimanjaro. *Hydrological Science-Journal-des Sciences Hydrologiques, 48,* 65-78.

Rotunno, R. and R. A. Houze (2007), Lessons on orographic precipitation from the Mesoscale Alpine Programme, *Q.J.R. Meteorol. Soc., 133,* 934-948, doi:10.1002/qj.71

Salathe, E. P., R. Steed, C.F. Mass., and P.H. Zahn (2008), A high-resolution climate model for the U.S. Pacific Northwest: Mesoscale feedbacks and local responses to climate change, *J. Climate, 21,* 5708-5726, doi:10.1175/2008JCLI2090.1

Schär, C. (2002), Mesoscale mountains and the larger-scale atmospheric dynamics: A review. *Meteorology at the Millenium,* edited by R.P. Pearce, 29-42. New York: Academic Press.

Shanahan, T.M. and M. Zreda (2000), Chronology of quaternary glaciations in East Africa, *Earth and Plan. Sci. Let., 177,* 23-42.

Smagorinsky, J. (1963), General circulation experiments with the primitive equations I: The basic experiment, *Mon. Wea. Rev. 91,* 99-164.

Soini, E. (2005), Land use change patterns and livelihood dynamics on the slopes of Kilimanjaro, Tanzania, *Agricultural Systems, 85:*3, 306-323, doi:10.1016/j.agsy.2005.06.013.

Still, C. J., P. N. Foster, and S. H. Schneider (1999), Simulating the effects of climate change on tropical montane cloud forests, *Nature, 389,* 608–610.

Thompson, L. G., et al. (2002), Kilimanjaro ice core records: Evidence of Holocene climate change in tropical Africa, *Science, 298,* 589–593.

Thompson, L.G., et al. (2009) Glacier loss on Kilimanjaro continues unabated, *Proc. Natl. Acad. Science*, *106*, 47, 19770-19775, doi:10.1073/pnas.0906029106

Torbick, N, J.Ge, and J. Qi (2009), Changing surface conditions at Kilimanjaro indicated from multiscale imagery, *Mountain Res. and Devel.*, *29*, 1, 5-13, doi:10.1659/mrd.981.

Tremback, C. J. (1990) Numerical simulation of a mesoscale convective complex: Model development and numerical results, *Atmos. Sci. Pap. 465*, Dep. Of Atmos. Sci., Colo. State Univ., Fort Collins.

Van der Molen, M. K. (2002), *Meteorological Impacts of Land Use Change in Maritime Tropics*, Ph.D. thesis, Vrije Univ., Amsterdam, Netherlands

Van der Molen, M. K., H. F. Vugts, L. A. Bruijnzeel, F. N. Scatena, R. A. Pielke Sr., and L. J. M. Kroon (2006), Mesoscale climate change due to lowland deforestation in the maritime tropics, in *Mountains in the Mist: Science for Conserving and Managing Tropical Montane Cloud Forest*, edited by L. A. Bruijnzeel et al., Univ. of Hawaii Press, Honolulu, in press.

Walko, R. L., et al. (2000), Coupled atmosphere-biophysics-hydrology models for environmental modeling, *J. Appl. Meteorol.*, *39*, 931–944.

Wastl, C. and G. Zangl (2010), Mountain-valley precipitation differences in the northern Alps: An exemplaray high-resolution modeling study, *Meteorol. Atmos. Phys.*, *108*, 29-42, doi:10.1007/s00703-010-0083-y.

Whiteman, C.D. (2000), *Mountain Meteorology: Fundamentals and Applications*, Oxford University Press, Oxford, UK.

Zhong, S. and J. D. Fast, (2003), An evaluation of the MM5, RAMS and Meso-Eta models at subkilometer resolution using VTMX field campaign data in the Salt Lake Valley, *Mon. Wea. Rev.*, *131*, 1301-1322.